Chemical Functionalization of Single-walled Carbon Nanotubes for Compatibilization with Unsaturated Polyester Resin

by

Matthew J. Kayatin

A dissertation submitted to the Graduate Faculty of
Auburn University
in partial fulfillment of the
requirements for the Degree of
Doctor of Philosophy

Auburn, Alabama
May 7, 2012

Keywords: Carbon Nanotube, Unsaturated Polyester Resin, Dispersion, Functionalization

Approved by:

Virginia A. Davis, Chair, Associate Professor of Chemical Engineering
W. Robert Ashurst, Associate Professor of Chemical Engineering
Steve R. Duke, Associate Professor of Chemical Engineering
Anne E. V. Gorden, Associate Professor of Chemistry

Abstract

This research represents the first fundamental investigation into the tailored surface chemistry of single-walled carbon nanotubes for incorporation with unsaturated polyester resin and provides a foundation for the development of a novel polymer nanocomposite or dispersion based on these two materials. The primary phenomenon limiting the applicability of single-walled carbon nanotubes (SWNT) in polymeric nanocomposites is a lack of nanotube dispersibility due to their intrinsically strong van der Waals attraction. Overcoming this problem for an industrially relevant polymer, such as unsaturated polyester resin, will enable great potential for applications requiring high-strength and lightweight materials. In order to facilitate these advances, the chemical functionalization of SWNT was examined for compatibilization with unsaturated polyester resin.

Guided by potential physicochemical interactions between the components, both covalent and non-covalent nanotube functionalization routes were investigated. Utilizing two known methods for individualization, reduction and sonication, nanotube surfaces were exposed for functionalization. It was found that the accessibility of desired surface chemistries was dependant on the individualization method used. For example, ester surface functionalization was not possible by nanotube reduction. Therefore, chemical functionalization schemes deemed appropriate for the method of individualization were pursued and developed in this work.

The sidewall esterification of SWNT was achieved through sonication using the Bingel reaction. Due to strong adsorption, the presence of 1,2-dichlorobenzene sonopolymer by-product

limited the dispersibility of the Bingel functionalized nanotubes. Based on resonant Raman spectroscopy, it was discovered that sonication of CoMoCAT SWNT in 1,2-dichlorobenzene did not induce doping, but damaged sp^2 hybridized carbons. The mechanical instability of so-called "non-SWNT" carbons towards sonication was discovered using careful thermogravimetric measurements. Furthermore, sonication degradation residues were found to skew the interpretation of functionalization effects. These "non-SWNT" carbons were identified to be high purity double-walled carbon nanotubes and multi-walled carbon nanotubes by resonant Raman spectroscopy and high-resolution transmission electron microscopy.

A functionalization scheme enabled by nanotube reduction was adapted for the in-situ polymerization functionalization of styrene, and optimized to achieve a high extent of sidewall modification. This methodology was evaluated using previously well-characterized SWNT reactions, such as reductive alkylation. The potential use of this single-pot functionalization method with a variety of unsaturated monomers extends the range of SWNT applications in polymers.

Finally, the passivation of single-walled carbon nanotubes with polyvinylpyrrolidone was an effective means for compatibilization. This was a result of this polymer's molecular solubility in unsaturated polyester resin, as discovered spectroscopically. By focusing on fundamental physicochemical interactions such and hydrogen bonding and doping, the decoupling and understanding of processing effects was possible for this system.

Based on the overall results of this study, two schemes were recommended for SWNT dispersion in unsaturated polyester resin: chemical modification based on the in-situ polymerization functionalization methodology and non-covalent stabilization with polyvinylpyrrolidone.

Acknowledgements

I would like to express my sincere gratitude for my committee's time and advice in the preparation of this manuscript. In addition, thank you to my outside reader, Dr. Michael Hamilton, for making special accommodations for my defense. Thank you to the U.S. Department of Defense and the U.S. Department of Education G.A.A.N.N. Fellowship for providing financial support for both this work and my academic studies. A special thanks to Brian Schweiker for access to his workshop and his expertise. Thank you to Dr. Virginia Davis, Dr. Christopher Roberts, and Dr. Anne Gorden for advice on many things not related to research. I would also like to thank my family for their support both morally and financially and Katie Sue for sending me so many packages. I would also like to thank my friends for making my time at Auburn so enjoyable. Thank you to Courtney Ober and Jenn (Boice) Duggan for helping organize my defense. Thanks to Courtney Ober for being my friend. Thank you to Dr. Richard Liang at Florida State for arranging TEM access and Dr. Yi-Feng Su of the National High Field Magnet Lab for his expertise with TEM imaging. Thank you to Ao Geyou for the DNA stabilized SWNT absorption measurements. Finally, a special thank you to Mr. Tanny Deliere, Sr., for instilling in me a curiosity and passion for chemistry, as well as a new perspective on learning and understanding, that has carried me through my educational career and still inspires me today.

Table of Contents

List of Figures

List of Tables

Chapter 1

Introduction

1.1 Introduction to Carbon Nanotube Research

Since the discovery of multi-walled carbon nanotubes (MWNT) by Iijima in 1991[1] and the intentional production of single-walled nanotubes (SWNT) in 1993,[2,3] the number of publications concerning polymeric composites containing carbon nanotubes (CNT) has rapidly increased.[4] The desire to incorporate CNT into polymers is a result of the extraordinary mechanical and 1-D quantum transport properties they possess.[5] These properties lend themselves to the polymer matrix via the enormous CNT specific surface area, which, when compatible with the matrix, can provide load transfer through the composite system.[6] In addition, CNT are essentially hollow cylinders of graphene which affords these unique physical properties in conjunction with a low particulate density. As shown in Section 1.2.4, due to the high aspect ratio of SWNT, the amount of nanomaterial required for mechanical property enhancement is low, which further enhances the strength to weight ratio of these remarkable new materials. Previous work on thermoset polymer composites and dispersions are discussed in this section as well as the current state of the art.

1.1.1 Thermoset Polymer Nanotube Dispersions

The incorporation of CNT into thermoset polymer resins has predominately been studied using epoxies.[7-13] Conversely, there have only been limited investigations of CNT dispersions in

unsaturated polyester resin (UPR).[14-16] This disparity is somewhat puzzling since UPR has owned twice the domestic market share, in the last thirty years, over epoxies.[17] Regardless, the preference for epoxy resins is likely a result of the great success by Sandler et al. (1999) in dispersing CNT using solvent intercalation.[7] In this technique, CNT are first dispersed in a low viscosity solvent and/or surfactant using ultrasonication before addition of the monomer and hardener. Finally, the volatile solvent is simply evaporated off providing a quick and easy protocol.[18-20] Unfortunately, this technique is unsuitable to disperse CNT in UPR for a number of reasons. UPR contains a significant amount of crosslinking agent (40 vol. % in this work), most commonly styrene monomer, which would be removed along with the solvent.[15] In addition, ultrasonication and thermal treatment often results in undesired premature polymerization. Thus, it has been necessary for some groups to migrate to "in-house" styrene-free formulations.[21] In the absence of intercalation, the preferred method for dispersion of CNT in UPR has been through high-shear calendering (3-roll milling).[14,15] Again, this technique has problems with solvent loss, and was not employed in this work. Instead, shear was applied using a closed vessel mixing apparatus allowing for control over the sample environment. It is important to recognize that the majority of the previous work on CNT dispersions in thermoset polymers was limited to use of MWNT.

1.1.2 Unsaturated Polyester Resin

Unsaturated polyester resins are thermoset pre-polymers comprised of linear short chain oligomers. These oligomers are formed from the condensation polymerization of either saturated/unsaturated acids or acid anhydrides with difunctional alcohols or oxides.[22] The resulting fluid is a viscous liquid or brittle solid depending on the degree of polymerization when initially terminated. Typical UPR molecular weights range from 1,200 - 3,000 g/mol represented

by only a few repeat units (n = 3, 4) in Figure 1.1.[22,23] UPR is readily soluble in styrene monomer and can be found in commercial solutions as high as 40 wt. % styrene. The styrene serves both to lower the polymer viscosity for processing as well as act as a cross-linking agent between unsaturation sites on adjacent oligomer chains to form a three-dimensional network structure.

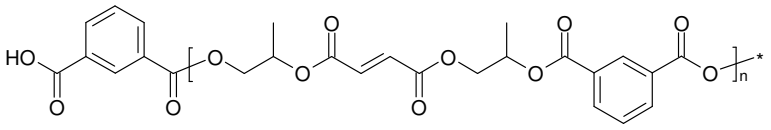

Figure 1.1: Chemical structure of a 1:1 isophthalic polyester constructed from equimolar ratios of isophthalic acid and maleic anhydride. Isophthalic polyesters are known for their corrosion resistance, superior mechanical properties, and higher heat distortion temperatures with respect to other types of thermoset polyester.[24]

With the exception of the new class of reversible topology thermosets,[25] it is the formation of a permanent network that distinguishes thermoset polyester resins from other linear thermoplastic polyesters such as poly(ethylene terephthalate).[26] Typical acids used in UPR production are phthalic anhydride, a saturated acid, or an unsaturated dicarboxylic acid such as maleic anhydride. Generally, a diol such as propylene glycol or diethylene glycol is also used. Depending on the desired resin properties, the UPR recipe can be adjusted. For example, the addition of a saturated acid, such as isophthalic acid, decreases crosslink density upon cure. This also decreases brittleness and increases tensile properties, but results in lower thermal stability. Figure 1.2 displays the chemical structure of isophthalic acid. Due to its 1,3 linkage to the oligomer backbone, stress is transferred across the phenyl ring as opposed to the 1,2 linkage in orthophthalic resins. Also, fumaric acid is commonly used in place of maleic acid to increase impact resistance. If the resin is meant to have a shelf life, an amount of a free radical scavenging inhibitor such as benzoquinone is added to prevent any premature polymerization.

More detailed recipes for tailoring UPR properties can be found in Mallick (1993).[27] In general, UPR can be formulated such that the final product is either hard and brittle or soft and flexible.

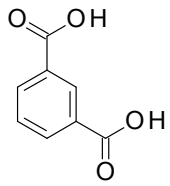

Figure 1.2: The chemical structure of isophthalic acid. In contrast to other unsaturated acids used in polyesters, there is no anhydride form of isophthalic acid.

Curing is initiated by the addition of some type of organic peroxide and crosslinking propagates via a free radical reaction mechanism across the styrene molecule. Generally, the peroxide is cleaved creating a free radical which attacks the unsaturated vinyl-carbon bonds in styrene, whose structure is shown in Figure 1.3.

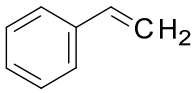

Figure 1.3: The chemical structure of styrene monomer. Crosslinking between UPR oligomers propagates through the vinyl bond.

Styrene radicals, in turn, attack unsaturation sites on the polyester oligomers and crosslink them by forming a bridge between adjacent molecules.[27] Typically, in low temperature curing, methyl-ethyl-ketone peroxide is used. To help facilitate curing, a cobalt based accelerator is added which aids in cleavage of the peroxide groups. The cure time and conditions as well as the mechanical properties of UPR vary with both the oligomer constituents, the degree of cross-linking, and the amount of condensation product trapped in the polymeric network. The fact that UPR can be cured at room temperature makes its application favorable for manufacture of large parts such as boat hulls or automobile bodies.[23]

From a manufacturing standpoint, UPR is an advantageous choice for its low viscosity, fast cure time, and low cost. UPR's mechanical properties, however, are generally not as favorable as those of epoxy resins. For cast UPR, a tensile strength of 34.5 - 103.5 MPa is expected with a tensile modulus of 3.10 - 3.45 GPa. On the other hand, cast epoxy resin can show a tensile strength and modulus as high as 130 MPa and 4.1 GPa, respectively. Conversely, the thermal properties of UPR show better high temperature performance compared to epoxy resins. The continuous working temperature for an epoxy resin is typically 150°C or less. UPR shows heat deflection temperatures as high as 205°C, making it a better choice for high temperature applications.[27] The mechanical disadvantages of UPR can be improved upon if processed as a composite material, however. In practice, the peroxide or curing catalyst is first added to the resin, blended, than the material is processed. Commonly, UPR is compression molded into parts but can be resin-transfer molded for intricate geometries which are allowed to cure before removal.[26] If not molded, UPR is typically applied as a glass-fiber laminate. The high strength to weight ratio of polyester-glass laminates, microwave transparency, and corrosion resistance have led to their use in many air transport applications.[23] One of the most common polyester laminates goes by the trade name Fiberglas® (Owens Corning). Fiberglas® is a glass-fiber laminate material which became popular in the 1940s and is widely used in the automotive, marine, construction, and aerospace industries. Fiberglas® found its way as an alternative to heavy porcelain shower stalls and bathtubs, but made a memorable impact in the construction of automotive parts when in 1953 Chevrolet produced the first Corvette with a Fiberglas® body.[26,28]

In the year 2000, UPR sales of 681 million kg were reported in the U.S. alone, ranking 3rd among thermoset plastics behind phenolic resins and polyurethane. This was over twice the amount of epoxy resin sold that year, but less than 2 % of the total market for plastics. For point

of reference, thermosets were responsible for less than 14 % of the total U.S. sales of ~42,900 million kg of polymer sold in 2000.[17]

1.1.3 Single-walled Carbon Nanotubes

Mechanical Properties of CNT

The source of the outstanding mechanical properties displayed by CNT is intuitively very simple to comprehend. In general, pristine CNT can be viewed as polymer chains consisting of only carbon atoms. The honeycomb lattice atomic arrangement in a cylindrical shape classifies CNT as a ladder polymer, i.e., a polymer where more than one bond needs to be broken to cleave the backbone. Here, "backbone" refers to the bonds along a position on the nanotube circumference. It is important to note that CNT are far superior to typical ladder polymers since approximately 10 - 20 highly ordered carbon-carbon bonds per repeat unit need be cleaved for tube scission to occur. Now, consider the fact that carbon atoms in CNT are interconnected by purely sp^2 hybridized bonds. Since the sp^2 hybridized carbon-carbon bond is among the strongest known it is unlikely that a more robust material will ever be discovered.[29]

Mechanical properties of CNT have been both measured experimentally and predicted theoretically and found to be in excellent agreement. For example, tensile loading of CNT reveals extraordinary stiffness with a Young's modulus approaching 1 TPa.[30,31] In addition, small diameter SWNT ropes have been extended elastically to approximately 6 %, giving SWNT tensile strengths on the order of 50 GPa.[32] While these values are on par with silicon carbide nanowires and fibers, they are somewhat unimpressive without considering differences in intrinsic material density.[33] Accounting for the low molecular density introduced as a result of the hollow tubular CNT structure, these normalized properties reveal remarkable comparisons to structural materials. Specifically, for typical SWNT the density normalized modulus is

approximately 19 times that of steel and 2.4 times that of silicon carbide nanorods. Likewise, the density normalized tensile strength is approximately 56 times that of steel wire and approximately 1.7 times greater than silicon carbide.[5] Thus, the ultimate goal for nanoscientists studying structural and mechanical properties are in constructing macroscopic CNT materials while retaining the outstanding properties of individual tubes.

Electronic and Thermal Properties of CNT

Since the radial dimension of SWNT is comparable with the de Broglie wavelength of electrons, SWNT can be considered as quasi 1-D materials.[34] In fact, conductance measurements on CNT have revealed the conductance to be quantized, measuring in at one unit of the conductance quantum. Physically, this indicates that length of the conductor is less than the mean free path and therefore displays ballistic electronic transport. Additionally, current densities in excess of 10^7 A/cm^2 were recorded with applied bias as high as 6 V.[35] Under these conditions heat dissipation was also consistent with ballistic transport as thermal conductivity for an individual MWNT has been reported in excess of 3,000 W/(m - K).[36] This conductivity is greater than that of diamond. For point of reference, current densities are typically on the order of 10^5 A/cm^2 in superconductors. Furthermore, measurements on CNT have shown reliable current densities in excess of 10^9 A/cm^2, even at elevated temperatures, making them ideal candidates for interconnects in electronic devices.[37] With respect to semiconductor properties, intrinsic carrier mobilities as high as 10^5 cm^2/(V - s) at room temperature were reported, exceeding known semiconducting materials. These properties, accompanied with thermal stability at temperatures as high as 2800°C in vacuum and 750°C under air, complete the picture for the exciting physical properties of nanotubes.[38]

Molecular Structure of SWNT

In general, SWNT can be considered as seamless hollow cylinders of rolled graphene sheets having diameters on the order of 1 nm and lengths typically on the order of μm. Similarly, MWNT consist of coaxially arranged, nested cylinders of graphene, with each layer spaced 0.34 nm apart, in accordance with the van der Waals radius. MWNT have typical lengths on the order of microns with outer diameters ranging from 2 - 20 nm.[4,39] Thus, SWNT and MWNT have aspect ratios on the order of 100 - 1000.[39] These measurements vary within, and between, samples and batches from various laboratories or manufacturers.[4] In absence of defects, the carbon atoms that comprise the graphene sheet are covalently joined to one another via sp^2 hybridized bonds. Note that all known methodologies for bulk SWNT synthesis give mixtures of diameters, lengths, and chiralities.[29] The chirality of a CNT refers to the number of ways a graphene sheet may be rolled upon itself. Specifically, tube chirality is identified with a pair of integers (*n*, *m*) which in turn define the circumferential chiral vector from which the graphene is rolled upon. Equation 1 defines the chiral vector, $\mathbf{C}_h$, in vector notation.

$$\vec{C}_h = n\vec{a}_1 + m\vec{a}_2 \tag{1}$$

Figure 1.4 displays the geometrical constructs of $\mathbf{C}_h$ on a graphene lattice. The length of $\mathbf{C}_h$ is represented by vector **OA**, the nanotube circumference. Orthogonal to $\mathbf{C}_h$ lays the translation vector **T** which serves to define a unit cell. The chiral indices (*n*, *m*) describe the number of steps along the hexagonal unit vectors $\boldsymbol{a}_1$ and $\boldsymbol{a}_2$.

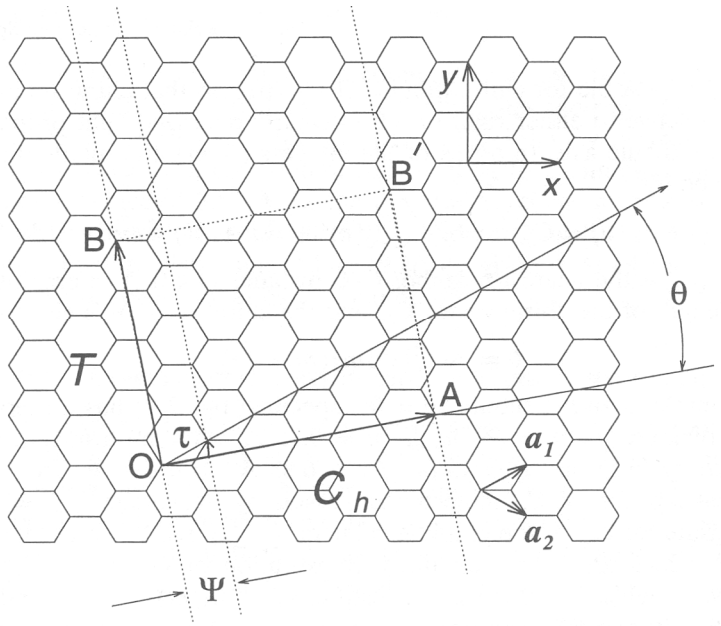

Figure 1.4: Unit vectors $\mathbf{a}_1$ and $\mathbf{a}_2$ define the chiral vector $\mathbf{C}_h$ (or equivalently **OA**) based on the chiral indices and/or the chiral angle θ. **T** (equivalently **OB**) defines the lattice vector of the 1-D unit cell. Rotation by angle Ψ and translation by τ yields the space group symmetry operation R = (Ψ | τ). Illustrated is (*n*, *m*) = (4, 2). Adapted from Dresselhaus, M.S. et al. (1996).[39]

The "magnitude" of the unit vectors $\boldsymbol{a}_i$ can easily be determined geometrically. The distance between adjacent vertices on a single hexagon is given by the carbon-carbon bond length ($L_{C\text{-}C}$), approximately 1.42 nm for graphite.[39] Considering that a hexagon can be divided into six equilateral triangles, each unit vector will bisect two equilateral triangles along a length of distance $(L_{C\text{-}C}) \times 3^{1/2}$, defining the lattice constant (0.246 nm). Likewise, the length of vector $\mathbf{C}_h$ shown by Equation 1 can be easily derived from Figure 1.5.

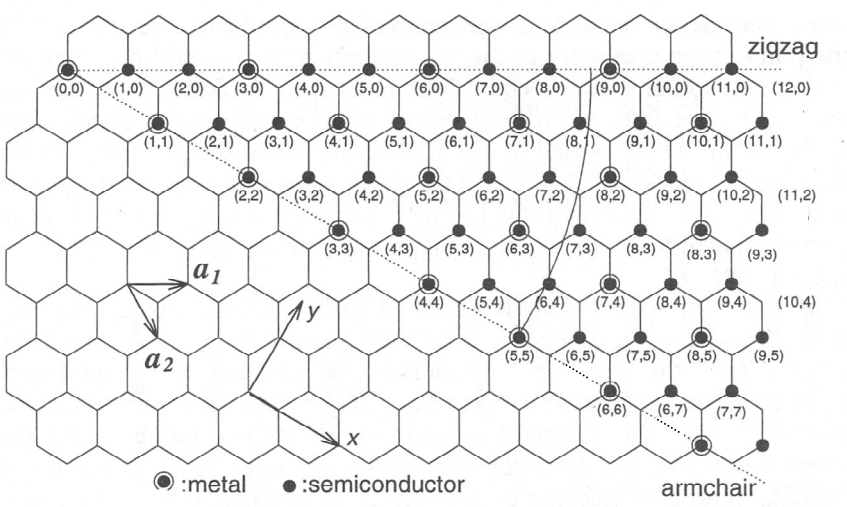

Figure 1.5: Map of possible chiral indices (n, m) for SWNT showing collinear $\mathbf{C}_h$ for zigzag and armchair SWNT. Indices with encircled dots denote metallic SWNT while all others are semiconducting. Adapted from Dresselhaus, M.S. et al. (1996).[39]

Equation 2 displays the relationship between nanotube diameter and the magnitude of $\mathbf{C}_h$.

$$d = \frac{\sqrt{3}L_{C-C}\left(m^2 + mn + n^2\right)^{1/2}}{\pi} = \frac{\left|\vec{C}_h\right|}{\pi} \tag{2}$$

Here, the division by π is necessary to relate the tube circumference to the diameter. The (m^2 + mn + n^2) term is found by simple geometric arguments for a triangle and the (n, m) indices are related to the real space using the lattice constant. As displayed by Figure 1.5 the indices (n, m), and therefore, $\mathbf{C}_h$ determine the tube's electronic structure. Despite the structural similarity to a single sheet of graphite (graphene), which is a zerogap semiconductor (low density of states at Fermi level due to conduction and valence band overlap), SWNT may be either metallic or semiconducting.[5] Specifically, when the difference n - m is nonzero and divisible by three, the nanotube is considered semimetallic (or simply metallic) with a bandgap on the order of 10^0 meV. On the other hand, when n - m is equal to zero the nanotube is metallic (ballistic conductor) with a bandgap of zero. In all other cases where the difference n - m is nonzero and not divisible by three the nanotube is semiconducting with a band gap ranging from

approximately 0.5 to 1 eV.[29] Structurally the vectors (n, 0) and (0, m) denote zig-zag tubes and the vectors having indices that match denote armchair tubes, named by examining a ring of carbon atoms around the circumference. Both armchair and zig-zag tubes are achiral since they have a mirror plane whereas all other vectors where n is not equal to m or zero are chiral (twisted). Figure 1.6 displays a schematic of each type.

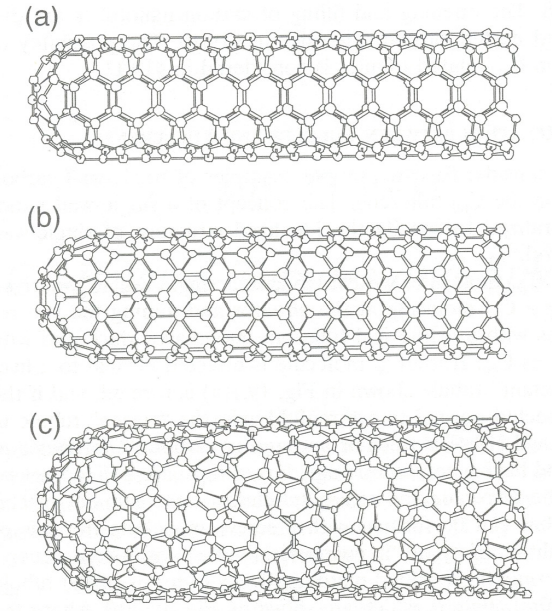

Figure 1.6: SWNT schematic models with the long axis normal to: (a) the $\theta = 30^{o}$ direction for a (5, 5) "armchair" SWNT, (b) the $\theta = 0°$ direction for a (9, 0) "zigzag" SWNT, and (c) the $0° < \theta < 30°$ direction for a (10, 5) "chiral" SWNT. Adapted from Dresselhaus, M.S. et al. (1996).[39]

The observed metallic/semiconducting behavior of CNT with different chiralities can be understood when compared to the band structure of graphite (graphene). Electron wavefunctions are subjected to additional quantization due to the rolled cylindrical geometry. The net result is a cutting of 1-D slices out of the formerly 2-D band structure of graphene .[40] What is important to note here is the fact that variable band-gap materials can be obtained based on geometrical considerations alone. This attribute is fascinating when compared to the typical required doping in semiconductor materials.

1.3 Resonant Raman Spectroscopy

The use of Raman spectroscopy in the characterization of CNT, and especially SWNT, offers an unparalleled degree of insight into the skeletal structure of CNT and is generally regarded as an essential function of any nanotube researcher. As described in the following sections, Raman provides non-destructive analysis of nanotube diameter, quality, chirality, and even charge transfer mechanisms. Furthermore, sample preparation is minimal, measurements are relatively easy and fast, and ambient conditions can be used.

1.3.1 Raman Spectroscopy of CNT

The Raman effect is described when an incident photon with energy E_i and momentum k_i is inelastically scattered by the interaction with a material. Specifically, when the associated electric field of the photon interacts with the atom, the electron and core/nucleus move in opposing directions to form an oscillating dipole which scatters light. A phonon (quantized vibration) is created by the coupling of the dipole with the photon electron field and this electron-phonon interaction is the essence of the Raman scattering process. As a result of this electromagnetic interaction, the incident photon energy and momentum are changed (scattered) such that these values are typically less by some amount E_q and k_q, properties of the resulting phonon. This process is summarized in Figure 1.7.

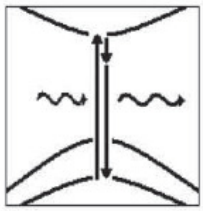

Figure 1.7: Incident resonance process resulting in Raman scattering. Incident (left) and scattered photons (right) are wavy arrows and vertical arrows show photon induced transitions between electronic states.[41] The small vertical arrow pointing down represents the phonon energy. Adapted from Jorio et al. (2011).

Scattering creating a phonon is known as Stokes scattering and is preferred to measure due to the increased intensity over the phonon annihilating process (anti-stokes scattering). Although both scattering processed can occur, the probability of phonon creation is more favorable. The intensity of the scattered photons leaving the sample with E_s and k_s is monitored with respect to the incident light and plotted a function of the change in energy. This change is known as the Raman shift and plotted as the inverse frequency (cm^{-1}), the wavenumber. The shift is positive for the Stokes process as $E_i > E_s$. In order to even be detected, the dominant elastic Rayleigh scattering must be first filtered out from the inelastic Raman scattering. Raman scattering is referred to by its order, the number of scattering events that take place. An interesting effect of 1-D systems like nanotubes is resonance, where a maximum in Raman intensity occurs with a certain laser energy (incident or scattered) that matches the excited electronic states (optical transitions). As a result of the optical transition energy E_{ii} for various types of SWNT, resonance occurs when E_{ii} matches E_i and when $E_i = E_{ii} + E_q$. These criteria are referred to as the incident and scattered resonance conditions, respectively, and involve absorption or emission across a transition. The Raman intensity follows a general dependence on the laser energy in 1-D systems (see Eq. 8 in Saito et al. [2011][42]). As a crude approximation, the intensity is proportional to the inverse incident and electronic transition energy difference squared. In other words, the energy denominators in the oscillator strength diverge and this enhances the signal by 10^3 times.[43] Thus, the Raman intensity is greatly enhanced with resonance and can be observed for even a single SWNT. Furthermore, specific chiralities are active only within a small window of laser excitation (~10 meV). Raman peaks are observed at various E_q depending on the specific nature of the Raman active phonons. The allowed phonons are determined from the SWNT unit cell symmetry and dipole allowed optical transitions. A summary of the potential

acoustic and optical phonons for graphene as well as possible scattering processes is given by Saito et al. (2011).[42]

Electronic Structure

SWNT carbons are held together by strong in-plane covalent bonds from σ electronic bands which are far below the Fermi level. These bonds are even stronger than the sp^3 bonds in diamond. Like graphene the carbon valence electrons in SWNT have $2p_z$ orbitals perpendicular to the C-C bond called π orbitals. Electronic transitions can occur between the occupied valence band π and the unoccupied conduction band π^*. Note that inter-atomic electron transitions between neighboring $2p_z$ states are allowed. Since SWNT are sp^2 nanomaterials based on graphene, their physical properties can be approximated by what is known as zone-folding of the 2-D graphene dispersion relations E(k) onto a 1-D Brillouin zone of SWNT that has discrete allowed wavevectors in the confined direction. While SWNT have translational symmetry along their axis, the quantum confinement of electrons/phonons about the circumference has quantized wavevectors shown as cutting lines. A detailed theoretical treatment deriving the electronic band structure for SWNT from that of 2-D graphene is beyond the scope of this text and discussed in more detail elsewhere.[44-50] The energy bands for SWNT are formed using parallel and equidistant cutting lines which extend from 2-D reciprocal space of graphene. Figure 1.8, from Saito et al. (2011), discusses this process.[42] An exhaustive review on the concept of cutting lines for nanotubes was given by Samsonidze et al. (2003).[51] For graphene, the dispersion relation is cone shaped near the Fermi level for the valence and conduction bands. The cutting lines slice energy bands for SWNT out of this cone as shown by the bold lines and parabolas to form SWNT energy bands. The number of energy sub-bands depends on the number of carbon atoms in a unit cell. Dresselhaus, M.S. et al. (2005) notes that a complete understanding of the 1-D

band structure is not required since the optical absorption/emission from SWNT are related to van Hove singularities in the density of states (DOS).[43] The corresponding DOS are shown on the right of Figure 1.8 and will be discussed in further detail.

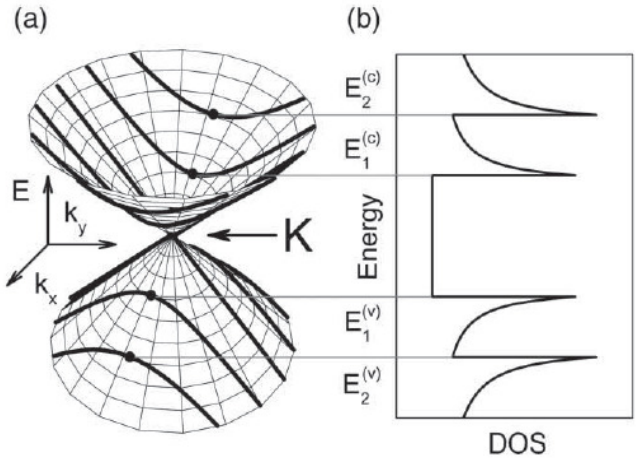

Figure 1.8: "(a) The energy-momentum contours for the valence and conduction bands for a 2-D system, with each band obeying a linear dependence for E(k) and forming a degenerate point K where the valence and conductions bands touch to define a zero gap semiconductor. The cutting lines of these contours denote the dispersion relations for the 1-D system derived from the 2-D system. Each cutting line gives rise to a different energy subband. The energy extremum E_i for each cutting line at the wave vector k_i occurs at a van Hove singularity. The energies $E_i^{(v)}$ and $E_i^{(c)}$ for the valence and conduction bands and the corresponding wave vectors $k_i^{(v)}$ and $k_i^{(c)}$ at the van Hove singularities are indicated on the figure by the solid dots. (b) The 1-D density of states (DOS) for the conduction and valence bands in (b) corresponding to the E(k) dispersion relations for the 1-D subbands shown in (a) as thick curves. The DOS shown in (b) is for a metallic 1-D system, because one of the cutting lines in (a) crosses the degenerate Dirac point (the K point in the graphene Brillouin Zone (BZ)). For a semiconducting 1-D system, no cutting line crosses the degenerate point, thus resulting in a band gap opening up in the DOS between the Van Hove singularities $E_1^{(v)}$ and $E_1^{(c)}$." Image adapted from Samsonidze et al. (2003).[51] Caption reproduced from Saito et al. (2011).[42]

1.3.2 Optical Properties

The resonance Raman spectra of SWNT originates from the optical properties of the material, linking phonon vibrations to electronic structure. It is important to note that idealized inter-band transitions, valence to conducting bands, are not actually observed in SWNT due to strong electron-hole binding (excitons). Nonetheless, an interpretation based upon inter-band

transitions is useful for understanding the underlying physics. Matching the incident (or exiting) photon to the optical transitions in SWNT results in resonance. For a 1-D material like SWNT, resonances are strong. This is a result of the electronic density of states (map of potential solutions to the Schrödinder equation) showing divergent behavior known as van Hove singularities. Van Hove transitions are general phenomena for 1-D systems rather than a unique property of carbon as shown by Figure 1.9. Typical semiconductors show parabolic 3-D behavior.

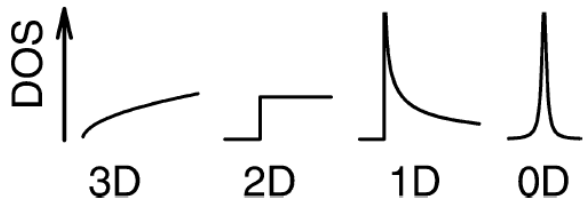

Figure 1.9: Qualitative density of states behavior for material dimensions. Adapted from Thomsen and Reich (2007).[52]

The inter-band model can account for the observed optical properties of SWNT, as highlighted in Figure 1.10. Here, the dispersion relation for a semiconducting nanotube was used as an example. The left hand side shows various valence energy bands v_i and conduction energy bands c_i. These bands result in the singularities ($\sim E^{-1/2}$) in the density of states shown on the right. For reasons beyond the scope of this text, transitions between symmetric sets of singularities are preferred as absorption probability is high there.[52] Optical absorption peaks thus represent transitions between van Hove singularities, the maxima in inter-band absorption probability. For example, from v_i to c_i with energy of E_{ii}.

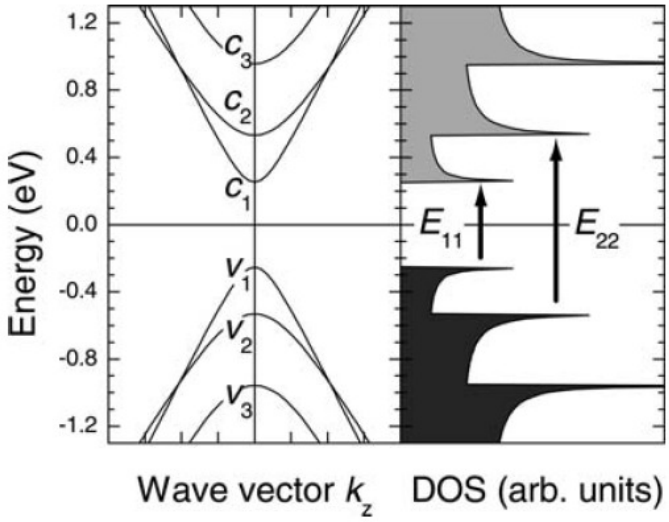

Figure 1.10: "Band structure and density of states of a zigzag nanotube. The band-to-band transition picture predicts that transitions between symmetrically lying pairs of valence and conduction bands contribute the most to the absorption. The transition energies are labeled E_{ii} where i labels the bands." Adapted from Thomsen and Reich (2007).[52]

1.3.3 The Katura Plot

Of particular importance for Raman spectroscopy is the plot of the van Hove transition energies as a function of nanotube diameter. This plot is known as the Katura plot, displayed by Figure 1.11.[53] The order of the grouped transitions can be understood by examination of allowed wavevector cutting lines through a plot of the electronic band structure of graphene [see Fig. 27 in Thomsen and Reich (2007)[52]]. The apparent spread among trend lines is a result of trigonal warping of graphene band structure and the possible nanotube structures possible based on (*n*, *m*). Also, metallic tubes show two close-by transition energies for each chirality due to these effects. Recall that a true connection between theory and experiment can only be complete with the inclusion of excitonic effects where a photon excites an exciton from ground state to an optically active state. Thus, assignments based off the Katura plot must take into consideration both theoretical and experimental measurements and mesh the results together to avoid error.

Measurement of metallic versus semiconducting SWNT is possible based on the incident laser energy matching inter-band (valence to conducting) van Hove transitions of SWNT. The energy gap for these transitions are labeled based on the metallic M of semiconducting S nature and indexed as M_{ii} or S_{ii} for the ith inter-band transition. Katura calculated the theoretical energy separation for SWNT based on their diameter or chirality.[53] In order to make use of this plot the diameter range of the SWNT under analysis must first be highlighted (orange highlight bar). As an example, CG200 CoMoCAT SWNT (Lot # 0004) from SouthWest NanoTech was used. Next the laser lines are overlaid. Any SWNT that fall on the laser line and within the diameter window are expected to be in resonance with the incident laser. Thus, for CG200 SWNT under 785 nm laser excitation, only semiconducting SWNT are measured. Specifically, the S_{22} transition is active. Under 514 nm laser excitation, primarily metallic (M_{11}) tubes are active but higher order transitions for larger diameter semiconducting SWNT, and even small diameter semiconducting SWNT can be observed at this wavelength.

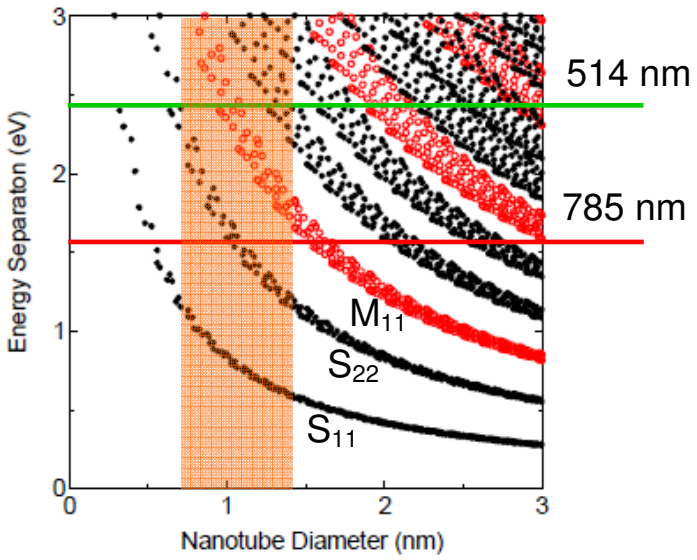

Figure 1.11: Example of Katura plot analysis. Plot adapted from Maruyama.[54]

1.3.4 Raman Modes of SWNT

The resonant Raman spectrum can be discussed in terms of each specific mode of interest. Herein, the radial breathing modes (RBM), the disorder induced mode (D-mode), the graphitic mode (G-mode) and the overtone of the D-band, called the D^* or G' mode, are discussed separately. The first order modes (RBM and G) are introduced followed by discussion of second order modes (D and G') from two phonon scattering (G') or defect scattering (D). The aforementioned Raman bands are highlighted as a basis for analysis in subsequent sections. This discussion is far from exhaustive, but a detailed summary of each possible mode is given at the end of the section.

The Raman RBM

From the perspective of the nanotube circumference cross section, the RBM vibrations appear as the in-phase radial displacement of carbon atoms shown by Figure 1.12. This mode is unique to SWNT and although it can be observed for DWNT, is considered a characteristic of SWNT presence as it is not observed for other sp^2 structures. The RBM are found from ~100 - 400 cm^{-1} and remarkably, their frequency is proportional to d^{-1}. The diameter dependence on frequency remains a controversial point in the literature due to slight differences in correlations seen between various samples and experiments. These differences have been attributed to "environmental effects" between systems. Individual RBM peaks can be extracted from bulk or bundled samples by fitting many Lorentzian peaks, guided by the Katura plot. Figure 1.13 shows the RBM excitation profile at 644 nm with metallic (red) Lorentzians and semiconducting (green) Lorentzians fit and compared to the Katura plot.[42] This figure shows not only the typical RBM spectrum but also includes an example for practical analysis.

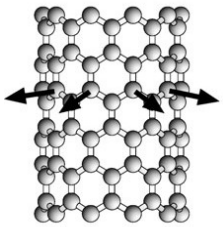

Figure 1.12: RBM vibrations in SWNT. Adapted from Jorio et al. (2003).[55]

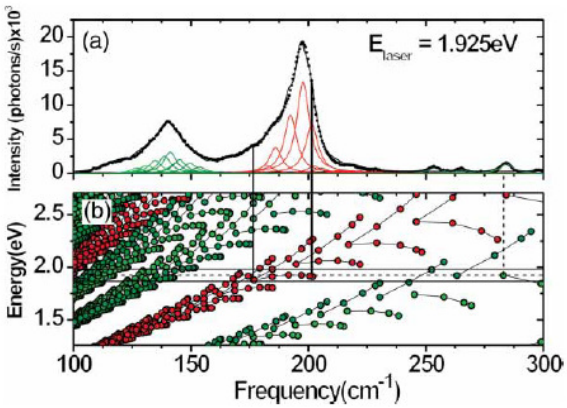

Figure 1.13: (a) Raman spectrum for SWNT bundles showing RBM mode at 644 nm laser. Lorentzians fit under the curve represent specific tube diameters (chirality). (b) Corresponding Katura plot guiding the Lorentzian fit at laser excitation energy. Adapted from Saito et al. (2011).[42]

The Raman G-mode

Simply stated, the G-band originates from out of phase C-C stretches of neighboring sp^2 carbons. It is often referred to as the tangential mode. Due to the strength of these bonds the G-mode is often referred to as the high energy mode (HEM). The G-band in SWNT is centered on the equivalent mode in graphene at ~1582 cm^{-1}, but consists of multiple peaks due to symmetry breaking nanotube curvature. Typically, two phonon modes (longitudinal and transverse) are dominant in intensity for SWNT. These peaks are found at ~1590 cm^{-1} (G^+) and at ~1570 cm^{-1} (G^-). This phenomenon is a result of nanotubes acting as nano-antennas which is observed via the depolarization effect. Vibrations along the tube axis are referred to as longitudinal optical (LO) and those perpendicular as in-plane transverse optical (iTO). Figure 1.14 highlights their

motions in a zig-zag SWNT. Given the nature of these modes, the LO (also called G^+) is insensitive to diameter whereas the iTO (also called G^-) is diameter sensitive since increasing curvature increases out of plane nature of the vibration (this is IR active, however). The G-band shape (for metallic SWNT) and position is also sensitive to doping and will up/down shift with non-covalent charge transfer. The G^- lineshape can be modeled as Lorentzian for semiconducting tubes but has a broad Fano lineshape in metallic tubes.

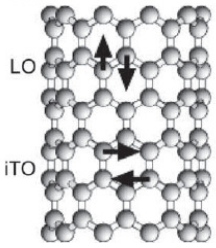

Figure 1.14: The LO and iTO G-band phonon modes in SWNT. Adapted from Dresselhaus, M.S. et al. (2005).[43]

The Raman D-mode

The presence of defects or disorder in a sp^2 hybridized carbon system is evident in resonance Raman spectra by observation of the D-band. It is a result of the interaction between one phonon and a defect, a second order scattering process.[56] Disorder can be introduced from structural defects or from chemical functionalization which introduces sp^3 character. The introduction of defects into pristine graphene results in the appearance of a band at 1345 cm^{-1} (514 nm). This peak is typically found at ~1350 cm^{-1} in SWNT. This band is dispersive and sensitive to the amount of defect sites introduced. Most notably, the inter-spectrum D-band/G-band intensity ratio (I_D/I_G) is used as a metric for qualitative degree of functionalization or sidewall damage between SWNT. Furthermore, the D-band is sensitive to compression and tension which can be useful for composite performance by monitoring stress transfer.[56] Figure 1.15a displays the physical origin of the D-band where after incident photon absorption and scattering by phonons,

the electrons in state $\boldsymbol{k} + \boldsymbol{q}$ interact with a defect and are elastically scattered (horizontal) to state $\boldsymbol{k}$. Finally, recombination occurs and a scattered photon is emitted.

The Raman G'-mode

The G'-mode is the 2nd harmonic of the D-mode and therefore can be found at ~$2\omega_D$. Remarkably, the presence of defects is not a requirement for the presence of the G' peak. For this reason, the D^* naming convention is often not used. The G'-band is dispersive with the incident laser energy as a result of a two phonon, second order scattering process. These characteristics make this band very sensitive to changes in the electronic structure such as doping and this peak, like the G-band, will up/down shift with non-covalent charge transfer.[57] This band is more sensitive to compressive and tensile strains than the D-band.[56] Due to its insensitivity towards defects, this peak is preferred for analysis of the electronic and phonon structures of SWNT. It is found between 2500 - 2800 cm^{-1} and along with the G-band confirms the presence of sp^2 carbons. For both metallic and semiconducting SWNT, the G' peak sometimes appears as a doublet. This observation indicates resonance with two different van Hove singularities of the same SWNT from incident and scattered phonons, independent of one another. The physical explanation for this observation differs for metallic and semiconducting SWNT, however.[58] Figure 1.15b displays the physical origin of the G'-mode and shows why no defect is required. In contrast to the D-mode, two phonons at $\boldsymbol{q}$ and $-\boldsymbol{q}$ are involved. The main difference for G' being that electrons in the $\boldsymbol{k} + \boldsymbol{q}$ states are inelastically scattered to a final state $\boldsymbol{k}$.

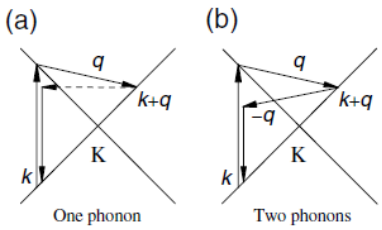

Figure 1.15: "The intravalley double-resonance Stokes process near the K point in the 2-D graphite Brillouin zone. a) The scattering process for activating a defect-induced mode where the resonance is with the incident photon. The broken line indicates the elastic scattering by a defect. b) The scattering process for the second-order modes...." Adapted from Souza Filho et al. (2002).[55]

Various Raman Modes

Although the four previous mentioned modes are the most common and most useful for analysis, a number of other Raman features exist as shown by Figure 1.16. It is important to be aware of the possible Raman modes to avoid misinterpretation when dealing with functionalized nanotubes or composites. Notably, the iTA mode falls within the typical RBM range of wavenumber. Also, the M^+ and M^- modes appear in the range of the IR active ester carbonyl. Finally, the 2G mode appears near a typical IR active aliphatic hydrocarbon vibration. Details of the origin of some of these lesser known modes can be found in Dresselhaus, M.S. et al. (2005).[43]

Properties of the various Raman features in graphite and SWNTs[a]

Name[b]	ω (cm^{-1})	Res.[c]	$d\omega/dE_L$[d]	Notes[e]
iTA	288	DR1	129	iTA mode, intravalley scattering ($q = 2k$)
LA	453	DR1	216	LA mode, intravalley scattering ($q = 2k$)
RBM	$248/d_t$	SR	0	Nanotube only, vibration of radius
IFM^-	750	DR2	−220	Combination mode oTO–LA ($q = 2k$)[h]
oTO	860	DR1	0	IR-active mode in graphite
IFM^+	960	DR2	180	Combination mode oTO + LA ($q = 2k$)[h]
D	1350	DR1	53	LO or iTO mode, intervalley scattering ($q = 2k$)
LO	1450	DR1	0	LO mode, intervalley scattering ($q = 0$)
BWF[f]	1550	SR	0	Plasmon mode, only metallic carbons
G	1582	SR	0	Raman active mode of graphite[g]
M^-	1732	DR2	−26	overtone of oTO mode ($q = 2k$)
M^+	1755	DR2	0	overtone of oTO mode ($q = 0$)
iTOLA	1950	DR2	230	combination mode of iTO and LA
G′	2700	DR2	106	overtone of D mode
2LO	2900	DR2	0	overtone of LO mode
2G	3180	DR2	0	overtone of G mode

[a] Mode frequencies for dispersive modes are given at $E_L = 2.41$ eV.
[b] See Fig. 5 and Section 5 for an explanation of names.
[c] The following notation is used to classify the Raman scattering process: SR: first order; DR1: one-phonon double resonance; DR2; two-phonons double resonance.
[d] $d\omega/dE_L$ denotes the change of the phonon frequency in cm^{-1} produced by changing the laser energy by 1 eV.
[e] Double resonance (DR) features are classified as intervalley and intravalley scattering processes (see Section 3.4).
[f] The Breit–Wigner–Fano lineshape is discussed in Section 3.6.
[g] G-band for graphite is at 1582 cm^{-1}. For SWNTs, there is a G^+ feature at 1590 cm^{-1} due to in-plane vibrations along the tube axis, and a diameter-dependent G^- feature at 1570 cm^{-1} for in-plane vibrations along the circumferential direction (see Section 6.2.1).
[h] The physics of the intermediate frequency modes (IFM) between 600–1100 cm^{-1} is interesting and complex, as discussed in Section 7.7.

Figure 1.16: Various resonant Raman modes in SWNT. Adapted from Dresselhaus, M.S. et al. (2005).[43]

Phonon-plasmon Coupled Modes

The shape of the G-band varies between metallic and semiconducting SWNT as shown by tuning the laser excitation to match transitions for metallic SWNT. A peak at ~1540 cm^{-1} dominates which was connected to the optical transitions for metallic SWNT but also dependant on diameter. The result is a broadening of the G-band spectrum. The underlying physics of this phenomena was revealed by Kempa (2002) who showed that the origin of this peak was due to coupling of metallic nanotube plasmons (delocalized electron oscillations) with optical phonons to produce phonon-plasmon modes in the spectra.[59] Alternate explanations involve opening of the band gap by distortions (Peierls instability) at the Fermi level which softens force constants.[60] The distortions caused by specific types of phonons result in gap formation even in metallic

nanotubes. This gap opening reduces the energy required to distort metallic tubes. This effect is broadened and characteristic in nanotube bundles, known as the Fano lineshape. Analysis of an individual metallic SWNT shows this band to be broad and softened when in resonance and dispersive at higher energy. Remarkably, at high energy the lineshape of this metallic SWNT resembles a semiconducting SWNT due to double resonance. This can be confusing and troublesome if not considered as semiconducting tubes can be misidentified in this case.

Raman Resonance

Raman scattering by a single non-resonant process involves the excitation of an electron from the ground state followed by phonon emission (Stokes scattering) and electron-hole pair recombination. Conversely, in a single resonance process the electron is excited to a real energy level by incoming resonant laser light. The enhancement in Raman intensity by resonance is described by mathematical arguments for the Raman efficiency as given by Thomsen and Reich.[52] To be specific, the authors showed the vanishing denominator representing the Raman matrix element when the incoming photon energy matches the electronic state energy. A double resonance process must also be considered where the incident photon is resonant and after transition to a real excited state, a second transition to a real state upon phonon emission is observed. In addition, the electron must be elastically scattered (defect or surface) in a non-resonant step and recombined in final steps to conserve initial momentum. Yet another possibility is scattering of the electron inelastically with a phonon. This second phonon will have equal and opposite momentum. This process results in twice the phonon energy in Raman signal and does not require a defect to scatter light upon recombination to conserve momentum. This explains the increased intensity of the G'-mode over the D-mode. It is backscattered by a second phonon rather than a defect. See Fig. 36 in Thomsen and Reich (2007) for an example.[52]

In fact, no defects need be present for the G' to appear, as shown for ordered and disordered graphite.[61]

Chiral Assignment Issues

The assignment of chiral indices is most conveniently done based on spectroscopic measurements. Unfortunately, assignments based on Raman RBMs can be troublesome due to instrument resolution, uncertainties in diameter correlations, and also unreliability in calculations of electronic energies. These uncertainties were avoided by the use of SWNT luminescence plots which relate the excitation wavelength (v_i to c_i transition) to the corresponding emission (c_i to v_i transition). This technique is insensitive to metallic SWNT, however. Metallic SWNT are accessible from Raman measurements though, and using a tunable laser, an experimental Katura plot can be mapped out which avoids correlation uncertainty. By overlaying the experimental and theoretical Katura plots, the theoretical plot can be stretched or shifted to match the experimental data.[62] This removes uncertainty and correlation parameters for the diameter can be extracted. From this plot, chiral assignments can be made with confidence as shown by Maultzsch et al. (2005).[63] Refer to Fig. 46 of Thomsen and Reich (2007) for a detailed plot.[52]

Doping Effects by Raman

The effect of SWNT doping on Raman spectra was carefully studied electrochemically Rafailov et al. (2005).[64] Doping reduces the characteristic metallic Fano lineshape from phonon-plasmon coupling to the point where semiconducting behavior is observed. The highest intensity peak of the G-band shifts up with positive applied potential and down with negative potential. Conversely, peaks in the Fano lineshape shift in a parabolic fashion and decrease drastically in intensity. This behavior is similar to what was seen when adjusting incident laser energy. If the

level of doping is high enough, the underlying physics explain that as doping proceeds, the Fermi level shifts from the point where the valence and conduction bands (away from the energy transition) cross and this results in double resonance. This is not the case for electrochemical doping and the observed change is result of the offset of Peierls transitions by doping. Refer to the discussion under the sub-section titled "Doping Effects on SWNT," found in Section 2.1.7, for more information.

1.4 Carbon Nanotube Dispersion

As a consequence of the inherent difficulty in separating and stabilizing CNT from their bulk, as-produced roped and entangled state, the range of tangible applications for CNT technologies has been limited. For example, dispersion is essential for realizing mechanical property enhancement in composites. The outstanding properties of SWNT must be communicated to the matrix through the enormous specific surface area of individualized SWNT. This enables reinforcement of the material by forming a percolating network phase. In this section, the thermodynamic framework governing the solubility of SWNT was described and the rich phase behavior of individually dispersed or dissolved CNT were discussed. Finally, the van der Waals interaction between SWNT was compared to classical colloids and the current state of the art regarding the dispersion of SWNT in UPR were reviewed.

1.4.1 The Dispersion Problem

Due to the smooth and polarizable sp^2 hybridized carbon interface, SWNT readily form undesirable aggregates and ropes, intimately held together by the van der Waals force.[65,66] For background on the nature of van der Walls interactions outlined in terms of SWNT, refer to the thesis of Kayatin (2008).[67] Continuum based methods have been employed for modeling the

pairwise interaction potential of parallel nanotubes showing a deep potential energy well at equilibrium separation on the order of 20 - 40 k_bT/nm.[66,68,69] Since typical CNT aspect ratios can be on the order of 100 - 1000, the work required to separate individual tubes is substantial.[39] For example, in separation of a 1 μm long nanotube from a rope, the energy required is on the order of 10^4 k_bT. This problem is compounded by the fact that the only known thermodynamically favorable solvents are superacids, such as chlorosulfonic acid.[70] Due to the obvious problems with both handling and extreme corrosiveness, this solvent is predominately only suitable for processing neat CNT films and fibers.

The thermodynamic driving force for dissolution of a solute into a solvent can be defined by the Gibbs free energy of mixing ΔG_{mix}. Alternatively, the partial molar derivative of the Gibbs free energy, the intensive chemical potential, can be equivalently used. Equation 3 displays the expression for ΔG_{mix} at constant temperature and pressure.[26,71]

$$\Delta G_{Mix} = \Delta H_{Mix} - T\Delta S_{Mix} \tag{3}$$

Spontaneous dissolution occurs only if the change in free energy upon mixing ΔG_{Mix} can be decreased, leading to the following criteria as displayed by Equation 4.

$$\Delta H_{Mix} < T\Delta S_{Mix} \tag{4}$$

Thus, it can be deduced that at constant temperature and pressure, minimizing the enthalpy of mixing ΔH_{mix} and maximizing the entropy of mixing ΔS_{mix} will drive solute solubility.

Direct individual particle tracking measurements of SWNT has revealed SWNT persistence lengths on the order of 20 μm,[72] an order of magnitude greater than their contour length, confirming they behave as Brownian rigid-rods in solution (viscosity permitting).[73] These persistence lengths are much longer than that for traditional rigid-rod polymers.[74] Fakhri et al. (2009) constrained individual SWNT with length less than 3 μm to be rigid rods, whereas, longer

SWNT behave as semiflexible filaments.[75] SWNT with a high degree of sidewall defect sites, affecting the bending stiffness, must also be categorized. Classical theories for the mixing entropy of rod-like molecules (Flory-Huggins, Onsager, DiMarzio), in conjunction with the high CNT stiffness and molecular weight, predicts a small positive ΔS_{mix}.[67,76] Therefore, the free energy of mixing is largely dependant on the magnitude of ΔH_{mix}. For rigorous arguments regarding the effect of flexibility on free energy, refer to the discussion of Flory (1956).[77]

1.4.2 Nanotube Phase Transitions

The inherent transition from a series of isotropic phases to that of a nematic liquid crystalline phase is one of the most important physical phenomena required to conceptually grasp the phase behavior of rod-like molecules such as SWNT. Simply stated, a nematic phase is one in which the rods have no positional order, but long-ranged directional order.[78] Why a dispersion of SWNT would transition from an isotropic phase, having random position and order, to an ordered state seems counter-intuitive from the standpoint of simple thermodynamics. How can the system afford a seemingly entropically costly phase transition from disorder to order? In this section, by the introduction of another free energy contribution, the excluded volume, the driving force for this phase transition will be described.

In order to quantify the orientation order of a fluid two ideas need be introduced; the director and the orientation distribution function. If one were to examine a small area of a fluid, the director is defined by the average local direction of alignment of all particles.[78] The orientation distribution function $f(\theta)$ is constrained as shown by Equation 5.[79]

$$\int f(\theta) d\Omega = 1 \tag{5}$$

Thus, its meaning is such that $f(\theta)\, d(\Omega)$ gives the fraction of molecules in a solid angle $d(\Omega)$ that happens to be orientated at angle θ to the system director. This function now provides all information regarding the state of order in the system. Since a rod does not have specified head/tail or N/S poles, the orientation of a rod is equivalent when orientated at 0 rad or π rad with respect to the director. The orientation distribution function therefore takes on a maximum value around these orientations with its magnitude varying depending on the value of the order parameter S. Equation 6 defines S and its value is 1 for complete order and 0 for complete disorder.

$$S = \int \frac{1}{2}\left(3\cos^2\theta - 1\right) f(\theta) d\Omega \tag{6}$$

It is noteworthy that the expected positive contribution to the free energy from alignment can also be outweighed by favorable attractive interactions along the rod length between particles, in addition to packing/excluded volume effects. These inter-particle interactions are neither necessary nor convenient to include in this discussion regarding phase transition. Thus, what is referred to as "steric" effects will be the focus moving forward.

Using the ideal scenario of no rod-rod interactions, the relevant approach is that of Onsager who described such a system as a solution of "hard-rods".[80] In this case, the interaction potential between rods is infinite when they overlap and zero otherwise. Similar to how van der Waals modified his equation of state from that of an ideal gas, Onsager considered the finite volume of the particles treated as a gas. If the particles have volume *b* the accessible system volume V_a is reduced from the container volume V in proportion to the number of particles present in the container *N*. Equation 7 gives the adjusted volume. This will come into play as a correction from the free energy of a perfect gas.

$$V_a = V - Nb \tag{7}$$

The scenario is slightly more complex when moving to a rod-like particle, as the degree of alignment must be quantified. To treat this situation, Onsager considered what the volume inaccessible to the second rod would be while requiring two rods to not intersect. In order to approximate the excluded volume, consider the drawings in Figure 1.18. Figure 1.17 details the relevant lengths for this discussion. The rods are both considered to be of identical length *l* and orientated with angle γ between them. Both rods have identical diameters d. The projection of the second, angled rod onto the horizontal rod is given by *l* sin(γ).

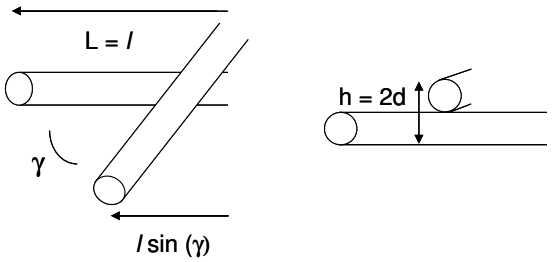

Figure 1.17: Geometry of crossed rods for calculating excluded volume showing the (left) projection of one rod onto the other and (right) the height.

In order to estimate the excluded volume, Figure 1.17 displays crossed rods with vanishing diameter (left) and the side view of their rod ends as two interacting circles (right). The center of mass in each case is marked with the small dot. If we define the excluded volume as the volume not accessible the center of mass of a second rod, then the areas enclosed by dotted lines are intuitive. On the left, we see the closest approach for two rods intersecting in the same plane. The center of mass of the second rod can only approach a distance *l*/2 from the horizontal rod. There is also symmetry above the horizontal rod and thus, the enclosed (dotted) excluded area is twice that shown. On the right hand side of Figure 1.18, we see that the upper rod-end cannot approach closer than 2d.

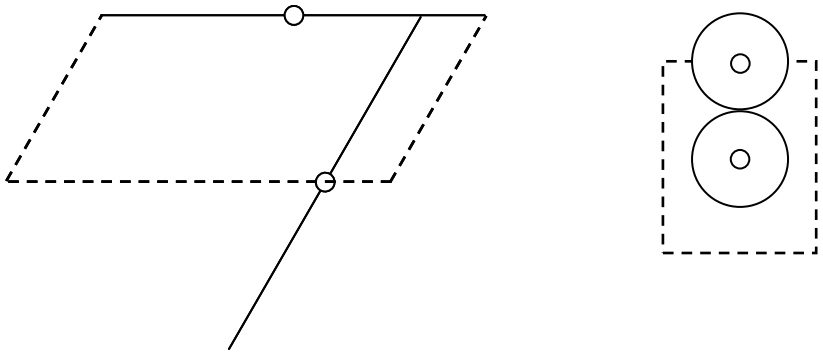

Figure 1.18: Excluded volume between rods. The excluded area is contained by the broken lines. Adapted from Jones (2002).[79]

Combining the length conventions given by Figure 1.17 and the excluded areas given by Figure 1.18, the resulting estimate is 2d $L^2 \sin(\gamma)$.[81] It is noteworthy that given the nature of the *sin* function, the excluded volume is obviously maximized when rods are perpendicular and vanishing when parallel. The excluded volume contribution to the free energy is calculated by considering the average value of $\sin(\gamma)$ for the system, $p[f(\theta)]$. According to Onsager, this is calculated using Equation 8.[80]

$$p[f(\theta)] = \iint f(\theta) f(\theta') \sin(\gamma) d\Omega d\Omega' \tag{8}$$

The value of $p[f(\theta)]$ for an isotropic system of rods is $\pi/4$ [$f(\theta) = 1/4\pi$] and decreases in magnitude with alignment. Finally, an expression for the free energy of the system as a function of concentration c and orientation can be formulated according to Equation 9.

$$F = F_0 + k_b T \left[\log(c) + \int f(\theta) \ln[4\pi f(\theta)] d\Omega + L^2 dc p[f(\theta)] \right] \tag{9}$$

Introducing the volume fraction of the rods ϕ, a more useful expression is formed by Equation 10.[79]

$$F = F_0' + k_b T \left[\log\left(\frac{L\phi}{d}\right) + \int f(\theta) \ln[4\pi f(\theta)] d\Omega + \frac{4L}{\pi d} \phi p[f(\theta)] \right] \tag{10}$$

Each term in this bracketed expression has a unique meaning, all of which is important in understanding the phase behavior of rods. The first term gives the free energy as a function of aspect ratio and concentration of rods, treated as a perfect gas. The second term arises from the loss in orientation entropy of the rods upon alignment. The third term takes into consideration the contribution from the excluded volume of the rods based on $p[f(\theta)]$. Examining this expression further, it is apparent that the free energy function is itself dependent on the orientation distribution function. This, functional expression is solved by choosing a trial function for $f(\theta)$ and then minimizing the free energy. This procedure requires the calculus of variations and is beyond the scope of this discussion. Following the results of Onsager, the crux of this exercise (the thermodynamic driving force for rods to align) is reached by examining the cartoon displayed by Figure 1.19.

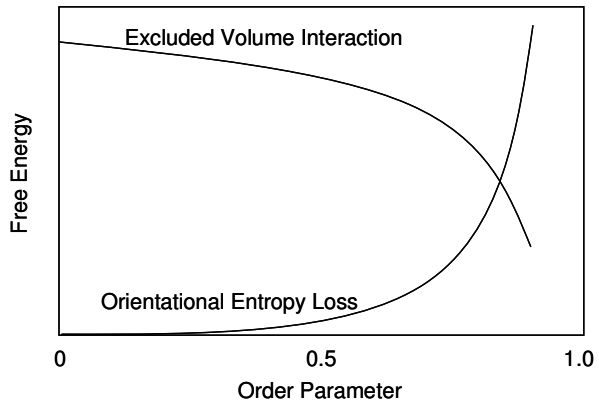

Figure 1.19: Contributions to total free energy upon alignment of rods. Adapted from Jones (2002).[79]

It is apparent that with increasing system alignment, the free energy penalty associated with a loss in orientational entropy of the rods is compensated by the reduction in free energy by the excluded volume interactions. Depending on the magnitude of $\phi l/d$, the relative magnitude of each term can vary. Increasing $\phi l/d$ by elongating the rods or raising the concentration favors

free energy reduction via excluded volume interactions and therefore, formation of nematic phase.

1.4.3 Carbon Nanotubes as Colloids

The general phenomena governing the dispersion of SWNT are typically treated via traditional colloidal theory in the literature. An approach based on the theory of Derjaguin, Landau, Verwey, and Overbeek (DLVO) is often used when describing the separate attractive and repulsive interactions.[82] On the other hand, a total interaction potential model may be more useful in describing polymer stabilized Brownian particles, as shown recently for spherical nanoparticles.[83] For the most part, these treatments are correct in that they describe various repulsive interactions such as entropic stabilization and electrostatic repulsion between SWNT. Uncertainties arise, however, when describing the attractive van der Waals interactions. These attractive potentials are often estimated to be on the order of 0.5 eV/nm of parallel tube contact; this number can be considered to be some ensemble average of the interaction potentials. Previous arguments have described interaction potentials via Hamaker constants as potentially troublesome due to the Hamaker approach deriving interaction magnitudes via bulk crystal properties.[67] Individual SWNT are not characteristic of bulk crystalline carbon such as graphite. Rather, depending on chirality the number of carbons interacting between two adjacent nanotubes varies. To calculate this, Equation 11, which gives the number of hexagons per unit cell N is needed. Here, d_R is the greatest common divisor of $(2n + m)$ and $(2m + n)$. Also required is d_v, the greatest common divisor of (n, m). The value of d_R is d_v when $n - m$ is not a multiple of $3d_v$, otherwise when $n - m$ is a multiple of $3d_v$, d_R is $3d_v$. To avoid confusion, example calculations are given in Dresselhaus, M.S. et al. (1995) including values for d_v, d_R, and N.[84]

$$N = \frac{2\left(m^2 + mn + n^2\right)}{d_R} \tag{11}$$

For SWNT with chiral indices of (n, n) or (n, 0), the number of hexagons per unit cell is simply $2n$.[84] For all chiralities, each of the six vertices of a hexagon splits one carbon atom into a third. Thus, we expect 2N carbon atoms per unit cell. For the indices described above, the number of carbon atoms per unit cell ($4n$) is small at 20 for a (5, 5) SWNT and 40 for a (10, 0) SWNT. On the other hand, when dealing with a (n, m) SWNT such as (6, 5) or (8, 3) the number of carbon atoms per unit cell increases significantly to 364 and 388, respectively. Thus, it could be expected that based on chirality of adjacent SWNT, the number of interacting carbons, and therefore the magnitude of interaction potential would vary. This phenomenon is not consistent with the Hamaker approach. Girifalco et al. (2000) show for (n, n) SWNT that with increasing tube diameter, both equilibrium separation distance and interaction potential increase for SWNT in a crystalline rope.[68] For example, doubling diameter from (10, 10) to (20, 20) shows a 143 % increase in cohesive energy. In addition, the variation in energy is not compensated by adjusting equilibrium spacing as discussed below. As, a result, it can be expected that various preparations of SWNT such as HiPco and CoMoCAT would have different attractive interactions and different dispersion protocols, even without considering aspect ratio discrepancies between the two.

Attractive interactions aside, there also exists a discrepancy between the scaling of potential for traditional colloidal rods and individual SWNT with separation distance. For parallel rods the interparticle potential scales with separation distance, D, as $D^{-3/2}$. As a result of this scaling, colloidal attractive interactions persist over longer distances than the D^{-6} scaling for atoms and molecules as described by Keesom, London, and Debye interactions.[82] Girifalco et al. estimated that inter-tube interactions are negligible at separation distances of just twice the tube radius.[68]

This means that in a SWNT rope, only the influences of nearest neighbors are felt. To put this scaling in context, consider Figure 1.20 below displaying the universal graphitic potential $\phi(R)$ where R is separation distance, and R_0 equilibrium spacing. Examining the figure, over a reduced separation distance of 1 unit (from 1 to 2 x-axis units), the attractive potential climbs to zero. For SWNT the distance parameter ρ is 1.357 nm and for a (10, 10) SWNT, R_0 is 1.672 nm. Thus, over 1 reduced unit distance we find inter-tube potential interactions to persist over only R_0, which is less than 2 nm. This scaling is much closer to the D^{-6} scaling of atoms and molecules than that of colloidal rods.

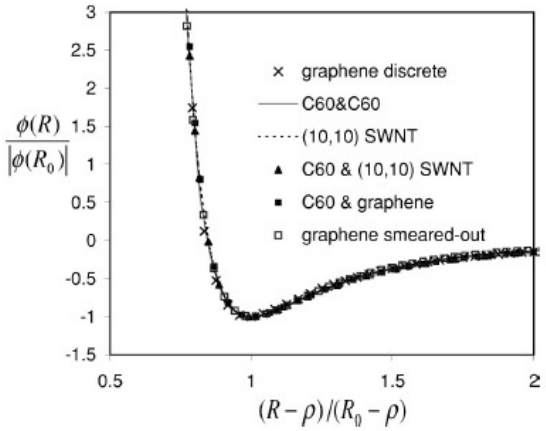

Figure 1.20: The universal graphitic potential curve for various carbon materials at reduced separation distance.[68]

To test this theory, Shvartzman-Coleman et al. (2004) put SWNT in context with classical colloidal systems and determined the stabilization criteria by examining the effect of adsorbed polymer chain length with varied surface coverage.[85] This was done by modeling the SWNT interaction potential with end-tethered polymers as well and supported by experiment. The repulsive potential was modeled using single-chain mean field theory which accounted for the possible geometric conformations of the adsorbed polymer chains. From this treatment, the free energy density per unit length of the CNT was derived for the solvent-polymer-nanotube system

as a function of separation distance. As a result of CNT being "nanometric" (which separates them from classical colloids), the large attractive energy minimum of 35 k_bT/nm is short ranged and decreases below thermal energy at ~5 nm inter-tube separation. While the range and strength of the repulsive potential was found to increase with chain length, a remarkable finding was the near independent behavior of attraction with surface coverage. Specifically, an energy barrier lower limit was found at 3 nm separation. Furthermore, the range of the repulsive potential was always greater than the attractive. Thus, the minimum polymer coverage required to stabilize the SWNT was investigated by fixing the molecular weight, then determining the number of chains needed to create a 5 k_bT/nm barrier at 3 nm separation. It was found that a repulsive barrier which prevented the attractive part of the potential from being reached was possible. This generalized strategy for SWNT dispersion by polymers was consistent with experimental evidence.

Based on a combination of experimental and theoretical considerations, interactions between individual SWNT, but not necessarily interactions between bundles of SWNT, are short-ranged. It is for this reason that the supposed "weak" but long-ranged entropic interactions of polymer stabilized SWNT can be exploited to maintain stable dispersions of individual SWNT. Shvartzman-Cohen et al. (2004) argued that the weak repulsion of polymer stabilized surfaces over long distances, such as steric repulsion, are all that is required to achieve individual SWNT.[85,86] Conversely, as seen with shear aggregation in dilute dispersions (50 ppm) of small bundled SWNT in unsaturated polyester resin, aggregation can be delayed by polymer viscosity but attraction must persist over long distances to interact at such a concentration.[87] It can be argued that a bundle of SWNT approximates a bulk crystal more closely than an individual, and

thus behaves as a classic colloidal rod. Thus, the colloidal nature of SWNT depends ultimately on the nanotube dispersion state.

The effective stabilization of SWNT with short polymers was also compared to classic colloidal particles by Shvartzman-Coleman (2004) et al..[85] Using polymer lengths and densities which stabilized SWNT, the interaction potential of larger colloids were modeled by the theory of de Gennes. It was found that while SWNT behaved like molecular objects with short-ranged attraction, colloidal attractions persisted over longer ranges (larger than the particle size) due to additivity of vdW interactions and thus could not be stabilized. These interactions are accounted for by the Hamaker constant. Basically, the range of the repulsive potentials was shorter than the attractive potential for colloids due to the steepness of the SWNT inter-tube potential. Experiments on fullerenes (15 nm) and VGCF (PR-24-PS) showed the inability of these polymers and experimental parameters to stabilize colloids. Remarkably, these results also indicate the ability to purify SWNT from impurities by polymer stabilization such as submicron carbonaceous particles and metals.

1.4.4 SWNT Dispersion in UPR

The motivation for the research presented herein was derived from the thesis by Kayatin (2008)[67] and also the previous work of Kayatin and Davis (2009)[87] on the dispersion, rheology, and shear stability of SWNT dispersions into UPR. In this study, various concentrations of SWNT with varied surface chemistry were dispersed in UPR by high shear mixing. The linear viscoelastic properties of the resulting nanotube dispersions were then characterized by rotational rheology, revealing evidence of a developing 3-D nanotube network structure in the fluid by measurement of a finite yield stress and elastic network response. The concentration dependence on the linear viscoelastic moduli was removed by colloidal mastercurve scaling using unique empirical

parameters. The success of such scaling indicated that the developing nanotube network was self-similar in nature. Figure 1.21 displays the behavior of the scaled storage (G') and loss (G") moduli against reduced frequency with respect to G" showing the Newtonian response for the neat UPR. The subscript c represents the critical concentration dependant parameters used for the scaling. The crossover between the two moduli delineates the hydrodynamic regime (right hand side of crossover), resulting from the interaction of fluid dispersed rods with the UPR, from the non-hydrodynamic response regime (left hand side), resulting from the inter-tube van der Waals network. The onset of network elasticity, where G' is independent of frequency, was dependent on the rheological percolation threshold, found to be ~0.1060 vol. % by comparison of many common criterion.

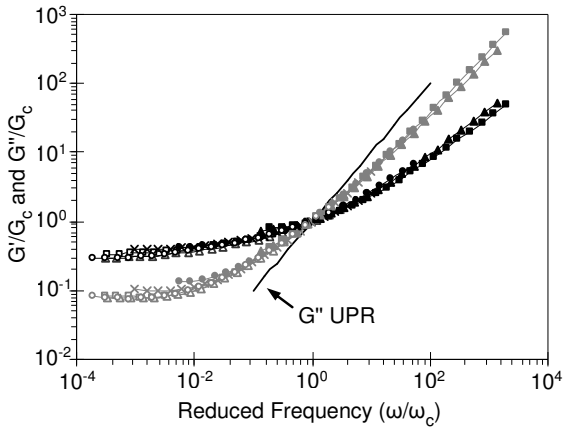

Figure 1.21: Reduced storage [black] and loss [grey] moduli with varying reduced angular frequency. The thin black line represents G" for neat UPR. Error bars indicate experimental range of values. Adapted from Kayatin and Davis (2009).[87]

Examination of the network scaling behavior, in conjunction with measurements of the reduced complex viscosity in the dilute regime, revealed non-Brownian dispersion behavior. This observation was revealing as individual SWNT are expected to show Brownian rigid-rod behavior.[88] Non-Brownian response occurs when the experimentally imposed shear stresses dominate the Brownian rotational diffusivity of the dispersed rods. This was a result of the

SWNT remaining dispersed as bundles, having an effective aspect ratio of ~650, as well as the strong van der Waals interactions between adjacent bundles. An interesting finding was that dispersions of various reactor batches of SWNT, and thus various surface chemistry, exhibited different low-shear viscosity behavior. Specifically, it was determined that SWNT with low surface oxygen content tended to show low-shear aggregation behavior (batches 183.6 Pure and Unidym). This can be observed by the upturn in transient viscosity in Figure 1.22 (left) as confirmed by optical microscopy as shown by Figure 1.22 (right). On the other hand, SWNT with significant surface oxygen content (batch 187.3) and SWNT with residual impurity from synthesis (batch 183.6 Unpure) were stable from aggregation. The dependence on type of surface oxygen content was also confirmed as carboxylated SWNT failed to disperse in UPR while SWNT having singularly bound oxygen species, such as hydroxyl or phenolic, (batch 187.3) both dispersed and were stable. These results provide a foundation for further study of the dispersion of carbon nanotubes in an important class of polymers as well as provide insights into future directions for tailoring nanotube surface chemistry in this system.

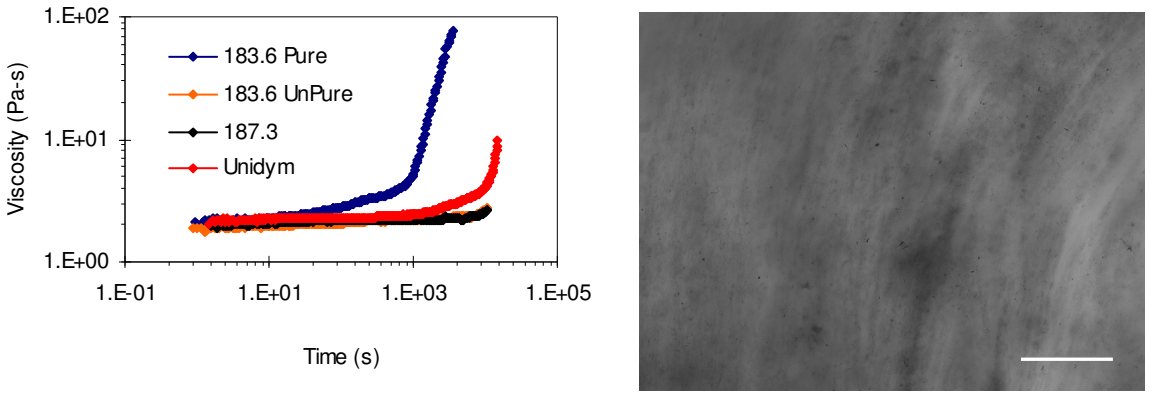

Figure 1.22: (left) Start-up flow curves for different SWNT samples dispersed in UPR at 50 ppm. The shear rate was constant at 0.01 1/s for all samples. (right) Shear aggregated dispersion of 183.6 Pure SWNT in UPR. Image taken with a 10x objective and 2x magnification. Scale bar = 50 μm.

1.5 Chapter Summaries

The focus of the research presented herein was to build upon the foundation for understanding developed by Kayatin (2008)[67] regarding the dispersion of un-modified SWNT in UPR by studying and evaluating potential functionalization methods and chemistries. Attention was specifically paid to the effect of processing during functionalization and how this influenced the functionalized SWNT or, in some cases, the dispersibility. By focusing on fundamental physicochemical interactions between components, experimental artifacts from processing were revealed in addition to characterization of functionalized material chemistry. Utilizing established processing methods for SWNT, nanotubes were either isolated prior to, or simultaneous with, functionalization reactions. To this end, a range of potential reaction and stabilization schemes were studied: (1) reductive alkylation of the Billups reaction and extending its applicability over a range of potential chemistries, (2) in-situ polymerization of styrene in presence of SWNT stabilized by reduction in lithium and ammonia, (3) the sidewall esterification of SWNT using the Bingel reaction by sonication in 1,2-dichlotobenzene, and (4) the non-covalent stabilization by adsorption of polyvinylpyrrolidone and isolation using centrifugation and lyophilization.

1.5.1 Chapter 2 Summary - Background Information

A theoretical framework for describing the interaction between SWNT and a solvent was described and used to motivate ideas for potential compatibilization chemistries. Constrains set by established individualization methods were discussed and chemical functionalization strategies were described. A brief picture of the factors influencing the chemical reactivity of SWNT was provided. Prior work and relevant details for each functionalization reaction of

interest were reviewed as deemed necessary to describe the current state of the art in the literature.

1.5.2 Chapter 3 Summary - Exploration of Small Molecule Functionalization

The reactivity of various chemical functional groups such as alcohols, esters, and in-situ generated ketals were studied to determine their ability for sidewall functionalization of reduced SWNT stabilized by Billups reaction conditions in dissolved lithium and ammonia. As displayed by Figure 1.23, the addition of Li to condensed ammonia results in formation of solvated electrons $\mathbf{e}^-$ capable of reducing SWNT sidewalls. Upon reduction and accumulation of n^- charges, SWNT are electrostatically stabilized. According to the Billups reaction, addition of an alkyl or aryl halide (X-R) results in a functionalized SWNT. In addition, the attachment of functional groups was attempted using the organometallic reduction of SWNT followed by metathesis re-oxidation. Functionalization chemistries were selected in order to induce specific and non-specific interactions between functionalized SWNT and UPR. The feasibility of such reactions was evaluated primarily using Raman spectroscopy and thermogravimetric analysis coupled with Fourier transform infrared spectroscopy. Finally, the discovery and implications of polymerization using an unsaturated monomer, 4-bromostyrene, in dissolved lithium and ammonia solvent was discussed.

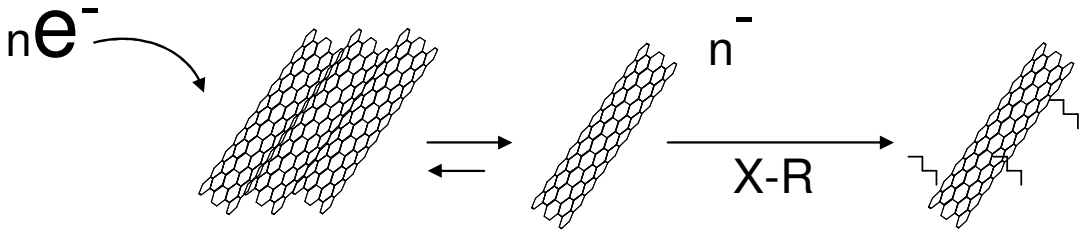

Figure 1.23: General reaction scheme for functionalization chemistries used in Chapter 3. The reduction of SWNT by Li/NH_3 results from transfer of a number of solvated electrons $n(\mathbf{e}^-)$ to the

nanotube, which stabilizes the dispersion by accumulating charges n^- along its length. Addition of an alkyl or aryl halide (X-R) affords a functionalized SWNT post-work-up.

1.5.3 Chapter 4 Summary - Functionalization with Polystyrene

The unexpected polymerization of 4-bromostyrene in lithium and ammonia was exploited to functionalize SWNT with polystyrene. Polystyrene was chosen as this polymer will swell and dissolve in UPR. The degree of functionalization was altered by varying the method and rate of styrene monomer addition, as well as the amount of lithium present, for a fixed amount of SWNT and styrene. The product was characterized in order to confirm the functionalization of SWNT with polystyrene and not simply over-coating of SWNT with polymer. A methodology for achieving a high extent of functionalization in a single pot reaction scheme was investigated and compared to the literature. Theoretical arguments were made for explaining the reaction mechanism. Figure 1.24 describes the reaction scheme used in this chapter showing the initial reduction of SWNT by Li/NH_3. Here, a number of solvated electrons $n(\mathbf{e}^-)$ reduces the nanotube sidewall, which stabilizes the dispersion by accumuulating charge n^-. Styrene monomer was added to this stable SWNT dispersion to initiate vinyl polymerization which after work-up, resulted in polystyrene functionalized SWNT.

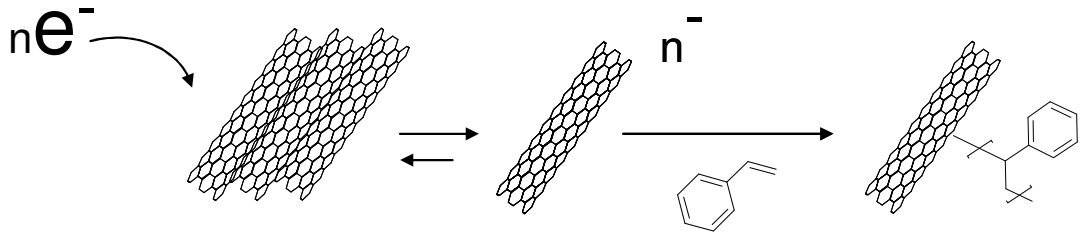

Figure 1.24: Reaction scheme for the in-situ polymerization of styrene studied in Chapter 4. The reduction of SWNT by Li/NH_3 results from transfer of a number of solvated electrons $n(\mathbf{e}^-)$ to the nanotube, which stabilizes the dispersion by accumulating charges n^- along its length. Addition of styrene results in polymerization of the monomer and termination on the sidewall of the nanotube to afford polystyrene functionalized SWNT.

1.5.4 Chapter 5 Summary - Functionalization by Sidewall Esterification

The sidewall attachment of ester functional groups to SWNT for compatibilization with UPR was studied using the Bingel reaction. SWNT were dispersed in 1,2-dichlorobenzene using high frequency bath sonication. To this dispersion, diethyl bromomalonate was reacted with SWNT in the presence of 1,8-diazobicyclo[5.4.0]undecene. The effect of sonication was investigated on the degradation of the solvent, the SWNT, and also the "non-SWNT" carbons in the sample. The nature of the "non-SWNT" species were identified. Charge transfer effects from doping were probed using Raman spectroscopy. Finally, bulk dispersion of functionalization products in UPR was also studied to characterize the dispersibility of the samples and determine controlling factors for mixing. Figure 1.25 highlights the reaction scheme used in this chapter.

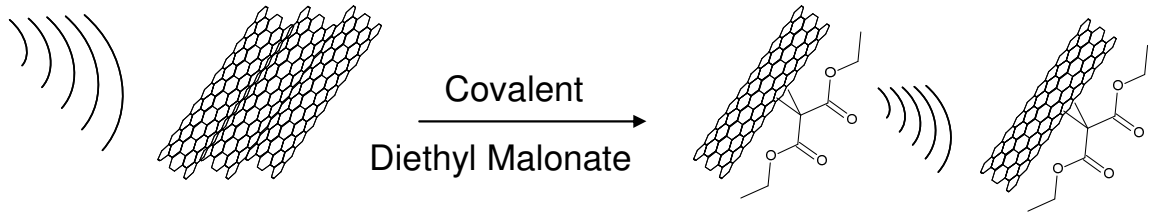

Figure 1.25: Reaction scheme for the sidewall esterification of SWNT via the Bingel reaction as studied in Chapter 5. SWNT bundles were broken up by bath sonication in 1,2-dichlorobenzene and SWNT were functionalized using diethyl bromomalonate, activated by an organic base. The sonication proceeded until the set reaction time had passed.

1.5.5 Chapter 6 Summary - Non-covalent Functionalization by Polymer Wrapping

The non-covalent functionalization of SWNT by polyvinylpyrrolidone adsorption was studied by first isolating stabilized SWNT from aqueous dispersions, then using lyophilization to isolate the nanotubes for re-dispersion in UPR. Detailed spectroscopic studies were carried out to determine the effect of processing on the polyvinylpyrrolidone chemistry itself as well as to characterize the compatibility with UPR. The molecular dissolution of PVP in UPR was discovered. The effects of charge transfer between polyvinylpyrrolidone and SWNT were

studied using Raman spectroscopy. Finally, the ease of dispersibility in UPR was demonstrated. Figure 1.26 highlights the stabilization scheme used in this chapter for dispersing and isolating SWNT. Intense tip sonication was used to break apart the SWNT bundles. Adsorbed polyvinylpyrrolidone prevented re-aggregation.

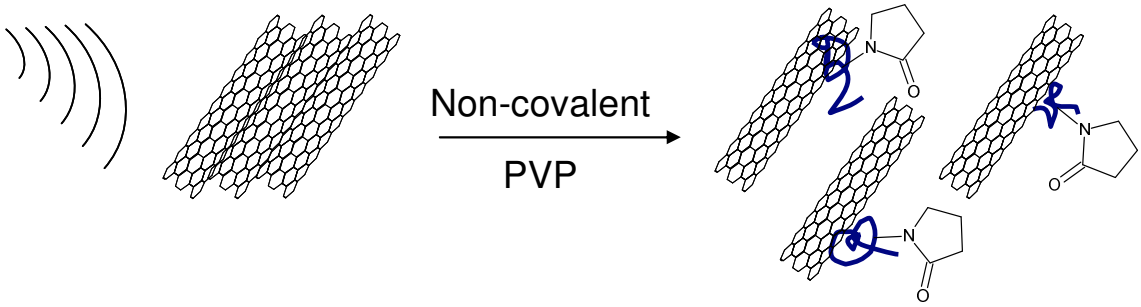

Figure 1.26: Scheme for the stabilization of SWNT by non-covalent adsorption of polyvinylpyrrolidone, as studied in Chapter 6. SWNT bundles were broken up by tip sonication in water and SWNT were stabilized from re-aggregation by the adsorbed polymer size and chemistry.

Chapter 2

Background Information

2.1 Carbon Nanotube Functionalization

Due to the inherent difficulties with CNT aggregation, significant research has focused on improving dispersion through intense mixing and sonication, and increasing nanotube - solvent compatibility using covalent or non-covalent functionalization techniques.[29,89,90] For the most part, these efforts do not result in true thermodynamic solutions, but rather, provide meta-stabilized dispersions with re-aggregation kinetics on a long enough timescale to exceed required processing times. The introduced meta-stabilities can originate in many forms (electrostatic, steric, viscous) and are best described using DLVO theory.[82] The total interaction potential for meta-stabilized particles can be represented as the sum of the repulsive forces and van der Waals attractive force. An energetic barrier is established at intermediate particle separation such that aggregation is prevented in absence of an external perturbation. DLVO theory is especially suited for describing Coulombic repulsion via surface charging (surfactants) and steric stabilization via attachment of polymer chains (via the osmotic pressure). While the simple attachment of bulky molecules or introducing surface charges does effectively decrease the nanotube surface energy, it does not guarantee improvement of solute-solvent compatibility.

The consequence of such a large inter-tube attractive potential manifests itself through a large and positive ΔH_{mix} in common solvents. A conceptual metric for the energetic cost of mixing CNT in a pure solvent was developed by Bergin et al. (2008).[91] Refer to Appendix A1 of

Kayatin (2008) for rigorous derivation.[67] Equation 12 displays the expression for ΔH_{mix} defined by the surface energy parameters.

$$\Delta H_{mix} \approx 2\frac{m_{NT}}{R_2 \rho_{NT}}\left[E_{Sur}^{NT} + E_{Sur}^{Sol} - E_{Inter}^{NT-Sol}\right] \tag{12}$$

Here, R_2 indicates the final bundle size after mixing a mass of CNT m_{NT} of density ρ_{NT}. The solvent-nanotube binding energy per surface area is given by E_{Inter}^{NT-Sol} and is of utmost importance for determining the magnitude of ΔH_{mix}. For example, the direct protonation of the CNT sidewall using superacids lends a strongly interacting contribution via this term. E_{Sur}^{Sol} is the specific solvent surface energy and E_{Sur}^{NT} is the specific CNT surface energy, a direct function of the inter-tube attractive potential. With respect to classical solution theory, this expression relies on parameters that are not easily measured but provides an outstanding tool for examining what factors control the total energetic cost of mixing. In this research, the solvent, and thus E_{Sur}^{Sol}, is fixed for that of UPR. Thus, the focus of research herein will be on modifying two parameters: 1) the CNT-UPR interface (E_{Inter}^{NT-Sol}) and 2) decreasing the inter-tube attractive potential (E_{Sur}^{NT}). It is noteworthy that for good solute-solvent interaction local ordering effects of the solvent can also impact ΔS_{mix}.

Covalent functionalization is an attractive route for CNT-UPR dispersion since the type of attached chemistry can be selectively chosen to match that of the solvent. After an exhaustive review of various metrics by Coleman (2009), it has been suggested that covalent functionalization yields the greatest individual CNT (outside of superacids).[92] The author even states that functional group chemistry controls the interactions with the solvent rather than the nanotube surface. This single experiment, however, would not be able to account for effects of functional group surface density and should be interpreted with care. When considering the

specific interaction between the solute and solvent, a more practical theory than described by Equation 12 can be employed and this can be used to rationally select functional group types. This is achieved by estimating ΔH_{mix} using the Flory-Huggins interaction parameter χ. An expression for χ was originally adapted from the van Laar heat of mixing by Flory.[93] Equation 13 displays volume normalized enthalpy in terms of the solvent molar volume $\overline{V}_s$ and the solute volume fraction ϕ.

$$\frac{\Delta H_{mix}}{V_{Mix}} = \chi \frac{RT}{\overline{V}_s} \phi(1-\phi) \tag{13}$$

Next, an appropriate expression for χ is introduced by Equation 14.[94]

$$\chi \approx \frac{\overline{V}_s}{kT}\left[\left(\delta_{NT}^{D} - \delta_{Sol}^{D}\right)^2 + \left(\delta_{NT}^{P} - \delta_{Sol}^{P}\right)^2 + \left(\delta_{NT}^{H} - \delta_{Sol}^{H}\right)^2\right] \tag{14}$$

Here, the Hansen solubility parameters δ^i are used where i represents the dispersive (D), polar (P), and hydrogen bonding (H) Hansen solubility parameters.[94] Note that the sum of the squares of all three parameters yields the familiar Scatchard-Hildebrand solubility parameter. The Hildebrand parameter can be found as the square root of the cohesive energy density, which is taken to be the heat of vaporization normalized by the molar volume of pure solvent. Conceptually, Hildebrand and Scott only considered regular solutions and, thus, no solute-solvent interactions.[95] By extending the theory for multi-component solubility parameters, various contributions to the cohesive energy density of a liquid can be accounted for. The Hansen Theory considers contributions from the dispersion cohesive energy, the polar cohesive energy, and the electron exchange parameter known as the hydrogen bonding cohesive energy. Hansen notes that the description of the hydrogen bonding parameter is an oversimplification, however, as this parameter also accounts for any interactions not accounted for by the other two

parameters. In Equation 14 the magnitude of χ is controlled by the square difference of the respective δ^i for the CNT and solvent. Thus, to minimize χ and therefore ΔH_{mix} the two parameters should match. Conveniently, these parameters are tabulated by Hansen and readily available providing a quick method to tailor specific functional group-solvent interactions. In addition, Bergin et al. (2009) have also examined CNT dispersions of many solvents by the Hansen method.[96] As a final note, it should be apparent that the use of solubility parameters fails to predict exothermic mixing enthalpy, as the square of any difference will be positive. Therefore, this theory is limited to predicting athermal ($\Delta H_{mix} = 0$) solutions. Hansen argues otherwise and cites examples in his book.[97,98]

2.1.1 Strategies for Increasing SWNT-UPR Compatibility

UPR consists of a two part system of 60 wt. % polyester oligomer and 40 wt. % styrene monomer. Thus, SWNT compatibilization strategies may be tailored towards either component as long as nanotube chemistry does not result in substantial solvent partitioning. Examining the polyester oligomer component, displayed by Figure 2.2, a striking feature is the abundance of oxygen rich groups found in the ester linkages decorating the oligomer backbone, specifically carbonyls. Figure 2.1 displays the ATR-FTIR spectrum for UPR after partial removal of styrene monomer using vacuum. Here, a strong peak at ~1640 cm^{-1} arising from the ester linkage can be seen as a dominant feature in the spectrum. These sites are available hydrogen bond (H-bond) acceptors. Typical values for H-bond energies are on the order of 25 - 100 k_bT,[79] making this interaction favorable due to the high concentration of possible sites. Therefore, one potential route for nanotube functionalization is to introduce H-bond donors to the CNT sidewall that can interact with polyester carbonyls. This strategy would generate a specific interaction between components. Specific interactions include geometric and/or complementary associations

between like molecules as well as geometric and/or ionic (acid-base)/h-bond complementary associations between un-like molecules.[82] Although never specifically referred to by the authors, a few studies have been using this functionalization strategy in the literature. Seyhan et al. (2006) obtained amine functionalized MWNT (MWNT-NH_2) and found that their cured composites had increased tensile strength.[14] Later this group also reported increased modulus as well as a higher glass transition temperature for MWNT-NH_2.[15] All of these effects can be attributed to increased CNT-UPR compatibility and the specific hydrogen bonding interaction (assuming dispersion states and aspect ratios were equal). Label S1 in Figure 2.2 summarizes this functionalization strategy by showing the hydrogen bond between a generalized amine functionalized SWNT and UPR oligomer carbonyl.

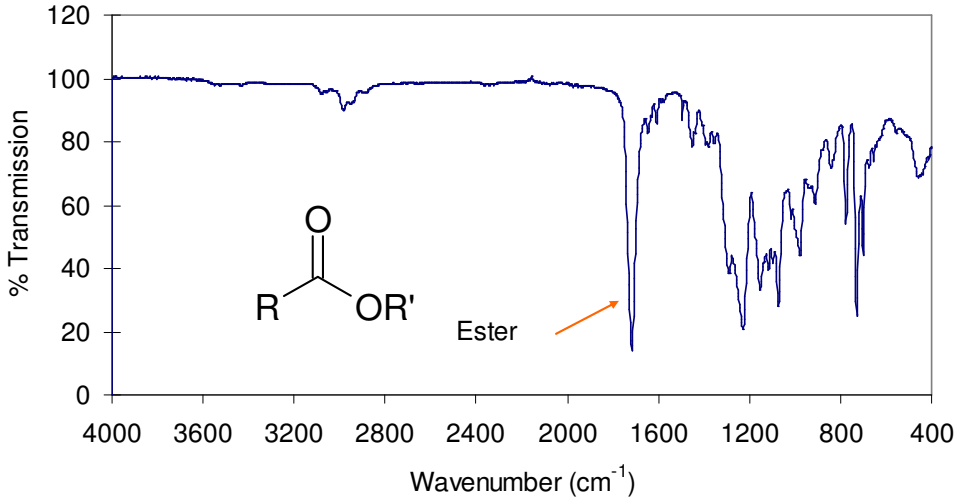

Figure 2.1: ATR-FTIR spectrum of Polylite® X31003-00 UPR after holding under vacuum for one week to remove the majority of styrene. The ester linkage is highlighted by the carbonyl peak at 1640 cm^{-1}.

A second promising functionalization strategy takes advantage of the Hansen solubility theory introduced by Equation 14. Schemes to increase SWNT solvent compatibility through matching of functional group physical properties are desirable to minimize the magnitude of ΔH_{mix}. One obvious choice of functional group to match a polyester oligomer is an ester itself. This strategy

takes advantage of mediating non-specific associations (electrostatic, vdW, steric, osmotic, hydrophobic) between molecules.[82] Label S2 in Figure 2.2 summarizes this functionalization strategy by showing an ester functionalized SWNT, as produced from the Bingel reaction. Note that the ethyl ester branches match the oligomer backbone exactly. In addition, a number of various other chemistries could potentially be used to compatibilize the SWNT sidewall with UPR such as carbonyl compounds.

As indicated previously, functional groups can also be chosen to match the chemistry of the styrene monomer. Label S3 in Figure 2.2 highlights one such chemistry. Here, styrene is polymerized in the presence of SWNT and terminated on the nanotube surface. The polystyrene chemistry can swell, and based on the molecular weight, extend into the UPR to sterically stabilize the SWNT. Due to the high concentration of styrene in the UPR, this technique could be just as beneficial to the dispersion state.

Finally, as discussed in Section 1.4.3, the shape of the overall inter-tube potential can be changed by the adsorption of polymers to SWNT. Not only can an adsorbed polymer induce a steric repulsion contribution, its chemistry can also provide specific or non-specific interactions for compatibilization with UPR. The chemistry of the chosen polymer for UPR stabilization must be unique, however, since dispersion preparation is typically done in the aqueous phase. This is especially challenging since hydrophilic polymers such as charged surfactants, non-ionic block polymers such as Pluronics, and biomacromolecules such as DNA are not compatible with UPR. It seems unlikely then, that one polymer chemistry would be compatible with UPR in addition to being water soluble. Fortunately, the water soluble polymer polyvinylpyrrolidone has one unique aspect that allows it to interact with many organic solvents and water, its resonance mesomerism behavior. This feature of the polyvinylpyrrolidone can be used to stabilize SWNT

in water then allow for re-dispersion in UPR using lyophilization to isolate the nanotubes. Label S4 in Figure 2.2 highlights this compatibilization strategy.

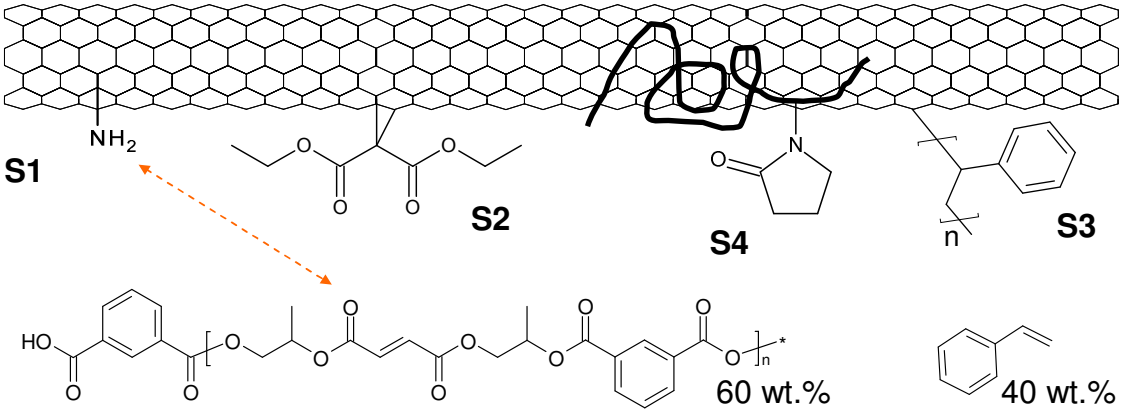

Figure 2.2: Summary of potential chemical functionalization strategies for compatibilization of SWNT with UPR: (S1) specific interaction between hydrogen bond donors and polyester oligomer, (S2) non-specific interaction of ester functionalized SWNT and polyester oligomer by "like-like" solubility from matching solubility parameters, (S3) non-specific interaction between polystyrene functionalized SWNT and styrene monomer, and (S4) non-covalent functionalization using polymer adsorption to sterically stabilize SWNT with non-specific compatibilization between pendant groups and polyester oligomer.

2.1.2 Constraints on Functionalization Chemistry Schemes

The fundamental requirement to successfully functionalize SWNT is to first expose the surface area that is hidden by aggregation or contained within SWNT bundles. A number of methodologies to separate SWNT have emerged as commonplace in nanotube processing. The most common approach involves sonication in an appropriate solvent, highlighted by Figure 2.3. Sonication breaks down SWNT aggregates or bundles and can be used to facilitate covalent and non-covalent functionalization. For example, sonication of SWNT in the presence of a water soluble polymer results in adsorption of the hydrophobic polymer backbone to the nanotube surface. Similarly, sonication in an appropriate solvent and addition of appropriate reagents can be used to covalently functionalize SWNT, with the energy of sonication aiding in the reaction kinetics. Both of these established methodologies were utilized in this research.

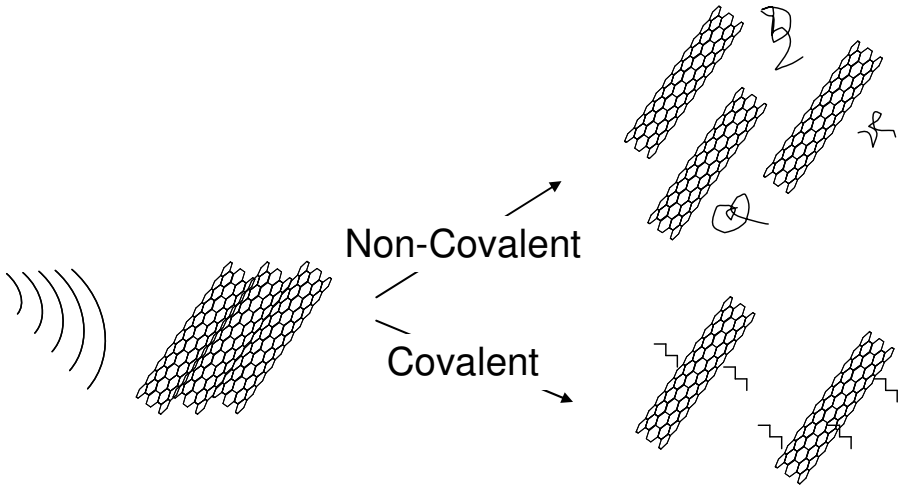

Figure 2.3: SWNT functionalization methods based on individualization by sonication. When sonicated in the presence of an adsorbing polymer, (top) SWNT are stabilized by non-covalent functionalization. Using sonication to expose SWNT surface area, (bottom) reagents can be added and the energy of sonication used to functionalize the surface covalently.

The stabilization of SWNT by electrostatic repulsion not only successfully exposes the SWNT surface area by individualization, it can be less damaging to the nanotube than sonication. In fact, the protonation of SWNT using chlorosulfonic acid, has been recognized as the only true thermodynamic solvent for SWNT, based on phase behavior studies[70] and thermodynamic modeling.[99] Superacids, however, limit the additional chemistries that can be carried out due to their extreme corrosiveness. Individualization of SWNT by reduction, on the other hand, has been used to functionalize SWNT, most notably by the Billups reaction.[100] Figure 2.4 highlights this process. Here, a number of electrons n($\mathbf{e}^-$) reduce the nanotube, which stabilizes the dispersion electrostatically by accumulating charges n^- along its length. From this point, an appropriate reagent can be added to covalently functionalize the SWNT. Using this individualization strategy, the range of possible chemistries that can withstand this strong reducing environment will be tested and extended for compatibilization with UPR.

Another common method employed for nanotube reduction utilizes the nucleophilic reactivity of organolithium compounds towards SWNT, such as methyl lithium. In this strategy, the

addition of the organolithium compound to the nanotube initially functionalizes the nanotube with whatever associated alkyl substituent present. This addition reaction transfers a negative charge across a double bond on the nanotube surface and electrostatically stabilizes the SWNT. It is important to remember that for each charge transferred to the SWNT, one functional group is added. This methodology will be used to complement studies based on the Billups reaction scheme.

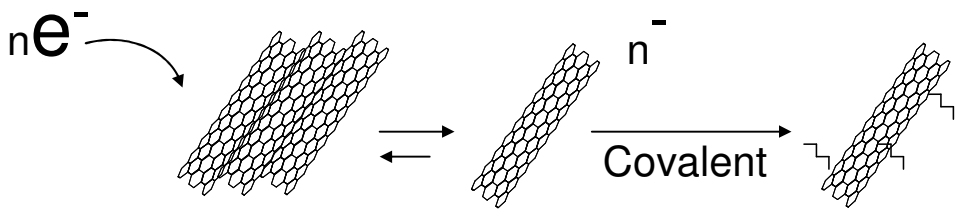

Figure 2.4: SWNT functionalization based on individualization by reduction. A number of electrons n(**e**$^-$) reduce the nanotube, which stabilizes the dispersion by bearing charges n$^-$ along its length. Once stabilized and individualized, chemistry can be done on the individual SWNT level.

2.1.3 Overview of SWNT Reactivity

The most fundamental description of nanotube reactivity was described by curvature-induced local strain and its correlation with nanotube diameter.[101] This simple concept explains the low reactivity of MWNT as compared to SWNT. The increased reactivity of high-strain, small diameter nanotubes can be understood as pyramidalization of sp^2 hybridized carbons and π orbital misalignment.[101,102] The apparent chiral selectivity of SWNT, and increased reactivity of metallic SWNT, has been explained for diazonium functionalization to be dependant on formation of a charge-transfer complex intermediate state which is stabilized by the increased metallic nanotube density of states.[103] Typical arguments for selectivity are made following the correlation between the presence of metallic density of states at Fermi energy and the absence in semiconducting SWNT.[104] Joselevich (2004), however, made compelling arguments regarding

the disconnect between the typical solid-state physics treatment of nanotube classes based on energy band structure and a molecular orbital picture which describes mechanistic effects.[105] In this matter, curvature was ignored and focus was given to the highest occupied molecular orbital - lowest unoccupied molecular orbital (HOMO-LUMO) band-gap and aromaticity, which governs stability. Note that metallic SWNT are slightly less aromatic than semiconducting SWNT.[106] Joselevich (2004) makes the comparison between annulenes and nanotubes using the Hückel rule. Aromatic benzene, for example, is stable due to having filled low-lying orbitals (bonding) and empty high-lying (antibonding) orbitals. Due to the large HOMO-LUMO gap, there is a large penalty for disturbing the electronic structure. Likewise, comparisons were made with semiconducting SWNT being considered aromatic and metallic SWNT considered antiaromatic. In addition, comparisons were drawn from annulenes to nanotubes having a full valence band (bonding) or an empty conduction band (nonbonding) with a bandgap, or having electronic states (nonbonding) at Fermi energy with no gap, to that of aromatic benzene. In both cases the increased reactivity was correlated with being less aromatic and having a smaller HOMO-LUMO gap. These arguments will be substantiated as necessary in each chapter for the reaction mechanism and type therein.

2.1.4 The Billups Reaction

The Billups reaction utilizes solvated electrons formed by the addition of lithium metal to condensed anhydrous ammonia. This strong reducing environment was used to transfer negative charge to the SWNT and individualize the nanotubes. Alkyl halides were then added to add hydrocarbon chains to the nanotube surface, termed reductive alkylation.

Solutions of Alkali Metals in Ammonia

The addition of alkali metals (M) such as sodium (Na), lithium (Li), and potassium (K) to condensed ammonia results in the formation of stable blue colored solutions which expand with non-ideal mixing volumes.[107] The characteristic electric blue color is a result of broad optical absorption in the near IR region (1500 nm) from solvated electrons. These electrons exist in a cage of ammonia molecules, but are not bound. In the absence of water and air, these solutions decompose very slowly and are stable for long periods. Equation 15 displays the initial reaction for dissolved Na.

$$Na \xrightarrow{liq\ NH_3} Na(NH_3)_n^+ + e(NH_3)_n^- \tag{15}$$

As a result of the free electrons in these systems, two unique properties that arise are high conductivity and strong reducing capacity. When acting as a reducing agent, the solutions readily oxidize to reduce π bonds. As discussed in Chapter 3, many compounds cannot survive this environment. Thus, dissolved metal reductions can be used to treat toxic waste contamination sites for pesticides and chlorinated compounds like PCBs[108,109] and even chemical warfare agents.[110] At high concentrations, at least 7 mole percent M,[111] the solutions transform from blue to a copper sheen and behave as liquid metals. The metallic behavior results as the complex loses an electron to a conduction band.[112] Specifically, for Na this high concentration behavior is the result of formation of $Na(NH_3)_n^+$ and $e_2(NH_3)_m^{2-}$. Over time, or in the presence of a catalyst, the solutions will decompose to form metal amides and liberate hydrogen as displayed by Equation 16. The decomposition is a result of the solvated electrons reducing excess ammonia.

$$2Na + 2NH_3 \rightarrow 2NaNH_2 + H_2 \tag{16}$$

It is noteworthy that $FeCl_2$ catalyzes rapid decomposition, and thus, HiPco SWNT must be thoroughly washed and neutralized from acid purification residues if placed in contact with M/NH_3 solutions. Conversely, the reduction of aromatic ketones in Li/NH_3 was found to be catalyzed, not quenched, when trace Co was present.[113] Therefore, unique reactivity might be anticipated with CoMoCAT® SWNT. Interestingly, no effect was observed from cobalt on the reduction of aromatic aldehydes[114] as explained by differences in their relative reaction rates.[115]

The dissolution of Li in NH_3 is known to form the stable complex $Li(NH_3)_4^+$. When cooled to very low temperatures, a solid ammoniate of $Li(NH_3)_4(e^-)$ will crystallize with a cubic-body-centered arrangement. Wasse et al. (2000) have shown that Li remains tetrahedrally coordinated to ammonia molecules even at temperatures as high as -43°C.[111] Overberger (1959) has formulated the dissolution of Li according to Equation 17, indicating a single free electron from Li.

$$Li + NH_3 \rightarrow Li^+(NH_3) + e^-(NH_3) \tag{17}$$

Even at low temperatures the alkali metals exhibit high solubility in condensed NH_3. For example, at -50°C the reported solubility are as follows (mol M/mol NH_3): lithium, 0.27; sodium, 0.19; potassium, 0.20. Given the reported atomic mass of Li to be 6.941 g/mol and taking its density as 0.534 g/mL, the solubility in liquid NH_3 (0.682 g/mL) is substantial at ~75 mg Li/mL NH_3.

Billups Reduction

The reductive alkylation of SWNT using Li in NH_3 was first studied by Liang et al. (2004).[100] In this scheme, NH_3 was condensed over dry SWNT and Li was added. The nanotubes were reported to be intercalated by Li ions and electrostatically separate as a result of charge transfer

to the sidewalls. It was later shown that liquid ammonia solvated lithium intercalates SWNT bundles.[116] The sidewalls were shown to saturate at ~$C_{1.6}$/Li but this electron/lithium uptake has been reported to be as high as C_2/Li.[117] Equation 18 and 19 show a proposed series of reactions by Borondics et al. (2005) outlining the formation of the carbanion complex.[118]

$$Li + nNH_3 \rightarrow Li^+ + e^-(NH_3)_n \tag{18}$$

$$e^-(NH_3) + C \leftrightarrow nNH_3 + C^- \tag{19}$$

Subsequent reactions that can occur are the hydrogenation via carbanion decomposition by addition of proton source such as methanol (Equation 20) and the alkylation/arylation reaction (Equation 21).[118]

$$C^- + CH_3OH \rightarrow CH + CH_3O^- \tag{20}$$

$$C^- + RX \rightarrow CR + X^- \tag{21}$$

Addition of an alkyl halide to the reactor was reported to form a radical anion that dissociates to a halogen anion and an alkyl radical. Radicals can readily add to the SWNT sidewall. A general side reaction was outlined according to Equation 22.[119]

$$2e^-(NH_3)_n + 2RX \rightarrow R_2 + 2nNH_3 + 2X^- \tag{22}$$

Borondics et al. (2007) suggest excess reagent can suppress the effect of this side reaction (probably meaning an excess reagent will react with bound carbanions after free reducing species were consumed). Notably, if the mechanism is radical coupling, as suggested, this would certainly increase formation of R_2. The suggested radical based mechanism was supported by GC-MS analysis which showed expected products from radical disproportionation and recombination. Both branched and linear alkyl halides were used containing iodine and bromine. In addition, tetrahydropyranal ether and carboxamide were also attached. The reaction has come to be known as the Billups reaction. SWNT in the presence of Li/NH_3 are referred to here as

Billups reaction conditions. It is noteworthy that the affinity of radical attachment to SWNT sidewalls was later shown by sidewall carboxylation (Billups conditions) using acyl peroxides of dicarboxylic acids[120] and assorted peroxy radicals[121] (in organic solvent). Furthermore, the choice of M determines the ultimate thermal stability of dodecylated SWNT as explained by addition pattern (ratios of 1,2 and 1,4 alkyl addition) relative to a benzene ring section on a SWNT sidewall.[122]

Further evidence for a radical based mechanism was given by studying the alkyl and aryl sulfides under Billups conditions. Chattopadhyay et al. (2007) found that alkyl sulfides form radical anions and dissociate to form an alkyl radical and mercaptide (RS^-) with the former attaching to the nanotube sidewall.[123] Similar results were obtained for diphenyl sulfide (and even disulfides) with a phenyl radical attaching to SWNT and biphenyl by-products. It is noteworthy that these reactions have lower yield than from alkyl and aryl halides. A control experiment with no addition of reagent showed < 3 wt. % loss from TGA. For further discussion on the single-electron transfer (SET) mechanism in organic synthesis, see Chattopadhyay et al. (2007) and references located within.[123] The salient point of the Billups reaction is that SET process from the SWNT surface is not a bond forming step, but involves non-covalent charge transfer. The re-oxidation conditions determine the bonding nature of the final product.

Billups Functionalization

Chattopadhyay et al. (2005) studied the reactivity of aryl iodides under Billups reaction conditions.[124] Phenyl, t-butyl phenyl, and aniline were attached to the SWNT. Benzoic acid and methoxy phenol groups were also attached, but to a lesser extent than the electron withdrawing substituents. Mukherjee et al. (2008) extended this work to include treatment with n-halosuccinimides and alkyl peroxides by generation of succinimidyl radicals and alkoxy radicals,

respectively.[125] Large batches of SWNT (100 mg) have been successfully processed with long chain carboxylic acid groups.[126]

MWNT can also be functionalized by the Billups approach. Stephenson et al. (2006) attached a number of functional groups to MWNT including phenyl, 4-aminophenyl, 4-benzoic acid, 4-benzyl alcohol, 4-tert-butylphenyl, 4-methoxy benzene, and docecyl groups.[127] Unlike, SWNT reactions, the MWNT reactions were homogenized before and during the reaction using a rotor-stator. Finally, using sodium instead of lithium MWNT in excess of 1 gram were functionalized by dodecyl chains in a single batch. Clark and Krishnamoorti (2009) have also studied the dispersion energetics of dodecylated and butylated MWNT.[128] The authors did not find use for homogenization but do note a difference in MWNT reactivity with respect to SWNT based on decreased nanotube curvature.

The Billups reaction has been shown to be selective towards small diameter (both metallic and semiconducting) and metallic SWNT when alkylation is carried out using Na and HiPco SWNT.[104] Interestingly, the functionalized semiconducting tubes still fluoresced. Re-oxidation with ethanol instead of oxygen, leading to protonation, shows a significantly lower extent of functionalization with no selectivity. While attractive from a standpoint of chiral separation and sorting of bulk SWNT, the prospect for dispersion is inhibited by this selectivity. This effect on small diameter tubes was compared to the ability of fullerenes to stabilize a negative charge by means of high degree of pyramidization in the carbon framework. The preference for metallic tubes can be explained by the accessibility and density of states per C atom near the Fermi level.

More detailed effects of hydrogenation reactions of SWNT under Billups conditions were given by Borondics et al (2007).[119] In this study, products from two dissolving metal reduction based functionalization reactions were compared: Billups (using two ammonia condensations)

and in tetrahydrofuran (THF) using lithium-naphthalenide. The carbanions were reacted with methyl iodide, butyliodide, benzyl bromide, dodecyl iodide, and 1,12-dibromododecane by dissolving in THF and dripping this solution into the reaction. TGA-MS analysis was carried out to determine the species evolved during heating and degradation temperatures. Interestingly, the highest degree of functionalization by Raman was for hydrogenation and dodecylation in NH_3. Mass losses were < 10 wt. % for all samples, indicating that hydrogenation was present in all functionalizations. In fact, more hydrogens than alkyl groups were attached. In general, smaller molecules are easier to attach using NH_3. The trends in degradation can be summarized by alkyl group losses at ~350°C followed by hydrogen at 500°C and more complex bond scission at 600°C. It is noteworthy that M naphthalene reduced SWNT can also be reacted by direct addition of acyl peroxides as displayed by Martinez-Rubi et al.[129]

Recently, Schmidt et al. (2009) have revealed the mechanism of diazonium coupling to SWNT.[130] Specifically, the selectivity of aryl radical addition to metallic SWNT was found to be a kinetic effect. In other words, metallic SWNT react faster with neighboring radicals in solution that do semiconducting tubes. This finding has a profound impact on the understanding of nanotube reactivity towards radical reactions. Furthermore, comparison of isolated carbanion SWNT films to those under pure Billups conditions, which have free reducing species, reveal effects increasing selectivity by delocalized charges migrating to find more favorable SWNT and non-uniform Fermi energy.

Controlling Extent of Functionalization

A significant advancement in the controlled functionalization of SWNT was made by Voiry et al (2010).[131] In this work, the authors isolated nanotube salts with varying charge/C ratios as solid films, removing the effects of free reducing species on reactions. The percolated isolated films

have common Fermi energy, and thus, did not show chiral selectivity towards functionalization. This required use of a glovebox system plumbed with anhydrous solvent delivery, in addition to considerable time. Nonetheless, napthalene dissolved in THF was converted to green naphthalene anion by addition of sodium. A certain amount of stock solution was then incubated with SWNT for 2 days to produce solid $KC_x(THF)_y$ nanotube salts ($10 < x < 370$) after isolation and washing with THF by filtration. The dry salts are then placed in DMSO to disperse as homogeneous suspensions. Reagents such as 1-bromo-decanoic acid or 4-(5-bromopentyloxy)-4′-cyanobiphenyl are added and stirred for 3 days even though functionalization is reported to occur rapidly (probably for analytical purposes). The extent of functionalization was found to correlate almost linearly with charge/C by Raman, XPS, and TGA data. Interestingly, extent of reaction by TGA mass losses correlated very well with XPS. The lower yield of these reactions of 15 - 25 % at highest charge was rationalized by a number of considerations. This included the steric hindrance, side reactions, and mechanism based kinetics enhanced when the salts are isolated from free reducing species. The authors gave a proposed reaction scheme based on previous observations of diazonium coupling to SWNT and formation of biphenyl. The free radical chain mechanism is given in Figure 2.5. The most important observation from this mechanism is the reaction of SWNT with radicals in close proximity to the surface, not from the surface.

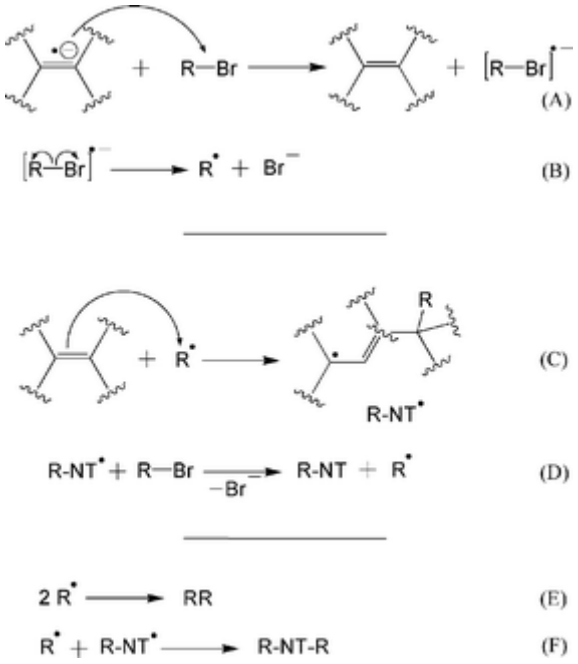

Figure 2.5: "The proposed free-radical mechanism for the functionalization of reduced SWCNTs. (A) and (B): initiation steps; (C) and (D): propagation steps; (E) and (F): termination steps. R stands for an alkyl group. The nanotube radical formed in step (A) can also react, as in step (D)." Adapted from Voiry et al. (2010).[131]

Interestingly, the stability of reduced SWNT in DMSO was investigated by Guan et al. (2009).[132] The evolution of gases from addition of SWNT reduced with sodium napthalide in THF to DMSO was studied. It was found that reduced SWNT can initiate radical reactions with scavengers such as DMSO leading to methyl and other unidentified addends. Thus, only neutral SWNT are stable in DMSO. This may or may not impact the result stated above.

Deng et al. (2010) exploited the diameter selectivity of reactions under Billups conditions (using Na) for separation by selective extraction using alkyl carboxylic acid groups.[133] The reaction was carried out using 6-bromohexanoic acid as the electrophile. Repeated cycles (N) of Na/6-bromohexanoic acid addition afford N-SWNT-$[(CH_2)_5COONa]_x$ very high degrees of functionalization with aqueous solubility (3.38 mg/mL) approaching chlorosulfonic acid (~5 mg/mL)[70] limits. With each cycle the suppression of RBM bands revealed preference to small

diameter tubes but not specific electronic type. The reasoning for higher reactivity was related to the trend in reduction potential with diameter. Extracting the product in hexane/water and removing all water soluble SWNT before drying and repeating the functionalization on the organic layer separated tube diameters.

A question of fundamental importance is how a covalent bond occurs on a sea of delocalized π-electrons over thousands of carbons. Deng et al. (2010) argued that the answer to this question may hold the key to controlling functionalization reactions on nanotubes.[134] The authors show that functionalization bands could be directly visualized by substrate enhanced SEM. In this manner, two distinct defect propagation modes were observed: propagation from nanotube ends and from a defect site. End bands were half as wide as sidewall bands due to propagation in two directions. Interestingly, the effect of banded functionalization retains some optical properties and is described by a kinetic model. Density functional theory calculations showed that charges accumulate around defect sites and extend to adjacent carbon atoms which promote propagation via edge effects.

In spite of the wide range of applicability of this reaction scheme, Gebhardt et al. (2011) noted that due to the harsh environment of free electrons in ammonia, the scope of electrophiles that can be used is limited due to the strong reducing nature of this medium.[135] Specifically, reagents such as ketones, esters, and carboxylic acid chlorides do not survive this treatment and must be used in a modified scheme to yield nanotubes functionalized with hydroxyl or keto groups. This is accomplished by the reduced and localized SWNT anions which act as electron donors to generate ketyl radicals instead of single electron transfer from the excess Li (this finding is in itself a telling revelation to the nature of Billups reduced SWNT). Figure 2.6 shows the SET addition to carbonyl compounds. This reaction is a single electron transfer from the

reduced SWNT themselves to the carbonyl containing electrophiles. Conversely, K in toluene has been shown to generate a radical anion with benzophenone (K associates with O to yield a carbon radical) that can attach to SWNT.[136] Here, the aromatic compound (benzophenone) accepts an electron from K to form a radical anion salt with K^+ counterion. In order to achieve these results, SWNT were first dispersed in THF and ammonia was condensed into this solution. Lithium metal was added, and ammonia was evaporated leaving the charged nanotubes in THF and excess Li phase separated for removal. Thus, the affect of excess free electrons was eliminated, confirmed by electron paramagnetic resonance spectra. After sonication, a series of carbonyl based electrophiles was introduced including acetophenone, 1,1,1-trifluoroacetone, methyl benzoate, methyl trifluoroacetate, and 3,4-dichlorobenzoyl chloride.

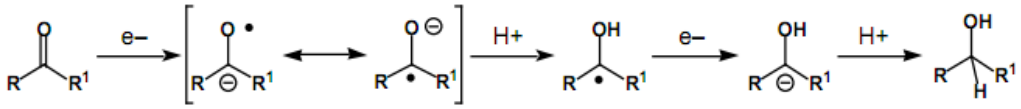

Figure 2.6: SET to a carbonyl compound generating ketyl radicals. The addition of protons and also a second SET are shown. Adapted from Rowlands (2006).[137]

Briefly, addition of a ketone will yield a tertiary alcohol and carboxylic acid derivatives result in acyl groups. The authors found that the extent of reaction to range from 0.3 % to 0.8 % for the reagents listed. These reactions were also carried out using THF/n-butyl lithium dispersions as well which introduced an alkyl substituent. The product was characterized as a doubly functionalized SWNT and yielded a lower degree of attachment. This can be explained by the nucleophilic reductive alkylation being in equilibrium with de-functionalized nanotubes, as discussed in subsequent sections. A key finding for the Billups approach was the correlation between radical stability and degree of functionalization with less stabile intermediates being

more reactive. The reactions were size selective but not sensitive to electronic type and optical transitions were retained.

2.1.5 Organometallic Reduction

Graupner et al. (2006) first showed the nucleophilic attack of t-BuLi (in benzene) accompanied by transfer of negative charge (n) can stabilize the SWNT.[138] The intermediate formed is described as t-Bu_nSWNT^n and can be re-oxidized by bubbling oxygen to recover the neutral product, t-Bu_nSWNT. It was hypothesized that due to accumulation of charges, the reaction is limited towards further attack. Thus, multiple reaction cycles were carried out and the C:addend ratio doubled after the third addition. From XPS measurements, charging leads to filling of previously unoccupied electronic states and shifts the Fermi level up. The reaction was selective to metallic SWNT.

Wunderlich et al. (2008) further studied reactivity of SWNT to a range of organometallic compounds (solvent) followed by oxygen re-oxidation: ethyllithium (butyl ether), n-butyllithium (hexane), t-butyllithium (pentane), and n-hexyllithium (hexane). Less reactive Gringard reagents n-butylmagnesium chloride (THF/toluene) and t-butylmagnesium chloride (THF) were also examined. A distinct preference for metallic SWNT over semiconducting was observed. This was a consequence of the finite density of states above the Fermi level for metallic tubes, thought to stabilize transition states during nucleophilic attachment, as well as their less aromatic nature. Furthermore, for all chiralities, the reactivity is inversely proportional to the diameter as explained by increased pyramidization angle in which high strain can be relieved with covalent functionalization. Due to steric effects, less bulky n-alkyl organometallics are more reactive towards metals (and small diameters for both electronic types). The bulky *t*Bu is less selective. Initial chemical reduction by fast electron transfer decreases the reactivity of metallic SWNT

towards bulky *t*Bu-Li but leaves semiconducting tubes available. It was thought that these effects might eventually aid in separation of SWNT by diameter and chirality.

Instead of re-oxidation or hydrogenation, Robeau et al. (2007) studied the feasibility of nanotubes to undergo nucleophilic reductive alkylation followed by an electrophilic attack. Various sources of SWNT and MWNT were reduced using MeLi or n-BuLi in THF to form Me_nNT^{n-} or n-Bu_nNT^{n-}. Although MeLi was more reactive nucleophile, it could not stabilize MWNT or arc-SWNT, even in excess. It was hypothesized by the authors that if a compound cannot easily oxidize the reduced tubes, but can act as an electrophile, a Lewis acid-base reaction occurs to yield a double functionalized neutral nanotube. To this end, 2-chloro-6-methyl-pyridine, 3-chloro-propionic acid, 1,2-dichloroethane, 1,-n- dibromoalkanes (n = 8, 10, 12), 12-bromo-dodecanoic acid, and 9-bromo-phenantrene were used as electrophiles in excess to the alkyl lithium. Destabilization of the dispersion upon electrophile addition and formation of LiX were observed. The highest reactivity was with HiPco SWNT where 1 in every 45 carbons were functionalized with 12-bromo-dodecanoic acid using a 20:1 ratio of organolithium to carbon. The degree of functionalization was lower for other types of nanotubes but some trends with the amount of reducing agent used were observed.

Maeda et al. (2010) added t-butyl-Li (R^1-Li) to a SWNT dispersion in benzene which generated "initial" carbanions.[139] A second addition of alkyl bromide (R^2-Br) was then added to produce R^1-R^2-SWNT. Small diameter tubes were preferred. Re-oxidation with ethanol hydrogenated the SWNT and showed the lowest extent of functionalization compared to various alkyl substituents in R^2-Br. The effect of alkyl substituent was thought to be relative to the steric effects of the adjacent t-butyl molecule. Thus, nBu-$SWNT^-Li^+$ was prepared and reactions were repeated and shown to have higher degrees of functionalization, confirming the steric effects.

The authors argued that the reactivity was too high for just a nucleophilic substitution reaction mechanism. When benzyl bromide was added to R^1-SWNT$^-$Li$^+$, 1,2-diphenylethane was isolated, indicating radical coupling. Note that the influence of steric substituents controls whether single electron transfer or substitution mechanisms occur with fullerenes.[140] So, depending on the steric consideration of R^1 and R^2, the R^2 radical may prefer to attach with the SWNT or it may prefer to dimerize. In the latter case, the unreacted radical bound to the R^1-SWNT$\cdot$ could re-oxidize with O_2 or disproportionate to give an unfunctionalized site.

A key finding contributing towards the fundamental understanding of these reactions was made by Syrgiannis et al. (2010) who found that the initial addition reaction is reversible if there is excess negative charge on the nanotubes.[141] The authors based this conclusion on the observation that the extent of functionalization towards nucleophilic addition kept increasing, even in excess of organolithium reagent. To display this effect, SWNT were functionalized and re-oxidized by lithium n-propylamide and n-butyl lithium. Functionalized nanotubes were then reduced using Billups conditions and re-oxidized with oxygen. After reduction, the extent of functionalization was reduced as hypothesized. Remarkably, after reduction of functionalized SWNT with Billups conditions (excess Li removed, THF), if n-propylamine is added the freed n-butyl lithium (the stronger base) deprotonates the amine and this n-propylamide enters the equilibrium reaction and can attach to the SWNT via nucleophilic addition. The freed nucleophile can also react with electrophiles such as acetophenone or methyl benzoate. As discussed above, this can also functionalize SWNT by single-electron transfer from carbon nanotubes to carbonyl containing electrophiles. Reduced pristine SWNT by the Billups reaction, however, did not deprotonate n-propylamine. This was thought to be a result of negatively charged SWNT behaving as weak bases, estimated to have a pKa near 5.7.

Bayazit et al. (2010) have also investigated the attachment of carbonyl groups to SWNT by the introduction of n-formylpiperidine to n-butyl lithium (cyclohexane) reduced nanotubes.[142] The formyl group of n-formylpeperdine reacted with n-BuSWNT^{x-}(Li_x^+) and was attached to the surface to give n-BuSWNT-CHO after re-oxidation. The authors noted that this carbonyl was susceptible to further C-C and C-N coupling reactions and some examples are demonstrated including the tethering of gold colloids.

It is noteworthy that Chen et al. (2005) treated SWNT with sec-butyl lithium in THF and then used gaseous CO_2, bubbled through, to re-oxidize and carboxylate the sidewalls.[143] The resulting product contains both alkyl and carboxyl groups.

2.1.6 Polymerization Reactions

The addition of sec-butyllithium to SWNT dispersed in cyclohexane results in nucleophilic addition across a double bond on the nanotube surface. This nucleophilic reduction stabilizes the nanotube dispersion electrostatically via a carbanion which can also serve as an anionic initiator.[144] Subsequent addition of styrene monomer results in anionic propagation across the vinyl bond. Conversely, SWNT carbanions from sec-butyl-lithium dispersed in THF failed to polymerize methyl methacrylate (other general problems with PMMA polymerization and methods for determining propagation mechanism are also discussed[145]). Conversely, addition of di-tert-butyl-biphenyl as a catalyst enables polymerization.[146] A hybrid approach using n-BuLi in THF to tether chlorinated polypropylene to a MWNT surface has also been displayed.[147]

Liang et al. (2006) used the nanotube salt generated under Billups conditions as an in-situ anionic polymerization initiator for the polymerization of methyl methacrylate to PMMA.[148] It has been noted that this polymerization scheme is applicable to a number of unsaturated monomers including acrylonitrile and acetylene.[149] It remains unclear if this initiator was truly

anionic or generated by SET as well. The basic argument being that an anionic chain would be met with electrostatic repulsion from the reduced SWNT.

2.1.7 The Bingel Reaction

The seminal work regarding the cyclopropanation of fullerenes (C_{60} and C_{70}) was reported by Carsten Bingel in 1993.[150] Bingel described the reaction as occurring in two segments; the Michael addition of a stabilized α-halocarbanion to the fullerene, followed by the intramolecular substitution of the halogen to form the second C-C attachment (cyclopropane ring closure) of the functional group to the fullerene. It is noteworthy that the mention of the Michael reaction refers to the α-halocarbanion addition which is resonance stabilized by the presence of carbonyls on either side. The traditionally activated alkene Michael acceptor is in this case a fullerene. In both the Bingel and Michael reactions, the carbanion is formed by proton abstraction using a base. This is rational since resonance stabilization renders the hydrogen attached to the α-C more acidic. Both sodium hydride (NaH) and 1,8-Diazabicyclo[5.4.0]undec-7-ene (DBU) have been used as the base for proton abstraction steps by Bingel. Figure 2.7 displays the chemical structure of DBU.

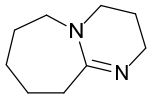

Figure 2.7: Chemical structure of DBU.

The solvent used for Bingel's fullerene reactions was toluene and a variety of halogenated nucleophiles were used. Figure 2.8 displays the reaction scheme for the Bingel reaction in presence of NaH and Figure 2.9 displays various moieties attached while using the base DBU. It is noteworthy that up to hexa-substituted fullerenes using malonates have been reported from the Bingel reaction.[151]

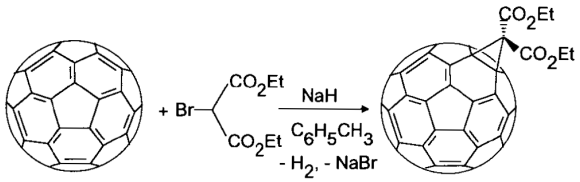

Figure 2.8: Bingel's original cyclopropanation reaction (Et = ethyl).[150]

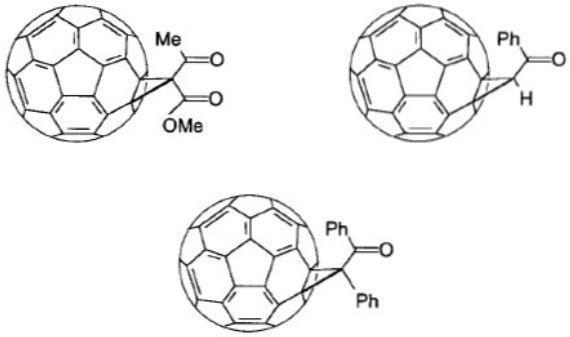

Figure 2.9: Attachment of various moieties by Bingel using DBU in toluene (Me = methyl, Ph = phenyl).[150]

Often, cycloaddition reactions use nomenclature in which the number of atoms in the sections of each molecule reacting are bracketed numerically. Following the proposed mechanism by Bingel, the reaction between the stabilized carbanion of the malonate and a double bond on a SWNT, followed by intramolecular substitution of the halogen atom, describes a [2+1] cycloaddition. The [i+j…] labeling system can be found described in detail via IUPAC.[152] Thus, any reference made using this nomenclature with respect to the Bingel reaction should not cause confusion as the descriptions remain ambiguous in the literature.

Bingel Reactions with SWNT

Coleman et al. (2003) published the first report on the reactivity of SWNT using Bingel reaction conditions and used chemical tagging by means of transesterification reactions to show successful functionalization by spectroscopy and microscopy.[153] SWNT were suspended in oDCB and diethyl bromomalonate was reacted in the presence of DBU under stirring only. After

work-up, the authors noted low solubility and reactivity of the SWNT under these reaction conditions. Thus, they tethered gold colloids and fluorinated compounds to the SWNT via the diethyl malonate functional groups using transesterification and proceeded to use AFM, XPS, and ^{19}F NMR to confirm functionalization. The low degree of functionalization in this work was likely a result of stirring only during the reaction and an absence of sonication. It has been shown that sonication is a necessary component under Bingel conditions as it simultaneously exposes SWNT surface area to the reagents and also increases the "energy of the reactants".[154] Unless otherwise noted, the Bingel reaction will refer to the addition of diethyl bromomalonate to the SWNT.

Bingel Reaction Mechanism

The mechanism of the Bingel reaction appears to be still controversial to this day. For example, Worsley et al. (2004) noted that even after hundreds of citations to the seminal work, the proposed reaction mechanism, described above, had not been validated.[154] In fact, with respect to SWNT, the reaction is described to proceed via a highly reactive carbene atom in a few reports.[89,120] The carbene atom would likely have to be formed by abstraction of not only the hydrogen atom but also leaving of the halogen, leaving a lone pair of electrons on the neutral central carbon of the malonate group. Conversely, scanning tunneling microscopy images of Bingel functionalized SWNT have revealed regularly patterned reaction sites over several nanometers of tube length.[154] It has been postulated that these patterns are the result of nucleophilic attack by the negatively charged diethyl malonate group. Specifically, the approach of the anionic molecule towards the sidewall of a SWNT was thought induce a spatial fluctuation in the delocalized electron rich surface and lead to not only improved reactivity but also a patterned reactivity. Such a detailed conclusion was made possible by scanning tunneling

microscopy images as displayed by Figure 2.10. Sidewall defects in SWNT are thought to be the initial origin of SWNT susceptibility towards such an ionic to covalent interaction from the anion and an sp^2 SWNT surface. This argument would discredit the carbene mechanism but unfortunately it remains partly conjecture at this time.

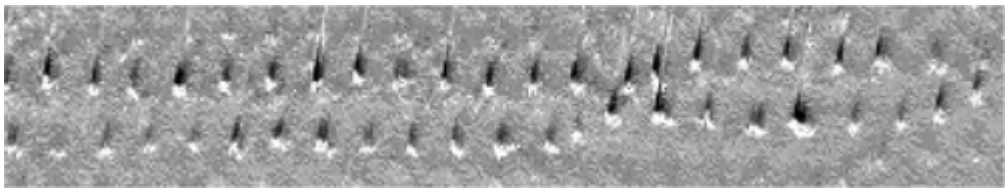

Figure 2.10: STM image of Bingel functionalized SWNT showing two tubes crossing. Adapted from Worsley et al. (2004).[154]

Sonopolymerization of oDCB

While sonication adds energy to the system, and in turn helps the reactants surmount activation energy barriers, it also can drive a polymerization reaction involving the preferred solvent, oDCB. Niyogi et al. (2003), studied the decomposition and subsequent polymerization of pure oDCB in detail and found it to be necessary to occur in-situ with SWNT for nanotube stabilization and dispersion; the pre-formed sonopolymer did not disperse pristine SWNT as would be expected for adsorption or wrapping.[155] Also, when sonopolymerization was inhibited by addition of ethanol, no dispersion stability was obtained. This hints towards a radical polymerization mechanism, as discussed below. Furthermore, the authors showed the importance of sonication power on this reaction by noting that differences in UV-vis-NIR absorbance depending on the shape and placement of the vessel in the bath sonicator (40.5 kHz). The authors found trends in Raman spectra consistent with covalent functionalization but do not specifically say whether they believed the sonopolymer was chemically bound to the surface. They concluded however, that sonication in oDCB irreversibly damages the sidewalls. Conversely, Kim et al. (2005) concluded that SWNT were covalently functionalized, showing a

decrease in UV-vis-NiR optical transition absorbance and an increase in the Raman D-band to G-band intensity ratio I_D/I_G. Using a centrifugation protocol, it was found what with increasing ultracentrifugation speeds up to 325,000 x g sample purity increased, but the SWNT population decreased. This would seem to indicate that the sonopolymer and the SWNT were closely density matched. Thus, purification by sedimentation separation is limited to a tradeoff between sonopolymer and SWNT concentration in the supernatant.

It was only recently that nature of the sonopolymer-SWNT interaction was revealed using careful experimentation by Moonoosawmy et al. (2009).[156] SWNT bath sonicated in oDCB (42 kHz, 70 W) were examined using Raman under varying incident laser power. The effect on the sample was monitored using the classic I_D/I_G Raman ratio as well as the I_D/I_{D^*} ratio since the G band intensity can be susceptible to intensity changes from doping.[157] Under low laser power (0.01 mW/μm^2) no change was seen for the samples before and after laser exposure; this power was taken as a control. Comparisons were made between unfunctionalized, functionalized, sonopolymer coated, and washed sonopolymer coated SWNT. Unfunctionalized SWNT may show some slight I_D/I_G decrease after laser exposure depending on how they were previously purified. This can be negated with annealing. Functionalized SWNT displayed an I_D/I_G decrease with increasing laser power due to laser induced thermal degradation/removal of the functional groups. In addition, for functionalized SWNT, there was an observed thermal effect during measurement which shows I_D/I_G decrease with increasing temperature and concurrently higher powers. If SWNT were covalently functionalized by sonopolymer then a similar trend would be expected. Instead, there was a slight thermal effect that may increase or decrease I_D/I_G depending on the measurement temperature but leaves a permanent increase in I_D/I_G after the experiment. This was linked to an artifact from the thermal charring of the sonopolymer sample

on the SWNT surface and not a covalent modification. Extensive washing of the samples and re-analysis by Raman showed no trend with I_D/I_G and laser power. Therefore, thermal charring leads to a misinterpretation of Raman data. Likewise, the supposed quenching of UV-vis-NIR optical transitions from covalent modification was removed with sample washing. This also disputes the evidence used for covalent interaction. Thus, the sonication of SWNT in oDCB does not lead to a covalent modification, and careful selection of Raman laser powers must be made so as to not impart sample artifacts into the spectra. It should be noted that the Bingel reaction is known to preserve the inherent electronic properties typically lost with functionalized SWNT, presumably due to low extent of functionalization.[158]

Doping Effects on SWNT

In addition to sonopolymer formation, sonication of SWNT in oDCB can also affect the electronic structure of SWNT by doping.[159,160] The doping of SWNT alters the population of electrons in the valence and conduction energy bands, depending on the nature of dopant. As a result, the carrier electron density is altered which in turn results in a shift from the "intrinsic" Fermi level of SWNT. The presence of doping is readily observed by quenching of the optical transitions[161,162] and varying Raman features.[163] Some of the observed Raman effects are varied spectral intensity, disappearance of the RBM mode, and a shift in the G'-band. For example, with electron donating dopants such as K, charge transfer is from the dopant to the conduction band (π^*) of the SWNT (n-type doping).[160] In this scenario, the RBM are not detectable and the higher frequency Raman modes are downshifted. The G-band is replaced with a lineshape known as the Breit–Wigner–Fano interference and Lorentenzian peaks appear from the expected D-band position down to ~1,000 cm^{-1} as charge-transfer modes. Conversely, the introduction of Br_2 results in charge transfer from the valence band (π) of SWNT to the dopants which results in

the formation of hole carriers in this band (p-type doping). P-type doping effectively removes electrons from SWNT and up-shifts in the Raman frequency are seen for the RBM and G-bands. A series of harmonic peaks are also observed between the RBM and G-bands. Other effects can be seen upon incorporation of $SOCl_2$ by non-covalent adsorption to SWNT.[157] The G-band up-shifts (blue) upon introduction and this is evidence of p-type doping, as mentioned previously. In addition, the D^* band was observed to up-shift. Likewise, controlled oxidation of metallic and semiconducting SWNT via applied potential in H_2SO_4 shows p-type doping characteristics as electrons are removed from the SWNT π band (oxidation).[164] The result is again an up-shift in the Raman spectra as well as a change in the metallic G-band lineshape. The RBM did not shift but only changed in intensity. Similar but less noticeable effects are seen for semiconducting SWNT under these conditions.

Effects of SWNT Sonication in oDCB

The sonication of HiPco SWNT in oDCB results in p-type doping as displayed by a noticeable Raman blue shift (9 cm^{-1}) in the D^*-band.[156] Other observed Raman (514 nm excitation) effects were a loss of the broad G^- shoulder (~1540 cm^{-1}) in the G-band and an increased relative intensity in G^+ with respect to annealed SWNT. After exhaustive comparison by Moonoosawmy and Kruse (2009), it was determined that sonication is necessary for doping to occur.[156] During sonication, C-Cl bonds are cleaved leaving behind a Cl radical. The Cl radicals can abstract H to produce HCl or terminate to afford Cl_2. Otherwise the solvent MW increases through propagation reactions, forming the sonopolymer. The decomposition products HCl and Cl_2 then interact with the catalytic Fe from the SWNT to produce iron chlorides which were identified as the dopant. It was concluded that the sonopolymer itself does not lead to doping. Interestingly, other molecules with two or more chlorine atoms such as dichloromethane, chloroform, and 1,2-

dichloroethane also dope HiPco SWNT with sonication. Conversely, monochlorinated atoms and fully chlorinated carbon tetrachloride, which lacks hydrogen, do not dope SWNT. Finally, the extent that HiPco SWNT are doped when sonicated in oDCB is dependant on the Fe content in the SWNT samples as this metal must be accessible to the solvent degradation products for conversion to iron chlorides. Note that confirmation of the extent of doping can be obtained by examining the C1s peak position shift by XPS. An exhaustive list of chemicals that are known to alter the chemical environment of SWNT and lead to doping is given by Moonoosawmy and Kruse (2008).[165]

The effect of sonication in oDCB on CoMoCAT SWNT has not been reported. If the above conclusions pinpointing iron chlorides as the only dopant are true, then doping should not be detected based on the absence of Fe catalyst. In addition, the presence of sonopolymer in CoMoCAT sonicated samples could confirm it has no role in doping.

Avoiding Sonopolymerization

There are a few possible strategies to mitigate sonopolymer contamination. The most obvious choice would be to change the solvent. For example, Bingel used toluene for his seminal work on fullerenes. Otherwise, an obvious choice would be a polar aprotic solvent such as THF or DMSO. Unfortunately, toluene and DMSO are poor solvents for SWNT dispersion, both having a dispersion limit on the order of 10^{-3} mg SWNT per mL of solvent.[166] Care would need to be taken with DMSO to ensure it remains anhydrous due to its affinity for water. THF suffers from having no solubility towards SWNT and also unfavorable solvent parameters for transferring shear stress via sonication such as surface tension and viscosity. A high shear environment is essential during the reaction to expose surface area to the reagents.[154] Thus, the best choice for a substitute solvent might be anhydrous dimethyl formamide or dimethylacetamide.

Another strategy to prevent sonopolymerization is by inhibition. It has been previously shown that sonopolymer formation can be inhibited by the addition of free radical scavenging agents such as alcohols and acetone.[155] This approach, however, does not lead to stable SWNT dispersions in oDCB. Furthermore, in the case of the Bingel reaction, the presence of an alcohol may react with DBU. The addition of a small amount of anhydrous acetone could be worth exploring.

A final strategy to prevent polymer formation is by not sonicating the SWNT during the Bingel reaction. This would require the SWNT to be first exfoliated by another method such as surfactant stabilization or functionalization. Umeyama et al (2007) attached hydrocarbon chains to end/defect site oxidized HiPco SWNT using thionyl chloride and octadecylamine.[158] These functionalized SWNT were then soluble in organic solvents such as oDCB and showed enhanced reactivity under Bingel conditions. Here, Bingel conditions were used to attach benzyl 2-ethylhexyl malonate to sidewalls. Instead of long sonication times, the reaction proceeded via short sonication in oDCB followed by stirring with the reactants or by microwave exposure. The successful re-dispersion of these doubly functionalized SWNT depends on the nature of the solvent. For example, the large presence of non-polar aliphatic chains would not be suitable for UPR. It is noteworthy that the reaction product did not appear to be selective towards metallic or semiconducting SWNT and the electronic properties were intact.

Optical Properties of Bingel SWNT

A unique aspect of Bingel functionalized SWNT are the retention of inherent nanotube electronic properties, as indicated by the preservation of optical transitions. Cho et al. (2006) studied the effect of electronic properties on the orientation of [2+1] cycloadditions. The effect of orientation of the cyclopropane plane with respect to the nanotube axis is important. With

random orientations expected during functionalization, however, the metallic and semiconducting SWNT have opposing effects. The band-gap of metallic SWNT is widened while that for semiconducting SWNT is closed, leading to a constant band-gap.

2.1.8 Non-covalent Polymer Wrapping

The non-covalent functionalization of SWNT using polymer adsorption provides a robust strategy for dispersing SWNT. The presence of bulky polymers, at minimum, can truncate the accessible range of the van der Waals attractive potential between SWNT. The selection of polymer pendant group chemistry can also serve to influence the interaction with the solvent.

Adsorption and Complexation of Polymers to CNT

In general, donor-acceptor complexes can be formed between electron-rich nanotubes and electron-deficient molecules. Similarly, a nonspecific π-π interaction exists in complexes that form between nanotubes and electron-rich molecules[167] such as polynuclear aromatics. For example, π-π interactions were observed in aromatic pyrenyl,[168] anthracene and anthracene derivatives,[169] and selective adsorption of porphyrins to nanotube sidewalls.[170] Calculations based on first principles have revealed that benzene and cyclohexane are weak donors to nanotubes compared to molecules that behave as charge acceptors. Nevertheless, when the molecule is aromatic, coupling of π electrons occurs (hybridization) which affects electronic structure significantly, but uniquely, depending on the molecule.[171] These features are characteristic of a general phenomenon.

Another nonspecific interaction driving polymer adsorption is the CH-π interaction or the alkyl – phenyl interaction.[172] Interestingly, not only is this interaction expected with "activated" alkyl groups but also non-acidic C-H groups in common alkanes. To paint a molecular picture,

this interaction occurs between the non-bonded hydrogen in C-H and the π electrons on the C atoms. The CH-π interaction has been characterized to be relatively weak with ~1/10 the strength of a hydrogen bond.[173] Estimates of its magnitude are on the order of 10^0 kcal/mol.[172] Like van der Waals interactions, however, multiple and cooperative bonds have a significant effect. These interactions have been described as soft acid/base.[174] It can be imagined that once a polymer chain first participates in a CH-π bond, adjacent C-H atoms in the backbone will also contribute.[167] The interaction of the total chain length is less likely in solution, and partial chain adsorption leaves exposed polymer for interaction with an adjacent nanotube, leading to aggregation. Baskaran et al. (2005) examined an array of common polymers for evidence of CH-π interaction with MWNT. These included polybutadiene, polyisoprene, polystyrene, polymethylmethacrylate, and polyethylene oxide, which lack conjugated π electrons and thus, do not form π-π complexes.[167] When polydimethylsiloxane, a polymer with less C-H bonds was used, the dispersibilty was decreased. It is important to note that these composites must be blended in absence of a solvent to first secure the polymer adsorption to the nanotube. If done in organic solvent, the dispersions are not stable. Due to low energy, the polymers have little to gain in exchange for decreasing their mixing entropy from solution. Nevertheless, polymer wrapping of this type constitutes a general phenomena in nanotube science. We can imagine that CH-π interaction would be more likely after a stronger interaction, like π-π or complexation, localizes molecules first.

The interaction between anionic surfactants with water soluble uncharged polymers has been known for some time.[175] One interesting nonionic polymer candidate is polyvinylpyrrolidone (PVP), having a hydrocarbon backbone with polarizable pyrrolidone side groups. PVP can complex with toxins and drugs and even reduce toxicity with dangerous chemicals by binding.[176]

For example, the iodine complex of PVP reduces the toxicity of iodine while retaining antiseptic properties.[17] It is also readily found in pharmaceuticals, detergents, and cosmetics. Interestingly, PVP is used to store blood cryogenically.[17] Much attention is paid to its peptide bond in the literature and therefore it is used as a protein model. Figure 2.11 displays the structure for PVP. A more realistic schematic is given by Figure 2.12. PVP lacks the ability for direct intra and intermolecular hydrogen bonding.[177]

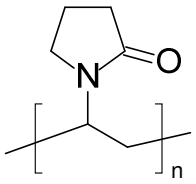

Figure 2.11: Molecular structure of PVP.

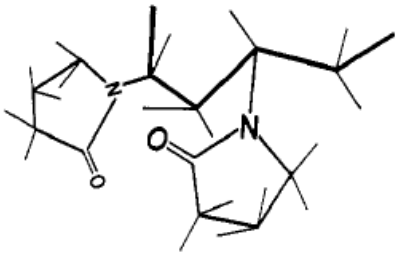

Figure 2.12: Perspective schematic of PVP.[177]

PVP's chemistry renders it soluble in water as well as a number of organic solvents. PVP also has a strong interaction with anionic surfactants such as sodium dodecyl [lauryl] sulfate (SDS). SDS monomers can adsorb on PVP with the hydrophobic part resting on the polymer backbone and the head groups available to interact either with the surrounding water or pyrrolidone rings.[175] A fine detailed study of this interaction by NMR was given by Roscigno et al (2003).[178] Two electrostatic interactions exist: one between the surfactant head group and charged N and a second between negatively charged oxygen and an electron deficient surfactant carbon. There is also a hydrophobic interaction between the methylene groups of PVP and the surfactant akyl

chain. PVP has been shown to induce aggregation of SDS below the CMC. The resulting complex has been measured to have a large negative zeta potential.[179] Adsorption of SDS onto a surface such as a nanotube renders a slightly different physical picture as the anionic head group is predominately exposed to solution. In this case, PVP conformation would be expected to behave differently than in free solution. One consequence of localized SDS adsorption is ion exchange at the solvent interface. Simulation has shown that adsorption of chains to the nanotube surface is a competitive process between adjacent molecules in the local vicinity of the surface.[180] Favorable competition for the exchange site between the PVP and hydronium ions is expected.[181] Previous studies have characterized the completive adsorption of PVP to be based on available sulfate sites, and thus complexation lowers interfacial pH.[182] The charge transfer occurring from sulfate to PVP drives complexation to the adsorbed SDS.[181]

O'Connell et al. (2001) first described the interaction between PVP and SDS stabilized SWNT.[183] The authors concluded that PVP was uniformly and tightly wrapped around the SWNT in monolayer or near monolayer coverage with robust interaction. A list of water-soluble polymers that do and do not wrap SWNT was given. Based on idealized calculations, the driving force for adsorption to the surface was to minimize contact of the hydrophobic SWNT surface with the water. Changing solvent to an ether resulted in desorption, supporting this theory. Interestingly, even amide functionalized nanotubes can be passivated by PVP wrapping.[184] Energetic estimates are as follows: the entropic cost of wrapping a linear polymer from solution around a nanotube ~17 kJ/mol per nm length. To offset this penalty, the gain in free energy from eliminating hydrophobic surface area contact with water was ~136 kJ/mol for each nm of SWNT.[183] Furthermore, polymer wrapping was characterized as a "general phenomenon" and described to be helical in nature. Many of these conclusions were confirmed via Monte Carlo

simulation by Gurevitch and Srebnik (2007).[180] Specifically, the conformation of adsorbed polymer is dependant on the physical properties of the polymer itself such as stiffness. It was found that multiple helical wrapping occurs for semiflexible chains but for stiff chains there exists a steric repulsion between chains which can limit chain overlap. Conversely, flexible chains experience large entropic loss upon adsorption so they exist as a random coil (globular) around the surface. A key finding was the nanotube diameter dependence on surface adsorption. A critical radius exists where below this value only partial adsorption of the chains occurs; significant entropic/bending penalties prevent full adsorption and the polymer partially extends into the solvent. In general, adsorption is easier for larger tubes. This indicates that the driving force for adsorption is entropic in nature, and thus, a general phenomenon where by adopting a helical adsorbed confirmation has some energetic gain which is compensated by the entropy lost by relieving bending energy. Experimental studies comparing the ability of PVP to disperse HiPco versus arc discharge SWNT find poorer dispersibility of HiPco SWNT due to the smaller average diameter.[185]

The long-term stability of PVP SWNT dispersions that were directly dispersed in DMF is intriguing.[186] It was determined that incubation of PVP dispersions for 14 days at 30°C caused the metallic SWNT to precipitate out. Based on Raman up-shifts, non-covalent charge transfer was found to occur between the PVP and the SWNT resulting from the electron withdrawing carbonyl group. The wrapping of SWNT was proposed to be an exothermic process with the addition of heat PVP triggering desorption. Metallic SWNT, due to the occupied density of states near the Fermi level, were proposed to be more susceptible to small temperature fluctuations leading to their destabilization. Thus, care should be taken to control the temperature of PVP SWNT dispersions both during preparation and storage. In addition to any

previous mentioned fractionations, PVP stabilized dispersions can also be separated based on length,[183] diameter/bundle size,[187] and by electronic structure.[188]

The most common methodology for the aqueous dispersion of SWNT using PVP wrapping was described by O'Connell et al. (2001).[183] In this work, SWNT were isolated by centrifugation from sonicated SDS solutions in water. These dispersions were then incubated with a 40 kD PVP solution before work-up to remove unbound polymer and surfactant. The interaction of the PVP and SWNT-SDS was shown to be robust and unable to be disturbed with water washing. To this end, dispersion and isolation of SWNT in SDS solutions followed by PVP adsorption has been common place in the literature.[66,187,189-193] Recently, PVP-SDS parameters were optimized to maximize SWNT content in supernatant dispersions.[194] The authors noted that by adjusting centrifugation force, various diameters could be separated from solution. It is noteworthy that SDS concentration is critical in the dispersion stability as micelle formation will induce depletion attraction between SWNT.[185] Direct dispersion of SWNT in 1-methyl-2-pyrrolidinone (NMP) using PVP wrapping has also been shown[195] and favors larger diameter tubes.[196] Conversely, based on the number of citations in literature, a less popular route is the direct dispersion of SWNT into aqueous PVP solutions to form nanotube dispersions[185,197] and films/composites[198,199].

Photoluminescence spectra have shown that complexation by the addition of PVP to sodium dodecylbenzenesulfonate dispersions is incomplete, leaving surfactant exposed that can be removed by dialysis.[200] Based on the given schematic and description, the authors seemed to paint a physical picture of surfactant/polymer exchange which is unfounded in the literature. Nevertheless, the persistence of charged surfactant to the SWNT surface post washing is

unacceptable for dispersion in UPR. Thus, dispersion stabilization of SWNT in PVP solutions without first isolation in anionic surfactant was pursued, herein.

Chapter 3

Exploration of Small Molecule Functionalization

Introduction

The direct attachment of small molecules to SWNT to induce specific interactions with UPR (e.g. hydrogen bond donation to UPR) and non-specific interactions (e.g. compatibilization with ester groups) was investigated. Due to the limited information on many of these reactions at the time of experiment, the functionalizations were considered to be exploratory. Thus, the required work-up of the reaction product was unknown and many times incomplete; residues such as grease or SWNT degradation product were left behind. As a result, mass losses determined from TGA were often not "calibrated" and not representative of the true extent of functionalization. In many cases, the coupled FTIR analysis of the evolved gases provided clarification. Therefore, the focus was on simply identification of whether the expected chemistry was present on the SWNT. Note that much of the direction for these reactions was guided by the dissertation of Chattopadhyay (2008) wherein the reactivity of alcohols, esters, acetals and ketals in Li/NH_3 was discussed.[124] Data in the subsequent sections provides evidence that many of these compounds cannot survive the strong reducing environment of the Billups reaction. Specifically, the results in this chapter show the attachment of alcohols and esters was not possible. The reaction of acetals and esters was also recently determined to not be possible by Gebhardt et al. (2011).[135]

The series of reactions in this chapter also spans a transition from HiPco SWNT sourced from Unidym (P0900) to CoMoCAT SWNT (CG200) sourced from SouthWest NanoTech. Although

not ideal for comparison between reactions, changes in the nanotube supply chain are still common nature in the field of nanoscience. This highlights the need for thorough characterization of as-received nanotubes.

The addition of 4-bromostyrene to SWNT dispersion in Li/NH_3 was also studied in an attempt to attach crosslink sites on SWNT sidewalls. An unexpected preferential reactivity towards the vinyl bond in 4-bromostyrene over the aryl halide was discovered. This finding was exploited for functionalization and motivated the idea of in-situ polymerization in Li/NH_3 discussed in the next chapter.

3.1 Functionalization via Billups Scheme

In this section, the functionalization of SWNT was carried out under Billups type conditions in an attempt to extend the range of applicable chemistries. Here, SWNT were dispersed via reduction from solvated electrons freed from the complex of Li in condensed NH_3. Subsequently, reagent (halogenated electrophile) was added to functionalize the SWNT, and NH_3 was evaporated before the reaction was quenched with alcohol and washed with copious amounts of solvents via filtration. The addition of alcohol to reduced SWNT has been shown to result in hydrogenation of the sidewall under certain conditions.[124] Unless otherwise noted, 3.2 mmol of reagent was added and 5 mg of dry SWNT was stabilized with 120 mg Li. An exhaustive description of the reactor setup can be found in Chapter 4 and Appendix A.

3.1.1 Reaction with 4-Iodoaniline

Based on the reported reductive arylation of SWNT salts, the sidewall functionalization by aniline should be possible to form functionalized Aniline SWNT.[124] This reaction was carried out by adding 4-iodoaniline to a stable dispersion of HiPco SWNT in Li/NH_3. Figure 3.1

displays the molecular structure of 4-iodoaniline. It was anticipated that after formation of a radical anion, aniline radicals would terminate on the SWNT sidewall with formation of LiI, in accordance with the results of reductive alkylation studies.[100]

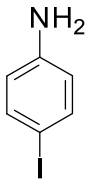

Figure 3.1: Chemical structure of 4-iodoianiline.

After work-up, TGA-FTIR analysis was carried out in order to confirm the presence of aryl or amine groups. Figure 3.2 displays the TGA mass loss and derivative mass loss curves. Peaks in the derivative mass loss curve correspond to mass loss events and were found at 235.5°C and 395.7°C. The first mass loss temperature of 235.5°C was within an acceptable range of temperatures for loss of functional groups. FTIR analysis of the effluent gas (Figure 3.3), however, did not provide convincing evidence for signs of aryl or amine features with respect to the background noise. Instead, only aliphatic hydrocarbon vibrations (< 3000 cm^{-1}) were present. Furthermore, the two bands expected for a primary amine were absent in the range of 3300 - 3500 cm^{-1}. Examining the effluent gas between the two loss events at ~325°C displayed some aryl character as well as the methyl vibrations shown in Figure 3.4. It was possible that only aryl SWNT was produced. The methyl stretch was attributed to polydimethylsiloxane (PDMS) contamination from vacuum grease. This was confirmed by examining the FTIR spectra in Figure 3.5 taken at ~400°C. The PDMS spectrum will be discussed in Section 3.1.2. Nonetheless, some modification to the initial structure of the SWNT sidewall was confirmed by Raman spectroscopy. Under 514 nm laser excitation, the pristine SWNT showed a Raman I_D/I_G ratio of 0.16 and this increased to 0.22 after work-up. High shear dispersion into UPR appeared

to exhibit improved kinetics, but aggregates persisted as shown by Figure 3.6. Based on the substantial extent of functionalization reported by previously by Chattopadhyay et al. (2005),[124] the SWNT were not functionalized by aniline groups herein. It was determined previously that based on mass losses between 200 and 500°C the C:aryl ratio was 16:1 for aniline functionalized HiPco SWNT.[201] As shown in subsequent sections, that mass losses from 400 - 500°C may not be representative of specific functional groups, due to the ubiquitous nature of this loss. Thus, it was possible that the aniline groups were present at low concentration. In fact, XPS analysis of the previously reported HiPco sample revealed 3.3 atom % N.[201]

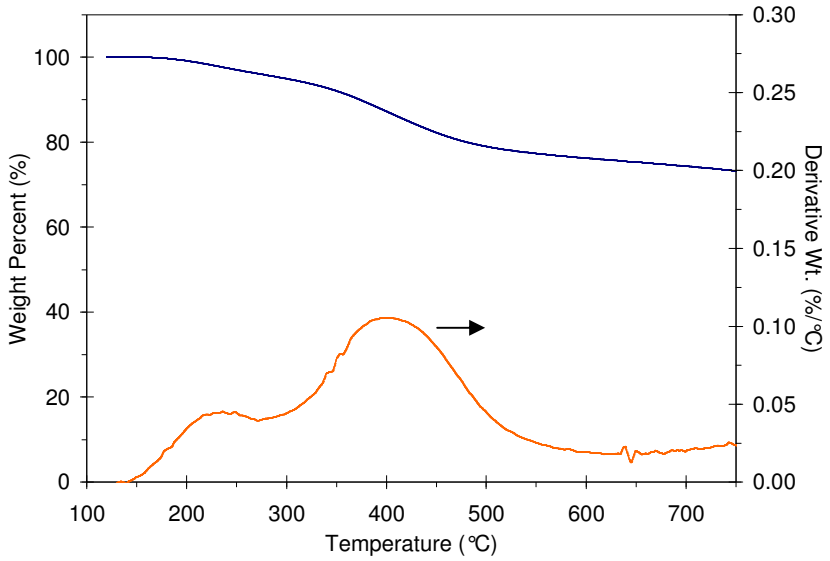

Figure 3.2: TGA mass loss curves for Aniline SWNT product.

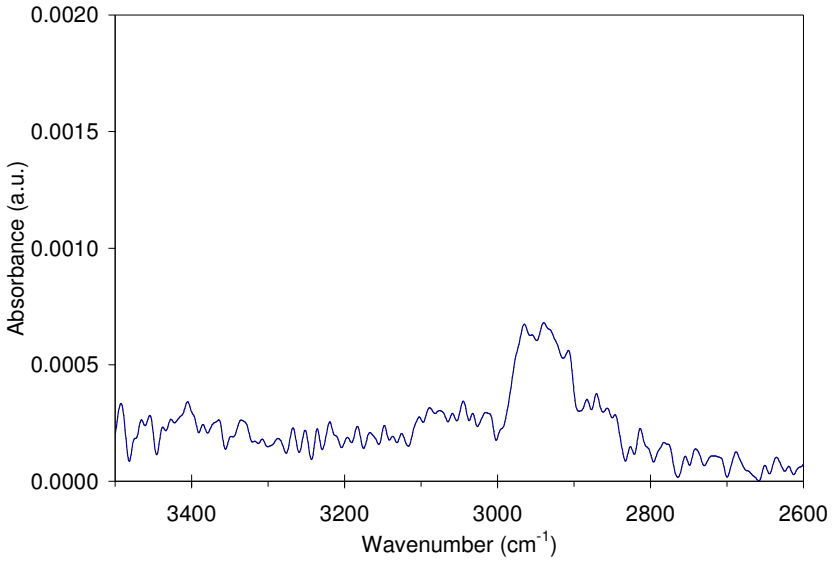

Figure 3.3: FTIR spectrum of Aniline SWNT effluent at ~235°C.

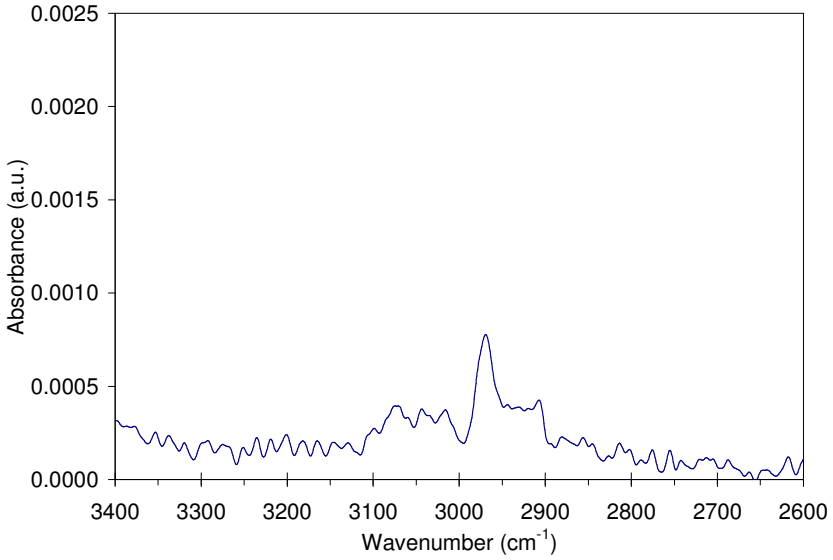

Figure 3.4: FTIR spectrum of Aniline SWNT effluent at ~325°C.

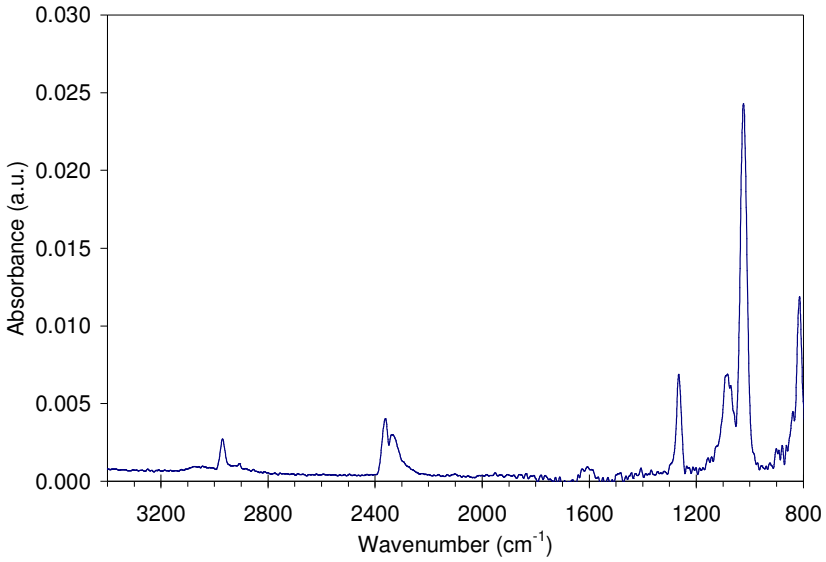

Figure 3.5: FTIR spectrum of Aniline SWNT effluent at ~400°C.

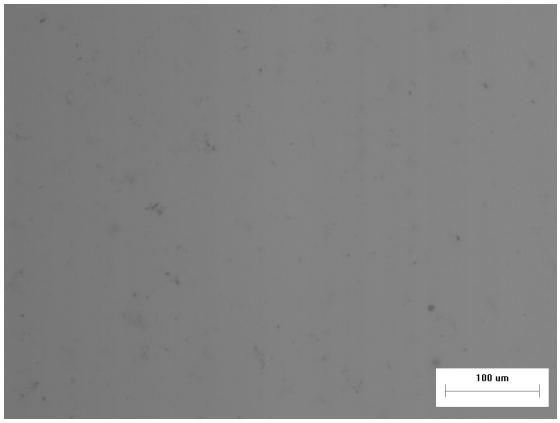

Figure 3.6: Aniline SWNT dispersion in UPR at ~50 ppm. A 20x objective was used with 2x magnification in front of camera. The Li mass used for stabilization was 120 mg. Scale bar was 100 μm.

In total, three batches of Aniline SWNT were collected and analyzed. Unfortunately, it was found that the product was not consistent between samples. Figure 3.7 displays the TGA analysis for a second batch of Aniline SWNT. The characteristic TGA mass loss peaks from Figure 3.2 were absent in this sample. Notably, FTIR analysis of the off gases at ~300°C and ~435°C were remarkably similar as shown by Figure 3.8 and Figure 3.9. Again, the expected N-H vibrations were absent, and the evidence for presence of aryl features was not compelling. In

this case, the Raman I_D/I_G ratio was found to be increased to 0.34 from 0.16 under 514 nm laser excitation. As shown by Figure 3.10, by comparison to a pristine SWNT dispersion, Aniline SWNT was inferior.

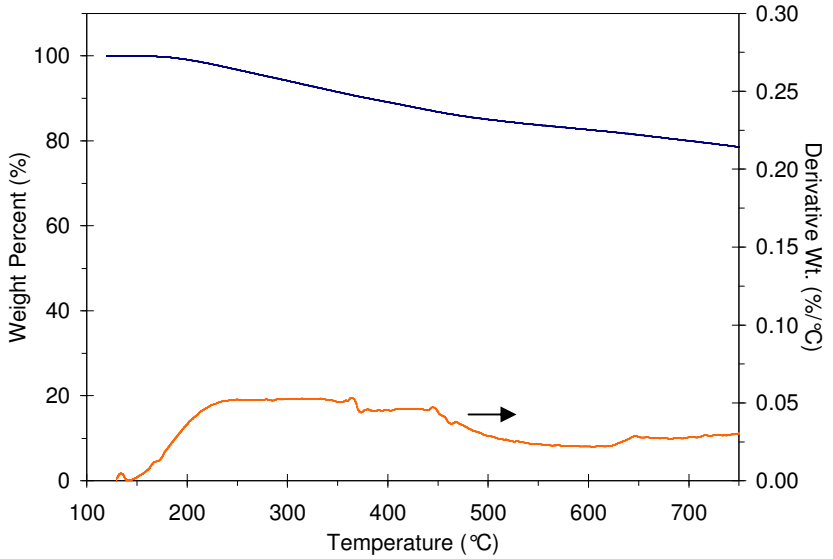

Figure 3.7: TGA mass loss curves for Batch 2 of Aniline SWNT product.

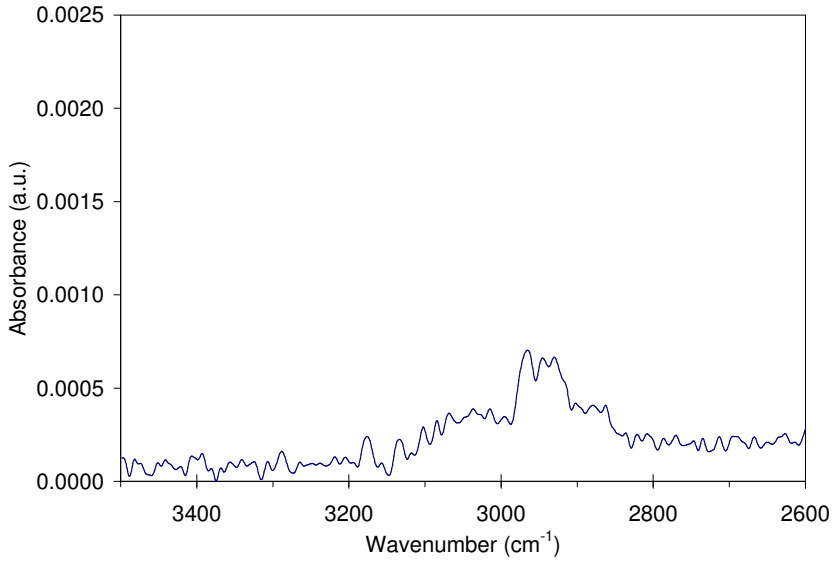

Figure 3.8: FTIR spectrum of Aniline SWNT (Batch 2) effluent at ~300°C.

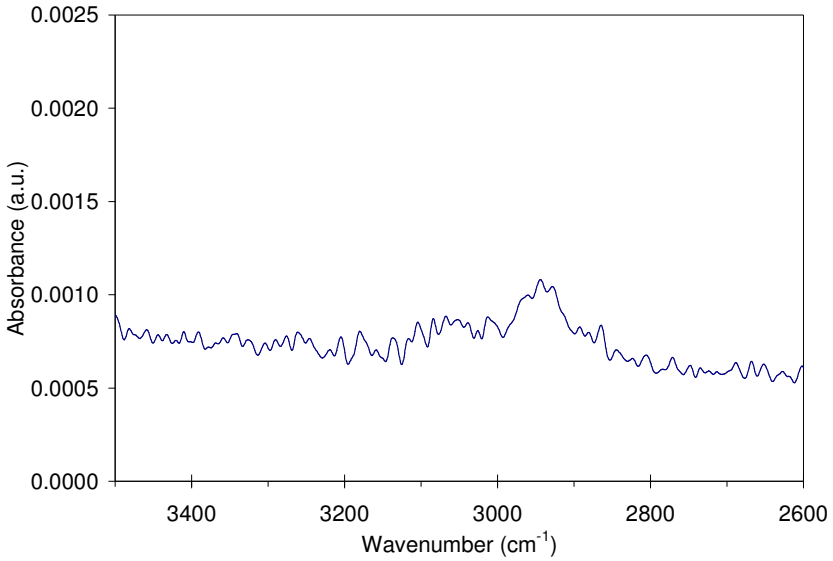

Figure 3.9: FTIR spectrum of Aniline SWNT (Batch 2) effluent at ~435°C.

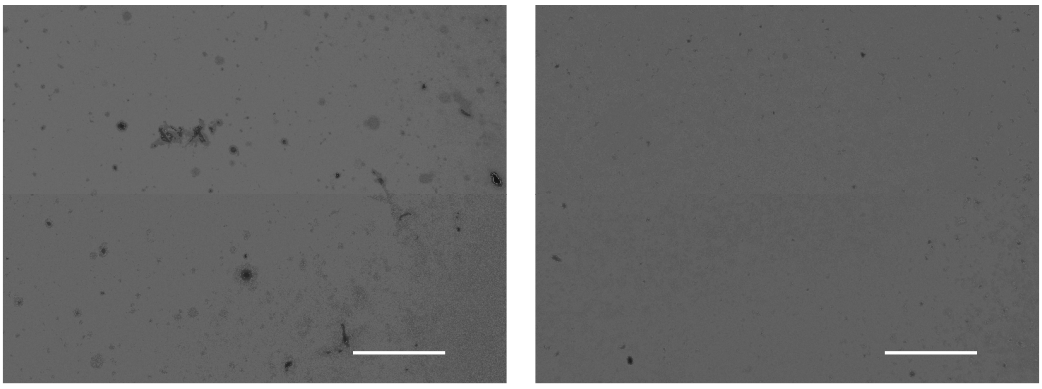

Figure 3.10: (left) A 50 ppm dispersion of Batch 2 Aniline SWNT [240 mg Li] versus (right) pristine SWNT in UPR. A 10x objective was used with 2x magnification in front of camera. Scale bar = 50 μm.

3.1.2 Reaction with 3-bromo-1-propanol

It has been shown that SWNT stabilized by Li/NH_3 are highly susceptible to functionalization by terminal alkyl and aryl carboxylic acids including 5-bromovaleric acid, 10-bromodecanoic acid[126] and 6-bromohexanoic acid.[133] Due to presence of the acidic carboxyl hydrogen, these products ionize to carboxylates during work-up, providing excellent water solubility. This structure was not acceptable for interaction with UPR. Thus, the attachment of a similarly structured primary alcohol, propanol, was desired. Figure 3.11 displays the structure of 3-

bromo-1-propanol, used for the production of Propanol SWNT. Note that a similar compound was previously reported to be reactive in Li/NH_3 (Scheme 2.21 in Ref.).[201]

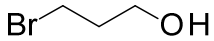

Figure 3.11: Chemical structure of 3-bromo-1-propanol.

The potential association of Li ions with the alcohol functional group, or hydrogen abstraction (since alcohol was used to quench), may affect the reaction, thus, the product was characterized by TGA-FTIR analysis. Figure 3.12 displays the TGA mass loss curves for Propanol SWNT. Mass loss events at 350°C and 446.5°C were measured. The corresponding FTIR spectrum for the first loss event was shown by Figure 3.13, highlighting the C-H vibration region, whereas Figure 3.14 displayed the full spectrum. While Figure 3.13 appeared promising, it showed only a methyl stretch and this did not represent the attachment of propanol. Instead, as shown by Figure 3.14, the first TGA mass loss was due to contamination by PDMS based vacuum grease from a non-optimized work-up procedure. Thus, the methyl stretch vibrations at ~2970 cm^{-1} in Figure 3.13 were a result of the $Si-CH_3$ side groups in the polymer. Examination of the full spectra from Figure 3.14 supports this conclusion as Si-O-Si deformations of the PDMS backbone were visible between 1020 - 1090 cm^{-1} and the symmetric methyl deformation was visible at ~1267 cm^{-1}.[202] The peak at ~817 cm^{-1} may be attributed to the Si-C vibration. The asymmetric methyl C-H vibration was not visible at ~1400 cm^{-1}. Even though this mass loss was dominated by the contaminant, the spectral features do not interfere with the expected -OH vibrations for Propanol SWNT. Unfortunately, no feature at ~3400 cm^{-1} was present. This confirmed that the alcohol did not survive the reducing environment or does not attach to SWNT. It was likely that the addition of 3-Bromo-1-propanol simply results in hydrogenation of the SWNT by hydrogen abstraction as alcohols are reactive in this manner.[201] This hypothesis was

supported by the complete lack of dispersibility in UPR. The second TGA mass loss event (Figure 2.15) at 446.5°C showed alkyl C-H vibrations as well as a vibration from an aromatic C=CH or in a vinylene (-CH=CH-) compound at 3015 cm^{-1}. An asymmetric CH_2 was also possible from a vinyl -CH=CH_2 group.[203] As was observed throughout this chapter, this high temperature fragment was nearly ubiquitous in modified SWNT.

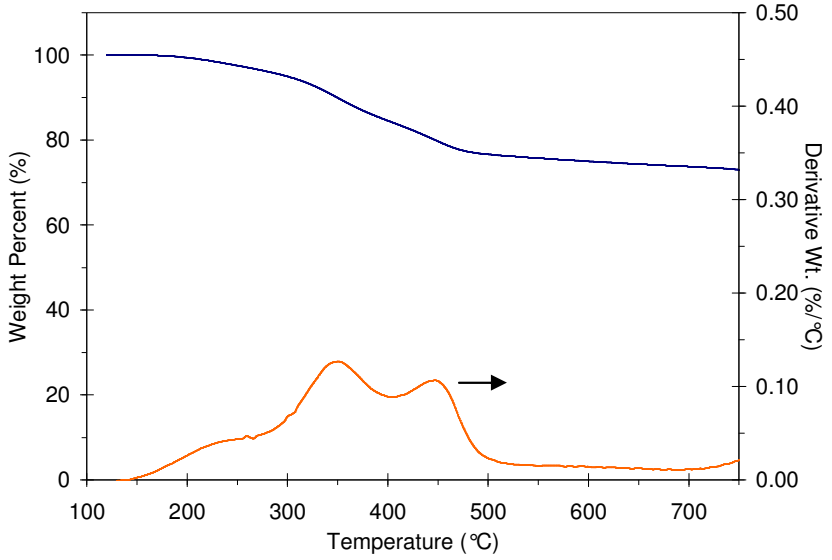

Figure 3.12: TGA mass loss curves for Propanol SWNT.

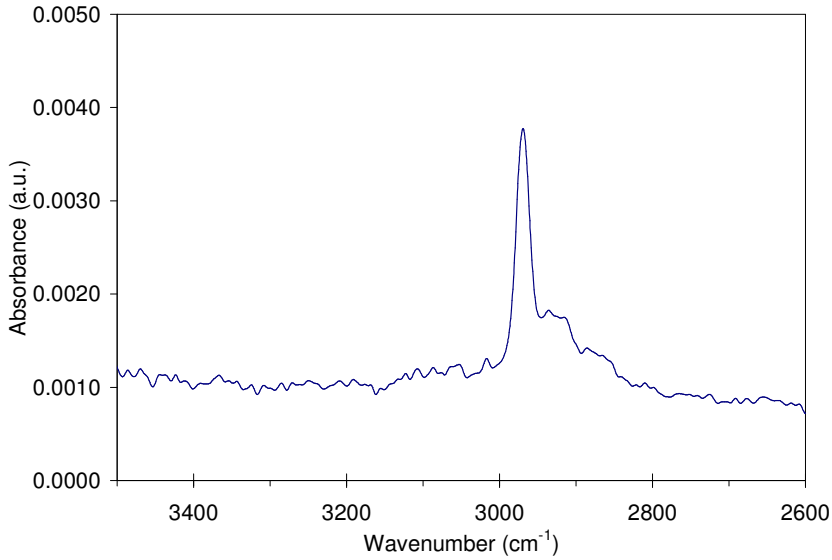

Figure 3.13: FTIR C-H vibrations of Propanol SWNT at ~350°C.

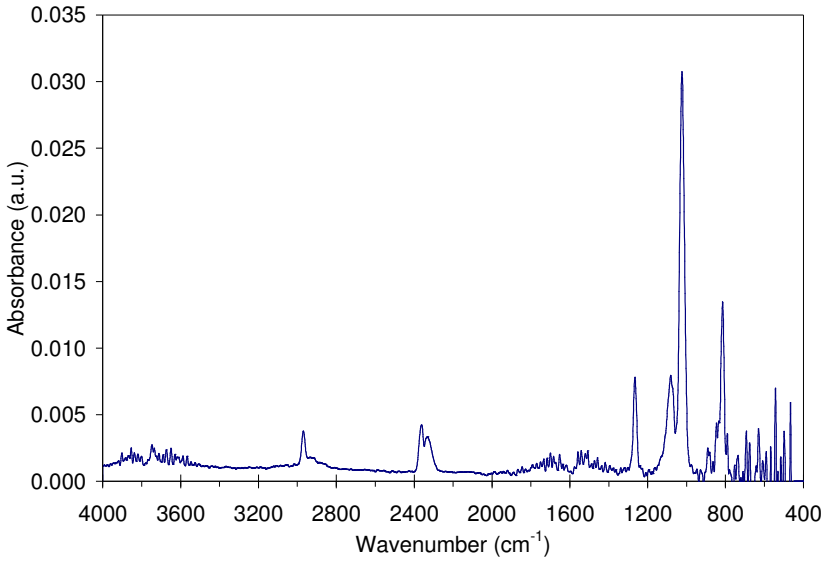

Figure 3.14: Mid-IR spectrum of Propanol SWNT at ~350°C.

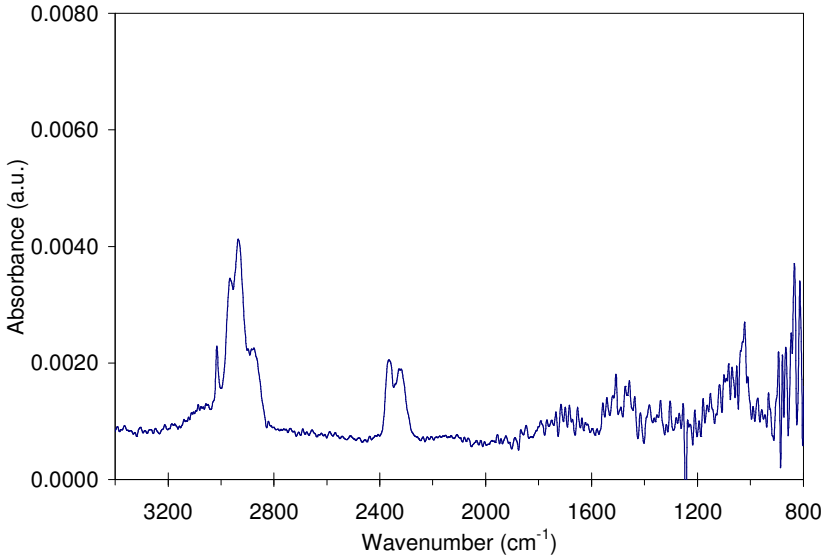

Figure 3.15: FTIR spectrum of Propanol SWNT at ~446°C.

3.1.3 Reaction with methyl 4-bromobenzoate

The direct sidewall addition of ester groups to SWNT was desirable for compatibilization with UPR by matching solubility parameters via non-specific interactions. As previously mentioned, reactions with long chain alkyl carboxylic acids are feasible in Li/NH_3. The carbonyl of an ester group is a prime association site for Li ions in solution, however. Methyl 4-bromobenzoate (3.2

mmol) was added to stable SWNT dispersions (10 mg) in Li/NH_3 (120 mg Li) to form Methyl Benzoate SWNT. Figure 3.16 displays the structure of methyl 4-bromobenzoate.

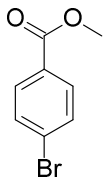

Figure 3.16: Chemical structure of methyl 4-bromobenzoate.

Figure 3.17 displays the TGA mass loss curves for Methyl Benzoate SWNT. Based on the derivative mass loss curve, slight continuous losses were observed at lower temperatures culminating with an event at 441.1°C. The FTIR spectrum at this temperature was shown by Figure 3.18 and matches the characteristic high temperature loss for modified SWNT samples (discussed in Section 3.1.2). The expected characteristic vibrations of the ester were not observed. According to the recent study by Gebhardt et al. (2011) this could be expected due to the excess Li/NH_3 available to the system.[135] The authors found that even though excess reducing agent was removed in their study, methyl benzoate was susceptible to Li association on the carbonyl and a ketyl radical was generated. This also cleaved the C-O bond and the resulting product can be described as benzaldehyde functionalized SWNT. Based on the Raman I_D/I_G ratio, the Methyl Benzoate SWNT produced in this work were modified in some way. Raman showed an I_D/I_G increase from 0.16 to 0.29 under 514 nm laser excitation and from 0.07 to 0.29 under 514 nm excitation. Thus, the sidewall was not modified with methyl benzoate but with some unknown addend or by inclusion of defects.

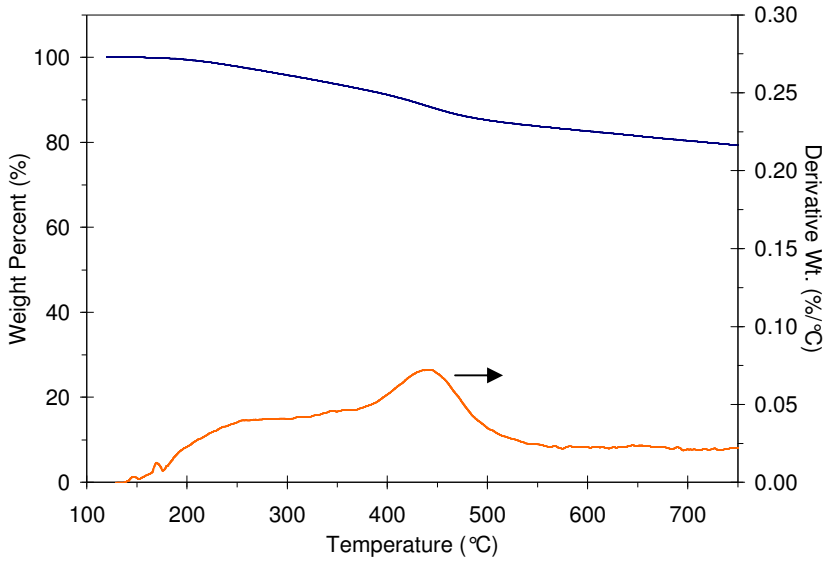

Figure 3.17: TGA mass loss curves for Methyl Benzoate SWNT.

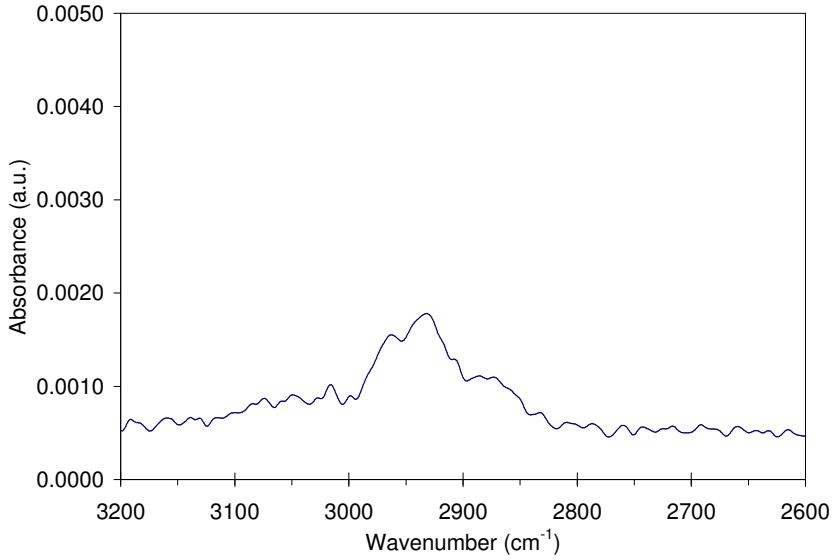

Figure 3.18: C-H vibration region of Methyl Benzoate SWNT at ~440°C.

3.1.4 Reaction with ethyl α-bromophenylacetate

Although the sidewall esterification with methyl 4-bromobenzoate was unsuccessful, a second reagent type was investigated. It was hypothesized that the relative stability of the intermediate aryl radical might be contributing to the final product. In the case of methyl 4-bromobenzoate, a reaction following the single electron transfer mechanism would form an aryl radical

intermediate. In the case of single electron transfer to ethyl α-bromophenylacetate, a secondary benzylic type radical would be formed on the adjacent phenyl carbon (after Br leaving). It was hypothesized that this conjugated structure would be more stable due to resonance within the phenyl ring. Due to steric considerations, the accessibility of this position to attach to SWNT might be troublesome. Figure 3.19 displays the chemical structure of ethyl α-bromophenylacetate.

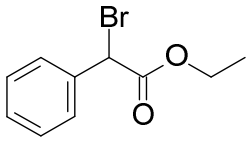

Figure 3.19: Chemical structure of ethyl α-bromophenylacetate.

In order to produce Ethyl Phenylacetate SWNT, ethyl α-bromophenylacetate was added to a dispersion of CoMoCAT SWNT in Li/NH_3 (68 mg Li). Figure 3.20 displays the TGA mass loss curves for this sample. A single high temperature loss was observed at ~460°C and was consistent with previous observations of a characteristic mass loss peak for modified SWNT. The FTIR spectrum in Figure 3.21 was also consistent with previous observations. The dispersion kinetics into UPR via high shear mixing were slow, and the resulting dispersion was poor.

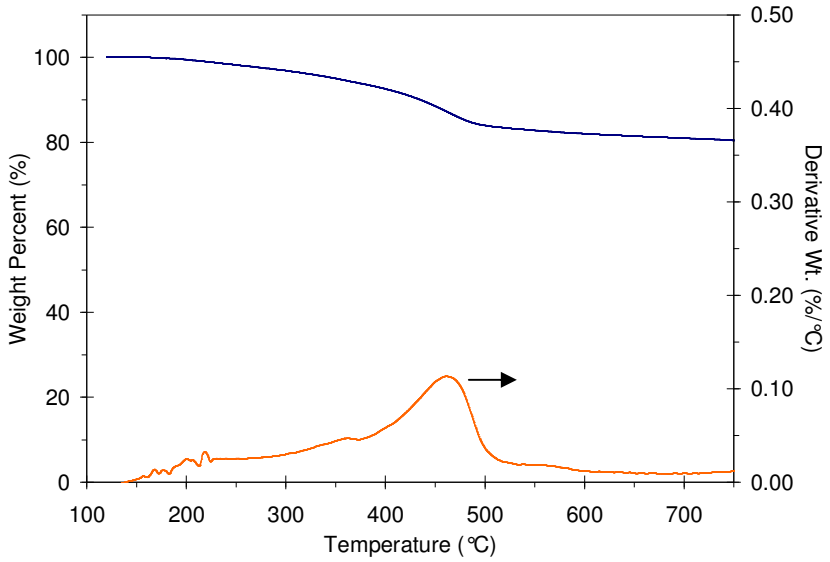

Figure 3.20: TGA mass loss curves for Ethyl Phenylacetate SWNT.

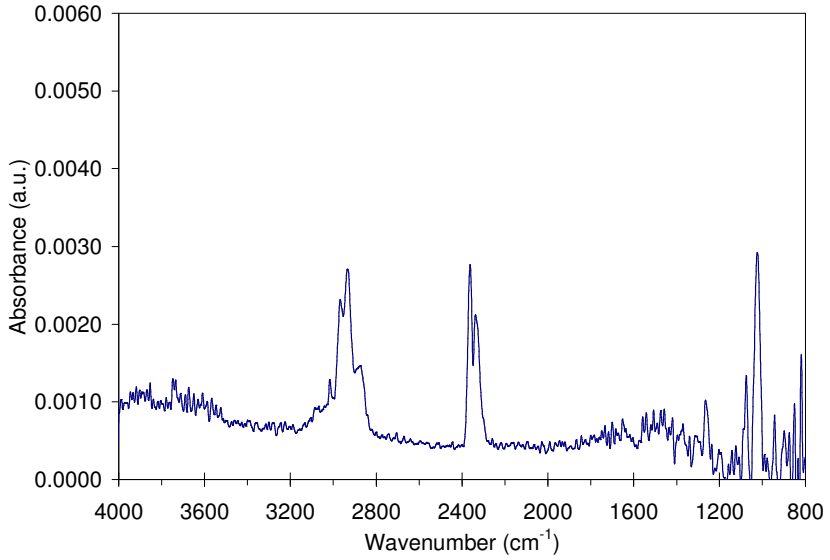

Figure 3.21: FTIR spectrum of Ethyl Phenylacetate SWNT at ~460°C.

3.1.5 Reaction with acetone

The addition of acetone to Li/NH_3 was thought to generate carbon centered radicals, which upon termination on SWNT, produced isopropyl functionalized SWNT.[201] This mechanism was supported by the presence of dimerized reagent in the reaction medium. Although noted in Chattopadhyay (2008) as a work in progress, this study appeared to be currently unpublished.

Similarly, although not carried out in Li/NH_3, the reduction of benzophenone in K and toluene has been shown to generate radical anions which terminate on the SWNT sidewall.[136] Figure 3.23 displays the suggested scheme. The K cation was thought to associate with the ketyl radical, localizing the radical to the carbon atom.

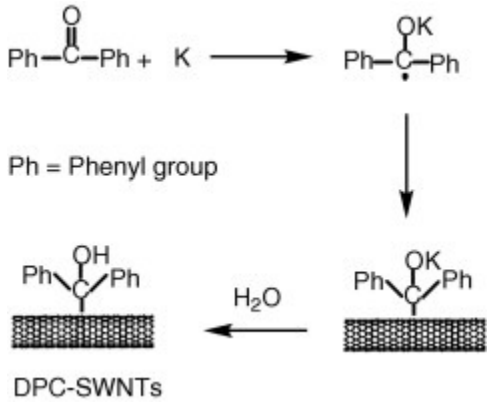

Figure 3.22: Reduction of benzophenone to generate radicals and functionalize SWNT. Adapted from Wei and Zhang (2007).[136]

In order to produce Isopropyl SWNT, HPLC grade acetone (Figure 3.22) was added to a stable dispersion of SWNT in Li/NH_3 (120 mg Li). Six additions of 250 μL were used and the dispersion quenched from a blue/black dispersion to clear ammonia after the final acetone addition.

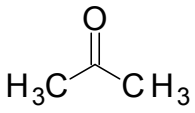

Figure 3.23: Chemical structure of acetone.

Figure 3.24 displays the TGA mass loss curves for the product. A peak derivative mass loss occurred at ~335°C, which was within the expected range for functional groups. Figure 3.25 shows the FTIR spectrum of the effluent which showed the familiar methyl hydrocarbon stretch from PDMS contamination. Absent, however, were the expected O-H vibrations at ~3400 cm^{-1}

for any O-H vibrations in Isopropyl SWNT. The high temperature FTIR spectrum was also examined, shown by Figure 3.26. Examining the Raman I_D/I_G ratio, this batch of Isopropyl SWNT was found to be modified only slightly, with I_D/I_G of 0.20, increased from 0.16 under 514 nm laser excitation. This was believed to be a result of the addition of excess acetone rapidly quenching the dispersion. Dispersion of the Isopropyl SWNT by shear mixing into UPR resulted in a dark liquid (Figure 3.27), but, due to presence of aggregates, this phase separated with time. Note that product was also freeze-dried after work-up but no dispersion was seen with this sample.

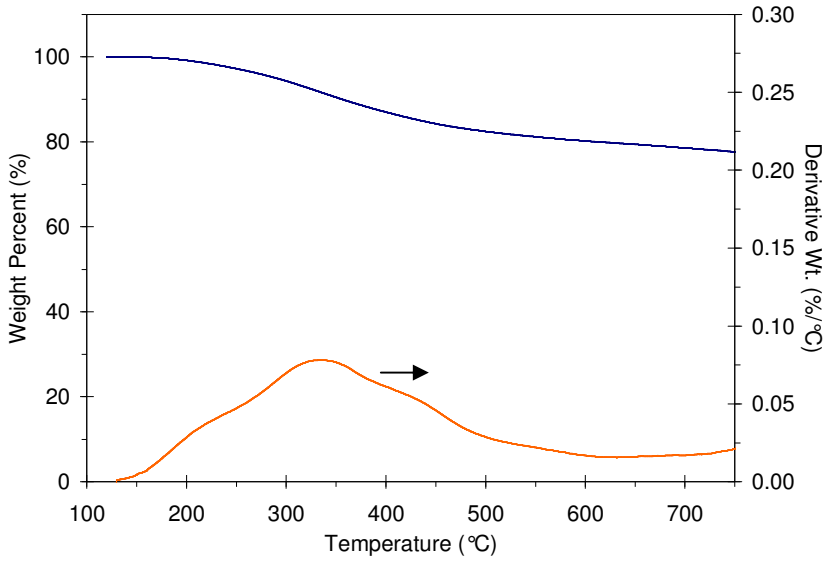

Figure 3.24: TGA mass loss curves for Isopropyl SWNT.

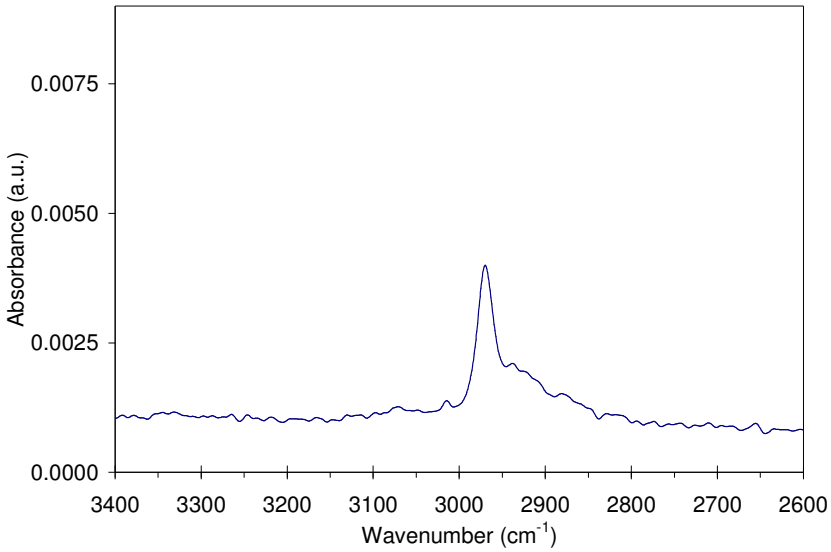

Figure 3.25: FTIR spectrum of Isopropyl SWNT at ~335°C.

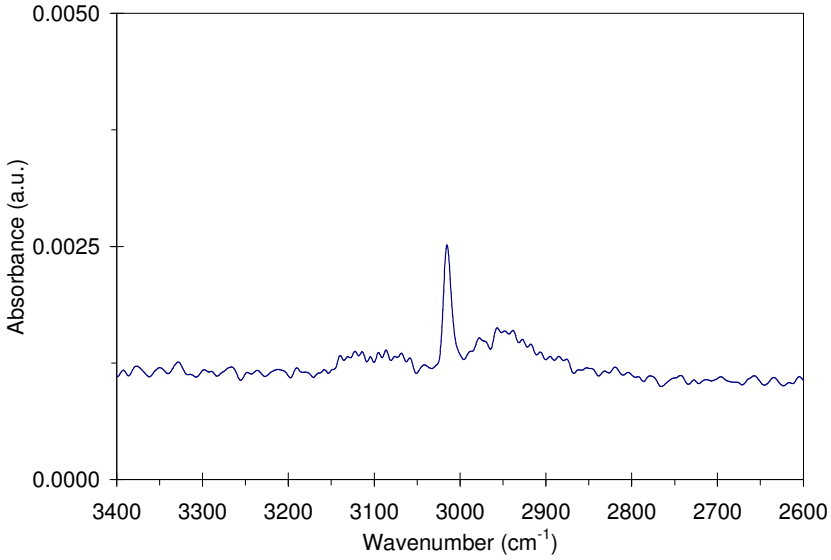

Figure 3.26: FTIR spectrum of Isopropyl SWNT at ~550°C.

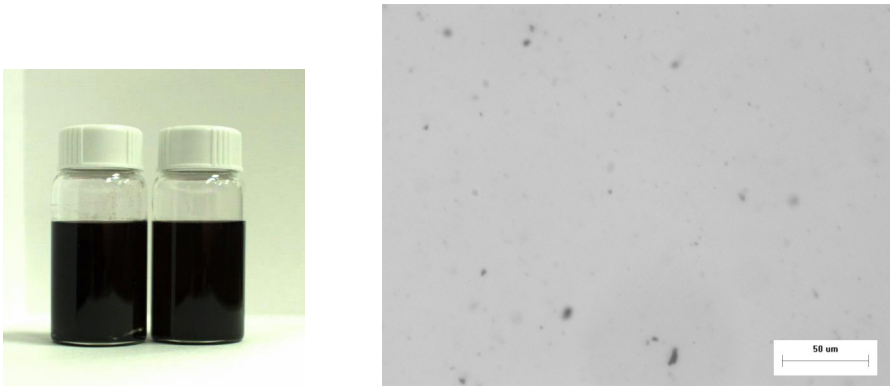

Figure 3.27: (left) Pure SWNT vs. Isopropyl SWNT dispersions showing bulk dispersion. (right) Microscale aggregate presence in Isopropyl SWNT dispersion using 20x objective with 2x magnification in front of camera. Scale bar was 50 μm.

3.1.6 Reaction with 2-dodecanone

Although not directly applicable for the dispersion in UPR due to its long hydrophobic chain, generation of in-situ ketyl radicals by addition of decyl methyl ketone was also investigated. Figure 3.28 displays the structure of 2-dodecanone. It was hoped this result would reveal more insight into the reaction with acetone. After 2-dodecanone addition to a stable SWNT dispersion in Li/NH_3, the resulting product was expected to be 2-Dodecanol SWNT.

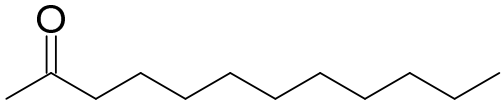

Figure 3.28: Chemical structure of 2-dodecanone.

Figure 3.29 displays the TGA mass loss curves for the reaction product. A substantial mass loss was observed at ~337°C. This was remarkably similar to the 335°C loss observed for the Isopropyl SWNT. Again, based on FTIR spectra shown in Figure 3.30 and Figure 3.31, this mass loss was undoubtedly from PDMS. Furthermore, the expected O-H vibrations for an alcohol were absent in Figure 3.31. Based on the near identical location of mass losses for both the Isopropyl SWNT and 2-Dodecanol SWNT, it was determined that PDMS grease occluded

within these samples. The presence of this contaminant might also have masked information in the aliphatic C-H vibration range of the IR spectrum. This can be argued since characteristic methyl vibrations would be expected in the functional group addend.

It was noteworthy that in contrast to all halogenated electrophiles studied above, the characteristic high temperature mass loss between 450°C and 500°C was not observed in the reactions with ketones.

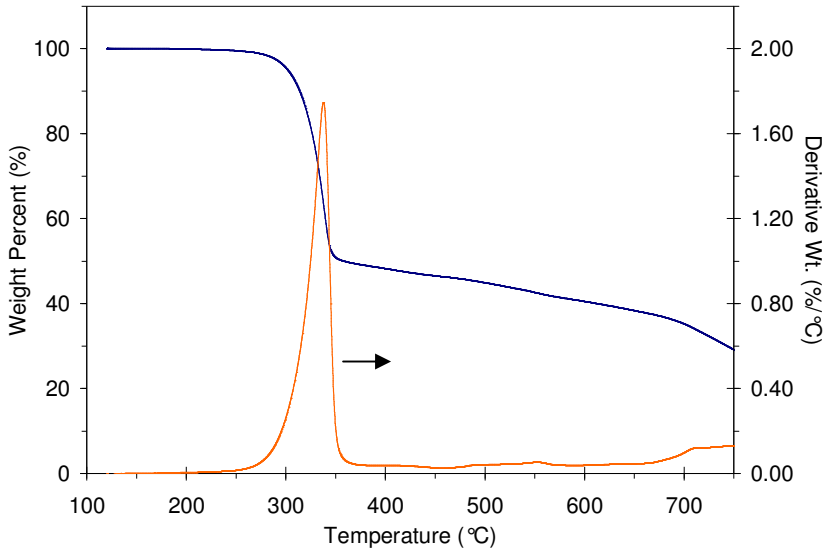

Figure 3.29: TGA mass loss curves for 2-Dodecanol SWNT.

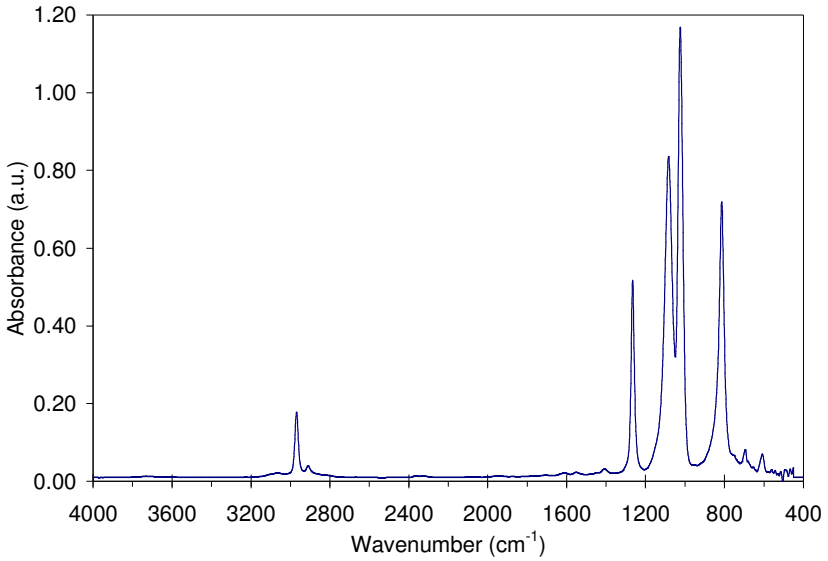

Figure 3.30: Mid-IR spectrum of 2-Dodecanol SWNT at ~337°C.

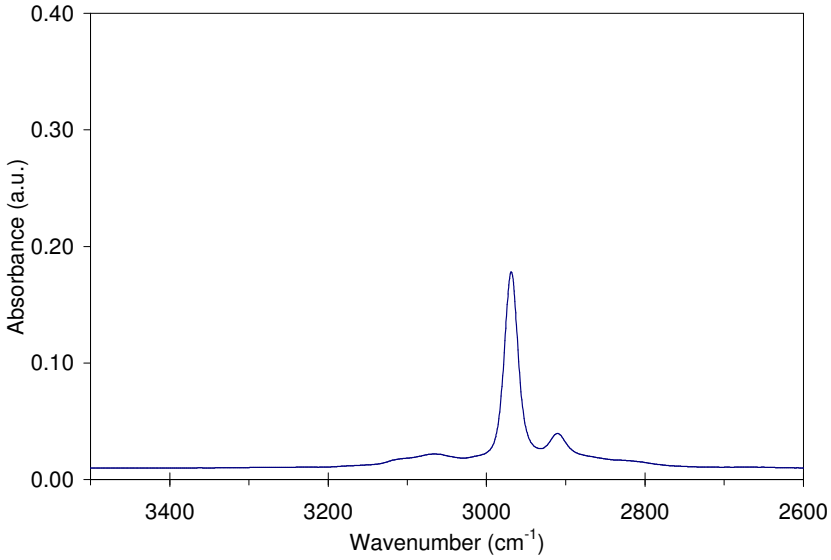

Figure 3.31: FTIR C-H vibrations of 2-Dodecanol SWNT at ~337°C.

3.2 Organolithium Based Functionalization

In this section, the stabilization of SWNT was carried out using methyl lithium (MeLi) in ether solution to reduce SWNT dispersions in THF. Due to nucleophilic attack by the MeLi across a carbon double bond, the reduction with MeLi resulted in a methylated SWNT sidewall and formation of an adjacent negatively charged carbanion. The SWNT were therefore stabilized

electrostatically. Addition of certain electrophiles has been shown to not re-oxidize the SWNT but react via a metathesis reaction.[204] It is important to understand that, at the very least, the SWNT are alkylated by the initial attack by MeLi and also can be subjected to hydrogenation upon reoxidation under certain conditions. Note that this reaction has been shown to be selective towards metallic SWNT, consistent with other nucleophilic additions to SWNT.

3.2.1 Experimental Method for Organometallic Reduction

Before attempting this reaction method, preparations should be made for handling pyrophoric reagents, including proper experimental design, protective gear, and location of a class D fire extinguisher for metals. Organolithium reagents should not be exposed to air or moisture. Also, syringe transfer should be avoided. In this work, vacuum bags with dry argon and the smallest volume of reagent required was used for safety. Since MeLi was received in a solution of ether, ignition sources were removed to prevent combustion.

In order to exclude trace moisture and prevent re-oxidation, a 3-neck 100 mL flask and 5 mg of SWNT were vacuum dried at 120°C overnight and cooled under vacuum. After the center port was plugged, dry ultra-high purity argon was connected to a flask side port and the remaining exhaust port was connected to vacuum. Note that all glassware was soaked overnight in a 1 M KOH solution in 75 vol. % mixed alcohols before use, rinsed well with deionized water, and rinsed with acetone before oven drying. All ports were sealed with Teflon sleeves. The reaction set-up was flame dried and cooled three times before purging with dry argon after exchanging the vacuum with a mineral oil bubbler. The system was purged with argon for 15 min and after isolating the flask, the dry SWNT was added in using a weigh paper cone. The system was purged for 45 min and 50 mL of anhydrous and non-stabilized THF was introduced. After purging for 15 min, the argon flow was minimized to prevent evaporation. The flask was

then bath sonicated for 1 hour to facilitate SWNT disentanglement. Next, the flask was immersed in a water ice and acetone bath (- 10°C) and a PTFE stir bar was added. In accordance with Roubeau et al. (2007), a C:MeLi molar ratio of 1:20 was used.[204] Assuming ~90 % SWNT purity, 5 mg of SWNT was calculated to be ~0.38 mmol of C. Thus, approximately 8 mmol of MeLi were required. Given that the MeLi was 1.6 M in ether, 4.75 mL (0.38 mmol C × 20/1.6 M) of this solution was required, but 6 mL was used to be in excess. The MeLi in ether was slowly added to the cold SWNT dispersion while stirring and after addition the ice bath was removed. Stirring and/or sonication continued for the desired amount of time. Next, the required amount of reagent was added to the reactor. Work-up was initiated by slow addition of water in an ice bath. The product was filtered and washed with ethanol, acetone, THF, and ethanol.

3.2.2 Addition of methyl 4-bromobenzoate

Previously, the potential attachment of ester functional groups to the SWNT sidewall was found not possible in the harsh reducing environment of Li/NH_3. The potential attachment of this addend to SWNT was revisited in this section by adding methyl 4-bromobenzoate (1.6 mmol) to reduced SWNT (5.2 mg). Reduction was carried out by MeLi addition (2 × 3 mL additions) during stirring in THF, followed by bath sonication for 1 h. After reagent addition, sonication continued for 1.5 h then stirred overnight before work-up. Figure 3.32 displays the mass loss curves in argon for the SWNT product. Gradual low temperature losses were observed followed by a peak in the derivative mass loss at ~455°C. The corresponding FTIR spectrum was displayed in Figure 3.33. Although this spectrum suffered from low relative intensity it appeared hydrocarbon vibrations were present, possibly from the initial methyl group attachment. The expected ester vibrations were not detected. At minimum, methylation was confirmed by the

selective nature of the Raman I_D/I_G ratio which showed an increase to 0.14 under 514 nm laser excitation and nearly no change to 0.11 at 785 nm. For reference, the initial SWNT I_D/I_G was 0.09 (σ = 0.006) under 514 nm and 0.07 (σ = 0.011) under 785 nm laser excitation. This result alone was ambiguous since methylation can occur without attaching the electrophile. Again, referring to the recent study by Gebhardt et al. (2011), this was a result of attack on the electrophile by the MeLi and generation of ketyl radicals.[135] Furthermore, based on the ketyl radical formation, if any reagent did functionalize the SWNT the expected chemistry would be expected to be that of benzaldehyde functionalized SWNT.

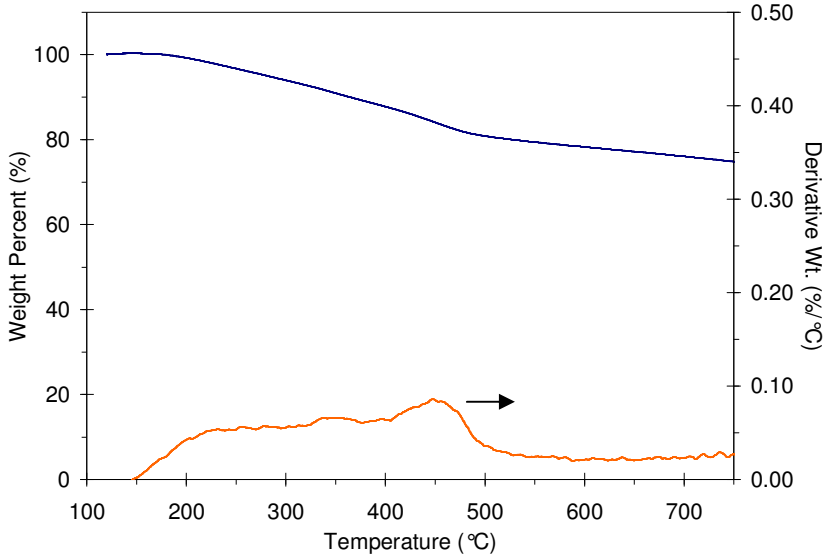

Figure 3.32: TGA mass loss curves for MeLi reduced/Methyl Benzoate SWNT.

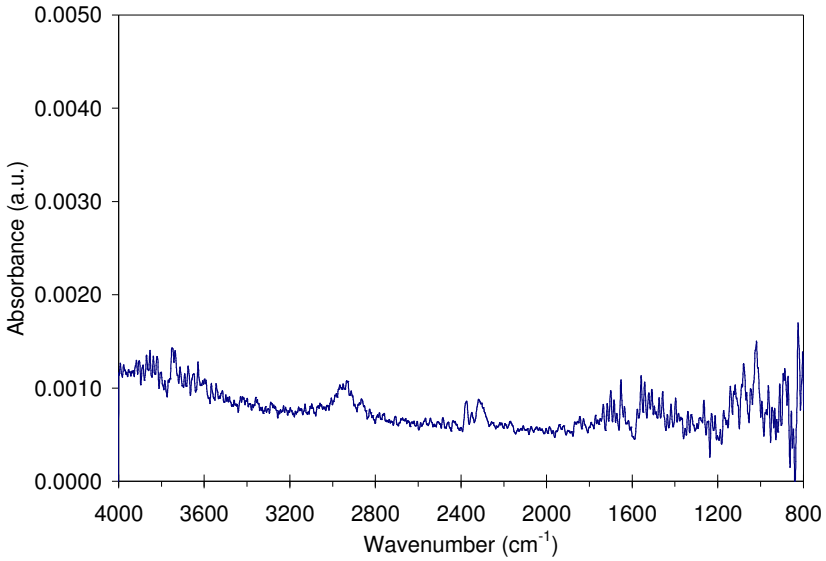

Figure 3.33: FTIR spectrum for MeLi reduced/Methyl Benzoate SWNT at ~455°C.

In order to better understand the expected FTIR signatures for evolution of methyl benzoate, a sample of the pure staring reagent, methyl 4-bromobenzoate, was analyzed by TGA-FTIR. In order to remove moisture, a large sample was heated to 100°C and then cooled under argon to 30°C before capturing background spectra and reheating. The resulting TGA mass losses were representative of the evaporation (m.p. ~80°C) of methyl 4-bromobenzoate, as shown by Figure 3.34. The peak mass loss was measured to be at ~118.8°C. Figure 3.35 displays the coupled FTIR spectrum. Here, the methyl C-H vibrations at ~2962 cm^{-1} and ester carbonyl at ~1747 cm^{-1} were observed. Interestingly, the phenyl C-H vibrations (> 3000 cm^{-1}) were barely visible. This means that detection of a low concentration of any SWNT addend by gas-phase FTIR was likely not possible.

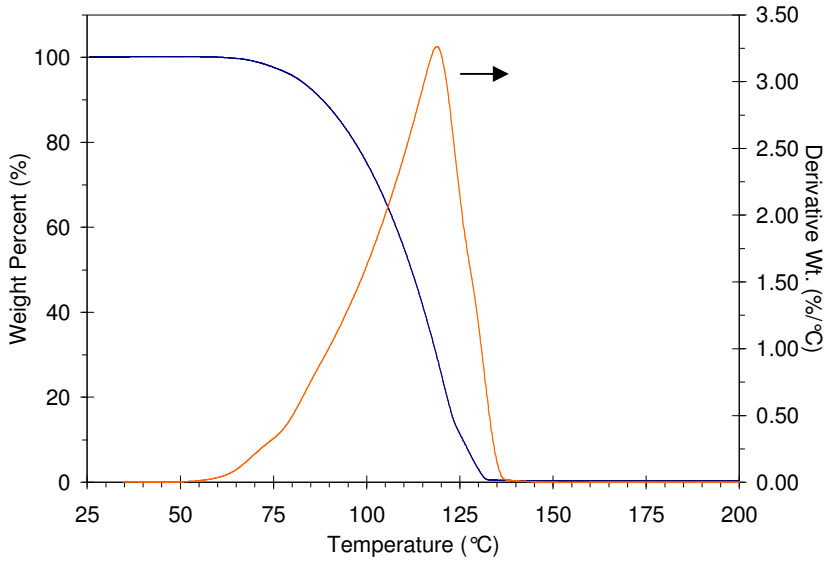

Figure 3.34: TGA mass loss curves for pure methyl 4-bromobenzoate.

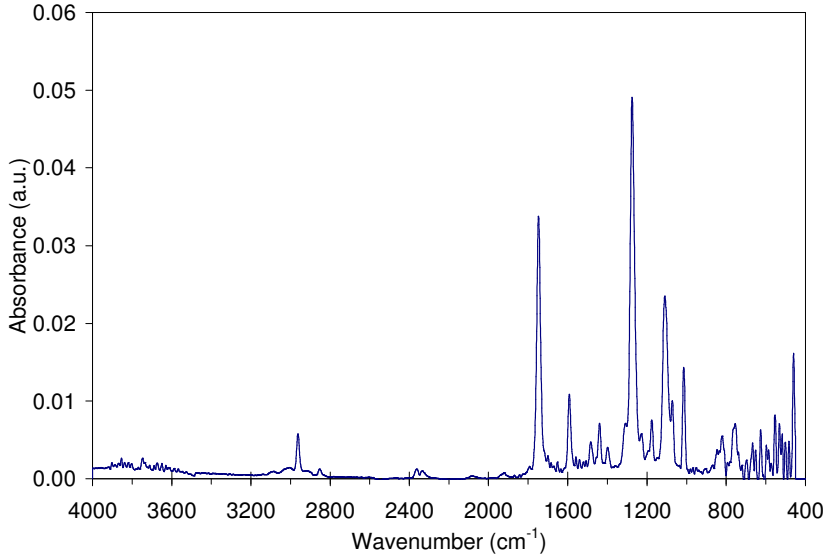

Figure 3.35: FTIR spectrum of pure methyl 4-bromobenzoate.

3.2.3 Addition of 9-Bromophenanthrene

Given the relative instability of many compounds in reducing environments, the strategy of attaching small molecules to induce interactions with UPR was partially abandoned. Instead, the introduction of bulky inter-tube spacers to help separate SWNT bundles via steric interactions was investigated. Care had to be taken to ensure that the introduced spacers would interact favorably with UPR. Thus, alkyl or greasy chains were not considered. Instead, the attachment

of polycyclic aromatic hydrocarbons (PAH) was considered. These molecules are attractive due to the relative stability of their aryl radicals. For example, Chen et al. (1989) studied the stability of hot PAH gases by observing hydrogen abstraction from toluene.[205] The authors found that the 9-anthracenyl radical was 15 times less likely to arylate toluene than phenyl radicals. Thus, the reactive radical intermediate from an electrophile, such as 9-bromophenanthrene, would be expected to be a stable candidate for attachment to SWNT. Indeed, Roubeau et al. (2007) report the fucntionalization of SWNT with phenanthrene upon addition of the corresponding halogenated electrophile displayed in Figure 3.36. The resulting Phenanthrene SWNT were expected to have modified equilibrium bundle spacing when dry and, in addition, were expected to facilitate adsorption of UPR.

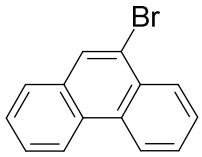

Figure 3.36: Chemical structure of 9-bromophenanthrene.

SWNT (5.2 mg) were dispersed in THF by bath sonication for 1 h. Reduction was carried out by MeLi addition (2 × 3 mL additions) during stirring in THF, followed by stirring for 1 h. The reagent was then added (1.6 mmol) and stirred for 1 h followed by bath sonication 1.5 h before work-up. Figure 3.37 displays the TGA mass loss curves for this sample. Peak mass loss events were observed at ~326.5°C and ~442°C. The first mass loss was attributed to PDMS contamination, which may be a consequence of occlusion with the methylated SWNT from the initial reduction step by MeLi. This was supported by the FTIR data in Figure 3.38. The next mass loss at ~442°C was found to be characteristic for modified carbons from functionalization reactions found previously herein. A subtle third mass loss feature was also present at ~570°C.

This may be the result of the strong adsorption of PAH to the SWNT sidewall. Interestingly, low temperature mass losses at ~200°C showed evidence of alkyl group removal, added during the initial nucleophilic reduction step. Figure 3.39 displays the FTIR spectrum showing evidence of possible methyl groups at ~2960 cm^{-1}. Functionalization via nucleophilic addition was confirmed by examining the Raman I_D/I_G intensity ratio shown by Figure 3.43. It is known that addition reactions are selective towards metallic SWNT due to accessible density of states near the Fermi level. This was precisely what was observed in Figure 3.43 where I_D/I_G increased from 0.09 to 0.15 under 514 nm laser excitation and from 0.07 to 0.12 under 785 nm laser.

For reference, Roubeau et al (2007) found the extent of phenanthrene functionalization could not be accurately estimated using electric-arc SWNT, but their mass loss between 150°C and 500°C was measured at ~13 wt. %.[204] Given that for every methyl group (~15 g/mol), one phenanthrene group (178.23 g/mol) was lost, the concentration of phenanthrene groups were approximately 12 wt. % in the present work.

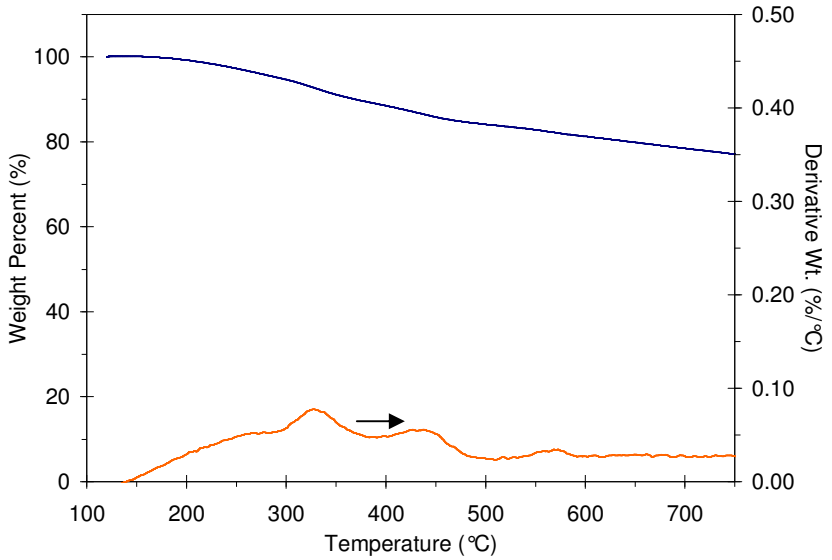

Figure 3.37: TGA mass loss curves for Phenanthrene SWNT.

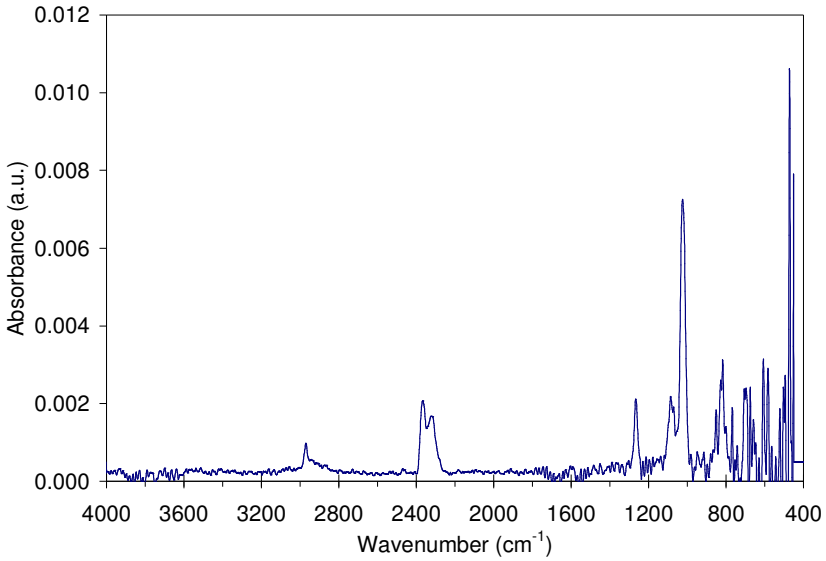

Figure 3.38: FTIR of Phenanthrene SWNT at ~330°C

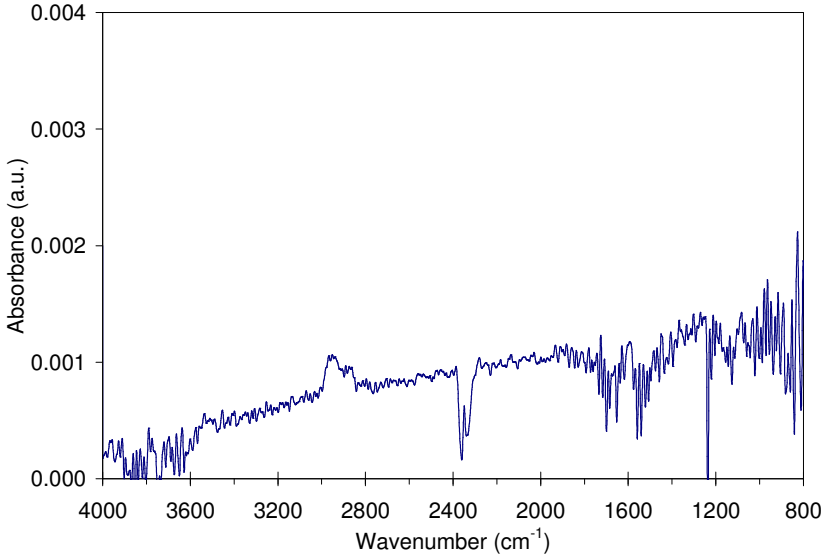

Figure 3.39: FTIR of Phenanthrene SWNT at ~200°C.

Due to the lack of detection of the expected aromatic C-H vibrations, an additional functionalization with longer treatment time was investigated (Sample 2). SWNT (5.2 mg) were dispersed in THF by bath sonication for 1 h. Reduction was carried out by MeLi addition (2 × 3 mL additions) during stirring in THF, followed by stirring for 1 h. The reagent was then added (1.6 mmol) and stirred for 1 h followed by bath sonication 1.5 h. The reaction was allowed to continue with stirring overnight. Prior to work-up, the dispersion appeared blue/green indicating

reduction of phenanthrene (similar to formation of charge transfer agents) from excess MeLi and displayed excellent dispersion. Figure 3.40 displays the mass loss curves for a second sample of Phenanthrene SWNT. Two prominent peaks were observed, one at ~185°C and one at ~342°C. The mass loss at ~342°C was quite substantial, likely due to chemical and physical adsorption. Remarkably, evidence of contaminants was not detected via FTIR. As displayed by Figure 3.41 and Figure 3.42, peaks at 3075 - 3080 cm^{-1} represented aromatic C-H vibrations. Therefore, these results provide evidence of the first CoMoCAT SWNT functionalized with phenanthrene. Again, the reaction was found to be selective towards metallic SWNT with the Raman I_D/I_G increasing from 0.09 to 0.19 under 514 nm laser excitation and from 0.07 to 0.11 under 785 nm laser.

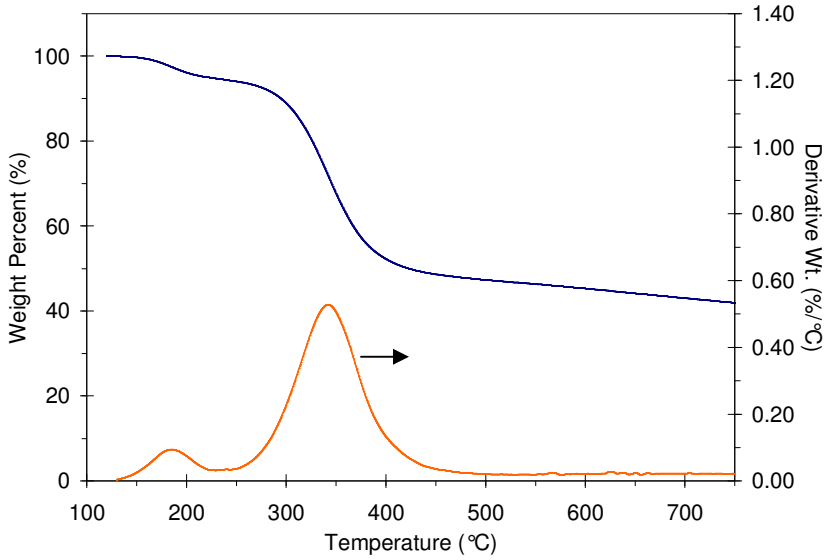

Figure 3.40: TGA mass loss curves for of Phenanthrene SWNT (Sample 2).

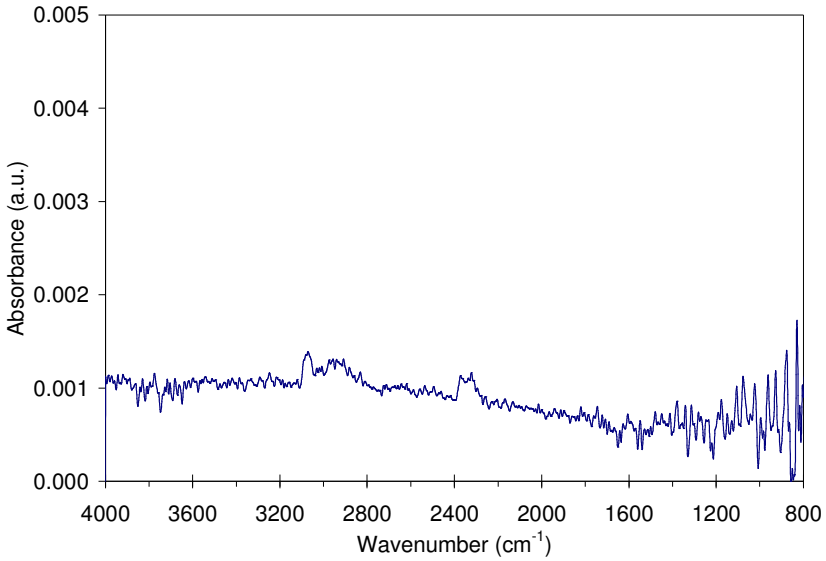

Figure 3.41: FTIR spectrum of Phenanthrene SWNT (Sample 2) at ~185°C.

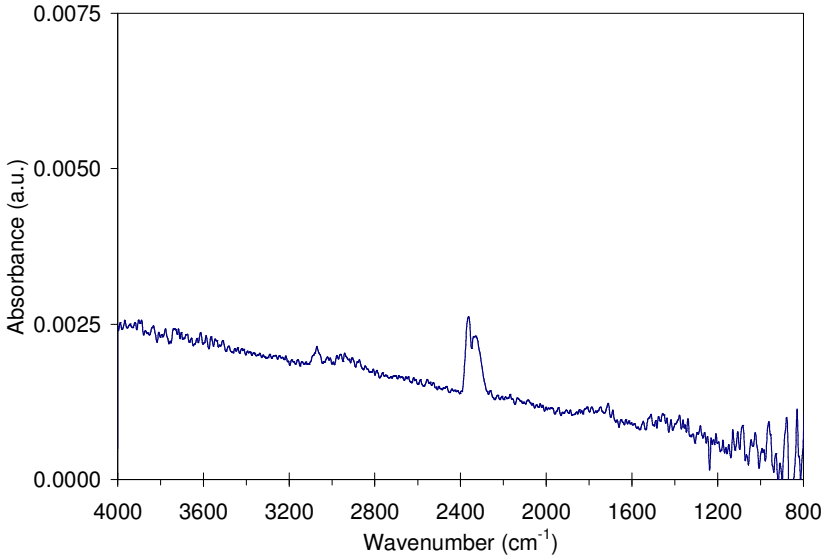

Figure 3.42: FTIR spectrum of Phenanthrene SWNT (Sample 2) at ~340°C.

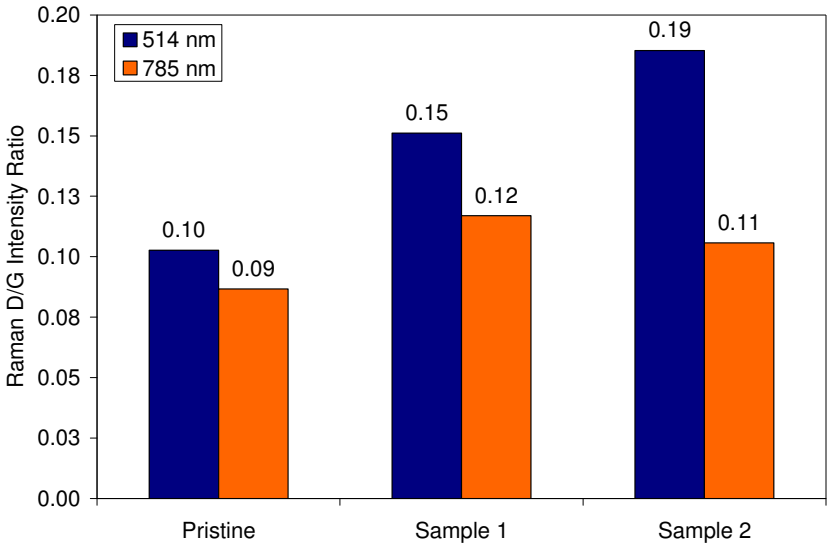

Figure 3.43: Raman I_D/I_G intensity ratio for Phenanthrene SWNT.

The FTIR signatures of 9-bromophenanthrene were investigated using TGA-FTIR for the pure reagent. The sample was held at 120°C to drive off residual moisture, cooled, and then heated after background calibrations. Figure 3.44 displays the TGA mass loss curves for 9-bromophenanthrene. A broad peak in the derivative curve was located centered at ~268°C. Figure 3.45 displays the FTIR spectrum of the effluent at ~210°C. Figure 3.46 also displays the FTIR spectrum at ~250°C. The strong aromatic C-H vibration at ~3080 cm^{-1} confirms the results of previous sections discussing the attachment to SWNT.

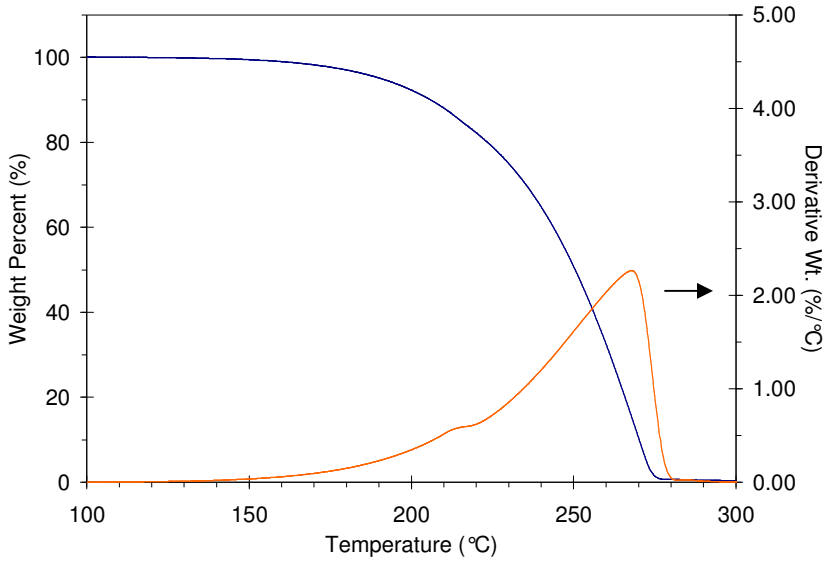

Figure 3.44: TGA mass loss curves for pure 9-bromophenanthrene.

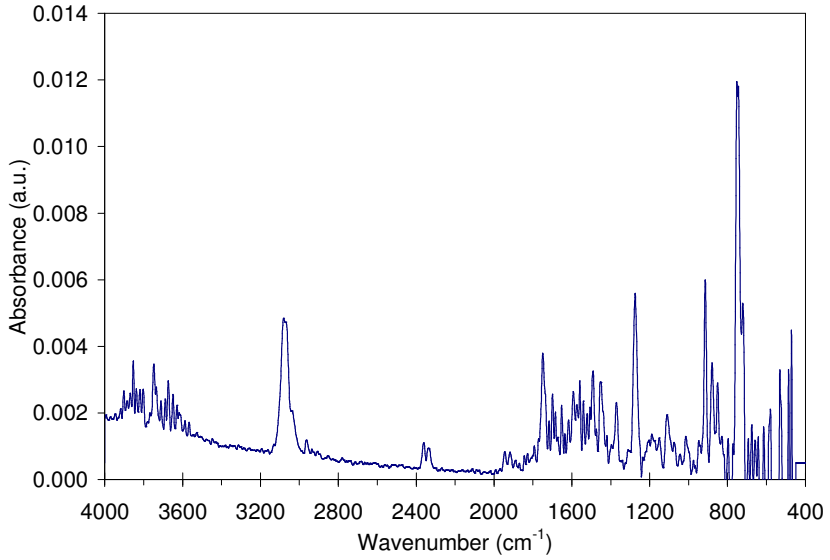

Figure 3.45: FTIR spectrum for pure 9-bromophenanthrene at ~210°C.

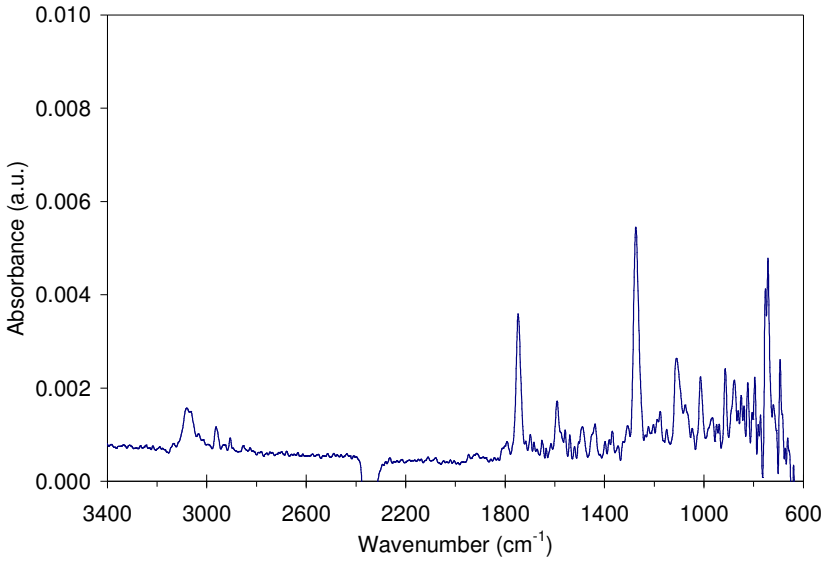

Figure 3.46: FTIR spectrum for pure 9-bromophenanthrene at 250°C.

3.3 Attachment of SWNT Crosslinks

The eventual curing of a SWNT-UPR composite involves the free radical propagation of crosslinks between polyester oligomers by styrene. It was anticipated that dispersed SWNT would become entrapped in this 3-D crosslinked network. In addition, due to the affinity of radicals to terminate on SWNT sidewalls some direct crosslinking might be expected. To facilitate stress transfer from the UPR matrix to the SWNT, the addition of crosslink sites to the nanotube sidewall was desired. Again, the selection of potential addends must be governed by the potential compatibilization with the UPR. Therefore, functional groups containing an unsaturation site must either be favorable to the polyester oligomer or the styrene solvent.

3.3.1 Reaction with 4-bromostyrene

It was found in previous sections that the addition of many compounds to SWNT dispersions in Li/NH_3 was not feasible. Evidence of the ability to add phenyl groups to SWNT was detected. In this manner, it was thought that the addition of 4-bromostyrene (Figure 3.47) would result in styrene functionalized SWNT (Styrene SWNT).

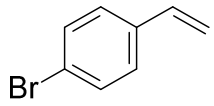

Figure 3.47: Chemical structure of 4-bromostyrene.

A number of reaction conditions and reagent addition steps were examined as displayed by Table 3.1. Based on alkylation reaction conditions, 120 mg of Li and drop-wise addition of 3.2 mmol (0.42 mL) of reagent were chosen for reaction with 10 mg SWNT. After evaporation of NH_3, the residue was reddish-brown in color, appearing similar to mud. This was unusual for this type of reaction. The product was extracted in hexane/water but did not show strong fractionation in hexane. The brown color was found in both phases. After removing the aqueous phase to neutralize the pH, brown color remained in the hexane. Thus, washing by filtration was done.

Sample #	Li (mg)	4-Bromostyrene	Details
1	60	105 µL	3 additions, quench to brown/yellow after
2	120	420 µL	1 addition
3	120	105 µL	Quenched at start of 4th addition

Table 3.1: Reaction conditions for Styrene SWNT.

Remarkably, in spite of varied reaction conditions, the post-work-up product was a white/gray SWNT powder. This powder appeared to have low solubility in a number of common solvents, including near complete lack of dispersibility in UPR by shear mixing (Figure 3.52). Figure 3.48 displays the ATR-FTIR spectra for Samples 1-3. The self-similarity between the three samples was evident by the matching spectra. The upturn in absorbance at low wavenumber was a result of the high optical absorbance of SWNT. One potential explanation for the chemical and physical properties of the products was the in-situ polymerization of 4-bromostyrene instead of the desired attachment of styrene monomer to SWNT. Under 514 nm laser excitation, the I_D/I_G ratio doubled, and this indicated sidewall modification or functionalization.

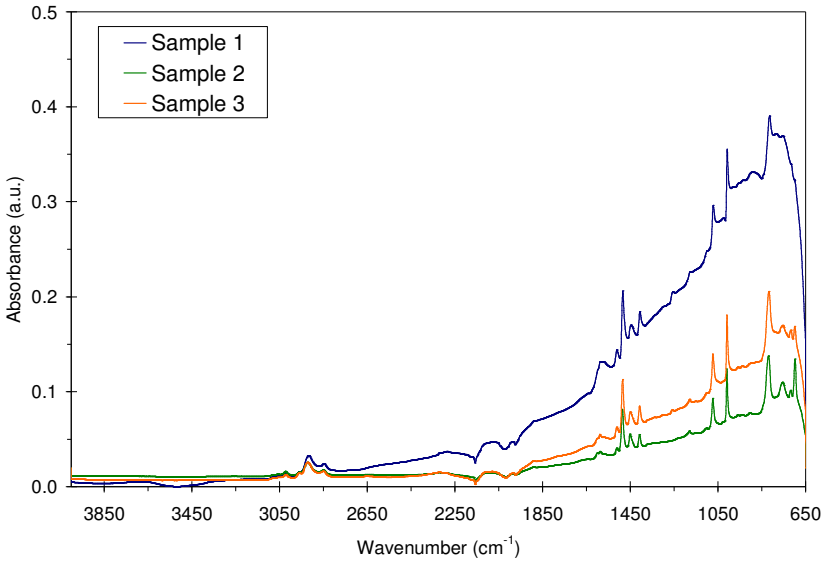

Figure 3.48: ATR-FTIR SWNT samples for Styrene SWNT reaction.

In order to determine the feasibility of polymerization, a reaction was carried out in the absence of SWNT. Using a Li:4-bromostyrene ratio of ~1:20, no polymer formed, however, upon increasing the ratio to 7:1 the reaction occurred. After washing and filtration with chloroform, a light brown polymer material was obtained. Figure 3.49 and Figure 3.50 compare the ATR-FTIR spectra for the polymerization product with that of pure atactic polystyrene (PS). Data were scaled with respect to largest absorbance peak. The results were remarkably similar with identical aromatic C-H vibrations located above 3000 cm^{-1} (Figure 3.49). These peaks were found at 3081.8, 3059.2, and ~3024 cm^{-1}. A peak found at 3000.8 cm^{-1} in the PS sample was found at ~3003 cm^{-1} in the 4-bromostyrene sample. For the aliphatic C-H vibrations of the polymer backbone, some apparent spectral up-shifting was observed for the 4-bromostyrene sample. Notably, the $-CH_2-$ peaks at 2848 (symmetric) and 2920.8 cm^{-1} (asymmetric) in the PS sample were found at 2853.3 and 2923.2 cm^{-1} in the 4-bromostyrene polymer, respectively. This up-shift was believed to result from the interaction between the electronegative Br and the polymer backbone of adjacent chains.[203] The asymmetric $-CH_3$ vibration found at 2959.8 cm^{-1}

resulted from the conversion of the once vinyl group of the monomer to terminal -CH_3 end groups, indicating low molecular weight chains were formed by the polymerization in Li/NH_3. A small peak was also found at 2985.9 cm^{-1} for PS.

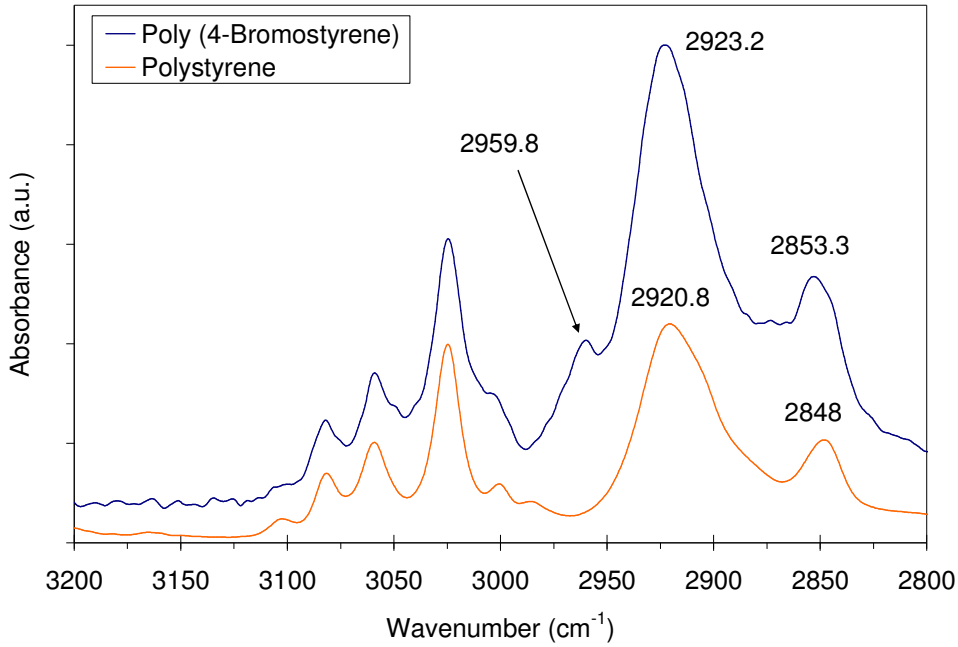

Figure 3.49: C-H vibrations for polystyrene and poly (4-bromostyrene) films.

Figure 3.50 shows the mid-IR spectra for each sample. Between 1750 cm^{-1} and 650 cm^{-1}, some slight differences were observed. Both samples share a band at ~1600 cm^{-1} which indicated aromatic, not olefenic species were present. For the PS, bands at 690 cm^{-1} (C-H out-of-plane vibration) and 760 cm^{-1} (ring out-of-plane deformation) represent vibrations for a monosubstituted aromatic group.[203] In conjunction with these bands, the peak at 822 cm^{-1} could mistakenly be interpreted as a 1,2-disubstituted benzene for the 4-bromostyrene sample, but it was known that the structural change in this region was not from a C-H bond *a priori*. Since the bands at 822 cm^{-1} and ~1009 cm^{-1} were present in the pure FTIR spectrum (obtained from Sigma-Aldrich) of poly (4-bromostyrene), they were assigned to halogen-sensitive bands on the aromatic ring. The two peaks at ~1512 cm^{-1} and 1408 cm^{-1} were believed to be a result of the

heavy Br found in the C-Br bond activating additional C=C stretching modes in this region, due to induction of asymmetry across the benzene ring not present in PS. It was concluded that this material was a form of polystyrene, specifically, poly (4-bromostyrene). Figure 3.51 displays the chemical structure of this polymer. NMR experiments have shown that the C-Br bond remains intact. This would indicate that activation of the vinyl bind in condensed Li/NH_3 was facile. Given that attachment of styrene was not possible under these conditions, this reaction scheme provides a route for the in-situ polymerization of vinyl or unsaturated monomers to attach to or coat individual SWNT.

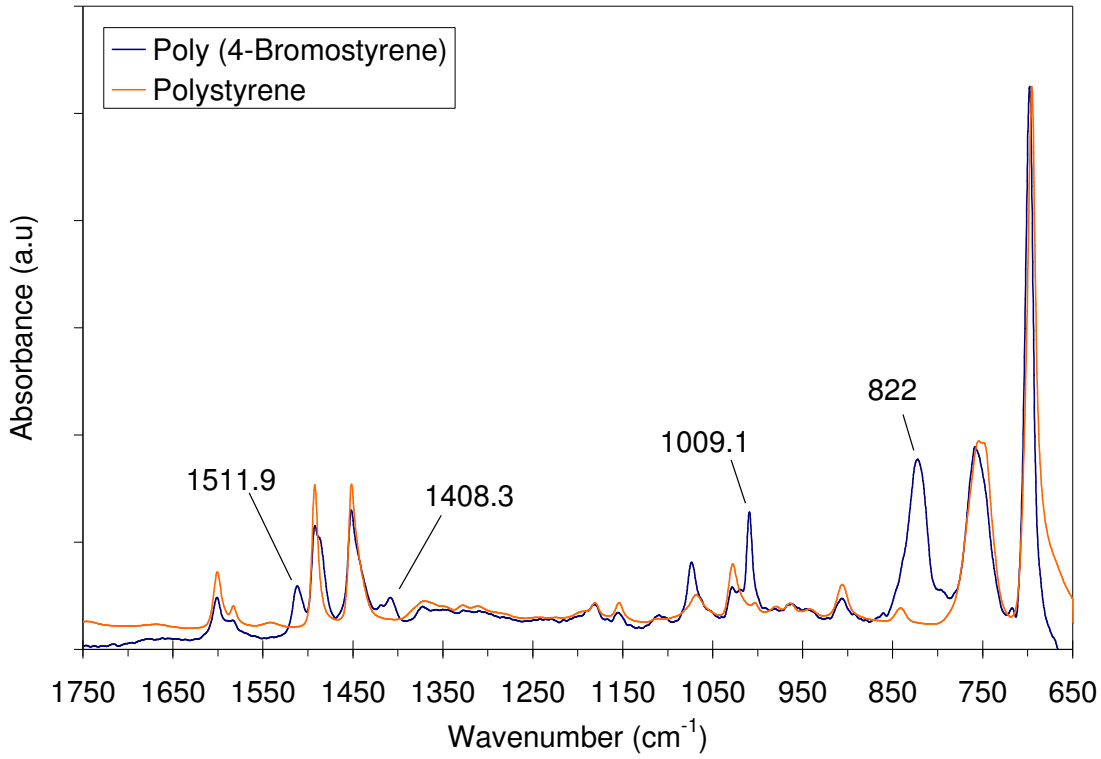

Figure 3.50: Mid-IR spectra for polystyrene and poly (4-bromostyrene) films. Peak assignments indicate peaks absent from pure PS.

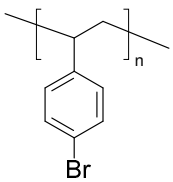

Figure 3.51: Chemical structure of Poly (4-Bromostyrene).

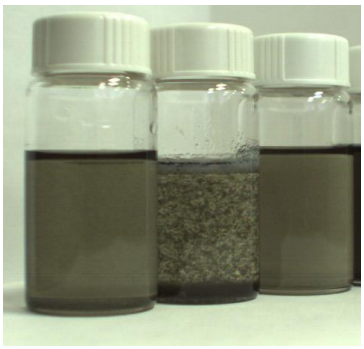

Figure 3.52: Lack of dispersion for styrene SWNT in UPR.

3.4 Conclusions

The chemical functionalization of SWNT via Billups type reduction and organometallic reduction conditions was explored in Chapter 3. The intention of the chosen SWNT functionalities was to induce specific and non-specific interactions with UPR.

The potential for functionalization of SWNT with a number of small molecules using the Billups reaction scheme was explored. Attempts to synthesize Aniline, Isopropyl, Propanol, Methyl Benzoate and Ethyl Phenylacetate SWNT were unsuccessful in attaching the intended functional groups. This was attributed to the strong reducing environment of Li/NH_3; these conclusions were supported by FTIR analysis of TGA pyrolysis gases. In general, however, FTIR and Raman analyses indicated either attachment of unintended functional groups such as alkyl/hydrogen species or simple sidewall disruption by processing. Remarkably, a characteristic FTIR spectrum appeared for a number of samples at temperatures greater than 440°C, indicating potential sidewall attachment of hydrogen to dangling bonds. Recent experiments in the literature have also shown that even under ideal conditions the yield from these types of functionalizations was quite low which further complicated the analysis.[135]

The reaction of ketones to form isopropanol and 2-Dodecanol SWNT under Billups conditions was unsuccessful. Analysis of the products was further hampered by the occlusion of

PDMS within each sample. Interestingly, the characteristic high temperature FTIR peaks were not seen in these samples.

Functionalization of MeLi reduced SWNT was also investigated in order to overcome environmental Li/NH_3 effects. The attachment of methyl benzoate (Methyl Benzoate SWNT) was unsuccessful but experimental evidence for the functionalization of SWNT with phenanthrene (Phenanthrene SWNT) was observed. To the author's knowledge, this is the first functionalization of CoMoCAT SWNT with phenanthrene groups. Raman spectroscopy showed preferential functionalization of metallic SWNT as expected for the organometallic reduction step. The unambiguous change in semiconducting SWNT by Raman supports this conclusion.

Finally, attempts to functionalize SWNT with styrene using 4-bromostyrene led to an unexpected but remarkable polymerization and functionalization of SWNT. Attempts to suppress polymerization by adjusting reaction conditions were unsuccessful indicating that activation of the vinyl bond was facile. This finding was promising for the addition other monomers, such as non-halogenated styrene. Specifically, this reaction scheme provides a route for the in-situ polymerization of vinyl or unsaturated monomers to attach to or coat individual SWNT.

Chapter 4

Functionalization with Polystyrene

4.1 In-situ Polymerization Functionalization with Styrene

Based on the attempted functionalization of SWNT by addition of 4-bromostyrene to Li/NH_3 stabilized nanotubes and the discovery of its polymerization, the in-situ polymerization of a number of unsaturated monomers should be possible. Potential candidates include acrylonitrile, acrylamide, and acetylene. For example, the functionalization of SWNT with acrylonitrile is extremely attractive for inclusion of SWNT into carbonized carbon fibers. For the specific interaction or compatibilization with UPR, the in-situ polymerization of methyl methacrylate (polyester) or styrene (polystyrene) was desired. Due to the instability of esters groups in the Li/NH_3 stabilized SWNT dispersions investigated in Chapter 3, the addition of styrene was first pursued. The use of styrene was also advantageous since only polymerization through the vinyl bond was possible. The lack of side reactions simplifies the analysis of the products. The polystyrene (PS) functionalized SWNT were expected to compatibilize the nanotubes with the styrene component in the UPR. This was based on the swelling and dissolution of pure PS in styrene monomer as well as UPR.

4.1.1 Experimental Method for Polymerization Reactions

In order to avoid re-oxidation with moisture or air, a dry and anhydrous environment was required during the reaction. Thus, a 3-neck 250 mL flask, a dry ice condenser, and the required

amount of SWNT were vacuum dried at 120°C overnight and cooled under vacuum before use. A PTFE stir bar was inserted into the flask and the condenser was secured to the center port. A line of anhydrous ammonia was connected to the condenser inlet port. One side port of the flask was connected to a dry line of ultra-high purity argon and the side outlet port was connected to vacuum. All ports were fitted with Teflon sleeves, except the condenser. The condenser port was wrapped with PTFE tape from the outside after flame drying. The set-up was flame dried and cooled three times before exchanging the outlet line with a mineral oil bubbler for purging with dry argon. After purging with argon for 15 min, argon flow was stopped and SWNT were added through the argon atmosphere by inserting the dry vial into a weigh paper cone. The bubbler was reconnected and the system gently purged for 45 min to no disturb the SWNT powder. Next, dry ice was added to the condenser and saturated with acetone (-78°C). Once a few drops of NH_3 wet the SWNT, the reaction flask was externally packed with dry ice using a plastic bowl and this was saturated with acetone. Due to condensation, the ammonia flow rate was increased far in excess of the saturation pressure so as to not pull vacuum on the bubbler and contaminate the atmosphere. After ~70 mL of ammonia was condensed, the ammonia flow was stopped and argon was used to flush the atmosphere. Next, the inlet ammonia line seal was cracked open from the condenser and the reaction flask outlet port to the bubbler was closed, forcing argon to flow up the condenser and out the unsealed port. While purging argon up the condenser, the condenser was separated from the flask and replaced with a dry glass plug fitted with a Teflon sleeve. The required amount of Li metal pieces were weighed out and added through the center port while purging out with argon by isolation of the bubbler. A stir plate was then powered on and the Li/NH_3 was stirred for 30 min to allow for saturated reduction of the SWNT. The required volume of reagent was pipetted in through a purging argon flow as

required. The argon flow rate was always throttled so that the center plug floated and purged the atmosphere for a few minutes, acting like a check valve, before re-opening the bubbler line. After the final reagent addition step, the reactor was purged for 15 min and the dry ice bath was removed. The argon flow was then stopped and ammonia was allowed to evaporate (-33°C) overnight. The product was referred to as functionalized SWNT (*f* SWNT). Note that all gas regulator diaphragms were closed when switching lines or opening a port to prevent sweeping the SWNT away from high pressure build-up.

Work-up was initiated by quenching of the reactor. A small volume (~15 mL) of methanol or ethanol was used to completely wet the flask sidewall and product. An ice bath was used to remove heat liberated by the reaction of excess lithium with the alcohol. Next, deionized water was added until the liquid level exceeded any dried residue on the glass. Under stirring, a few mL of 10 vol. % HCl was dripped in to lower the pH. After stirring for some time, the entire volume of the flask was poured into an extraction funnel containing an equal volume of water plus an additional amount of hexane (~15 mL). The funnel was vigorously shaken to extract the *f* SWNT into the organic phase. The funnel must be vented after shaking to avoid over pressurization. The aqueous phase was drained and discarded. More water was added and the extraction was repeated until the aqueous phase pH checked to be neutral (3 - 4 times). The remaining *f* SWNT and organic was washed on a 0.2 μm PTFE coated polypropylene filter paper (Pall) using denatured ethanol (denatured with alcohols only). The residue was washed with ethanol and acetone and the filter paper was washed clean of residue into a beaker using a 1:1 ethanol to acetone solution (~30 mL). The beaker was bath sonicated until homogeneous (~30 min). Next, the *f* SWNT dispersion was poured into the extraction funnel containing a 1:1 ethanol to water mixture with a small layer of hexane. The sample was extracted three times in

this mixture, venting often, and discarding the lower layer between each time. The sample was then extracted into water three times, discarding the aqueous layer in between. The filtration, washing, and bath sonication steps were repeated. Extraction cycles using the ethanol and water mixture followed by filtration, washing, and sonication were completed a total of three times. Finally, the *f* SWNT dispersion was filtered down and washed with ethanol, acetone, hexane, chloroform, and finished with ethanol. The *f* SWNT was carefully scraped from the filter paper to avoid grease contamination and placed in a weigh boat to air dry before being moved to a glass vial. The product was vacuum dried overnight. Dry samples were easily broken up with a spatula before use and exhibited low bulk density as compared to the starting material.

4.1.2 Styrene Addition Methods

The reactivity of SWNT in condensed NH_3 was examined at a constant loading of 60 mg Li with various means of styrene addition. For these experiments, the SWNT loading was fixed at 10.2 mg and ~70 mL NH_3 was condensed. A total of 600 μL of styrene monomer (dried over molecular sieves) was introduced to a stable blue dispersion of SWNT in Li/NH_3 (*liq.*) in three different fashions: (1) by single drop-wise dose, (2) by 3 drop-wise doses of 250 μL with 15 minute separation in between doses, and (3) by a single addition of 600 μL styrene dissolved in 50 mL of anhydrous THF. Figure 4.1 compares the TGA mass loss under argon atmosphere for each sample. The mass loss for one single drop-wise addition of styrene was 37.5 wt. % at 500°C. For three styrene additions the mass loss increased to 48.9 wt. %, indicating longer PS chain length or increased extent of functionalization. Conversely, when the monomer was diluted in THF before addition, the mass loss was much less at 14.3 wt. %. For point of reference, if all 600 μL of styrene polymerized and attached to the SWNT surface, a mass loss of

98.16 wt. % would be expected since mass was conserved upon polymerization. Thus, it was believed any free PS was effectively removed during work-up.

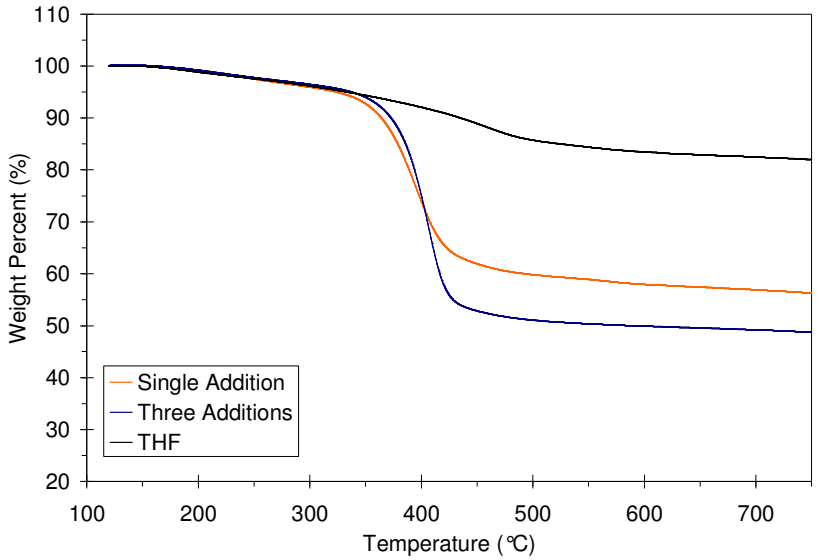

Figure 4.1: Effect of styrene addition type on TGA mass loss.

The effect of styrene addition method on functionalized SWNT was further studied by means of derivative mass loss curves displayed by Figure 4.2. For the single drop-wise styrene addition, the onset of mass loss occurred at lower temperature and was centered at 396.1°C whereas for three additions the mass loss occurred at 406.7°C. This difference of 10.6°C may indicate a larger polymer molecular weight resulted from the three addition method. For the THF sample, gradual mass losses were seen with increasing temperature and a small derivative mass loss peak was observed, centered at 458.1°C. Clearly, the thermal degradation of the THF product was quite different than the single and triple addition samples, suggesting functionalization was not consistent with this method. Further insight was obtained by comparing the Raman spectra of these samples and contrasting the observations regarding dispersion stability throughout each reaction.

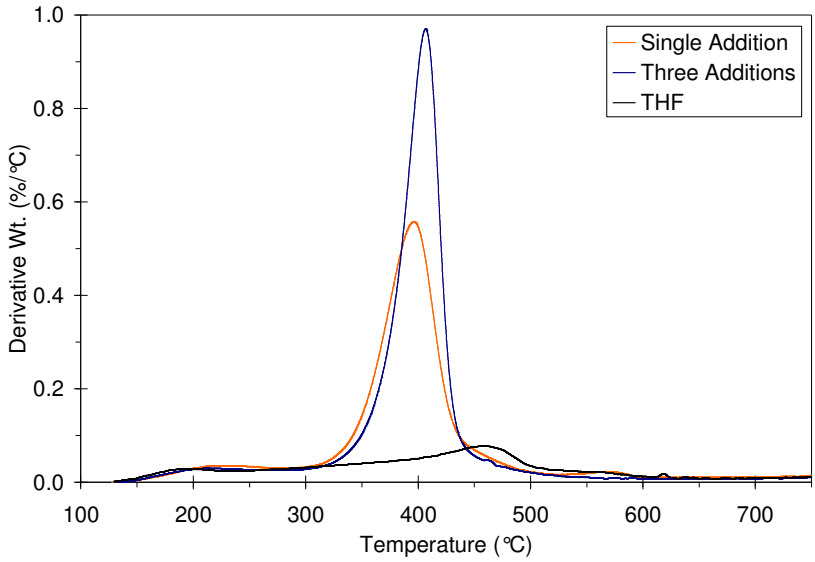

Figure 4.2: Derivative mass loss of products from various styrene addition types.

For the 60 mg loading of Li used for studies in this section, the reactions were "quenched" soon after complete styrene addition. Quenching was defined herein as destabilization of the SWNT dispersion and was accompanied by a color change from electric blue/black to clear ammonia with the return of SWNT aggregation in two incompatible phases. When multiple doses were added there was increased residence time of styrene in the reducing environment before quenching. On the other hand, for a single addition the reaction was likely kinetically limited by the quenching. The effect of these observations was apparent upon comparison of the Raman I_D/I_G ratio between products in Figure 4.3 where the extent of sidewall modification approximately doubles between these two samples. For reference, the initial SWNT I_D/I_G was 0.09 (σ = 0.006) under 514 nm laser excitation and 0.07 (σ = 0.011) under 785 nm laser. Mechanistic arguments based off the single electron transfer model can also be drawn. Due to side reactions such as radical disproportionation and self termination coupling steps, it was beneficial to keep the local monomer concentration low to increase the probability of reaction with SWNT, as in the multiple addition scheme. Overall, considering the observed quenching of

the dispersions, it was remarkable that Raman spectra showed high I_D/I_G for semiconducting SWNT under 785 nm laser. This was in spite of recent reports showing faster kinetics for metallic SWNT to neighboring aryl radicals under diazonium coupling to SWNT.[130]

When the monomer was first dissolved in THF and then added to the reactor, a new variable, the effect of dilution was introduced. The final concentration of styrene with respect to total liquid fraction (70.6 mL) was 0.85 vol. % in the case of drop-wise addition. This concentration drops to 0.49 vol. % with the inclusion of THF (120.6 mL liquid). As a result, the local styrene concentration was further reduced when the reaction was quenched. This should limit the molecular weight of the chains. It may also inhibit the degree of attachment of the chains to the SWNT. For example, it was shown by Figure 4.2 that the thermal degradation of the THF addition sample did not match the others. Upon comparison of the Raman I_D/I_G ratio (Figure 4.3) of the THF addition product to that of the styrene only additions, appreciable modification was observed. The measured I_D/I_G of the THF addition was intermediate to the styrene only addition results. Based on the degradation profile showing low mass losses at high temperature, the possible effect of functionalization by hydrogenation cannot be ignored. Hydrogen losses were previously observed near 500°C by Borondics et al. (2007).[119] This result was puzzling but will be discussed in more detail in Section 4.1.6.

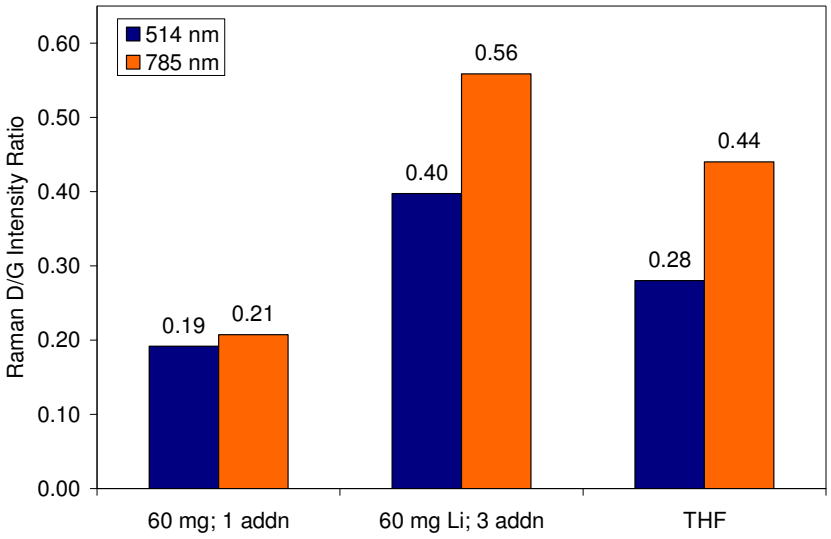

Figure 4.3: Raman I_D/I_G ratio of PS SWNT by additions type.

4.1.3 Identification of PS SWNT Mass Loss Species

Analysis of the gaseous species evolved during PS SWNT mass loss confirmed the presence of oligomeric PS fragments. Figure 4.4 shows the FTIR spectrum from the three styrene addition PS SWNT sample, during peak mass loss. This spectrum was characteristic of all PS SWNT samples. A special case was observed when styrene was first dissolved in inert solvents as discussed in Section 4.1.6. Strong aromatic C-H vibrations (> 3000 cm^{-1}) expected from the pendant phenyl rings of PS were clearly observed. Aliphatic C-H vibrations were also found (< 3000 cm^{-1}), as expected for the hydrocarbon polymer backbone. These peak assignments were further discussed in detail below.

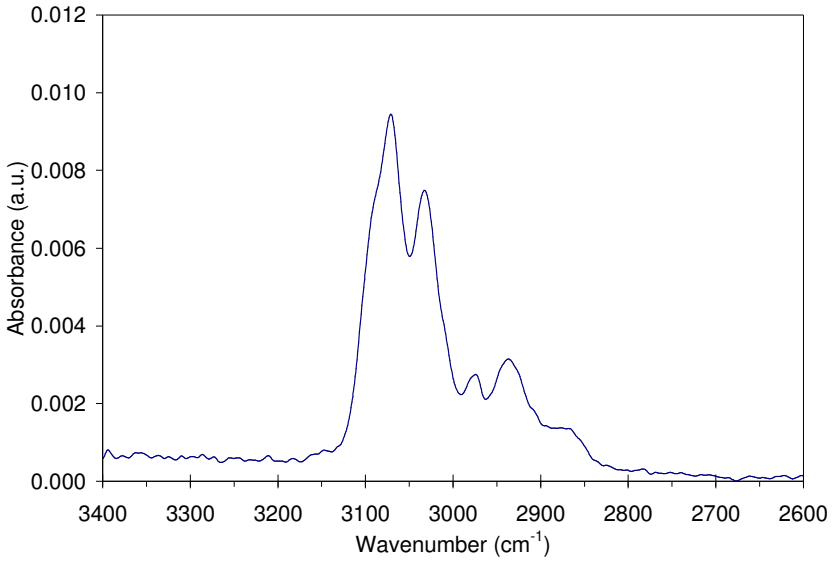

Figure 4.4: FTIR spectrum of TGA effluent from PS SWNT peak mass loss showing C-H vibrations of PS fragments.

Figure 4.5 compares the mid-IR spectra for PS SWNT TGA effluent at its peak degradation temperature and a solid phase ATR-FTIR spectrum of a PS sample obtained from a Millipore (PD2004700) Petri dish. It was challenging to determine the exact structural differences between the two since each sample was observed in a different state of matter. It was expected, however, that due to thermal degradation of chains from PS SWNT, some changes would be apparent. For example, the aliphatic C-H vibrations (< 3000 cm^{-1}) were not as pronounced in the gas phase. Conversely, the aromatic C-H vibrations were dominant in the gas phase. These peak positions appeared to be smeared and decreased in number, compared to the pure PS film, which may be related to symmetry changed from ring cleavage, as discussed below. Both samples preserved the band at ~1600 cm^{-1} (aromatic C=C stretching) which indicated aromatic, not olefenic species were present. The bands at 690 cm^{-1} (C-H out-of-plane vibration) and 760 cm^{-1} (ring out-of-plane deformation) represent vibrations for a substituted aromatic group, as expected. For the gas phase sample, two subtle differences were found: (1) an increase in the relative intensity of the peak at ~910 cm^{-1} and (2) a decrease in intensity of the peak at 1452 cm^{-1} found in the pure

PS sample (1456 cm^{-1} in gas phase). These observations were interpreted to result of cleaving of the benzene ring from the PS upon thermal degradation. In the PS film, the two bands at 1492 cm^{-1} and 1452 cm^{-1} represent C=C aromatic stretching vibrations that are active due to the asymmetry of the C-C bond tethering the ring to the backbone (mono-substituted benzene). In the gas phase, these peaks were found at ~1495 cm^{-1} and 1456 cm^{-1}, but the peak intensity at 1456 cm^{-1} was greatly subdued. This indicated disruption of the current status of ring symmetry and was interpreted as either ring cleavage to some radical or cleavage along the backbone. The presence of both peaks indicates more than one type of degradation fragment was present. To investigate changes to the backbone, the aliphatic C-H bonds below 3000 cm^{-1} were compared. In the PS film, peaks at 2920 cm^{-1} and 2848 cm^{-1} (72 cm^{-1} difference) were representative of C-H stretching vibrations in acyclic -CH_2- groups.[203] The vibration from the single acyclic hydrogen bound to the backbone carbon atom opposite from the benzene linkage expected between 2880 - 2890 cm^{-1} was not readily visible but appeared to be located within the lower wavenumber side of the 2920 cm^{-1} peak. For the gas phase spectrum, the peak at 2936 cm^{-1} was dominant. This was assigned to the single C-H vibration that was previously opposite the benzene linkage in the PS film. The activation of this vibration supported the ring cleavage conclusion. The other two peaks at 2977 cm^{-1} and 2870 cm^{-1} were interpreted to be from the acyclic -CH_2- vibrations, which were apparently depleted in concentration in the degradation product. Note that the vibrations located between 2300 and 2400 cm^{-1} in the PS SWNT sample were a result of carbon oxides. The similarities between the two spectra confirmed the presence of PS in the PS SWNT degradation products.

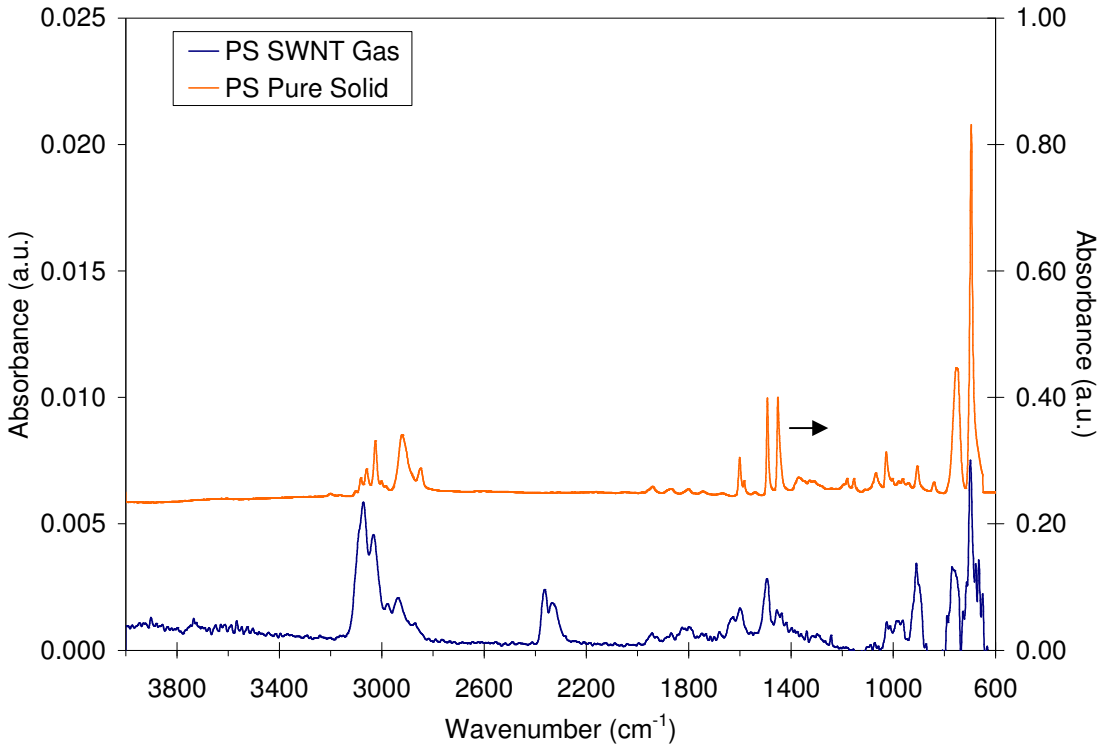

Figure 4.5: Mid IR spectra for a gaseous PS SWNT effluent (left axis) at peak degradation temperature compared with solid PS via ATR-FTIR (right axis).

4.1.4 Evidence for PS Functionalization

In order to confirm the functionalization of SWNT with PS, versus the simple overcoating of SWNT with PS, UV-vis analysis and high magnification SEM studies were completed. Figure 4.6 displays the UV-vis absorbance spectra for PS SWNT and polyvinylpyrrolidone (PVP) wrapped SWNT. PS SWNT were dispersed in chloroform and compared to aqueous dispersions of SWNT wrapped with PVP (as described in Chapter 6). All data were scaled with the optical absorbance at 450 nm. Covalent modification of SWNT alters the inherent electronic structure by conversion of sp^2 carbons to sp^3 carbons. As a result, the molecular like nature of SWNT optical transitions between bands of high density of electronic states, known as van Hove singularities, were quenched. Compared to the polymer wrapped SWNT, the smooth and featureless absorption curve for PS SWNT was apparent. The first van Hove transition of

metallic nanotubes M_{11} can be found between 400 - 600 nm and the second van Hove transition S_{22} of semiconducting nanotubes is located between 550 - 800 nm.[66] A closer inspection of the M_{11} transition was given by the left of Figure 4.7 whereas the S_{22} transition was displayed on the right. Based on the direct comparison to non-covalently functionalized PVP SWNT, PS SWNT were covalently modified.

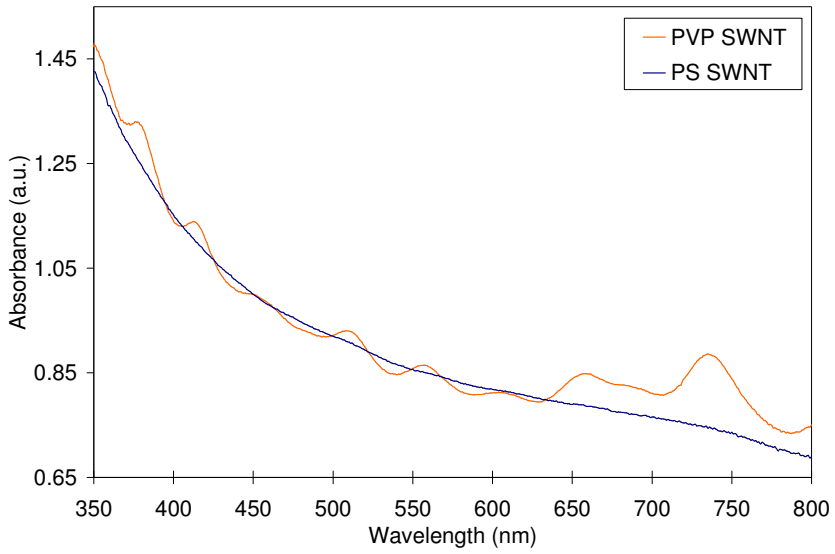

Figure 4.6: UV-vis spectra for PS SWNT compared to non-covalent stabilized SWNT.

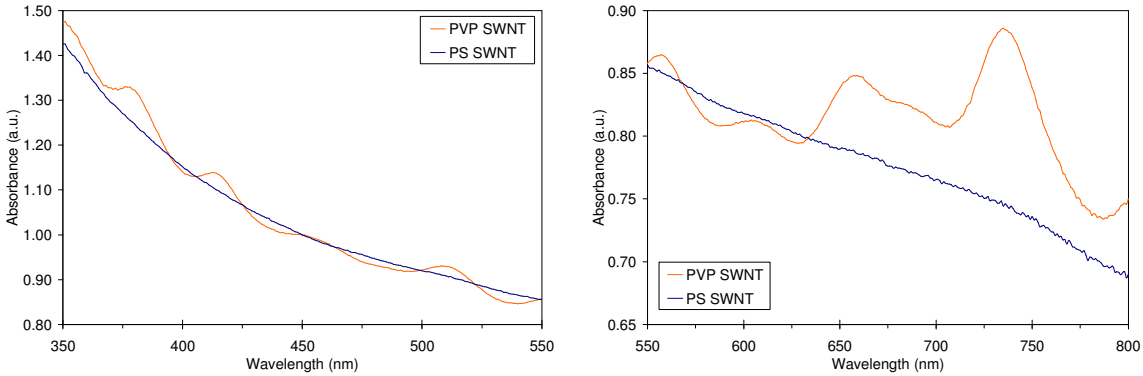

Figure 4.7: UV-vis spectra showing van Hove transition regions for PS SWNT.

PS SWNT samples were also analyzed for presence of excess or free PS by SEM microscopy. Using the same PS SWNT dispersion in chloroform used for UV-vis, some sample was dropped onto a flame cleaned aluminum SEM stub and vacuum dried. Figure 4.8 displays the SEM

image of the PS SWNT film bridging a gap in the surface of the SEM stub for contrast. This allowed for view of the nanotube bundles that may have formed due to capillary forces. The left image shows the sample under a magnification of 80,000 x and the image on the right was twice that at 160,000 x. The scale bars are 100 nm. No large free PS clusters were visible in the sample and PS over-coating was not apparent.

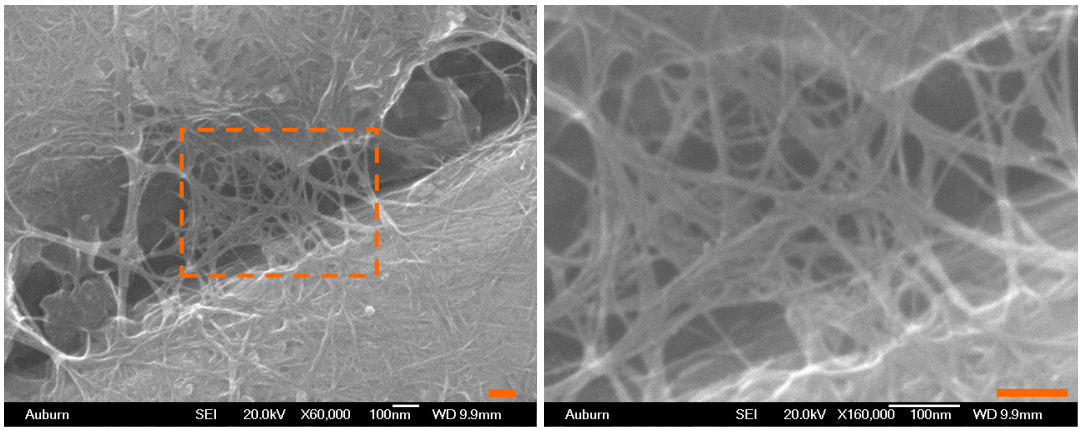

Figure 4.8: SEM of PS SWNT film (left) under a magnification of 80,000 x and the inset (right) at 160,000 x magnification. Scale bars are 100 nm.

4.1.5 Effect of Lithium to Carbon Ratio

All experiments on CoMoCAT SWNT used a constant SWNT mass of 10.2 mg and a constant volume of NH_3 of ~70 mL. When using 60 mg of Li, the reaction quenched shortly after full styrene addition. Based on the increased mass loss and extent of sidewall modification by Raman for a three step styrene addition reaction over a single addition, there was a concern that this quenching introduced a kinetic limitation into the extent of reaction. Thus, by increasing the amount of Li added to the system the Li:C ratio was adjusted accordance with Table 4.1 in an attempt to increase dispersion stability from quenching. The C content was also adjusted for 92 wt. % SWNT purity.

	Li:C ratio		Li:C ratio*	
Li	Mass	Molar	Mass	Molar
60 mg	5.88	10.18	6.39	11.06
90 mg	8.82	15.27	9.59	16.59
120 mg	11.76	20.36	12.79	22.13

Table 4.1: Various Li:C ratios studied. *adjusted for SWNT purity of 92 wt. %.

It was found that by increasing the Li from 60 to 90 mg, the dispersion could be stabilized from quenching until complete evaporation of NH_3. Interestingly, doubling the Li content from 60 to 120 mg introduced unexpected character to the product. Figure 4.9 displays the TGA mass losses in argon for samples with varying Li content. All samples were prepared using three additions of styrene monomer with ~15 min wait time in between. Increasing the Li content from 60 to 90 mg decreased the mass loss at 500°C from 48.9 wt. % to 43.8 wt. %,. Also, it was found that slight mass losses occurred at lower temperatures with 90 and 120 mg Li samples, than for the 60 mg Li sample. Recall that the low temperature mass loss behavior of 60 mg samples was very consistent in Figure 4.1, even between addition methods. The change in behavior of the higher Li mass samples could be a result of a broader molecular weight distribution due to the increased number of polymerization initiator sites. Examining the derivative mass loss curves in Figure 4.10, the peak mass loss increased from 406.7°C at 60 mg Li to 419.5°C at 90 mg Li. Further increasing the Li content to 120 mg decreased the mass loss to 40.9 wt. %, but the peak loss decreased to 382.2°C in this case. The low temperature behavior of the 120 mg Li sample matches that of the 90 mg sample, but at high temperatures (> 550°C), mass loss continued which may indicate some additional influence on styrene polymerization from the excess free Li. Therefore, based on the conditions studied, 90 mg Li appeared to be an

ideal concentration of Li as it stabilized the reaction from quenching but did not induce any unexpected high temperature mass loss behavior. From these experiments, TGA mass losses at 500°C appeared to be inversely proportional the Li:C ratio. Based on single electron transfer, it can be argued that more initiator (free electrons, Li) sites consume monomer more rapidly and initiate a greater number of chains. This, however, simultaneously lowers molecular weight since local concentrations adjacent to these initiator sites are consumed rapidly. The same effects, although manifested by different means, was observed previously when one addition versus three additions of styrene monomer were used.

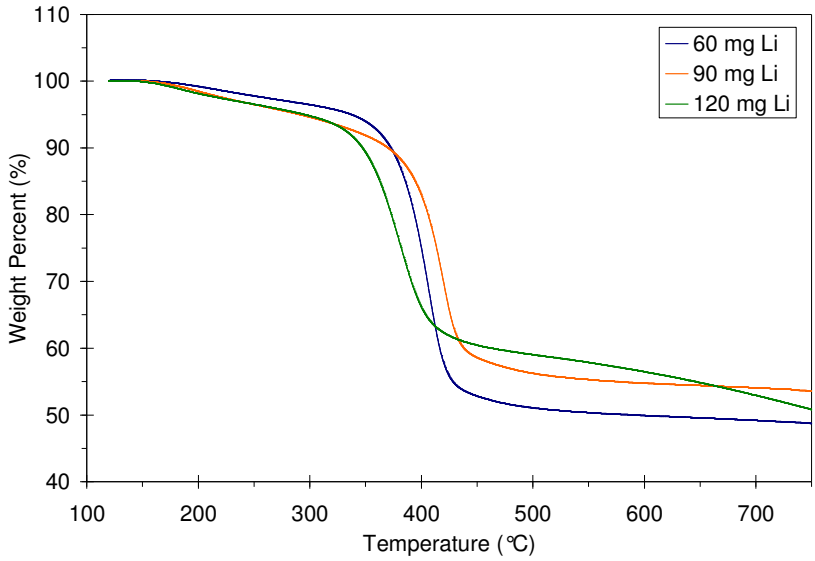

Figure 4.9: Effect of Li:C ratio for PS SWNT by TGA mass loss.

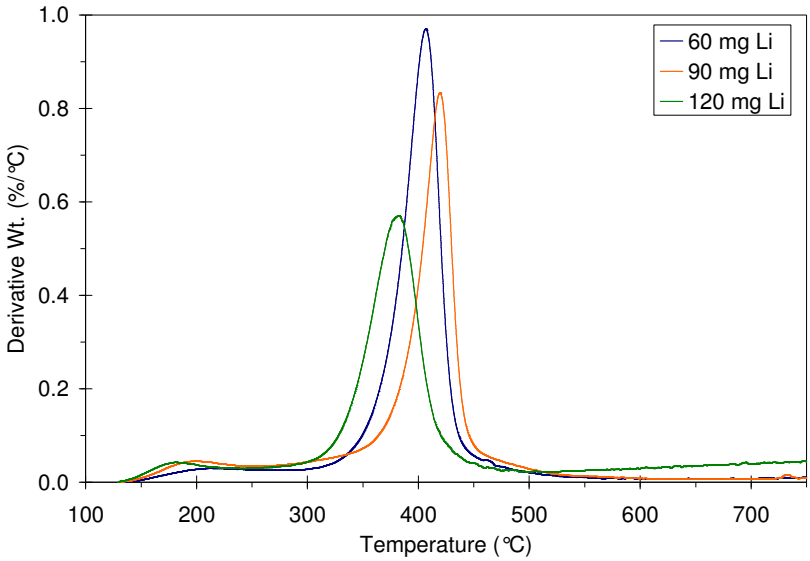

Figure 4.10: Derivative mass loss curves for PS SWNT with varying Li:C ratio.

The relative change in the extent of functionalization with Li content was apparent upon examination of the Raman I_D/I_G intensity ratios shown by Figure 4.11. The I_D/I_G for the 60 mg single styrene addition sample was also shown for point of reference. The magnitude of I_D/I_G nearly doubled for all Li amounts when three additions were used compared to a single dose at 60 mg Li. With the exception of a larger I_D/I_G for the 60 mg Li sample under 785 nm laser, the 60 and 90 mg Li samples were similar. However, the 120 mg Li sample showed a decrease in the functionalization of the metallic SWNT (514 nm laser) which was attributed to this mass of Li introducing too many polymerization initiation sites in the system.

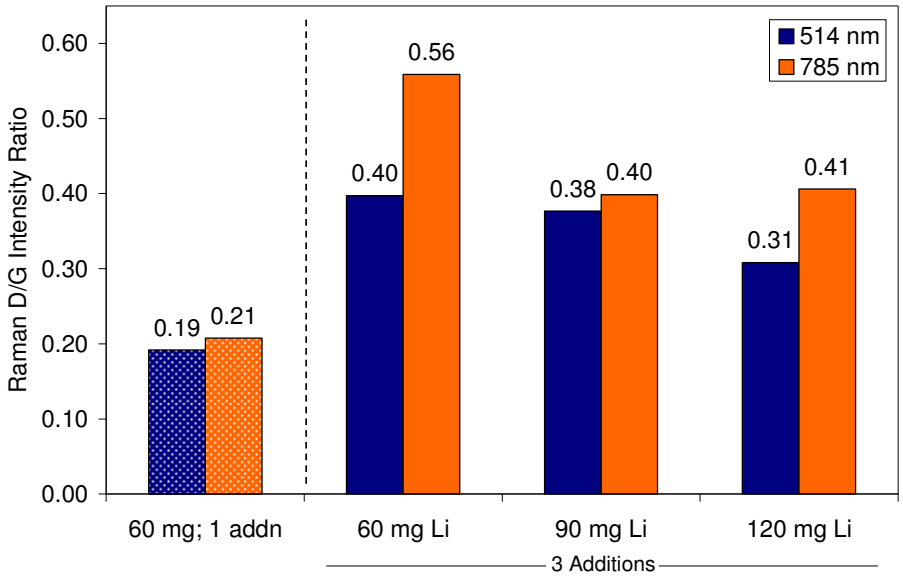

Figure 4.11: Raman I_D/I_G ratio of PS SWNT with varied Li:C ratio. For reference, the I_D/I_G was 0.09 under 514 nm laser excitation and 0.07 under 785 nm laser.

4.1.6 Effect of Solvent for Monomer Dilution

The addition of styrene/THF to stabilized SWNT in Li/NH_3, discussed in Section 4.1.2, resulted in immediate quenching of the dispersion and produced functionalized SWNT having thermal properties inconsistent with PS SWNT. Therefore, a second inert solvent was also studied in order to determine its effect on monomer polymerization. Anhydrous n-hexane was chosen to dissolve 600 µL of styrene monomer, prior to addition to the reaction flask. Figure 4.12 displays the TGA mass loss curves for both samples. The mass loss of the n-hexane sample was very similar to that of THF. The THF solvent system showed a 14.3 wt. % loss at 500°C and the n-hexane solvent system showed a 15.4 wt. % loss. In addition, as shown by Figure 4.13, the derivative mass loss curves were similar, with the THF system showing peak loss at 458.1°C and the n-hexane sample at 462.3°C. This seemed to indicate that a fundamental controlling mechanism was present when the reaction was quenched and diluted with inert solvent. Furthermore, the Raman data in Figure 4.14 showed similar degrees of sidewall modification.

Due to the low mass losses in these samples, acceptable FTIR data resolution could not be obtained from the effluent gases. Thus, samples were analyzed again with pan loading of ~5 mg; the resulting mass loss was 12.2 wt. % at 500°C for the THF solvent system and 16.6 wt. % for the n-hexane solvent system. The shape of the derivative mass loss curves matched each respective sample, as was shown by Figure 4.13. Figure 4.15 shows the high loading FTIR spectra for each system. The primary species present were aliphatic hydrocarbons, not the aromatic vibrations expected from PS; clear evidence of PS functionalization was not observed. It can be argued, however, that trace aromatic species were present. Thus, introduction of a non-reactive diluent with styrene was not an effective means for PS SWNT functionalization. Instead, evidence of alkylation or hydrogenation was observed in spite of THF's ability to stabilize the Li ions.

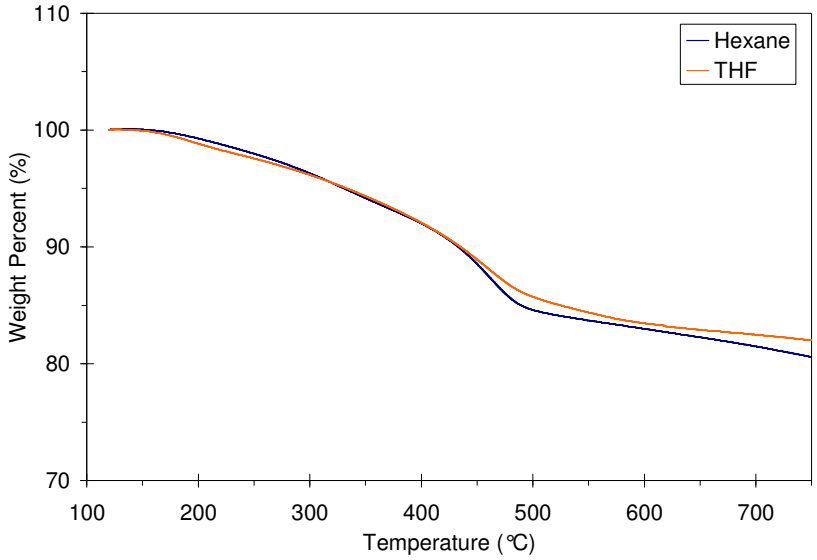

Figure 4.12: TGA mass loss curves for solvent diluted styrene systems.

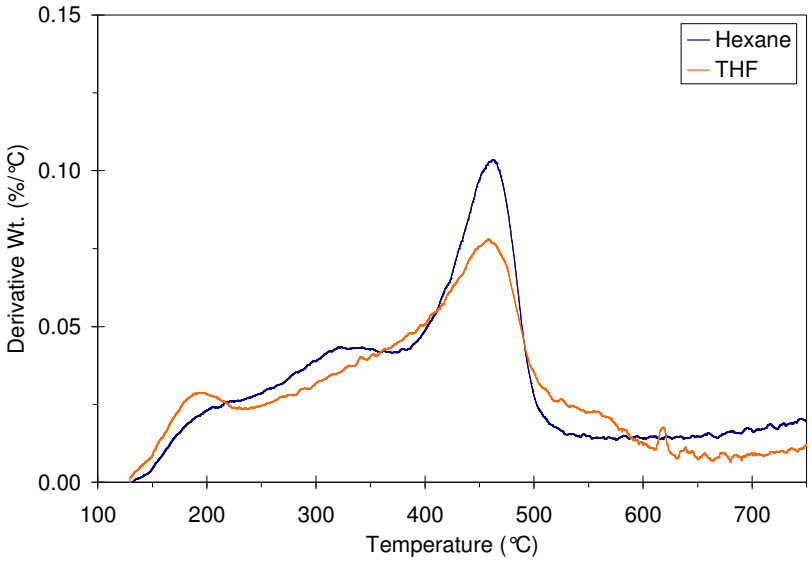

Figure 4.13: Derivative mass loss curves for solvent diluted styrene systems.

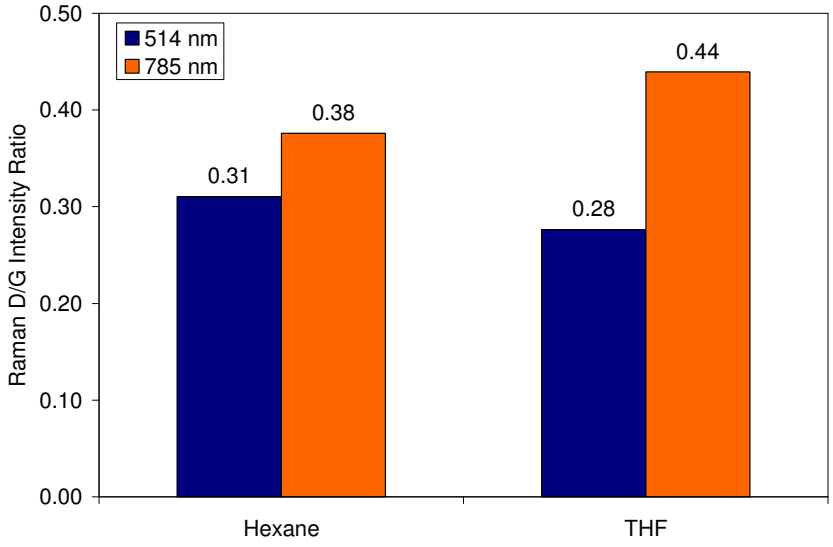

Figure 4.14: Raman I_D/I_G ratio of PS SWNT with diluent type.

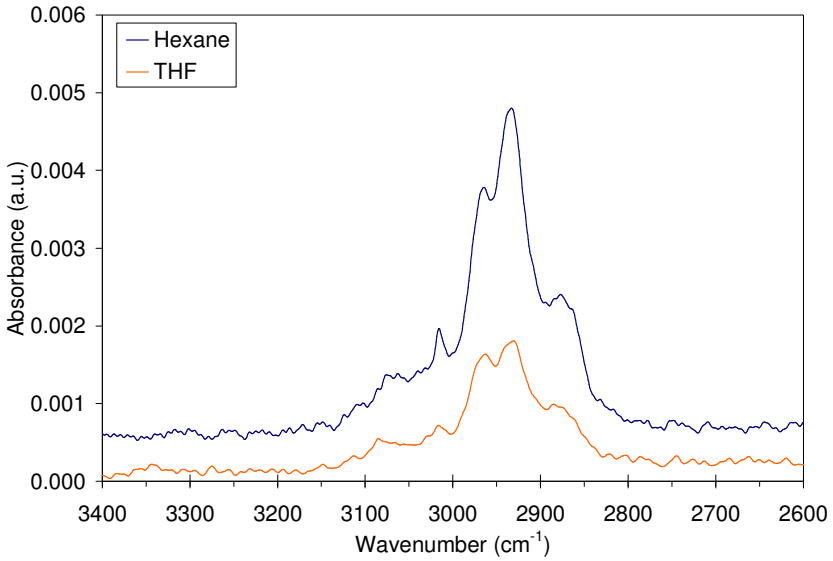

Figure 4.15: FTIR spectra of gas effluent for peak losses in THF and Hexane systems.

4.1.7 Mechanism of Styrene Polymerization

From the comparative analysis between drop-wise (single and triple) addition of styrene and the influence of diluents on the product, the most effective method mode of addition was using three styrene additions with a wait time between steps. This was based on TGA mass losses and Raman spectra of the products from various methods. Recently, the state of the art for reactions utilizing dissolving metal reduction to stabilize SWNT has moved past single-pot reactions[131,133] and the use of additional solvents to isolate excess free electron[131,135] sources have been utilized. These steps add to both the complexity of the reaction scheme and time consumed during functionalization. Their necessity, however, was required due to the inherent lack of selectivity for the strong reducing environment used to stabilize SWNT as well as limitations that SWNT reduction places on nanotube reactivity. For example, Deng et al. (2010) used product recycling to progressively tune the water solubility of functionalized SWNT by systematically increasing the extent of functionalization in order to separate SWNT based on their reactivity (diameter).[133]

Similarly, Gebhardt et al. (2011) isolated the stabilized SWNT to prevent the undesired side reaction with carbonyl compounds.[135]

It has been demonstrated that reduced SWNT will bear their maximum allowed charge density.[116,206] Meanwhile, it was also demonstrated that charge saturation limits the extent of SWNT functionalization.[133] Thus, without a method for easily tuning surface charge density,[131] due to the inherent nature of the reduced SWNT surface, re-processing is required to augment extents of functionalization. Simply stated, a reduced SWNT becomes saturated with charges and this limits the degree of functionalization in one reaction cycle. Thus, after work-up, the product can be dried and then exposed to another functionalization reaction. It would be advantageous, from a processing standpoint, to identify a reaction methodology which utilized a single-pot reaction scheme to achieve high extent of functionalization. In this research, the multiple addition steps of styrene monomer to SWNT stabilized by Li/NH_3 met these desirables. For this scheme, the SWNT were saturated with charges, but excess Li was also available. The presence of excess charges, however, immediately limited the breadth of chemistries available for processing in this manner, as shown by Chapter 3. Thus, simple chemistries that can survive the strong reducing character of the dispersion with only one possible route of functionalization are best.

The methodology outlined in this chapter, utilizing multiple addition steps of reagent to functionalize SWNT, was considered an in-situ reaction cycling method. Figure 4.16 displays the proposed scheme. One can imagine the addition of styrene to a saturated reduced SWNT dispersion will remove some charges as polymerization is initiated with monomer adjacent to the surface. Since Li was in excess, as initiation by the diffusion of charges from the surface completes, and the propagation steps consume monomer, additional free electrons can reduce the

SWNT surface again. The re-saturated SWNT surface would be identical to the starting material for a product recycled SWNT. This process repeats in a cyclic fashion after each styrene addition until all charges, and concurrently the dispersion, was quenched by termination steps. Therefore, this method can be considered an in-situ reaction cycling polymerization functionalization of SWNT.

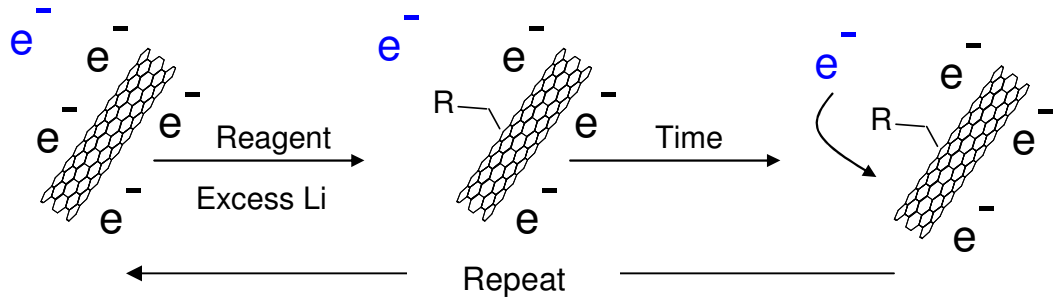

Figure 4.16: The proposed in-situ reaction cycling functionalization method. The blue electron represents an excess charge.

The nature of the interaction between Li and SWNT reduction was previously found to be not purely covalent.[116] In this model, Li was required to reside near the SWNT surface which contributes to the intercalation process. The salient point of this proposed model was that reduction and re-oxidation of SWNT was not a bond-forming process. Recent proposed functionalization mechanisms also support this idea, with reduced electrons leaving the surface to react.[131] Thus, the so called "grafting-from" polymerization mechanism can be eliminated. Furthermore, "grafting-from" the surface with a propagating radical would be expected to crosslink some SWNT. Instead, the "grafting-to" polymerization model must be realized for the polymerization of unsaturated monomers, as discussed herein. In order to further understand the possible mechanistic arguments with this approach, consider Figure 4.17. Here, a free excess solvated electron, or an electron that diffused from the SWNT surface to react, was shown attacking the vinyl bond in styrene. Based on the well studied Birch reduction mechanism,[207] the

resulting structure was proposed to be that of a radical anion $M^{-}\cdot$. A similar mechanism was responsible for charging the nanotube sidewalls upon reduction. Indeed, the addition of styrene to Na/NH_3 was shown by Buick et al. (1970) to result in the formation of monomeric styrene radical anions using electron spin resonance spectroscopy.[208] In Figure 4.17, the benzyl radical was simply shown due to its resonance stability over the alternative position, which would produce a less stable primary radical. A carbanion was shown in the adjacent position where charge had accumulated. These positions were shown simply for point of reference and may be reversed in the physical system. As described in the seminal work of Szwarc et al. (1956), the electron transfer to styrene results in styrene radical ion monomers.[209] When excess styrene monomer is added, both reactive ends can independently propagate via radical or anionic polymerization mechanisms. If the polymer chain was of sufficient length to not be repelled by the reduced SWNT surface, the radical end may terminate here. Note that this initiator has also been formalized elsewhere as a dimeric species itself such that the radical anion $M^{-}\cdot$ forms a dimeric ion radical $\cdot M\text{-}M^{-}$, which can undergo both radical and anionic propagation in the same manner.[210] Known for a short lifetime, the dimerization of the radical anions $2M^{-}\cdot$ was also expected to the distyryl anionic dimer $^{-}M\text{-}M^{-}$.[208,209] The formation of the dianionic species initiates classic "living" polymerization, which continues to completion in the presence of styrene. Accompanied by the characteristic red color of the anionic styrene ends, this polymerization will not self-terminate. Dissociation is also kinetically unfavorable.[211] Due to the lack of metallic selectivity in the PS SWNT, the incomplete styrene mass conversion to polymer by TGA, and the repulsion of the anionic ends to a saturated reduced SWNT, functionalization by this mechanism was not supported. To summarize, starting from the $M^{-}\cdot$ structure, the initiation step, three distinct possibilities can be imagined: (1) radical propagation

in one direction, (2) anionic propagation in one direction, (3) radical-radical coupling and then anionic propagation in both directions. For two of these possibilities, the electrostatic repulsion of saturated reduced SWNT provides a significant barrier between polymerization termination from the attack of the carbanion on the reduced SWNT. Thus, with the reaction of saturated and reduced SWNT, an anionic polymerization would have to be "grafted-from" the SWNT surface, a process already ruled out. Furthermore, the expected metallic SWNT selectivity for a nucleophilic addition was not observed in the PS SWNT products. From these arguments, the anionic propagation in two directions was ruled out as the functionalization mechanism. The one-dimensional anionic propagation was possible, but the radical on the opposite end would have to survive long enough for polymerization to complete before coupling to the SWNT sidewall or terminating with another radical. In other words, the chain length would have to be of sufficient length to not inhibit radical coupling with the SWNT from the anionic tail. Furthermore, in the absence of a catalyst such as potassium amide, it has been argued that the presence of ammonia retards anionic propagation.[210] The radical propagation mechanism, however, does not suffer from the repulsion effect from the reduced SWNT surface. The lack of metallic selectivity in PS SWNT supports this. Furthermore, the termination of radicals onto a SWNT surface was well known from the Billups functionalization.[100] Thus, a rational description was that polymerization and functionalization of PS SWNT occurred by a single-electron transfer or radical mechanism.

Remarkably, a fourth propagation mechanism exists, and was supported by studies of the copolymerization of styrene and methyl methacrylate.[212] Based on analysis of styrenic and methacrylic components, the copolymers formed did not match the expected composition for a standard radical (~51 % styrene expected) or anionic (>99 % methacrylate expected) mechanism.

Thus, evidence for simultaneous mixed mechanism polymerization using lithium initiator was demonstrated.[212] To explain this phenomena, O'Driscoll and Tobolsky (1958) proposed simultaneous radical propagation by the species $\cdot M\text{-}M^{-}Li^{+}$ wherein the free electron was transferred to the unoccupied π orbital of the unsaturated bond.[213] This fascinating ion-radical growth mechanism was also outlined in a later work.[214] The ion-radical species proposed can participate in propagation by either mechanism simultaneously, as previously mentioned above. In this case, however, the Li counterion was present. Note that Na in NH_3 followed the anionic mechanism, highlighting the importance of choice in metal.[214] The structure of O'Driscoll and Tobolsky was rational since due to the relatively high dielectric constant of ammonia, as compared to ethereal solvents and inert hydrocarbons, the lithium ion is well solvated. Therefore, in addition to a radical only mechanism, the dual ion-radical propagation was feasible to explain the functionalization of PS SWNT herein. Further experiments concerning the co-polymerization of styrene and methyl methacrylate may prove useful to elucidate the nature of the propagation mechanism.[212]

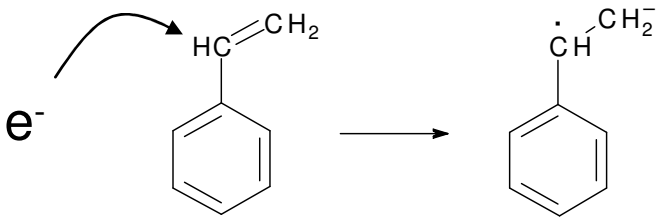

Figure 4.17: The polymerization initiation step and generation of a styrene radical anion, $M^{-}\cdot$.

Based on the discussion in Section 4.1.7, a physical description can be drawn where the polymer chain length may be controlled by the thickness of the electrostatic double layer, specifically the Debye screening length.[82] There are many unknowns which complicate estimation of the layer thickness, however. For example, calculation of the ionic strength is

challenging because the exact charge carried by the Li/NH_3 complex formed in solution and the nature of the Li counterions occupying the Stern layer is unknown. Further investigation of the correlation between double layer thickness and grafted polymer MW would be interesting.

4.1.8 Comparative Validation of Proposed Reaction Scheme Effectiveness

The proposed in-situ recycling functionalization procedure was tested against the most well studied addend in the Billups reaction scheme, a dodecyl (C12) group. The reductive alkylation was carried out under identical conditions for the PS scheme with the exception that three additions of 175 μL of 1-iododododecane were used. The Li content was 90 mg. Since C12 SWNT extract well to hexane, work-up was identical to the PS scheme. Figure 4.18 displays the TGA mass loss curve for C12 SWNT under argon and Figure 4.19 displays the corresponding derivative mass loss curves. At a temperature of 500ºC the TGA mass loss was 29.1 wt. %. Note that a second functionalization batch showed a mass loss of 29.6 wt. %, in excellent agreement. These losses indicated a high extent of functionalization for a small alkyl chain. For point of reference, a mass loss of 41 wt. % was observed for HiPco SWNT.[100] In the CG200 CoMoCAT SWNT used, however, approximately 10 wt. % of the total mass was "non-SWNT" carbon material. Thus, direct comparisons cannot be made, but these numbers converge when considering the "non-SWNT" content to be less reactive. Examining the derivative curves it appeared the mass loss consisted of two events, one at 250ºC and one at 460ºC.

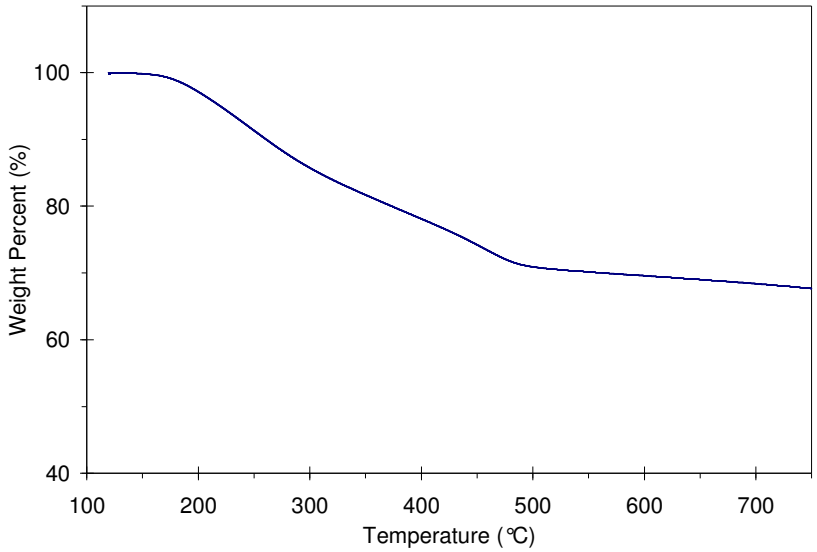

Figure 4.18: Mass loss by TGA under argon for C12 SWNT.

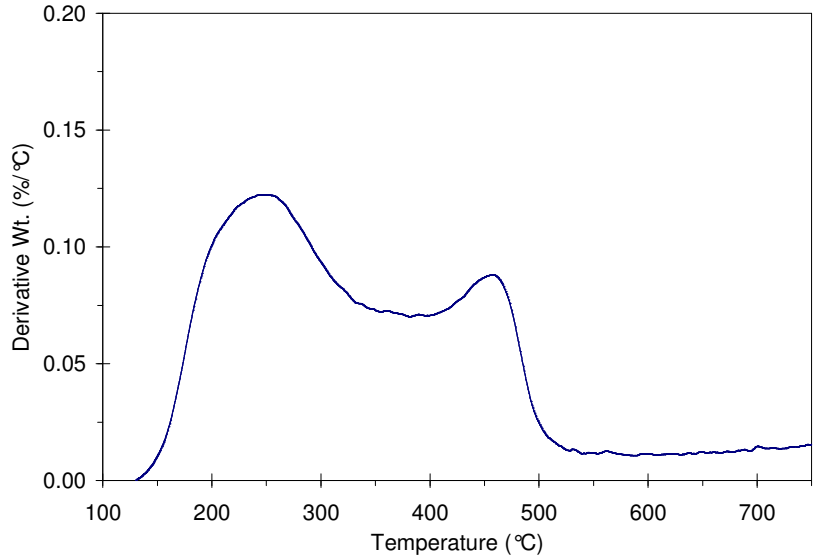

Figure 4.19: Derivative mass loss for C12 SWNT.

Identification of the evolved species was investigated via coupled FTIR analysis of the effluent gas. Figure 4.20 shows the C-H vibration region for the first mass loss peak centered at 250ºC. Examination of this region undoubtedly displays the evolution of the C12 chain addend. The next loss event at 460ºC was also probed as shown by Figure 4.21. While this is also an alkyl based subsistent, it was a high temperature for the loss for simple chain attachment. This FTIR

signature was identical to the high temperature mass loss species evolved from the THF and n-hexane diluent samples, having some small aromatic character. This seems to indicate a self-similar evolution of some species across many types of these reactions.

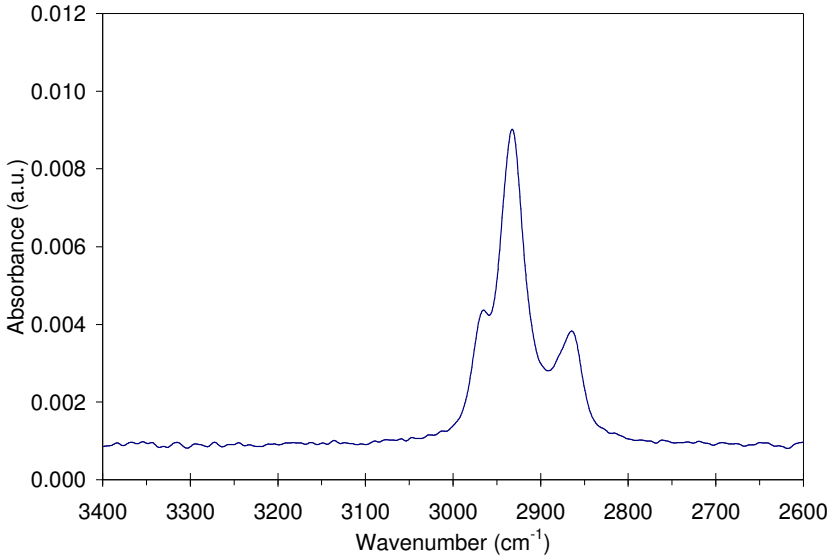

Figure 4.20: Evolution of C12 chains from SWNT by FTIR at 250ºC.

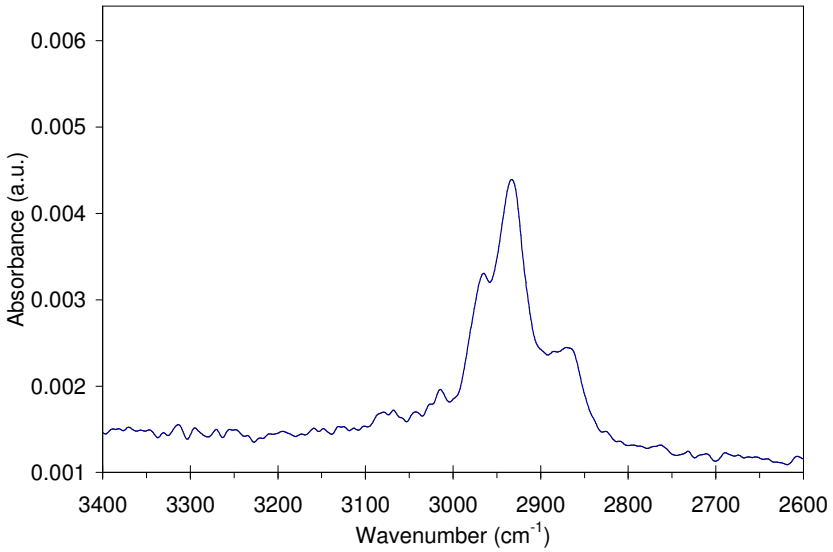

Figure 4.21: High temperature loss by FTIR for C12 SWNT at 460ºC.

The C12 SWNT was also analyzed by resonant Raman spectroscopy in order to characterize the relative extent of functionalization. The I_D/I_G Raman ratio was found to be 0.52 under 514 nm

laser excitation and 0.57 under 785 nm. This was a substantial increase from the starting material where the I_D/I_G was 0.09 under 514 nm laser excitation and 0.07 under 785 nm laser. More importantly, the Raman resonance was found to be significantly quenched in intensity, including the RBM mode, which indicated a high degree of modification. Furthermore, under 785 nm laser excitation the intensity was quenched to an extent that the baseline spectrum was readily visible. These remarkable features displayed the effectiveness of the multiple addition method. For a more complete picture supporting the high extent of functionalization, the pristine and functionalized SWNT Raman spectra were compared. Figure 4.22 displays the 514 nm Raman spectra and Figure 4.23 displays the spectra under 785 nm laser excitation. The relative decrease in spectral intensity brought on by the functionalization was readily apparent.

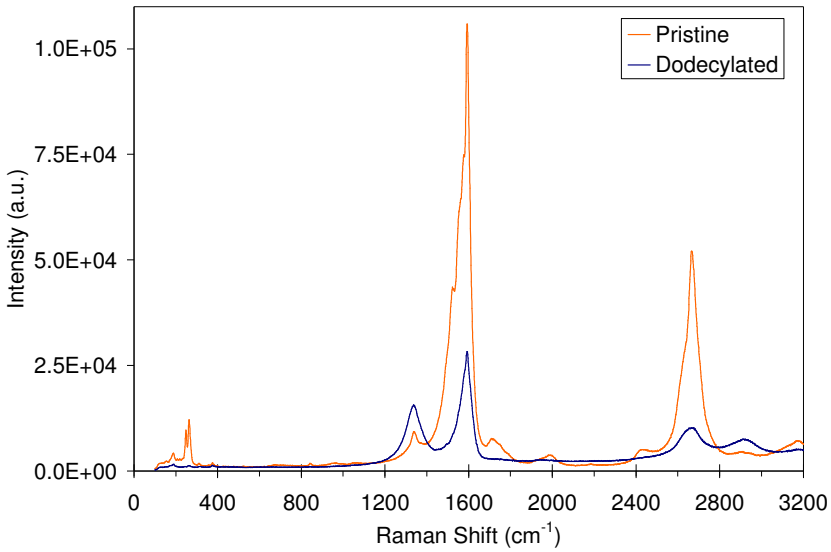

Figure 4.22: Raman spectrum of C12 SWNT under 514 nm laser.

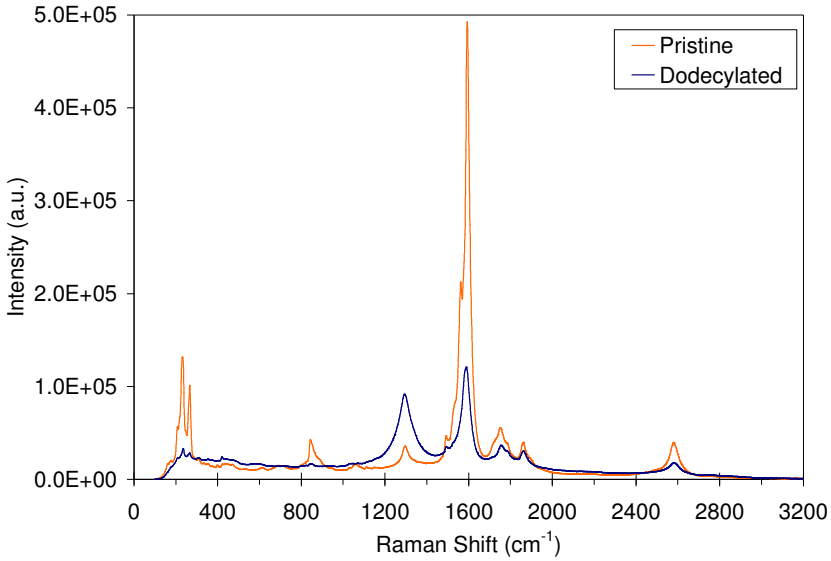

Figure 4.23: Raman spectrum of C12 SWNT under 785 nm laser.

4.1.9 Comparison to PMMA SWNT

The functionalization of SWNT with PMMA under Billups conditions was studied for HiPco SWNT by Liang et al. (2006).[148] In that work, the Li: C molar ratio was 0.9 and 3.2 g (32 mmol) of methyl methacrylate was added in a single addition. A detailed work-up was not given by the authors; only filtration and washing the buckypaper with solvents were used. An experiment was carried out to determine the viability of the cycling addition method developed herein to that of the PMMA work done with HiPco SWNT, as well as to determine if comparisons can be made between the two studies. Three 200 µL additions of methyl methacrylate were used. The product, not surprisingly, would not extract into hexane due to the nature of the saturated polyester chains attached. Thus, the sample was simply was washed with repeated dispersion and filtration cycles in various solvents. Due to the low efficiency of this washing method, residual Li remained in the sample. Nevertheless the sample was characterized by TGA-FTR analysis. As shown by Figure 4.24, the mass loss from PMMA SWNT was determined to be 22.1 wt. % at 500ºC. This number was not representative of the true relative concentration of the

species evolved since the residual mass after oxidation was 18.03 wt. %. The residual mass from SWNT should be ~8 wt. % or less due to CoMo catalyst. Adjusting the mass loss, the PMMA content was ~24.5 wt. %. Two loss events were observed in the derivative mass loss curve. The first at 370ºC was determined to be from PMMA as shown by the FTIR spectra of the gas effluent in Figure 4.25. This temperature is in agreement with the range found for PMMA HiPco SWNT previously. The next at 460ºC was again attributed to hydrogenation/alkylation during work-up. According to Figure 4.26, aliphatic hydrocarbons at ~3000 cm^{-1} are present as well as the ubiquitous carbon oxides at ~2400 cm^{-1}. The features at ~1750 cm^{-1} and ~1730 cm^{-1} are carbonyl vibrations of an ester functional group, confirming the PMMA presence. The aliphatic C-H vibrations likely originated from the terminal methyl group of the pendant ester containing groups or the methyl group of the adjacently attached to the polymer backbone. Raman spectroscopy revealed I_D/I_G to be 0.23 under 785 nm laser and 0.31 under 514 nm. The I_D/I_G for the starting material was 0.09 under 514 nm laser excitation and 0.07 under 785 nm laser. Thus, PMMA SWNT could be produced by the functionalization procedure developed in this work.

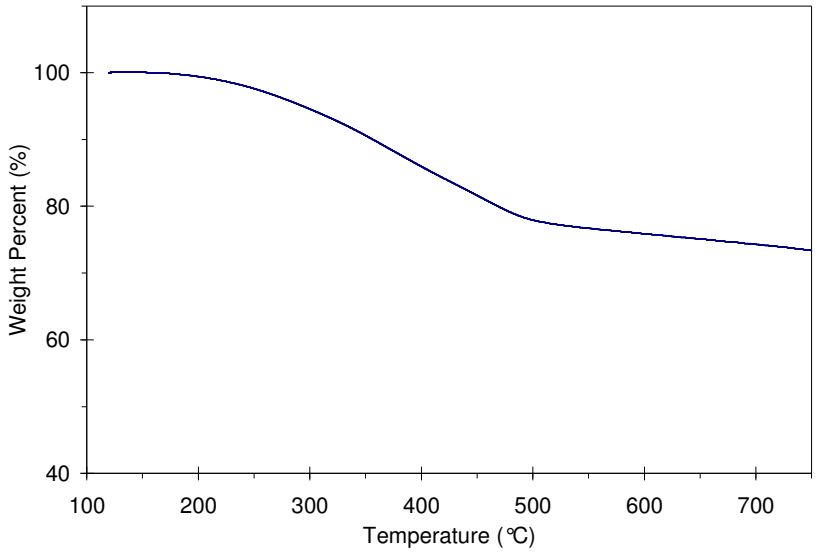

Figure 4.24: TGA mass loss from PMMA SWNT under argon.

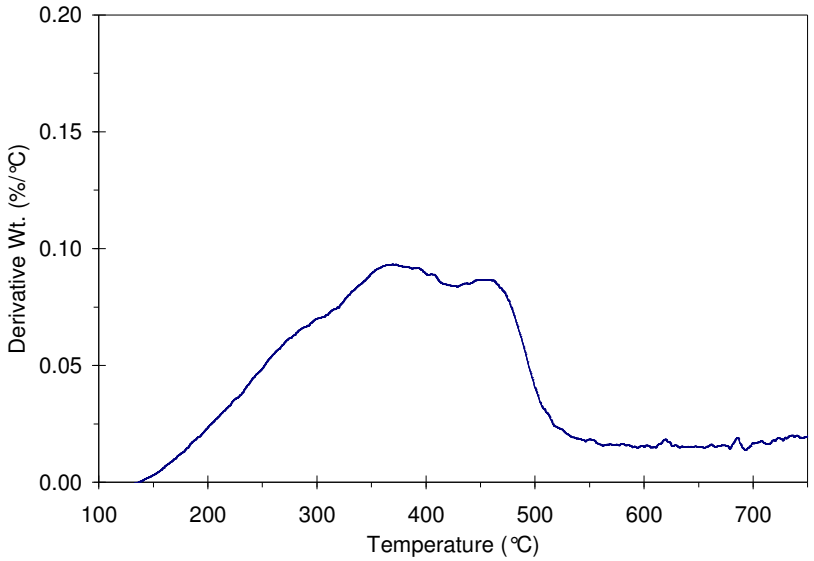

Figure 4.25: Derivative TGA mass loss from PMMA SWNT under argon.

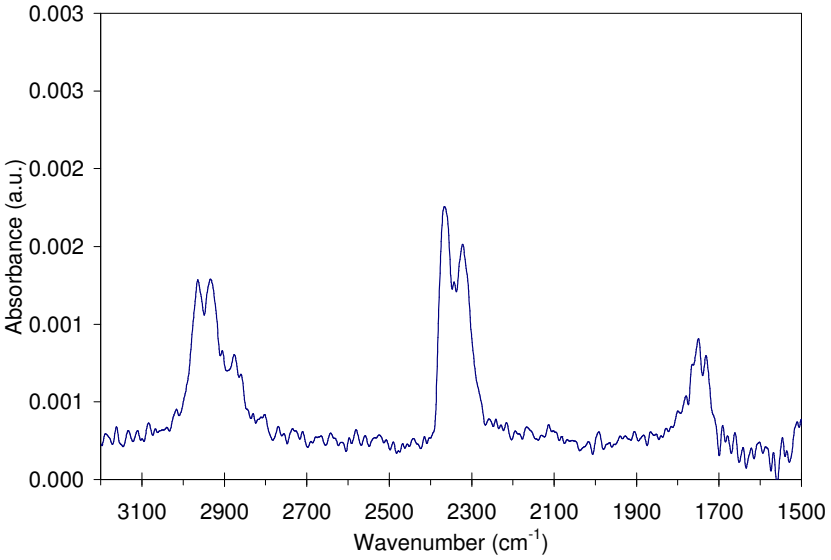

Figure 4.26: FTIR spectra of PMMA SWNT.

4.2 Dispersibility of PS SWNT

In order to gauge the feasibility of using the PS SWNT produced herein for nanocomposite applications the dispersibility of PS SWNT into UPR was characterized. Qualitative comparisons of the dispersion state were made between PS SWNT and a dispersion of pristine SWNT into UPR by high shear mixing. A quantitative comparison was made by measuring the

rheological properties of the two dispersions using controlled strain linear viscoelastic measurements. The dispersibility results provided useful insights to guide future PS SWNT functionalization experiments.

4.2.1 Dispersion of PS SWNT in UPR

To test the dispersibility of PS SWNT in UPR, PS SWNT were shear mixed for 72 hr after 24 hr of high stress, low shear rate mixing (see Appendix A1). Figure 4.27 displays the comparison between 100 ppm (by volume) dispersions of pristine CG200 starting material and the PS SWNT using transmission optical microscopy. Samples were dispersed at 100 ppm by volume assuming an intrinsic SWNT specific gravity of 1.45. For the PS SWNT, the residual mass at 500°C was obtained from TGA mass loss in argon and the appropriate mass of functionalized SWNT was calculated, based on adjusting for PS content. The dispersibility of the functionalized PS SWNT was surprisingly worse than the starting material. For example, two large aggregates, having a diameter of approximately 10 - 15 μm, were observed in the PS SWNT dispersion (Figure 4.27) whereas no aggregates of this scale were visible in the dispersion of CG200 starting material. This suggests two possible effects were observed: (1) the apparent incompatibility of PS functional groups with UPR or (2) aggregates produced during processing. Based on the observed swelling and dissolution of 180,000 g/mol PS pellets in UPR, the observed aggregation appeared to be a result of processing. Specifically, the effect of PS chain length appeared to be of insufficient length to overcome the liquid phase functionalization processing and drying steps. Therefore, future studies using PS SWNT for UPR dispersion should investigate the effect of an additional number, or increased volume, of styrene monomer additions during functionalization.

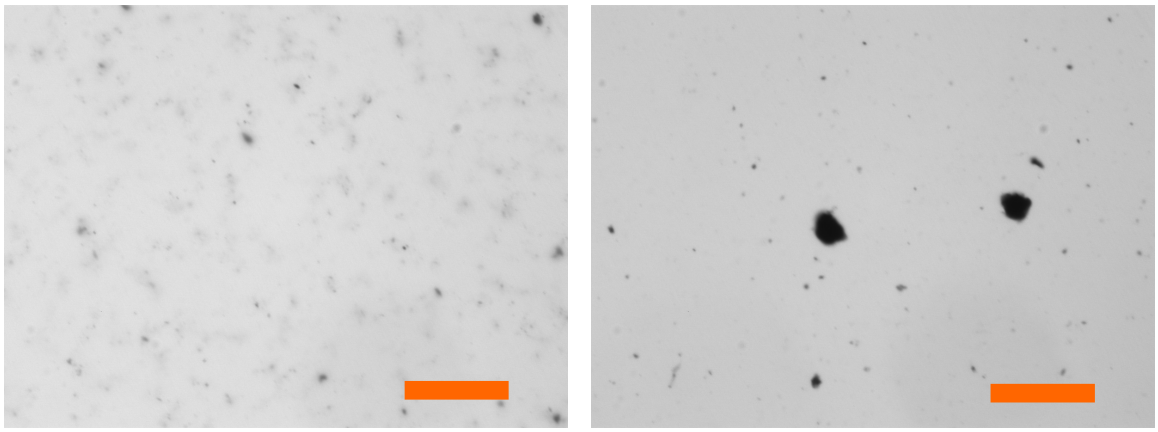

Figure 4.27: SWNT dispersion at 100 ppmv in UPR via high shear mixing protocol of (left) pristine CG200 SWNT and (right) PS SWNT [60 mg Li and three 200 μL styrene additions]. Samples were imaged through a cover slip using a 20x objective with 2x magnification in from of digital camera (40x total magnification). Scale bars were 50 μm in length.

Dispersions were also characterized by small strain oscillatory shear measurements carried out in the linear viscoelastic regime. A 50 mm cone and plate rheometer operating in controlled strain mode was used to measure complex viscosity and modulus for each sample at 20°C. Figure 4.28 displays the complex viscosity as a function of angular frequency for each sample. The inclusion of PS SWNT increased the neat UPR viscosity from 1.7 to 2.2 Pa-s and displayed Newtonian-like behavior over all shear rates. Conversely, after the inclusion of pristine CG200 SWNT, the sample showed shear thinning behavior. This was attributed to the increased dispersion state observed in the optical micrographs. Figure 4.29 displays the corresponding storage modulus G' over the experimental range of shear rates. A dramatic difference can be seen between the two samples. Indeed, the PS SWNT sample appears to be Newtonian with a very low and nearly immeasurable G', showing properties similar to the neat UPR. Examining G' for the CG200 sample, the effect of the inclusion of SWNT was observed. Again, these effects were attributed to the improved dispersion state of CG200 SWNT. Although small

clusters exist, the complex viscosity was modified by the presence of the CG200 SWNT in a slightly non-Newtonian fashion, manifested via the storage modulus of the fluid.

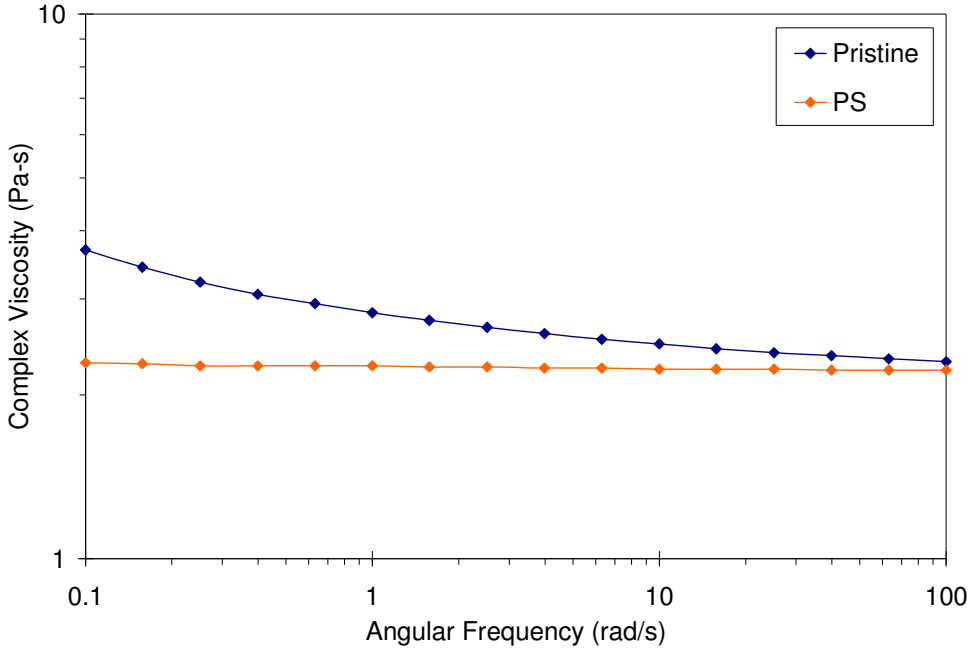

Figure 4.28: Complex viscosity of SWNT dispersions in UPR under small strain (5 %) oscillatory shear. All sample concentrations at 100 ppmv.

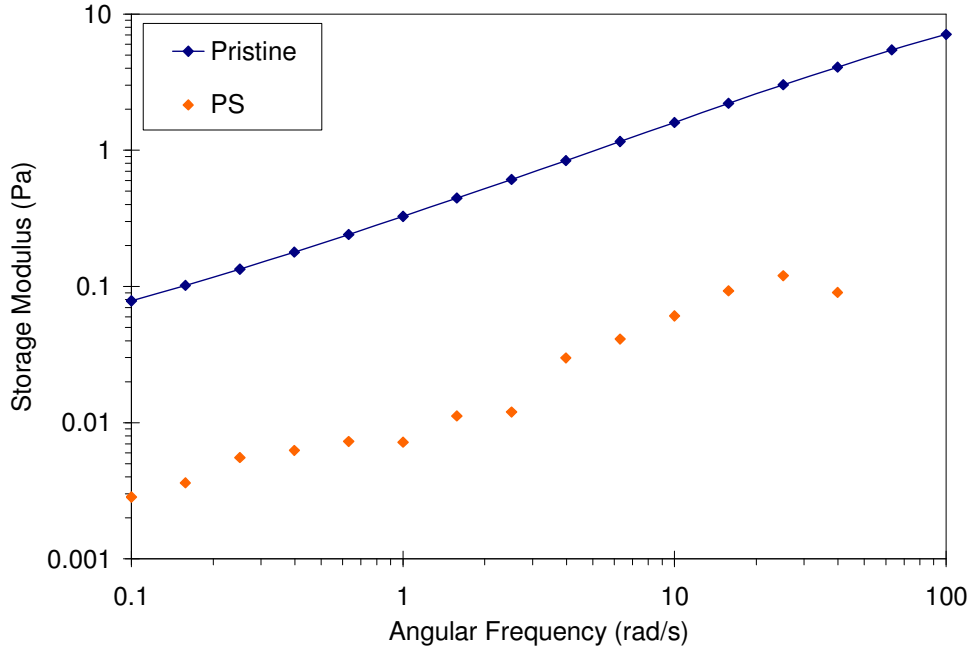

Figure 4.29: Linear viscoelastic response of SWNT dispersions in UPR under small strain (5 %) oscillatory shear. All sample concentrations at 100 ppmv.

4.3 Detection and Removal of Reaction Contaminants

The unexpected generation of contaminants in a functionalization reaction can have detrimental effects on the interpretation of experimental data. For example, if the contaminant has a similar thermal degradation behavior to the functionalized SWNT, a misinterpretation of TGA mass loss data will result in over estimation of the degree of functionalization. Therefore, it is important to use redundant measurements when exploring new experimental procedures to identify these artifacts. One such example illustrating this point was the contamination of certain PS SWNT reactions with fluoropolymer. The detection of this contaminant and mitigation of its influence are discussed below.

4.3.1 Contamination of Products with PTFE

Throughout the PS SWNT experiments, a recurring problem was product contamination with PTFE flakes and residues. It has been shown that Li/NH_3 attacks and reduces PTFE to high density polyethylene and carbonizes the PTFE surface.[215] In addition, this change was well known to occur experimentally, as the white PTFE stir bar turns black after even one reaction using Li/NH_3. It was noteworthy that in past experiments there were no signs of contamination, even with many repeated reaction cycles using the same stir bar. In fact approximately six years of in-house experiments were without incident until recently. This raised concern that some material was not performing up to the same specification previously expected. Since Li and NH_3 typically last for years at a time these reagents were ruled out. On the other hand, the other reagents used for functionalization such as alkyl halides were also often changed often due to purchasing in small volumes. So, it was unlikely that this problem would not have appeared until now if due to these materials. The final component was the PTFE coated magnetic stir bar itself. Interestingly, the in-house supplier of stir bars recently changed from Fisher Scientific to

VWR. In order to determine any differences between suppliers, ATR-FTIR spectra were obtained by pressing each polymer against a diamond crystal. As displayed by Figure 4.30, the spectra were remarkably similar with the exception of the appearance of peaks at 1449.3 cm^{-1} and 876.5 cm^{-1} in the Fisher sourced fluoropolymer. The peak at 1449.3 cm^{-1} was assigned to CH_2 deformation and the peak at 876.5 cm^{-1} was assigned to CH_2 rocking. According to Socrates (2004), these bands occur in dangling -CH_2F,[203] however attributing these peaks to the presence of a common ethylene tetrafluoroethylene fluoropolymer was more plausible. The peak found in both samples at 1201 cm^{-1} was assigned to the asymmetrical CF_2 stretching mode. Likewise, the shared peak at 1146 cm^{-1} was assigned to the CF_2 symmetrical stretch.[216] These two bands were expected for aliphatic difluorinated compounds.[203] Based on the experimental evidence, the presence of these additional functional groups helps prevent chemical attack by the Li/NH_3 reducing environment on PTFE based resins.

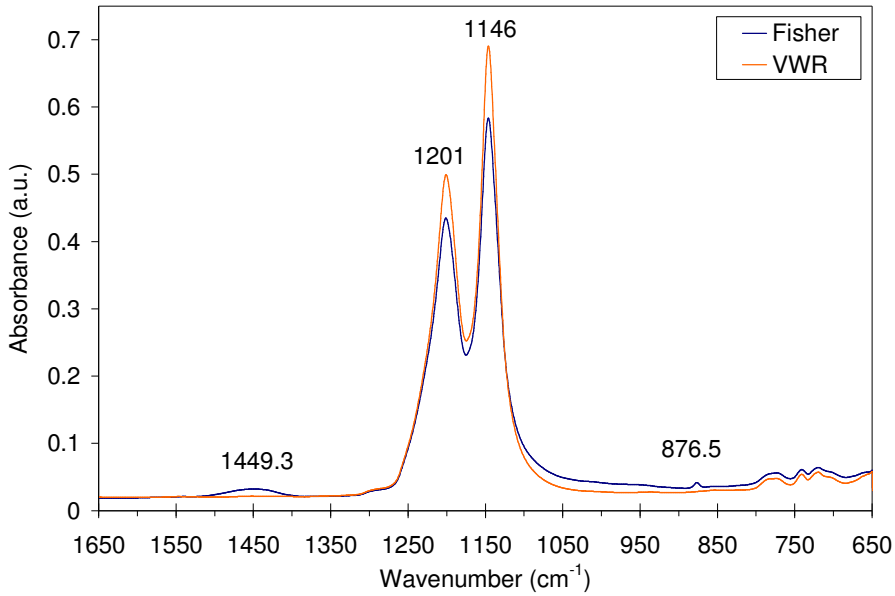

Figure 4.30: ATR-FTIR spectra of PTFE sources.

4.3.2 Separation of PTFE and PS SWNT by Flotation

The separation of PTFE contamination from the functionalized SWNT should be possible for a physical mixture of the two components. The density of SWNT, PS, and PTFE are ~1.45 g/mL, ~1.05 g/mL, and ~2.20 g/mL, respectively. It can be calculated that the density of a PS functionalized SWNT would be less than pure SWNT based on mixing rules. Realistically, the density of PS SWNT was considered to be much less given the coiled nature of polymer tethered chains and potential void volume. Nevertheless, the nature of the interaction between PTFE and any solvent must also be considered. Based on density alone, the PTFE should separate during the repeated extraction cycles of work-up by sinking to the bottom of the funnel in aqueous steps. Since water will not wet the PTFE surface, however, air appears to be entrapped at the interface and as a result, the denser PTFE actually floats in water. Furthermore, within an immiscible water/hexane system, PTFE prefers the interface either due to hexane's relatively low density of 0.655 g/mL (n-hexane isomer) or thermodynamic considerations of said interface. Thus, PTFE contamination was not removed during typical work-up. It was noteworthy that during filtration steps, PTFE flakes were visible at the top of the buckypaper and did not appear to even be entrapped in the fiber network. Based off these observations a post-work-up treatment was examined where dry contaminated SWNT was dispersed in water by bath sonication, sedimented, and decanted repeatedly. Since water alone will not wet the PTFE or PS SWNT, a drop of water miscible, low density, organic solvent must be added. Since acetone (0.791 g/mL) has a higher vapor pressure than ethanol (0.789 g/mL), it was preferred. PTFE rich supernatant phases were discarded and the PS SWNT rich sediment was collected using a pipette from the bottom of vials. The flotation separated product was isolated by dropping separated sample on the center of a 0.2 μm PTFE coated filter paper, pre-wet with ethanol, and scraping

the sample to a clean vial for vacuum drying. Figure 4.31 displays the TGA mass loss curves for each sample. The PS loss in the starting material was barely visible due to the large fraction of PTFE present. This also made detection by coupled FTIR difficult at low pan weight loading. Examining the sample separated by flotation, a dramatic change can be seen in the high temperature residual mass. This was attributed to removal of PTFE. To ensure that both species were self similar the relative amount of PS was calculated before and after treatment. By inspection it appears the starting material consisted of ~14 wt. % PS, ~41 wt. % PTFE, and 45 wt. % SWNT/catalyst. Scaled with respect to SWNT there was ~23 wt. % PS in starting material. After separation, the sample consisted of 20 wt. % PS, ~12 wt. % PTFE, and 68 wt. % SWNT/catalyst. This amounted to a relative PS concentration of ~22 wt. %. Thus, the flotation treatment did not remove functional groups/polymer and both samples were consistent.

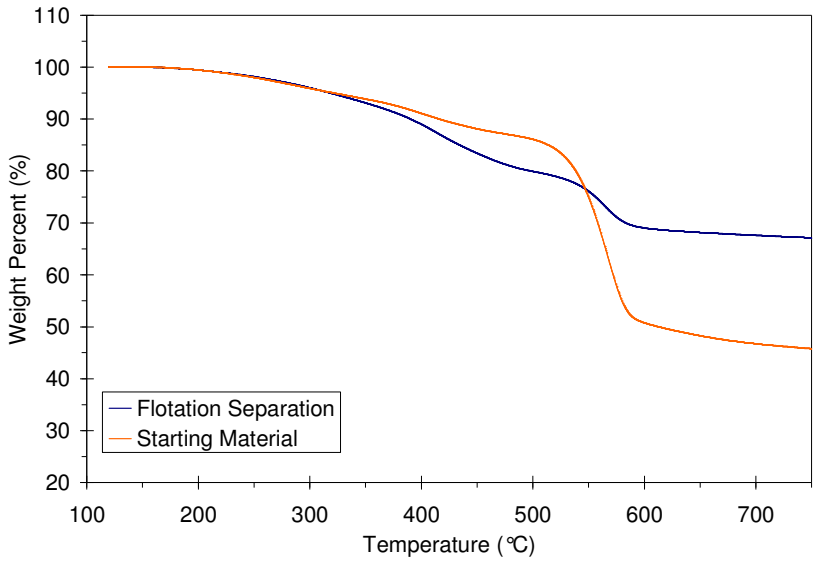

Figure 4.31: Effectiveness of PTFE flotation separation by TGA.

A clearer picture of mass loss events can be seen by examining the derivative mass loss curves. Figure 4.32 displays the derivative weight loss percentage with temperature for both samples. The starting material shows PS degradation at ~401°C followed by PTFE removal at 567.7°C.

Based off the magnitude of the curve it was clear that the PTFE step loss dominated the spectrum. After flotation separation, the step losses occur at ~413°C for PS and 564.3°C for PTFE. While the degradation temperature for PTFE was similar between the samples, the loss for PS differed considerably by ~12°C. The source of this up-shift may have been a result of removal of carbonized PTFE by the washing steps.

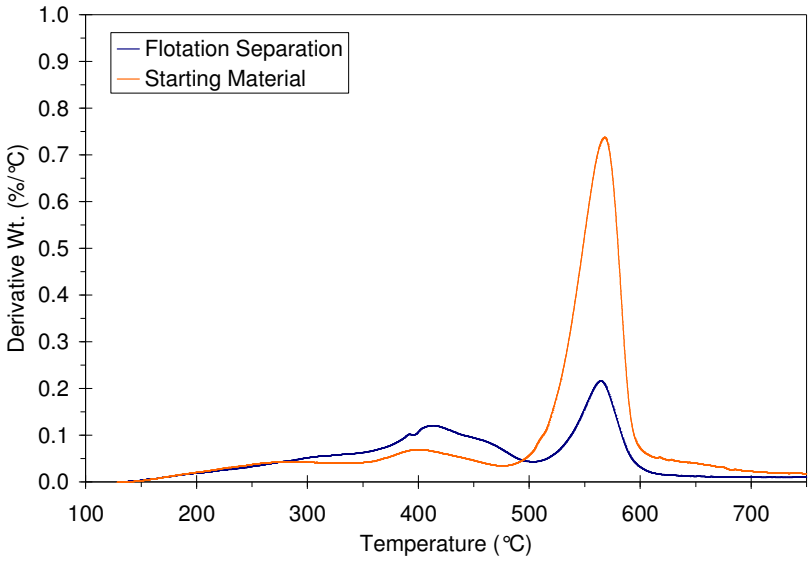

Figure 4.32: Derivative mass loss curves for flotation separation of PTFE.

Identification of the specific components was be achieved by examining the gaseous FTIR spectra during peak mass loss events. Figure 4.33 displays the C-H region of the FTIR spectrum for the flotation separated sample at ~401°C. Note, in the starting material the relative mass percentage of PS was too small to be observed. In spite of still low relative concentration, clearly, aromatic C-H vibrations (> 3000 cm^{-1}) were observed and match the expected spectrum of PS SWNT. Figure 4.34 shows the next mass loss event at 567.7°C having a spectrum matching that for thermal degradation of PTFE. Based on FTIR spectra no two polymer species were lost at the same temperature.

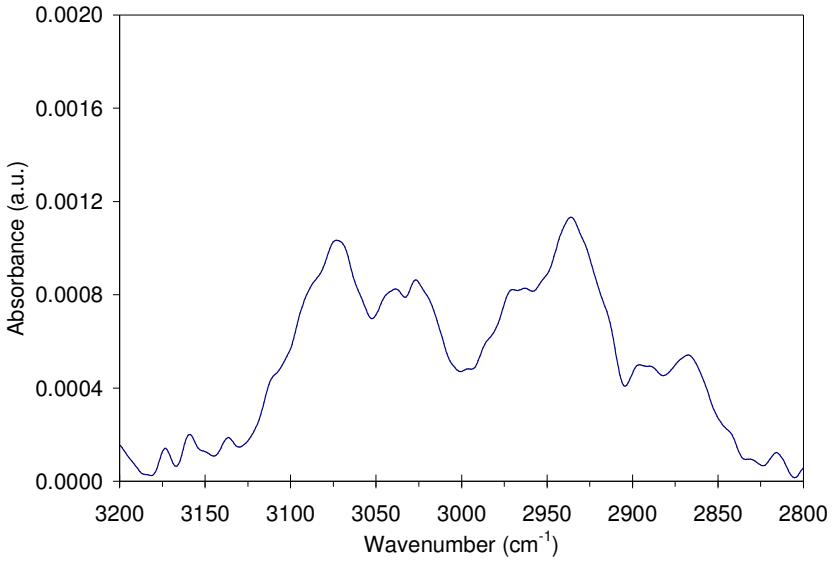

Figure 4.33: Gaseous FTIR spectra of flotation separated sample, ~401°C.

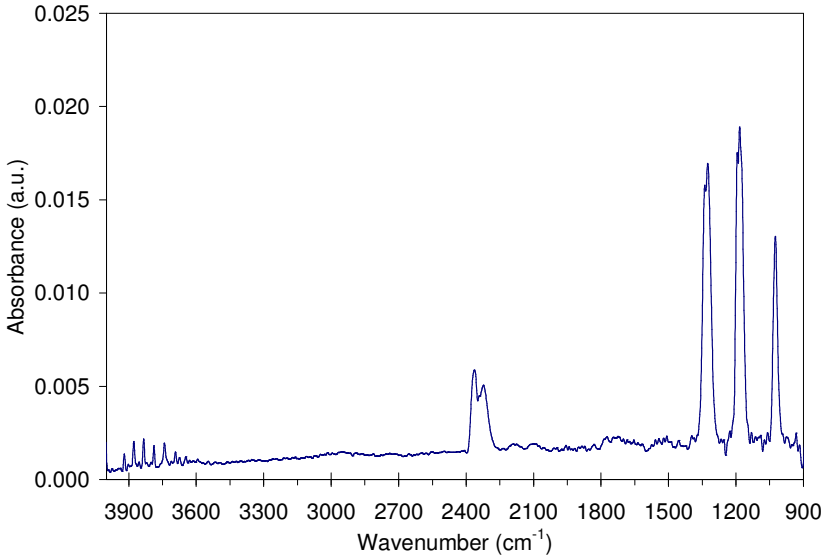

Figure 4.34: Gaseous FTIR spectra of flotation separated sample, 567.7°C.

In summary, it appeared that PTFE separation by the flotation procedure is a potential means to sort contaminated material. It was also shown that further separation cycles are needed for complete removal. The procedure shown herein was suitable for enhancing step losses in the TGA spectrum which helps extract meaningful data regarding the functionalization of SWNT from an otherwise useless sample. Unfortunately, when PTFE contamination was present, it was

unknown how much Li/solvated electrons were unavailable to reduce SWNT due to attack on the fluoropolymer. Thus, data gathered on the functionalization of SWNT in the presence of PTFE contamination cannot be included within analysis of pure PS SWNT samples. Glass coated stir bars and a customized round-bottom flask with a flat bottom area slightly larger than the size of the stir bar (to prevent shattering) was recommended for future work.

4.4 Conclusions

SWNT were successfully functionalized with polystyrene by addition of styrene monomer to stable a dispersion of SWNT in Li/NH_3. This was confirmed by coupled TGA-FTIR analysis, ATR-FTIR spectroscopy, SEM imaging, and UV-vis spectroscopy. Based on various means of monomer addition, an in-situ reaction cycling polymerization functionalization was found to be ideal. The effectiveness of this method was characterized by the reductive alkylation of SWNT with dodecyl chains. Theoretical arguments were made regarding the nature of the radical polymerization mechanism versus other methods based on the observed reactivity of SWNT and electrostatic considerations. Raman spectroscopy showed a high degree of functionalization and quenched resonance intensity indicating heavy functionalization, confirming the effectiveness of the method. UV-vis absorbance was in agreement with Raman showing quenched optical transitions for PS SWNT. In addition, SEM analysis revealed no evidence of free PS or over-coating, indicating work-up was thorough and the SWNT were functionalized rather than simply over-coated. Finally, this method was tested with methyl methacrylate monomer and resulted in polymethylmethacrylate by TGA-FTIR analysis.

The stabilization of SWNT throughout the reaction addition steps was found to be sensitive to the amount of Li metal present. In the presence of too little Li, the reaction/dispersion quenched.

An optimum amount of Li of approximately 90 mg was required for the reaction to progress through all three monomer additions and remain stable until ammonia evaporation.

Dilution of the monomer in non-reactive solvents prior to addition to the reactor results in fast quenching and little to no polymerization. FTIR and Raman show evidence of alkylation or hydrogenation.

Contamination of the reaction with PTFE residues was determined to originate from the stir bar. FTIR analysis of source materials showed that the fluoropolymer composition varied between manufacturers resulting in different chemical stabilities in Li/NH_3. A separation of a contaminated sample by simple flotation in water was effective and showed this to be a physical mixture. Unfortunately, data analysis of a contained sample was uncertain due to Li being consumed by the degradation reactions.

Finally, the identification of a single-pot functionalization methodology that was capable of achieving high degrees of functionalization was an important result in advancing the potential applicability of functionalized SWNT in new nanocomposite technologies. This method reduces time and cost over product recycling strategies by overcoming limitations introduced by saturated reduced SWNT. The general applicability of this procedure towards many unsaturated monomers offers exciting potential applications.

Chapter 5

Functionalization by Sidewall Esterification

5.1 Sidewall Esterification of SWNT via the Bingel Reaction

The direct functionalization of SWNT with ester functionalities was not possible using Billups based reaction conditions or organometallic reduction based routes. This was a result of the strong reducing environment necessary to disperse the SWNT also attacking the desired addend. In order to facilitate the attachment of ester functional groups to SWNT, other routes were explored for compatibilization. The Bingel reaction was selected for this functionalization, utilizing SWNT dispersion in 1,2-dichlorobenzene by bath sonication. The motivation for this functionalization strategy was to increase the chemical compatibility of SWNT with UPR as well as provide interruption from close inter-tube contacts. While the seminal work discussing the Bingel reaction on SWNT was highly cited,[153] no studies exist discussing the effects of processing on this material. By focusing on the characterization of fundamental product properties, the effect of desired and/or undesired changes could be deconvoluted and the effect on bulk dispersibility better understood.

5.1.1 Bingel Reaction on SWNT

Based on the seminal work of Carsten Bingel (1993) regarding the cycloproponation of fullerenes, the Bingel reaction has been adapted for SWNT.[150] Unfortunately, studies on SWNT are limited to a few cases and no reports on CoMoCAT SWNT exist. What is known, however,

is that issues arise from nanotube sonication and the formation of an undesired sonopolymer. Figure 5.1 displays the reaction scheme for generating the initial SWNT dispersion for the Bingel reaction. The exclusion of moisture was essential to avoid a side reaction with the base, therefore a 3-neck 100 mL flask, as well as the required mass of SWNT, were vacuum dried at 120°C overnight and cooled under vacuum. After the center port was plugged, an inlet of dry ultra-high purity argon was connected to one side port and vacuum was pulled through the other. Note that all glassware was soaked overnight in a 1M KOH solution in 75 vol. % mixed alcohols before use. The set-up was flame dried and cooled three times before purging with dry argon and exchanging the outlet line from vacuum to a mineral oil bubbler. Dry SWNT (5 - 15 mg) was added through the gently flowing argon atmosphere via an open exhaust port, and after closing, the contents of the flask were purged for 45 min. SWNT were then bath sonicated after addition of 50 mL anhydrous 1,2-dichlorobenzene (oDCB), under constant purge of dry argon. The bath sonicator was placed to maximize internal surface agitation. As shown by Figure 5.1, in addition to generating exfoliated SWNT, the sonication of oDCB decomposes the solvent by evolution of chlorine and hydrogen chloride, along with sonopolymerization to a polyphenyl sonopolymer (SP). During functionalization, the generated gases were continuously purged by the argon flow through the mineral oil bubbler. Once a satisfactory initial dispersion was generated, reagents were added to the reactor. This step was necessary because, in contrast to reactions involving the reduction of SWNT, only surfaces exposed by sonication will be able to react. The reaction scheme in Figure 5.2 displays the addition of diethyl bromomalonate and the base 1,8-diazobicyclo[5.4.0]undecene (DBU) with continuous bath sonication for a predetermined amount of time. DBU was stored over activated molecular sieves. The addition of DBU was thought necessary to abstract hydrogen from the halocarbon position, generating an

anion which then attacks the SWNT sidewall. After work-up (see Appendix A.1), the final product contained functionalized SWNT and SP.

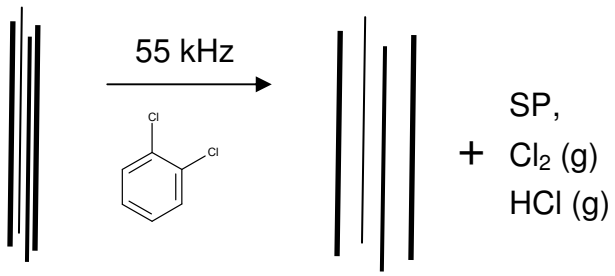

Figure 5.1: Initial dispersion of SWNT in oDCB by sonication.

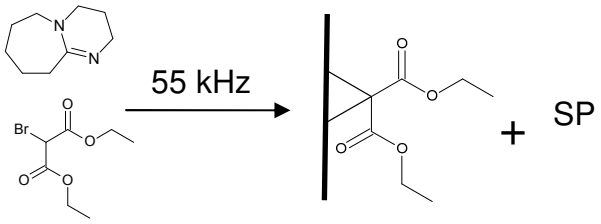

Figure 5.2: Bingel reaction scheme for dispersed SWNT.

5.1.2 Characterization of CoMoCAT SWNT

A detailed understanding of the thermal stability of pristine CG200 SWNT was required to interpret and analyze the effects of Bingel functionalization. Figure 5.3 displays the TGA mass loss curves for the starting SWNT material under both air (oxidation) and argon (pyrolysis). Under argon, the mass loss at 500°C was only measured to be 3.7 wt. %. As displayed by Figure 5.4, the derivative mass loss curve is free of any thermal events. The upswing at 750°C was an artifact generated by the TGA controller ramp rate slowing. This slight loss over the entire temperature range was attributed to the slow removal of amorphous carbons. Conversely, when SWNT were oxidized, the mass loss curve was quite complex. Examining the derivative mass loss shows a prominent peak centered at 488°C and a smaller tail at ~550°C. The first mass loss was attributed to SWNT and the second was described by the manufacturer to be the result of

"non-SWNT" carbons, which was investigated in subsequent sections. A unique feature for CoMoCAT SWNT was the high temperature change to the catalyst. It was hypothesized that this was loss of surface oxides and/or sintering. This event was observed as the derivative peak centered at 700°C. As a result of this loss, the residual catalyst was measured at a temperature of 625°C for all CoMoCAT SWNT. For CG200, this was measured to be ~8 wt. %. The final high temperature residual mass was ~2.6 wt. %. Note that other preparations of SWNT, such as the HiPco process, only have one characteristic mass loss curve for SWNT oxidation.

Raman spectroscopy on the oven dried and cooled as-received SWNT showed a I_D/I_G intensity ratio of 0.09 ($\sigma = 0.006$) under 514 nm laser excitation and 0.07 ($\sigma = 0.011$) under 785 nm excitation.

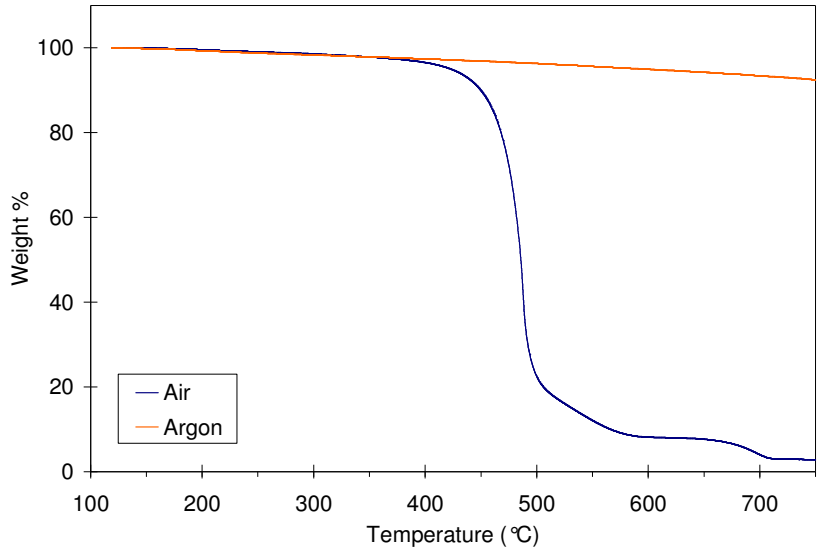

Figure 5.3: TGA mass loss curves for CG200 in air and argon.

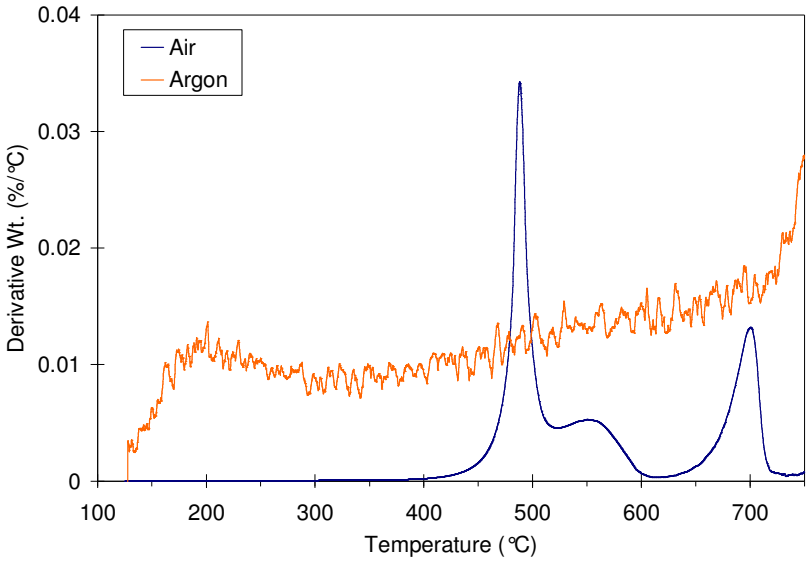

Figure 5.4: TGA derivative mass loss curves for CG200 in air and argon.

5.1.3 Product Mass Balance

Thermal characterization of the SWNT and SP product resulting from sonication in oDCB has not been carried out in the literature. Working with the dry product revealed a surprisingly noticeable increase in bulk density while weighing. In order to determine the relative components in the product, a control experiment was carried out. A SWNT sample of 5.2 mg was reacted with 166 µL diethyl bromomalonate (32 µL/mg SWNT) and 260 µL DBU (50 µL/mg SWNT) for 12 h of sonication time. After work-up, the product was vacuum dried and weighed. The final mass was found to be ~17 mg, a substantial increase in the initial SWNT mass. From these masses, the relative amount of SP and functional groups in the product was found to be 70 wt. %, with respect to the SWNT mass. Considering the well known low extent of functionalization for the Bingel reaction, this mass increase consisted of a substantial amount of SP by-product. It was noteworthy that 70 wt. % was considered a lower bound only since it was likely some sample was lost during the many repeated ethanol dispersion and filtration steps during work-up. Thus, a slightly greater amount of SP was expected in the true measurement of

relative mass content. Figure 5.5 shows TGA mass loss curves for this sample under argon. Continuous low temperature mass losses (> 200°C) were observed and believed to be a combination of SP and SWNT degradation product. A high temperature mass loss peak was found at ~441°C. This peak was also found in many processed/modified samples, as was shown in Chapter 3. Intermediate losses, as shown by the FTIR spectrum in Figure 5.6, were a complex combination of both SP and functional groups. The quantized HCl spectrum (~2900 cm^{-1}) characteristic of SP degradation was overlaid with the alkyl C-H vibrations (found just below 3000 cm^{-1}) expected for diethyl malonate. Furthermore, carbonyl stretching vibrations at ~1717 cm^{-1} were found. These peaks were difficult to always detect as cleavage of the functional group formed carbon oxides. Remarkably, the residual mass from the TGA analysis exhibited only a 30 wt. % loss at high temperatures. A mass loss of 30 wt. % was unexpected considering that the mass balance calculation found almost 70 wt. % SP was present. It was hypothesized that the SP must persist on the SWNT surface, even at high temperatures, which would indicate good thermal stability as well strong SP adsorption. Additional experiments were needed to verify this hypothesis.

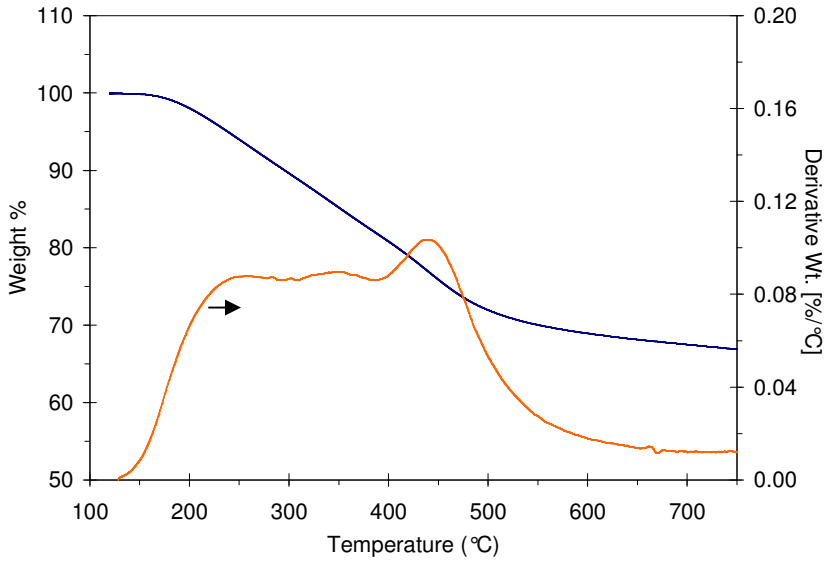

Figure 5.5: TGA mass loss curves for 12 h Bingel SWNT mass balance in argon.

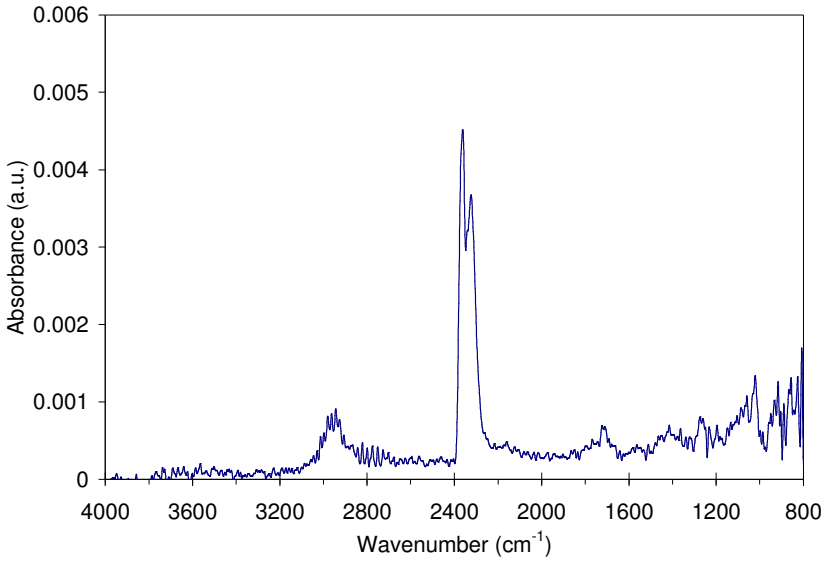

Figure 5.6: FTIR spectra of 12 h Bingel SWNT at ~330°C.

A fraction of the same 12 h Bingel product was also analyzed in an oxidizing atmosphere of air. Figure 5.7 displays the TGA mass loss curves. It was noteworthy that unlike the case of argon, complete oxidation was achieved in air with no residue. As shown by the derivative loss curves, the thermal degradation was complex, exhibiting prominent peaks at 474.6°C and 530.3°C. The position of these peaks were very confusing since the oxidation temperature of the pristine SWNT sample was measured to be 488.2°C, intermediate to the measured values for the Bingel product. Therefore, more analysis was required to determine which peak resulted from the SWNT oxidation. Recall, based on the calculated mass balance, it was expected that at least 70 wt. % SP and functional groups would be lost. Examination of the minima between the peaks in the derivative mass loss curve, in relation with the weight loss curve, (shown by dotted line in Figure 5.7) revealed a residual mass of 24.6 wt. % at 507.6°C. Therefore, the first mass loss event resulted in removal of 75.4 wt. % of the product. This value was in agreement with the estimate made for SP and functional group content to be in excess of 70 wt. %. Thus, the first mass loss derivative peak is primarily from SP and was a substantial amount of SP contaminant

which can drastically alter the desired dispersion properties of the ester functionalized SWNT. Furthermore, FTIR analysis of the effluent showed evidence of hydrogen chloride, which was a signature for the degradation of SP in this work; this will be discussed in other sections. Finally, this experiment also confirmed the persistence of SP to the SWNT surface, even at high temperatures in argon.

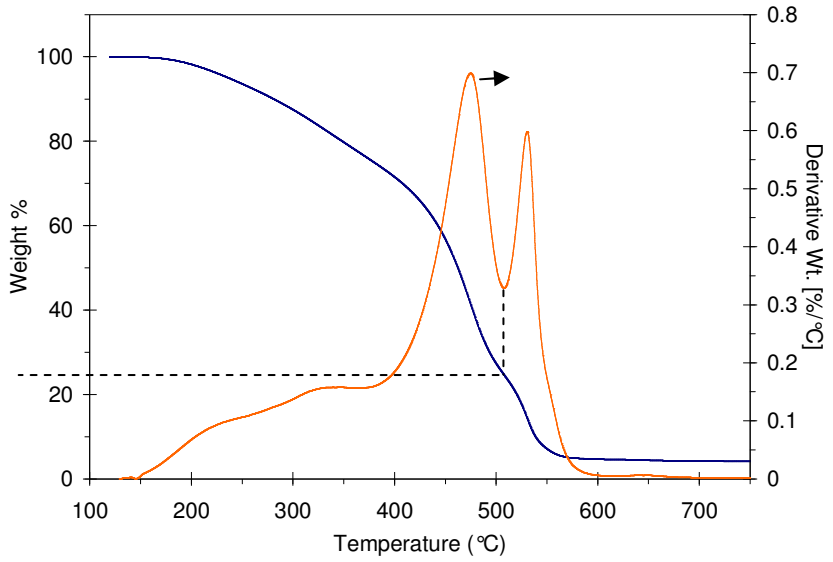

Figure 5.7: TGA mass loss curves for 12 h Bingel SWNT mass balance in air.

Since the derivative first mass loss peak in Figure 5.7 was primarily a result of SP degradation, the second mass loss peak found at 530.3°C was due to SWNT oxidation. A puzzling observation, however, was the substantial 42.3°C up-shift in the SWNT ignition temperature, from 488°C. In order to determine if the SP presence or a change to the SWNT structure was leading to this up-shift, the effect of sonication alone (i.e. without sonopolymerization) was also studied.

To confirm the strong adsorption and high temperature persistence of SP, a coupled experiment in argon and air was performed. Figure 5.8 displays the TGA mass loss curve overlaid with the corresponding temperature profile. An initial heating and cooling cycle was

performed in argon, as shown by the left hand side of the figure. The intermediate residual mass was ~62.4 wt. %, consistent with what was seen previously, but slightly increased due to the reagent concentration being twice that of the previous experiment for this sample used. After allowing the temperature to equilibrate at 40°C, the atmosphere was switched to air and the temperature ramped to oxidize the sample to a residue of ~4.7 wt. %. It was noteworthy that the SWNT oxidation temperature was measured to be 527.8°C which was consistent with the sample shown by Figure 5.7.

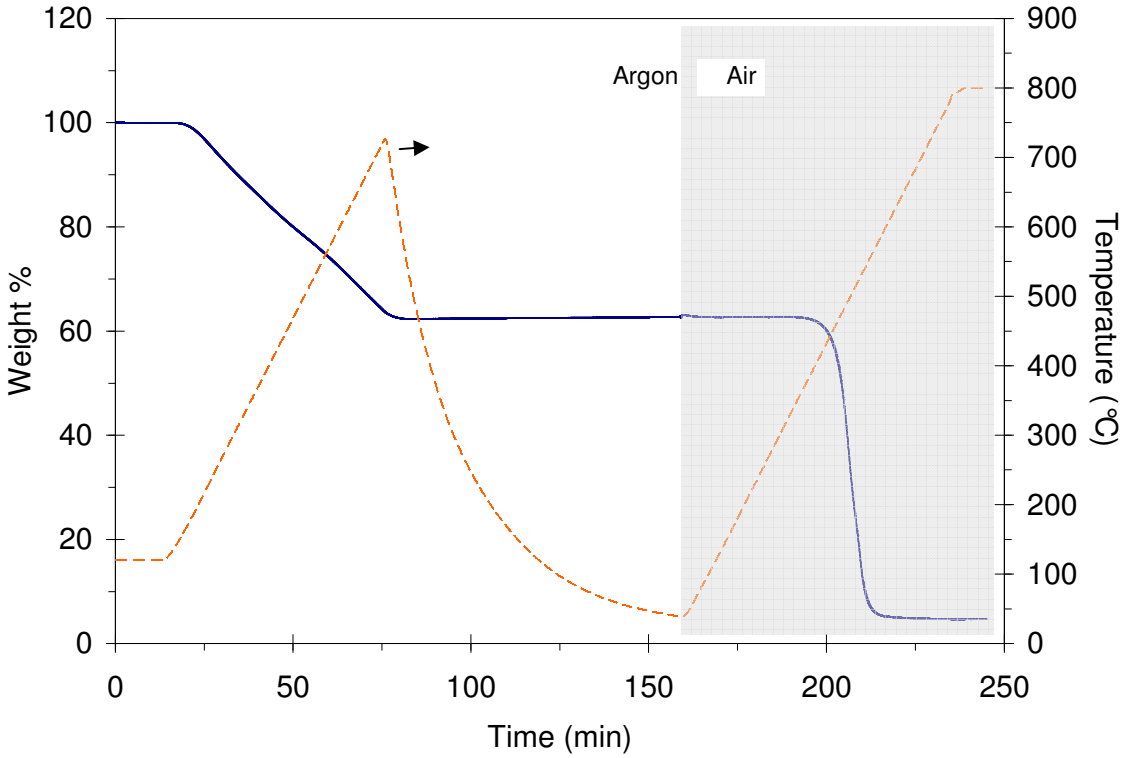

Figure 5.8: TGA mass loss with time in argon and then air (gray highlight) for 12 h Bingel SWNT (double reagent concentrations). The dotted orange line represents the experimental temperature profile.

5.1.4 Effects of the Sonication Process on SWNT

The apparent up-shift in SWNT oxidation temperature after Bingel functionalization motivated interest in studying the effect of sonication, either without introducing ester chemistry, or in

absence of sonopolymerization, on SWNT. A fundamental understanding of how the sonication process impacts the nanotube allows for observations resulting from the functionalization and those resulting from the processing conditions to be decoupled. In this manner, experimental artifacts that may be misinterpreted to be a result of surface chemistry can be identified.

Effects on Thermal Stability

In order to determine the effect of sonication on SWNT, various non-polymerizing solvents were chosen based on their solvent properties such as surface tension, viscosity, and vapor pressure. According to theory, the shear stress applied to the sample by a cavitating sonication bubble is related to these solvent properties, such as the surface tension.[166] The surface tension of oDCB was reported to be 37 dyne/cm. Dimethyl sulfoxide (DMSO) was chosen as a suitable stress transfer analog for oDCB due to its comparable surface tension of 43 dyne/cm. Ethanol, (EtOH) possessing a surface tension approximately half that of DMSO, was also chosen to expose SWNT to a less intense sonication environment. Table 5.1 displays these values.

Solvent	*γ, dyne/cm*
EtOH	22
oDCB	37
DMSO	43

Table 5.1: Surface tensions for various solvents from MSDS.

The TGA mass loss curves in air for SWNT (5.2 mg) bath sonicated in each non-polymerizing solvent for 19 hours, was shown by Figure 5.9. In addition, a comparison between oxidation of the pristine SWNT starting material and a pristine SWNT sample that was heat treated by ramping to 750°C in argon and cooled (Heat Treated) was shown. The effect of heat treatment was investigated to determine if samples could be cleaned of any sonication degradation products that might skew the TGA degradation profile analysis. It was found that the pristine

and Heat Treated samples were identical with the exception low temperature mass losses associated with amorphous carbon. Therefore, samples sonicated in DMSO and EtOH were also heat treated prior to analysis. Figure 5.10 displays the low temperature overlay of all curves which displays the obvious differences between the heat treated samples and the as-received SWNT.

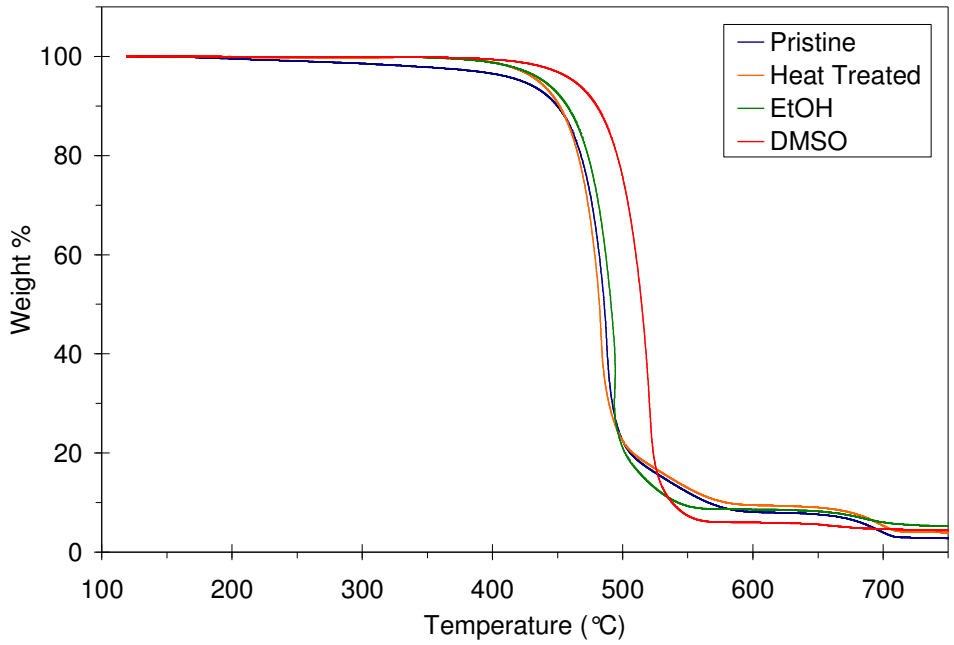

Figure 5.9: TGA mass loss curves in air for heat treated SWNT sonicated in various solvents.

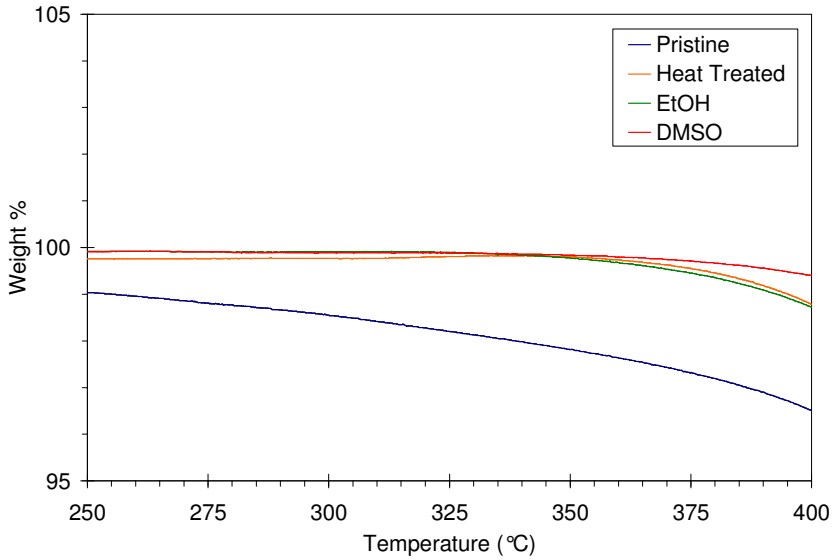

Figure 5.10: Amorphous carbon mass loss region from Figure 5.9.

Based on examination of Figure 5.9, subtle differences in the "non-SWNT" mass loss area, located around 550°C, were observed. The differences in samples were better seen upon examination of the corresponding derivative mass loss curves as displayed by Figure 5.11. Sample oxidation temperatures were taken to be the peak derivative curve temperature, as summarized in Table 5.2. Due to removal of amorphous carbons, the oxidation temperature of the starting material slightly decreased from 488.2°C to 483.6°C upon heat treatment. At 625°C, the residual masses were 7.9 wt. % for the starting material and 9.3 wt. % post heat-treatment. This slight increase was correlated to the change in relative masses from amorphous carbon removal. In addition, the oxidation temperature has been shown to correlate with the residual catalyst mass in SWNT samples and could have also contributed to the oxidation shift. After the milder sonication treatment in EtOH, the SWNT oxidation temperature up-shifted to 493.4°C, a 5.2°C increase. The residual mass at 625°C was ~8.5 wt. % for the EtOH treated sample which was slightly higher than the heat treated starting material. This was correlated to the removal of degradation products, or loss of some catalyst, which redistributed the relative masses. On the other hand, when DMSO was used, a substantial up-shift of 33°C to 521.2°C was observed. This up-shift approached what was found for the sonication of SWNT in oDCB (530.3°C) and was expected due to the similar surface tensions of each solvent. The residual mass at 625°C was ~5.9 wt. % for the DMSO treated sample. These results confirmed the assigned peak position of the SWNT oxidation temperature in Bingel product.

Sample	*Oxidation (°C)*
Pristine	488.2
Heat Treated	483.6
EtOH	493.4
DMSO	521.2

Table 5.2: Oxidation temperatures for starting materials and sonicated samples.

For point of reference, sonication in EtOH and DMSO for a period of only 6h resulted in oxidation temperature up-shifts to 489°C and 513°C, respectively. The observed up-shift of ~25°C in the DMSO treated sample, for what is considered a relatively short reaction time for Bingel functionalization, is discouraging for CG200 SWNT applicability in this scheme.

As mentioned previously, subtle effects from the sonication treatments were observed by a change in the shape of the mass loss curves, centered around 550°C. These changes were made more evident in Figure 5.11 by examination of the corresponding derivative mass loss trends. In order to better contrast between samples, the derivative curves were shifted with oxidation temperature (Table 5.2) to align peak mass losses as shown by Figure 5.12. The temperature range in this figure highlights mass losses from the so called "non-SWNT" carbons. It was found that the shape of the starting material and the heat treated sample were identical. The derivative mass loss curves for both samples showed a tail feature, extending from 510°C to almost 600°C. Sonication in EtOH appears to destroy or damage some of this material and the tail was nearly cut in half, extending from only 500 - 560°C, with more mass losses accumulating at lower temperatures. This effect was even more pronounced when DMSO was used for stress transfer. The "non-SWNT" carbon mass loss tail was shortened nearly by half again, extending from only 500 - 535°C. Thus, the up-shifts in oxidation temperatures for each sample correlated with destruction or damage of "non-SWNT" carbons, which appeared to simultaneously down-shift the associated "non-SWNT" carbon oxidation temperature. The accumulation of higher oxidation temperature materials in the region overlapping with the SWNT oxidation temperature, explained the observed up-shifts seen for SWNT. Unfortunately, this result presents a significant challenge for proper analysis of the effect of nanotube functionalization on SWNT. Note that TGA mass losses at 500°C during the heat treatment step

were found to be 3 wt. %, 12.9 wt. %, and 13.4 wt. % for Heat Treated, EtOH, and DMSO samples, respectively. This result indicated that while DMSO sonication was more destructive than EtOH sonication (by Table 5.2 and Figure 5.12), the actual effect was increased sidewall defect sites and not a difference in the amount of sample breakdown to low molecular weight carbonaceous materials between solvents. Nonetheless, when simultaneous changes are made to the surface chemistry and the sp^2 carbon surface quality, even sensitive techniques such as TGA and Raman can not decouple these effects. Therefore, functionalization routes utilizing nanotube sonication steps cannot be used for CG200 SWNT to determine the effect of functionalization. This result has far-reaching impact in the field, possibly affecting past and present results in the literature.

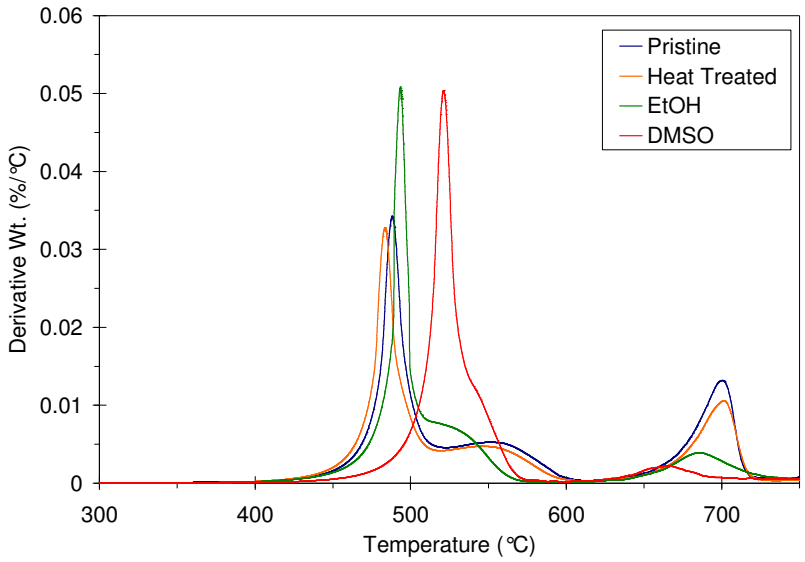

Figure 5.11: Derivative mass loss curves for heat treated SWNT after sonication in various solvents.

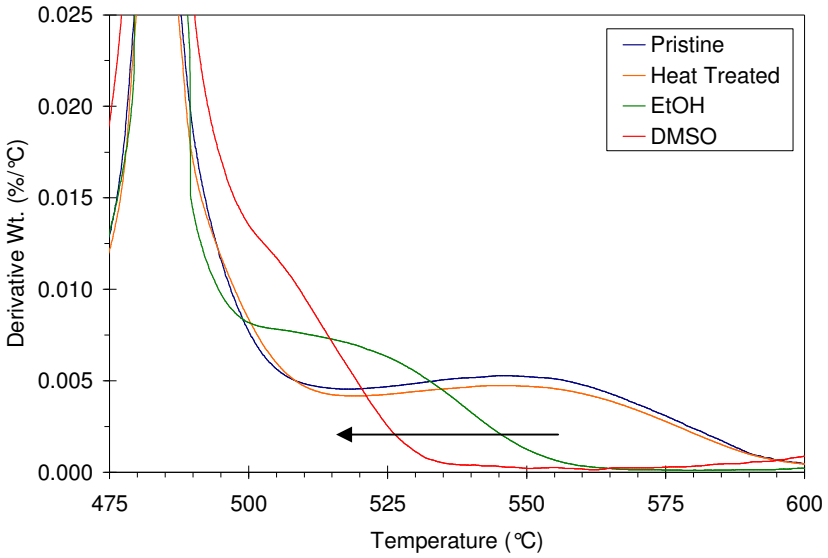

Figure 5.12: Derivative mass loss curves (from Figure 5.11) shifted with oxidation temperature. The arrow highlights the effect of increased stress transfer to the SWNT, damaging "non-SWNT" carbons.

Effect of Sonication Time

In order to further examine the effect of sonication on SWNT, a series of experiments were carried out. Based on the TGA results which showed substantial "non-SWNT" degradation, the effect of sonication time was investigated to determine if the influence of these artifacts could be mitigated. SWNT was sonicated in oDCB at 0.1 mg/mL and two 1 mL aliquots were extracted at various times and placed in polypropylene microcentrifuge tubes. To each of these samples, 0.5 mL of ethanol was added, so as to not dissolve the container. The ethanol lowered the solvent density and reduced the effective solubility parameter of the solvent. The samples were briefly vortex mixed and then centrifuged for 1 h at 10,000 x g. After this time, the samples were decanted and the supernatant was discarded, the pellet was gently rinsed with ethanol, and re-dispersed in ethanol by vortex mixing before being centrifuged a second time. After the second decanting, the residues were oven dried for Raman. Note that at 19 h reaction time, the sample was impossible to isolate, and a dark supernatant remained, even after spinning at 17,000 x g.

This was attributed to extensive oDCB degradation. Figure 5.13 displays the Raman I_D/I_G ratio for each sample time under both 514 nm and 785 nm laser. A monotonic increase was observed with treatment time and trends were identical whether or not Bingel reagent was added. This was remarkable because previous studies show a low extent of functionalization by the Bingel reaction. Furthermore, it was previously suggested that this reaction operates via a nucleophilic addition to SWNT. Thus, a metallic SWNT selectivity was expected. Instead, the observed trends indicated continuous destruction of sp^2 hybridized carbons with sonication time. This conclusion was supported by the TGA study showing the effect of solvent shear stress on the "non-SWNT" carbons in the sample. Here, the observation of destruction was tracked by the formation of sp^3 carbons. Again, there was no certain way to decouple the effects of functionalization and damage to the SWNT, since they occur simultaneously. This result, however, stresses the dominant effect of sample damage by sonication and supports the introduction of experimental artifacts.

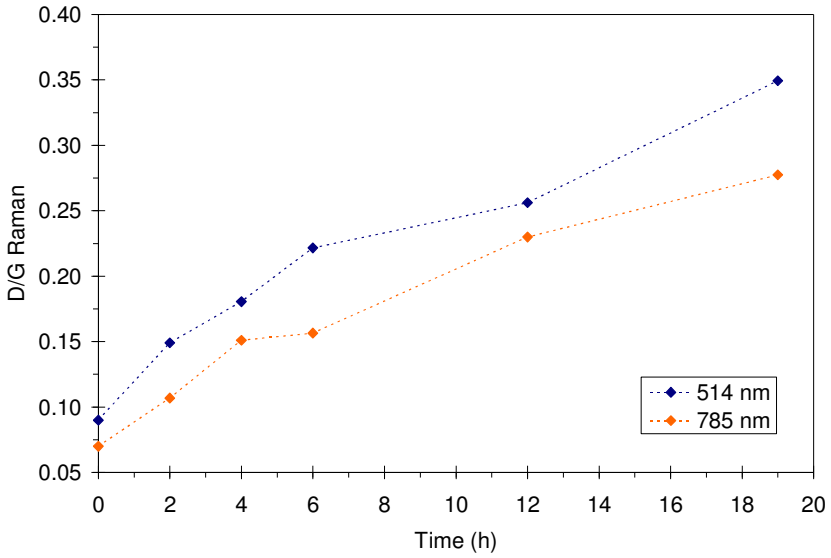

Figure 5.13: Raman I_D/I_G ratio of SWNT with sonication time in oDCB.

Further, evidence supporting that the increasing trend in Figure 5.13 was from SWNT degradation products and damage was given by the UV-vis absorption on Bingel functionalized SWNT. After filtration and washing, the Bingel SWNT was dispersed in ethanol by bath sonication then centrifuged at 17,000 x g for 45 min. The supernatant liquid, which was assumed to have retained SWNT based on the dark color, was collected for UV-vis analysis. Raman spectroscopy revealed a I_D/I_G intensity ratio of 0.33 under 514 nm laser and 0.30 under 785 nm for this sample, which indicated that the SWNT were either substantially functionalized or damaged. Conflicting evidence was observed by UV-vis analysis, however. As shown by Figure 5.14, the van Hove singularities were still observed in the UV-vis spectrum which indicated SWNT were present with low degrees of functionalization or damage.[158] This observation was remarkable based on the Raman analysis and could only result from selective degradation of the SWNT sample, specifically the "non-SWNT" carbons. For reference, Umeyama et al. (2007) showed that loss of van Hove transition occurs with an extent of functionalization as low as 1 functional group per 10 - 100 C atoms.[158]

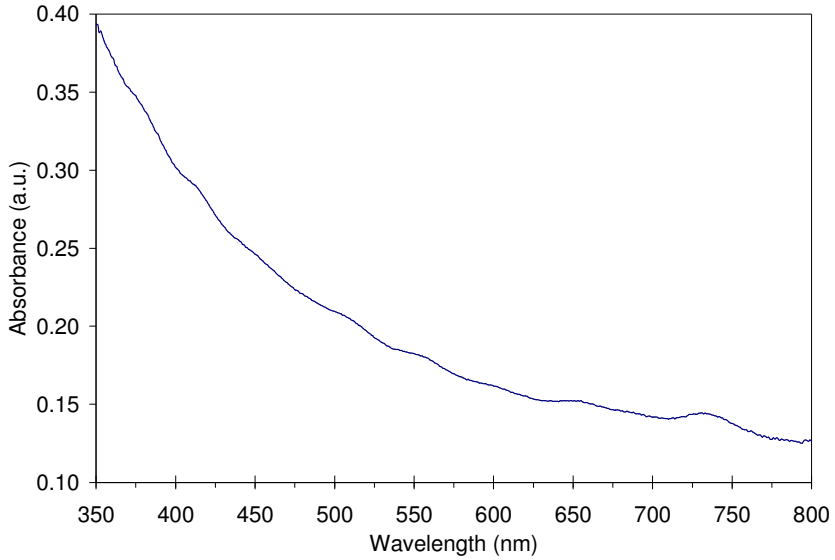

Figure 5.14: UV-vis absorbance for Bingel SWNT Supernatant in ethanol. Concentration was estimated to be 0.005 mg/mL based on the extinction coefficient discussed in Chapter 6.

5.1.5 Effect of Sonication on Electronic Structure

Previous investigation into the effect of oDCB sonication on HiPco SWNT revealed the presence of doping, which effects the SWNT electronic structure.[165] Specifically, the gaseous HCl and Cl_2 by-products from oDCB sonication were found to etch the iron HiPco catalyst to form iron chlorides. Iron chlorides are a known p-type dopant for SWNT. This dopant acts as an electron acceptor from the π valence band of SWNT. Transfer of electrons results in increased hole carrier density, which lowers Fermi energy. Evidence for modification of the SWNT electronic structure by doping was tracked using Raman spectroscopy. The most obvious feature was a 9 cm^{-1} up-shift in the G' band. In addition, a loss of the metallic G-band shoulder and an increased peak intensity, which can be gauged between spectra by comparing the G/G' peak ratio, were observed doping effects. In order to determine the presence of doping upon oDCB sonication with CoMoCAT SWNT, a similar experiment was designed. SWNT were sonicated in anhydrous oDCB under an inert argon atmosphere. A mineral oil bubbler was not used as this would have swept away the etchant gases. These gases were instead allowed to accumulate within the sample, via Henry's Law. A SWNT concentration of ~0.02 mg/mL was chosen since this was near the reported SWNT dispersion limit in oDCB.[166] Sonication at this concentration ensured that the solvent can access the catalyst. After 1 h of bath sonication, the dispersion was dripped onto the center of a pre-wet (with anhydrous oDCB) 0.2 μm PTFE filter (Pall) until enough material accumulated to move it to a glass slide. The sample was then immediately analyzed using Raman spectroscopy while wet. As mentioned previously, the most apparent characteristic of doping was a horizontal G' shift. Figure 5.15 shows the doping test product, compared against the vacuum dried starting material, both scaled with max peak intensity. The horizontal Raman shift was on the order of 1 cm^{-1}. A closer view of this peak can be seen by

Figure 5.16. Since this change was below the resolution of the instrument, this shift was not interpreted as doping. Therefore, based on the analysis thus far, sonication of CoMoCAT SWNT in oDCB does not result in doping.

Further investigation into the potential doping of CoMoCAT SWNT was pursued by comparing the Raman G-band for each sample. Figure 5.17 shows the G-band scaled with G^+ peak intensity. A noticeable loss of the metallic band shoulder (arrow) was seen after sonication. While this could be a symptom of doping, the $I_G/I_{G'}$ ratio within each spectrum was found to be 2.2 in the starting material and 2.1 after sonication. The $I_G/I_{G'}$ ratio was anticipated to increase in accordance with the previous doped HiPco results showing spiking in G-band intensity. Comparing the I_D/I_G peak ratio between samples reveals insight into the observed trends. Remarkably, evidence of covalent modification or sidewall damage was observed. The pristine SWNT sample showed a ratio I_D/I_G of 0.08 and the oDCB sonicated sample was 0.16. Note that doping is a reversible and non-covalent process. Therefore, it was concluded that CoMoCAT SWNT do not dope in oDCB, rather they undergo sidewall damage from the sonication. This was supported by an increase in the relative I_D/I_G peak ratio as well as by a loss in the asymmetric shoulder at ~1450 cm^{-1}. The shoulder results from electron-phonon coupling in bundles of metallic SWNT and is lessened from charge transfer under doping but also is modified upon damage. The lack of doping behavior in CoMoCAT SWNT can be simply explained by the absence of iron catalyst found in HiPco SWNT. Treatment with HCl can be expected to form cobalt chlorides but to the author's knowledge this was not a known SWNT dopant.

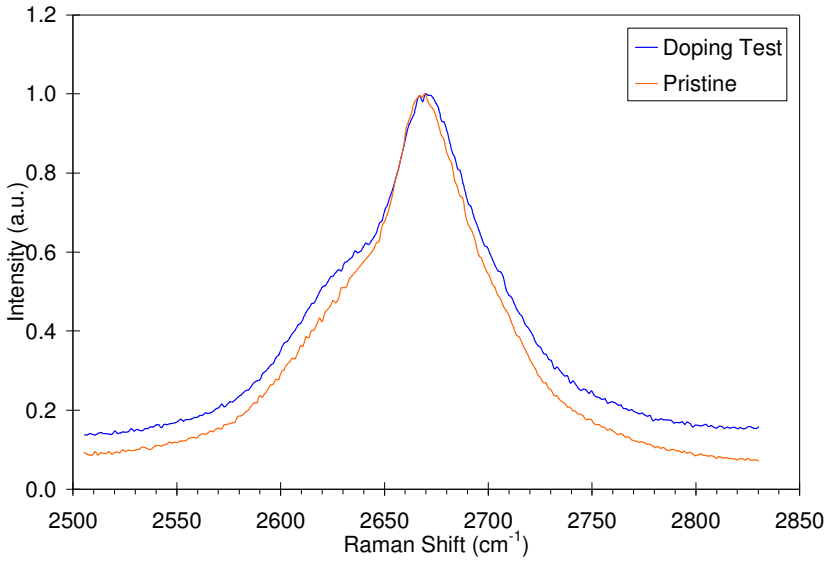

Figure 5.15: Comparison of Raman G'-band for investigation of SWNT doping.

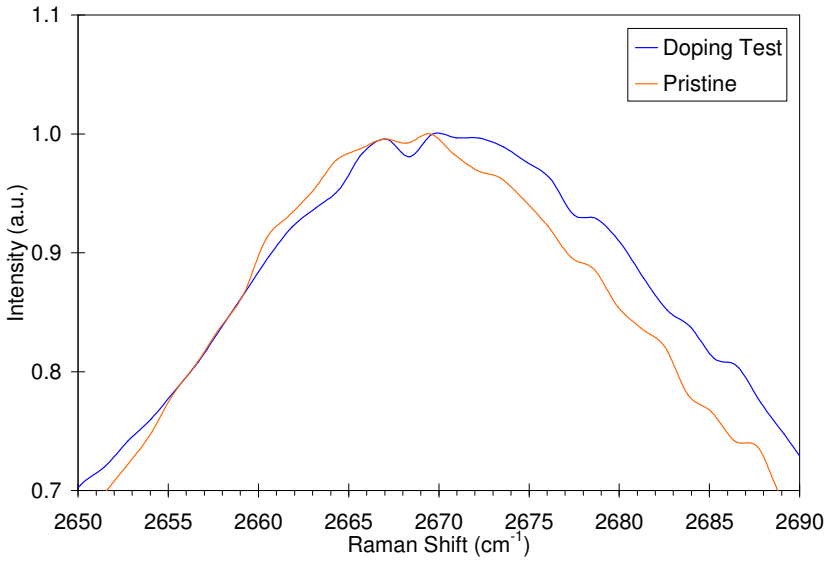

Figure 5.16: Close-up comparison of G'-peak for investigation of SWNT doping.

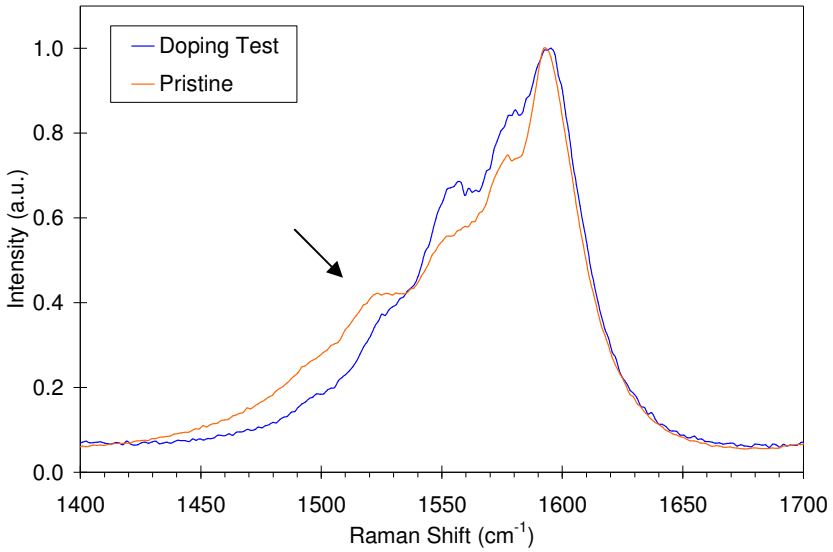

Figure 5.17: G-band comparison for investigation of SWNT doping. The arrow points to the characteristic metallic SWNT shoulder.

5.1.6 Sonopolymer Characterization

SP was isolated by sonication of oDCB under identical conditions to that of the Bingel reaction but without addition of SWNT or reagents. The dark oDCB and SP produced was then set aside for a few days so that the solids could precipitate and aggregate. This step was necessary because direct filtration of the product was not possible as little to no solids were entrapped on a 0.2 μm PTFE filter paper. After resting, the SP product was collected and washed with fresh oDCB and before vacuum drying for analysis. Figure 5.18 displays an SEM image of the SP product. The sample appears to be an amorphous polymeric material. In order to probe the chemical profile, energy dispersive x-ray analysis (EDS) was also performed, as shown in Figure 5.19. It was found that the SP consisted primarily of carbon with some residual chlorine. This was expected for the polymerization of oDCB into a polyphenyl sonopolymer.

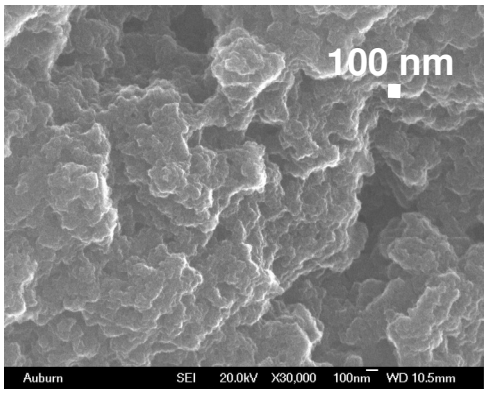

Figure 5.18: SEM image of 12 h SP under 30,000 x magnification. Sample was uncoated.

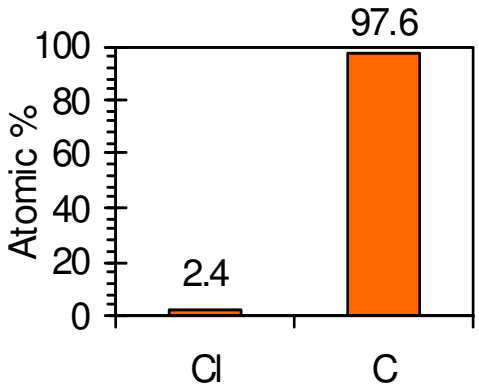

Figure 5.19: EDS profile of 12 h SP taken at 30,000 x magnification.

A sample of SP dispersion that was not vacuum dried, but instead washed repeatedly with ethanol and acetone using centrifugation at 17,000 x g, was added drop-wise to a tared TGA pan. The pan was kept under vacuum at 60°C to remove solvent and more sample was repeatedly added to slowly accumulate mass. The pan was moved to the TGA and kept under dry argon before drying at 120°C. Approximately 2 mg of dry pure 12 h SP was loaded to the pan. Figure 5.20 displays the TGA mass loss curves under argon atmosphere. As expected for free polymerization by sonication, a large range of molecular weight material was present and losses were seen over the entire temperature range. It appeared that subtle mass loss events occurred at ~250°C, 400°C, and 675°C. Remarkably, at 800°C ~20 wt. % residual mass still remained. This sample completely degraded after an isothermal hold at this temperature for 45 min.

Nonetheless, the pure SP exhibits impressive thermal stability with delayed degradation kinetics. This feature explained the mass loss behavior observed for the 12 h Bingel product where SP persisted on the SWNT at high temperature. Figure 5.21 shows the gas phase FTIR spectrum of the SP degradation products at 400°C. The spectrum confirmed the unique FTIR signature for SP degradation seen in previous sections, and clearly shows the unique quantized rotation-vibration spectrum of HCl, centered at ~2900 cm^{-1}. In addition, the generation of carbon oxides (2000 - 2400 cm^{-1}) was observed. It was hypothesized that cleaved Cl atoms react with desorbed H to produce hydrogen chloride, in-situ. Figure 5.22 highlights the quantized branches for the HCl spectrum. Based on the application of the Born-Oppenheimer approximation, the vibration-rotation energy can be modeled by combination of the harmonic oscillator and rigid rotor model for diatomic molecules. An example and discussion for HCl was given in Atkins and De Paula (2006).[217] Approximately 10 or 11 quantized transitions were observed. Due to the unique FTIR spectra of SP degradation, and formation of hydrogen chloride, this signature can be used to identify SP degradation in SWNT samples.

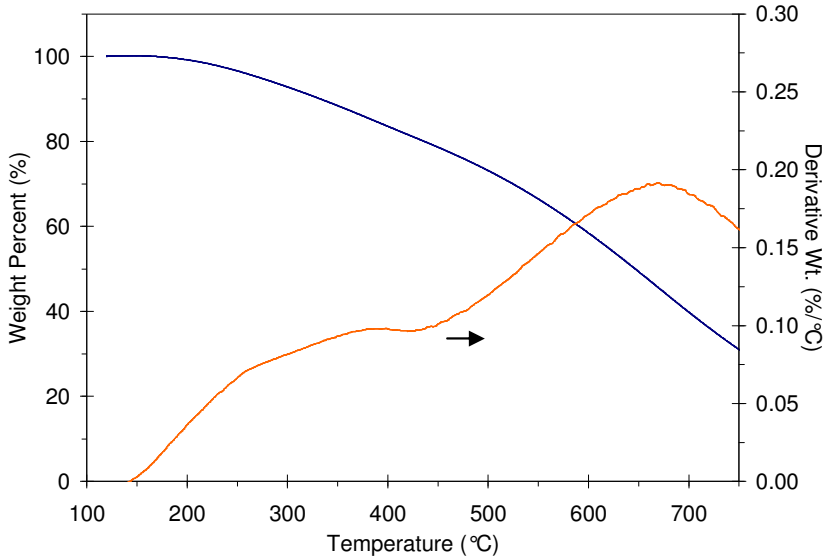

Figure 5.20: TGA mass loss curves for 12 h SP degradation in argon. No SWNT present.

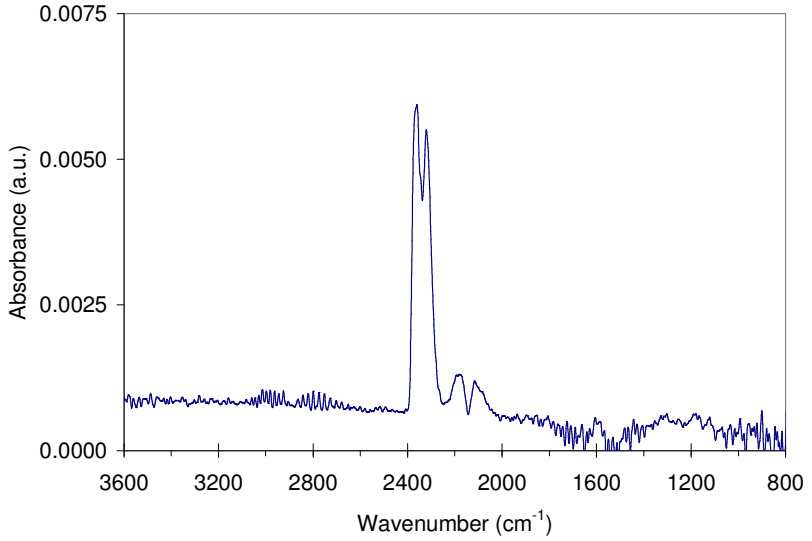

Figure 5.21: FTIR spectrum of 12 h SP degradation gases at 400°C.

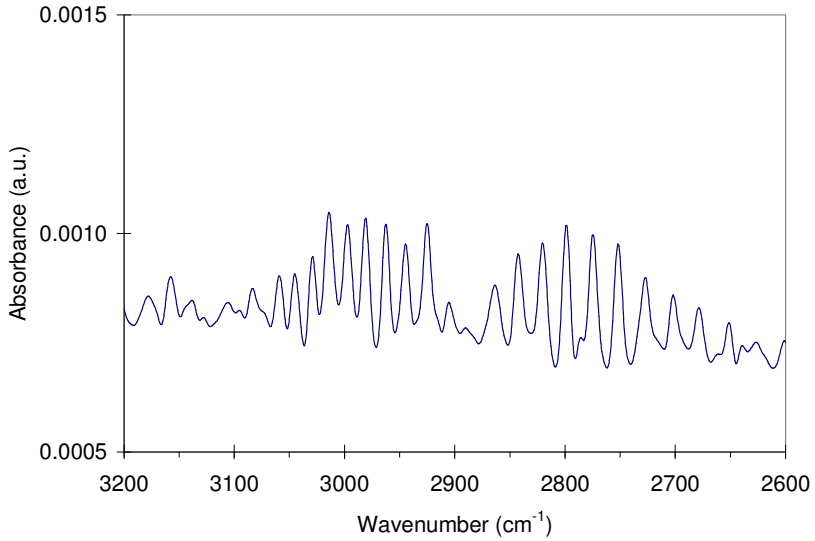

Figure 5.22: Gas phase rotation-vibration spectrum for hydrogen chloride evolution from SP.

The 12 h SP was unable to be characterized by ATR techniques. Similar to SWNT, the high index of refraction prevents total internal reflection at the crystal interface. Both Ge and diamond crystals were used to overcome this measurement difficulty, but unsatisfactory spectra were obtained. Instead, the FTIR spectrum was gathered by grinding dry SP with dry KBr powder. Approximately 100 mg of KBr was placed in two vials and dry SP was added to one.

Both vials were dried and cooled under vacuum before grinding with mortar and pestle and compressed into a disk using a screw type pelletizer. Extensive drying was required to limit moisture interference with the spectrum. Figure 5.23 shows the SP transmission spectrum after baseline correction to flatten the background absorbance. The peak assignments were contrasted with those published by Niyogi et al. (2003) who described the SP spectrum as a type of crosslinked polystyrene.[155] Based on the observed weak aromatic C-H vibrations in both that work and the present study, this description of a polystyrene analog was not supported. Nevertheless, the spectra herein appear similar with comparison of peak assignments shown in Table 5.3. The measurement of a peak ~1730 cm^{-1} by Niyogi et al. (2003) was also found with a similar position (1710 - 1720 cm^{-1}). This was a puzzling observation since vibrations in this region were typical of a carbonyl. Koshio et al. (2001) also found this feature, but for SWNT sonicated in monochlorobenzene.[218] Assuming the aromatic structure remains, for aromatic compounds vibrations in the region from 2000 - 1650 cm^{-1} originate from combination and overtone bands from C-H out-of-plane deformations. In addition to carbonyls, olefinic unsaturated bonds absorb here. According to Socrates (2004), the location of the observed peak might indicate a tetra-substituted aromatic ring structure.[203] The final structure from the sonopolymerization was likely the result of radical formation (recall Cl_2 and HCl evolution) and due to these highly reactive sites, the resulting structures were hard to predict. Nevertheless, the similarities between spectra from multiple studies allowed conclusions to be drawn between works. Table 5.4 displays additional peaks and possible assignments.

Figure 5.23: Transmission FTIR spectrum of 12 h SP suspended using KBr pellet.

Experimental, cm^{-1}	Assignment	Niyogi et al. (2003), cm^{-1}	Assignment
754	Aromatic C-Cl combo mode*	748	C-Cl bend
1031, 1049, 1093	Ortho aromatic C-Cl, unassigned, para aromatic C-Cl	1035	Substituent sensitive phenyl mode
1442	Aromatic C=C stretch	1430, 1450	Aromatic ring
1710 - 1720	Possibly substituent sensitive phenyl combo & overtone bands*	1730	Unknown
2852, 2919, 2952, 2967	CH_2, CH_2, CH_3 asymmetric (2), respectively	2800 - 2900	Alkyl C-H stretches
3070, 3078	Aromatic C-H	3068	Aromatic C-H

Table 5.3: Comparison of FTIR assignments for SP. *Socrates (2004)[203]

Experimental cm^{-1}	Assignment
435	Aromatic C-Cl str and ring def.*
1581 (strong)	Aromatic C=C stretch
1371	CH_3 symmetric
1407	Possibly C=C
1257	C-H bend, methyl
804, 881	Aromatic C-H para or meta
1132, 1157	Unknown C-O/unassigned

Table 5.4: Additional SP FTIR peaks and potential assignments.

To complement the FTIR spectrum, the Raman spectrum of the dry SP was measured under 514 nm laser excitation as shown in Figure 5.24. Good signal to noise was not possible using 785 nm wavelength excitation. A prominent peak at was found at 1586 cm^{-1} and was characteristic of aromatic C=C bonds. A C=C band at 1580 cm^{-1} has been identified with a conjugated structure.[203] This was similar to the G-band in SWNT. The shoulder at lower wavenumber was not well defined but may represent tetra-substituted benzenes.[203]

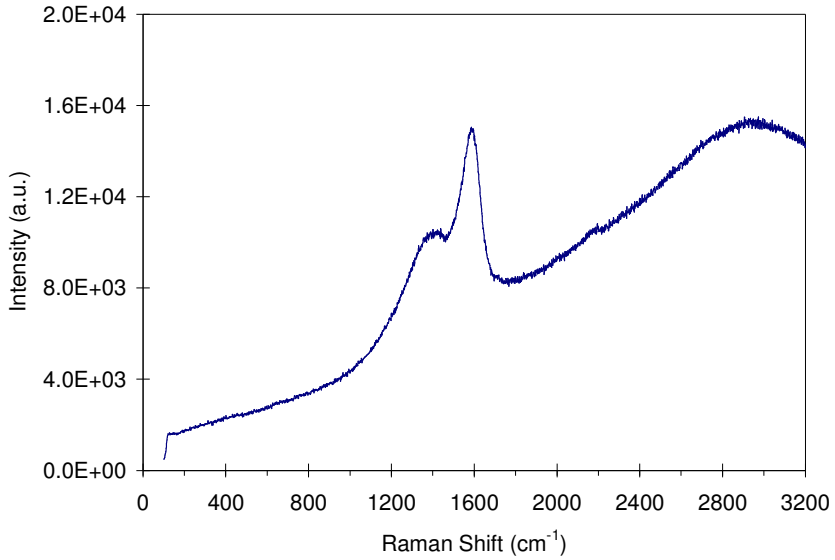

Figure 5.24: Raman spectrum of 12 h SP under 514 nm laser.

5.1.7 Dispersibility of Sonopolymer in Solvents

A 3:1 mass ratio of SP to SWNT was discovered for 12 h Bingel SWNT by coupled TGA analysis and mass balance. This large amount of SP was generally undesirable for most applications of the functionalized SWNT. For example, the addition of a large amount of a 3rd component could have detrimental effects if this material was not compatible with the solvent or polymer system of interest. As shown in subsequent sections, the SP acts as a SWNT glue in UPR and therefore must be removed to exploit the full potential of this system. Thus, the dispersion and/or solubilization of SP was desired. In order to determine how to best wash the

SP from the SWNT, a range of solvents were investigated to disperse or dissolve the SP. This was done by taking a dispersion of SP in oDCB, prior to isolation by filtration, and dropping equal volumes in small vials. After the vials were thoroughly dried various solvents were added in an attempt to re-disperse or dissolve the dry SP. The vials were allowed to set for a few days and checked before vortexing and bath sonication. Table 5.5 displays the Hansen solubility parameter (dispersive, polar, hydrogen bonding) for each solvent as well as the molar volume *v*. A vast range of solvent polarity was covered in this study, from 0 to 16.4 $MPa^{1/2}$. Unfortunately, none of the solvents appeared to dissolve or even sufficiently disperse the SP for any substantial period of time. The lack of solubility is similar to the SWNT themselves and this may be a result of strong π-π interactions between the polyphenyl groups. This behavior was unfortunate for the potential success of washing of SP from SWNT. Selection of a solvent was made based on the ability of dimethylformamide to restore optical properties in SP SWNT.[156] Thus, dimethylacetamide (DMAc) was selected due to its similar structure and nearly identical solubility parameters.

-	Solubility Parameter [$MPa^{1/2}$]			[mL/mol]
Solvent	d	p	H	*v*
Acetone	15.5	10.4	7.0	74.0
Ethanol	15.8	8.8	19.4	58.5
Chloroform	17.8	3.1	5.7	80.7
DMAc	16.8	11.5	10.2	92.5
DMSO	18.4	16.4	10.2	71.3
Hexane	14.9	0	0	131.6
THF	16.8	5.7	8.0	81.7
Toluene	18.0	1.4	2.0	106.8

Table 5.5: Hanson solubility parameters for various solvents used to disperse SP.[94]

5.1.8 Washing Protocol for Sonopolymer

In order to investigate the potential removal of SP from SWNT, a washing protocol was carried out. The goal was to promote desorption of SP from the SWNT surface and isolate SWNT by SP removal. The sonication product both with and without functional groups was isolated by filtration on a 0.2 μm PTFE filter (Pall) and re-dispersed in ethanol (denatured with alcohols only) by bath sonication. This was repeated three times to remove residual oDCB and any reagents. At this point the product was split up and half was set aside. This half was labeled as "filtered" sample to signify work-up by filtration only. The balance of the sample was then dispersed in DMAc by bath sonication. This dispersion was placed into a number of 2.0 mL polypropylene microcentrifuge tubes and centrifuged down for 1 hour at 17,000 x g. The samples were decanted and the residue was re-dispersed in DMAc. This process was repeated three times. Between each cycle the supernatant and the residue of the sample was collected and referred to by these descriptions. Both supernatant and residue were isolated by filtration, washed with ethanol, dispersed in ethanol by sonication and isolated yet again before being collected for vacuum drying. The effectiveness of this protocol was tested against SWNT sonicated in oDCB for 12 h alone and also 12 h Bingel functionalized SWNT.

Effect of Washing on Measured Raman Ratio

As shown by Moonoosawmy and Kruse (2009), high Raman excitation laser power can generate artifacts in the analysis of Raman data.[156] Briefly, for functionalized SWNT, with high enough laser power the I_D/I_G ratio should decrease in accordance with the thermal degradation of functional groups. Conversely, there should be no change with annealed pristine tubes. Note that there may be a slight decrease with as received, un-annealed tubes due to methods used for their purification. Comparing tubes sonicated in oDCB and BzCl before and after washing the

following was observed:[156] at lowest power, no changes were seen but at high powers the SP was charred leading to changes in the I_D/I_G ratio during and after laser exposure. It was found that at laser powers greater than 0.12 mW/μm^2 (25 % power) thermal charring occurs. The resulting increase in I_D/I_G at moderate/high powers can be misinterpreted as covalent functionalization. Therefore, the functionalization product and washing protocol used were tested by Raman spectroscopy at different laser powers to look for artifacts which might result in incorrect data analysis in subsequent sections. The lowest laser powers which resulted in a good signal to noise ratio in the background intensity were chosen to be 5 % laser power under 514 nm laser and 1 % under 785 nm laser. Bingel SWNT were analyzed after filtration and ethanol washing only and also after going through the DMAc washing protocol with centrifugation. A reaction time of 19 h was used to exaggerate the effect of SP and possibly outweigh the effect of functional groups. Multiple sample areas were measured by Raman for each condition under both lasers. The results showed no change in the average Raman I_D/I_G ratio which indicated that no sonopolymer charring was occurring under these conditions and all data could be trusted to be artifact free.

Washing Protocol on SP SWNT

Figure 5.25 displays the TGA mass loss curves in argon for SP SWNT filtered, residue, and supernatant samples with no added functional groups. The initial sonication treatment time was 12 hours. It was thought that an ideal separation would show the starting filtration material TGA trace being intermediate between the mass loss traces for the supernatant and residue. This observation would have indicated that the SP was removed and preferentially extracted to one of the phases during centrifugation, leaving behind a thermally stable sample. Instead, as shown below, both the residue and supernatant curves are below that of the filtered sample. This

indicated that SP was successfully desorbed from the SWNT surface during the washing protocol but did not preferentially transfer to a single area during centrifugation. The supernatant sample exhibited the greatest mass losses. The derivative mass loss curves were also analyzed as shown in Figure 5.26. Remarkably, the filtered sample was nearly featureless, indicating that SP remained adsorbed over this temperature range, and losses were at constant rate. Conversely, the samples washed with DMAc (residue and supernatant) show similar trends. The SP SWNT residue shows losses at ~330°C and ~444°C. Supernatant losses were also similar at ~319°C and ~424°C. The lower temperature events for the supernatant sample, and more prominent low temperature curve, were consistent with the observed losses of desorbed SP being greater. All samples were held at 800°C for 45 min. Figure 5.27 displays the final mass losses at long test times. Remarkably, at tests end, the description for an ideal separation, as described above, was observed with the residue sample showing only 37 wt. % losses and the supernatant showing a 65 wt. % loss. The filtered sample before DMAc washing ended up at 50 wt. %, an intermediate value. This result was very encouraging for the applicability of the washing protocol.

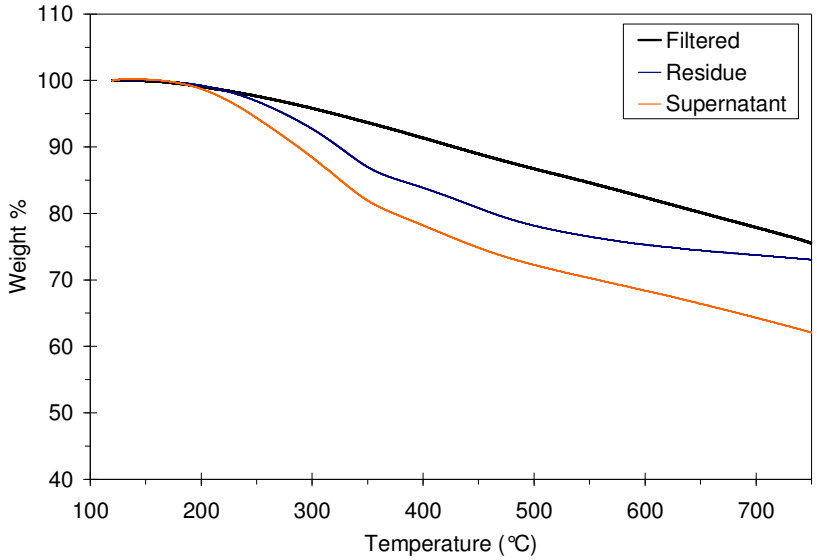

Figure 5.25: TGA mass loss in argon for SP SWNT washing protocol samples.

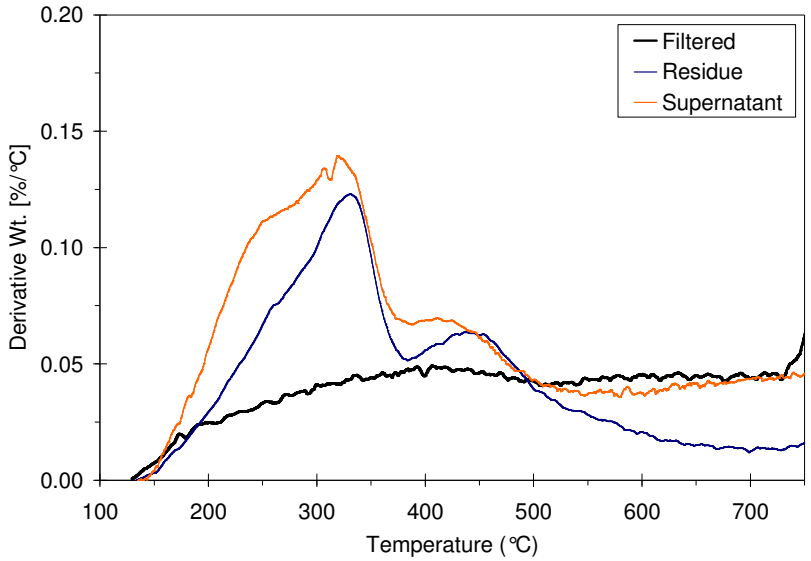

Figure 5.26: Derivative mass loss curves for SP SWNT.

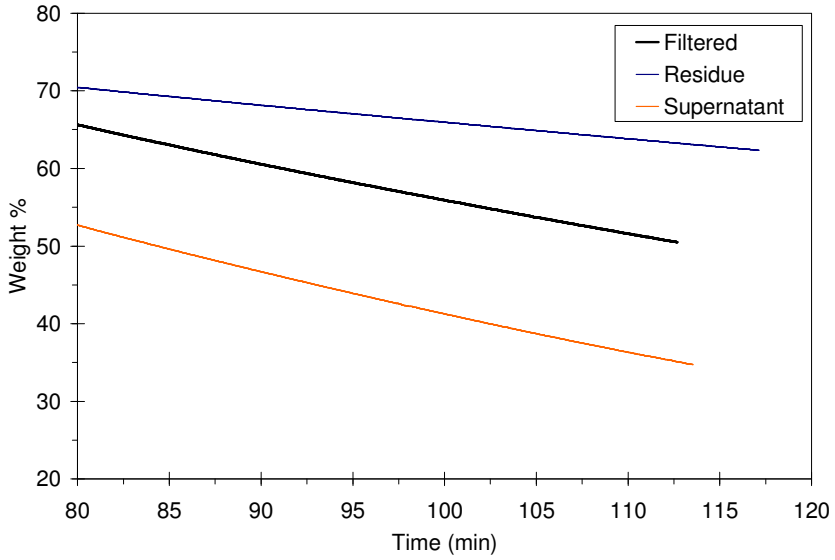

Figure 5.27: TGA loss curves at test end for SP SWNT during 800°C hold.

In order to identify variations or any preference for SWNT transfer to each centrifugation phase, each sample was characterized by Raman spectroscopy, shown by Table 5.6. Remarkably, for the SP SWNT sample, the I_D/I_G intensity ratios were quite similar indicating sidewall damage was consistent between each phase.

	Raman I_D/I_G	
Sample	514 nm	785 nm
Filtered	0.21	0.20
Residue	0.22	0.19
Supernatant	0.23	0.23

Table 5.6: Raman I_D/I_G ratio for SP SWNT washing protocol samples.

Washing protocol on Bingel SWNT

Figure 5.28 displays the TGA mass loss curves in argon for 12h Bingel SWNT samples. Samples were labeled as filtered, residue, and supernatant, in the same fashion as the previous section. Similar to the SP SWNT sample, the supernatant sample showed the greatest mass loss. Remarkably though, all curves had surprisingly similar losses post washing protocol; this was not the case for the non-functionalized SWNT. The derivative mass loss curves were also analyzed as shown by Figure 5.29. In contrast to the SP SWNT, the filtered sample exhibited two prominent features; a broad shoulder was observed at ~222°C and a large loss at 449°C. Interestingly, after washing, the low temperature shoulder remained for both residue and supernatant samples. This loss was at lower temperature than in the non-functionalized SP SWNT as was interpreted to contain functional group losses. For both residue and supernatant, the high temperature peak was lessened in intensity and shifted slightly down in temperature as compared to the filtered sample. The previously mentioned similarity in mass losses was better seen upon examination of Figure 5.30 which displayed the final high temperature losses after being held at 800°C for 45 min. The ideal separation seen previously for SP SWNT was not realized for Bingel SWNT. The losses at test end were 42 wt. %, 45 wt. %, and 49 wt. % for filtered, supernatant, and residue samples, respectively. An explanation for this behavior was found by examination of the Raman I_D/I_G data shown by Table 5.7. Based on Raman analysis, the damaged or functionalized SWNT preferred the supernatant phase. Since this behavior was

not seen for the SP SWNT sample, it was concluded that the effect of functionalization was observed in this case. Likely the ester functionalized SWNT prefer the supernatant phase due to their increased affinity for the solvent. Note that the starting filtration samples had similar I_D/I_G for both the SP SWNT and the Bingel SWNT. Thus, the ideal separation hoped for by the washing protocol was not possible for functionalized Bingel SWNT. Remarkably, the supernatant shows increased functionalization towards damaged or metallic SWNT. This behavior was anticipated for the nucleophilic addition mechanism, but the influence of sonication effects on "non-SWNT" carbon prevents a definitive interpretation.

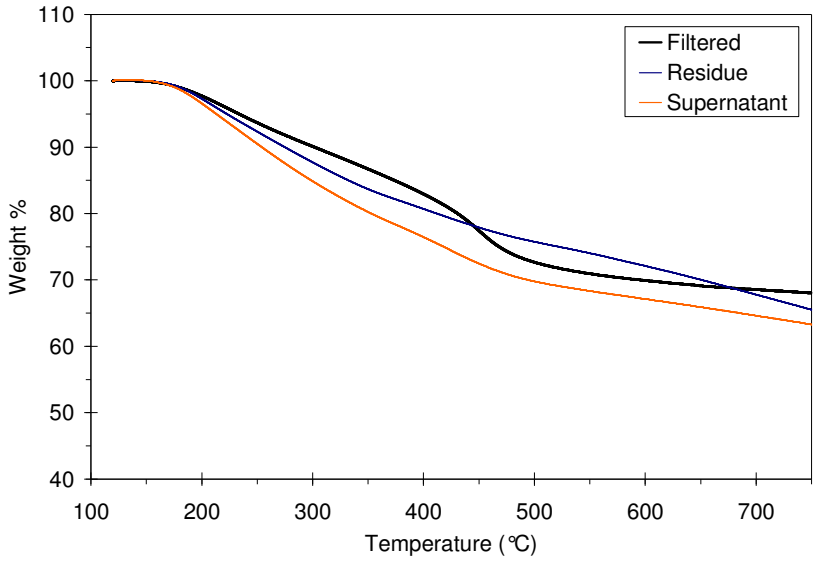

Figure 5.28: TGA mass loss curves in argon for Bingel SWNT washing protocol samples.

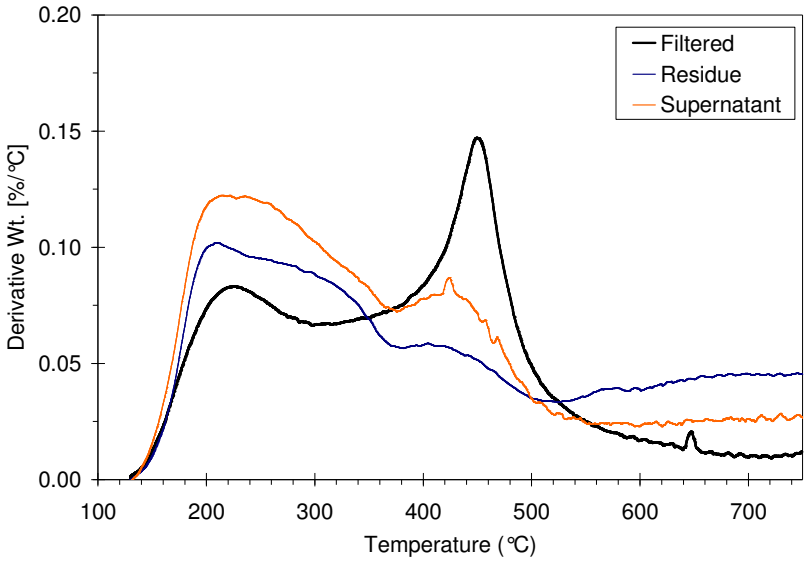

Figure 5.29: Derivative mass loss curves for Bingel SWNT.

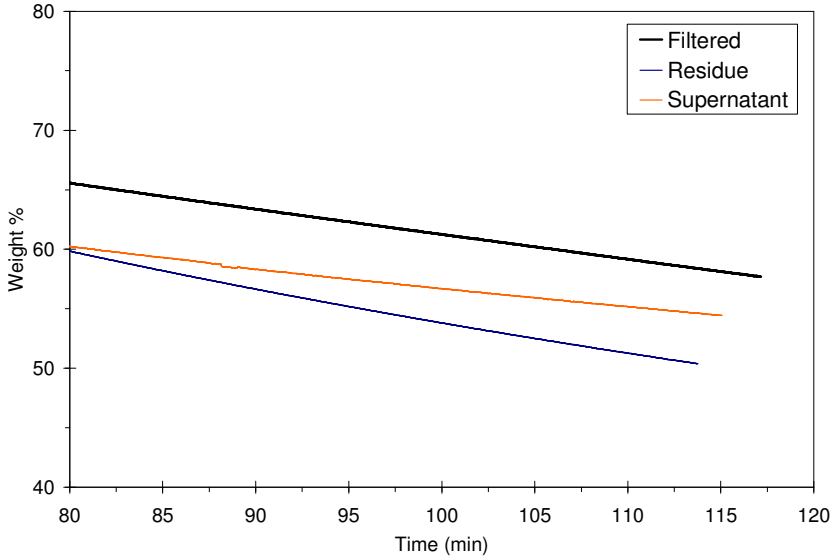

Figure 5.30: TGA loss curves at test end for Bingel SWNT during 800°C hold.

	Raman I_D/I_G	
Sample	514 nm	785 nm
Filtered	0.20	0.18
Residue	0.19	0.12
Supernatant	0.25	0.21

Table 5.7: Raman I_D/I_G ratio for Bingel SWNT washing protocol samples.

5.1.9 Bulk Dispersibility in UPR

A key finding in studying the effect of processing on Bingel functionalized SWNT was the degradation of "non-SWNT" carbons which masked the ability to decouple sidewall damage from functionalization through TGA and Raman analysis. Therefore, the effect of functionalization and SP adhesion was investigated by bulk dispersion into UPR via high shear mixing. Figure 5.31 compares the effect of SP on the bulk dispersion of SP SWNT. The filtered sample (left) contained all SP generated during sonication since it was not treated with the DMAc washing protocol. In addition, SP remained adhered to the SWNT in this sample. No dispersion was seen for the filtered SP SWNT, which was clearly evidenced by comparing the two vials. The clear vial, which appeared to contain essentially neat UPR, had SP SWNT clusters settled out on the bottom due to a complete lack of dispersibility. On the other hand, the right vial in Figure 5.31 showed that after treatment in DMAc, the partial desorption of SP was enough to allow bulk dispersion of SP SWNT. The black color of the SP SWNT residue dispersion was in stark contrast to the SP SWNT sample. Therefore, it was concluded that the presence of SP was detrimental to the dispersibility of SWNT in UPR and must be removed prior to processing into composite systems and/or to achieve its full potential for dispersion.

The effect of surface chemistry on the bulk dispersion of SWNT in UPR was displayed by comparison of the vials in Figure 5.32. Remarkably, in Figure 5.32 both vials contain SWNT without any DMAc washing protocol treatment. The Bingel SWNT sample, however, has the advantage of surface bound ester functional groups. The left hand vial shows the bulk dispersion of the filtered Bingel SWNT and the right vial again shows the complete lack of dispersion from bound SP in the filtered SP SWNT sample. The dispersibility of the filtered Bingel SWNT sample indicated that the presence of ester surface chemistry dominated over the dispersion

hindering effects of the bound SP, since neither sample was washed with the DMAc protocol. Thus, the best dispersion of Bingel SWNT in UPR would be anticipated for a sample with no SP present. This conclusion affirms the importance of establishing a proper washing protocol. Due to the lack of solubility and strong adsorption to SWNT, however, SP removal might not be possible without damaging the Bingel functional groups (e.g. acidic or basic treatments).

Figure 5.31: Effect of sonopolymer on SWNT dispersion. (left) SP SWNT filtered and (right) SP SWNT residue.

Figure 5.32: Effect of surface chemistry on SWNT dispersion. (left) Bingel SWNT filtered and (right) SP SWNT filtered.

5.1.10 Analysis of "non-SWNT" Carbons

A unique feature shown by the oxidation of CoMoCAT SWNT by TGA was the post-SWNT high temperature mass losses described by the manufacturer to result from "non-SWNT" carbons. This feature was shown herein to significantly complicate SWNT characterization post-processing and functionalization. Thus, a more descriptive investigation into the true nature of this "non-SWNT" material was warranted. In order to isolate the "non-SWNT" material from the bulk SWNT starting material, a TGA experiment was designed to thermally separate the sample by selective oxidation in air. To do this, the TGA temperature was ramped to 500°C,

where SWNT degrade, and held until the mass losses leveled off, this took approximately 10 min. After this point, the sample was cooled under argon and collected for analysis. Two batches of this sample were isolated under these conditions. The first batch was used for SEM and Raman and the second batch was analyzed using TEM after confirming consistent Raman spectra between them. As displayed in Figure 5.33, SEM images reveal that even after this high temperature oxidation, fibrous material remains. Based on the fiber diameter, this material consisted of either SWNT/DWNT bundles or MWNT. Insight into the chemical structure of the material was revealed by its resonant Raman spectrum. Figure 5.34 and Figure 5.35 displayed the spectra under 514 nm and 785 nm laser excitation, respectively. Remarkably, in both samples, the D-band Raman feature resulting from sp^3 hybridized carbon defects (~1300 cm^{-1}) was arguably absent. Calculation of I_D/I_G ratios could not be made as the D-band intensity would be representative of the background intensity. The absence of defect bands appears to favor the sample containing mostly ultra-high purity SWNT or DWNT over MWNT. The presence of only MWNT species was ruled out by the measurable RBM modes, although a mix was possible. The observation of what appears to be a dual-mode overlapping G' band under 514 nm laser excitation was interesting. Pfeiffer et al. (2005) studied the overlapping Raman mode for DWNT and showed this to be a result of resonance from inner and outer tube diameters.[219] On the other hand, Souza Filho et al. (2002) identified all possible chiralities in SWNT which exhibit a two-peak resonance.[56] For those SWNT, the electronic structure allows a double resonance process involving the incident and exiting/scattered photon to occur; the tubes were all large diameter semiconductors in resonance with the 514 nm laser. Interestingly, the measured Raman Shift of the lower G' peak at ~2665 cm^{-1} did not match well with the peaks in this study, better highlighted by Figure 5.36. Furthermore, the dominant peak was found at higher

wavenumber in both SWNT and DWNT whereas the lower wavenumber peak dominated in the spectrum shown by Figure 5.36. Evidence of DWNT species was investigated by detailed RBM analysis. Although, exact fitting parameters are controversial in the literature, the relationship between SWNT diameter d_t and RBM mode wavenumber ω_{RBM} is well known. Dresselhaus, M.S. et al. (2010) gave the general relationship, as shown by Equation 23, with C_e as an environmental fitting parameter.[220]

$$\omega_{RBM} = \frac{227}{d_t}\sqrt{1 + C_e d_t^2} \tag{23}$$

The inter-wall spacing in DWNT and MWNT is well known to be ~0.34 nm based on the plane spacing of graphite. Therefore, by taking the difference between specific RBM modes and solving Equation 23, the differences in two SWNT diameters can be calculated. Comparing their radii, a difference of ~0.34 nm would be necessary for existence of DWNT. Calculating a difference between peaks also removes any controversy regarding the analytical expression and also physical origin or value of C_e. Figure 5.37 displays the RBM region of the Raman spectrum. The two peak positions at 173.8 cm^{-1} and 322.0 cm^{-1} have theoretical diameters of 1.37 nm and 0.71 nm, respectively. This represents a calculated inter-tube spacing of 0.33 nm which is remarkably similar to the expected value. It is possible that the local chemical environment might affect this result as was cautioned by Dresselhaus since the exact nature of C_e remains unknown. Otherwise, the slight difference could simply be a result of instrument resolution. Thus, Raman and SEM analysis cannot rigorously determine the structure of the "non-SWNT" material. It appears, however, that high purity SWNT with presence of some high purity DWNT was possible.

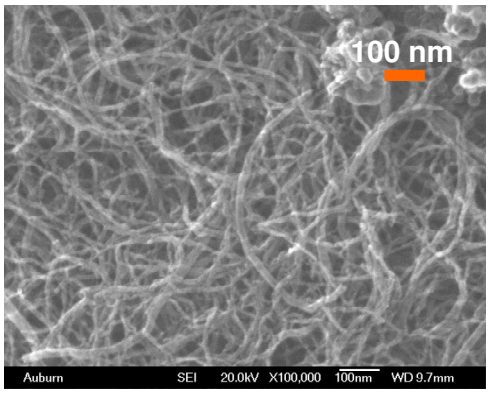

Figure 5.33: SEM analysis of "non-SWNT" carbons. The sample was held at 500°C for approximately 10 min in air.

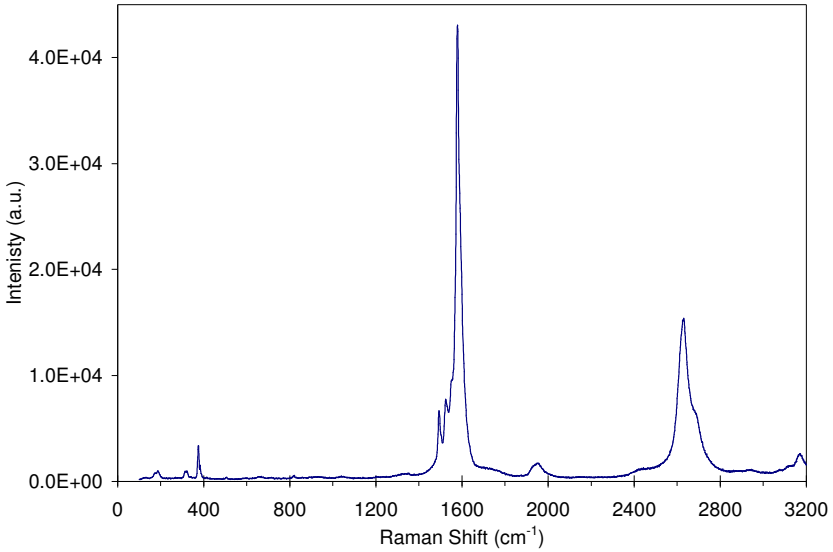

Figure 5.34: Raman spectrum of "non-SWNT" under 514 nm laser. The sample was held at 500°C for approximately 10 min in air.

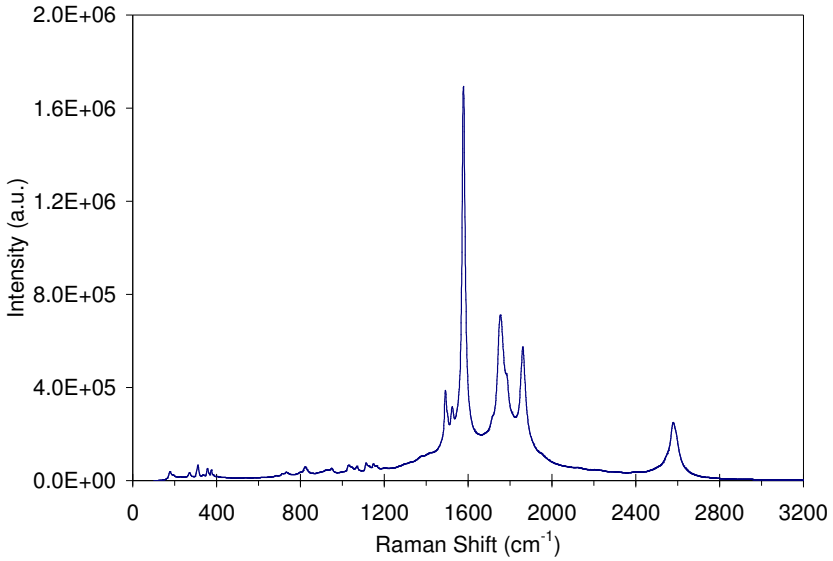

Figure 5.35: Raman spectrum of "non-SWNT" under 785 nm laser. The sample was held at 500°C for approximately 10 min in air.

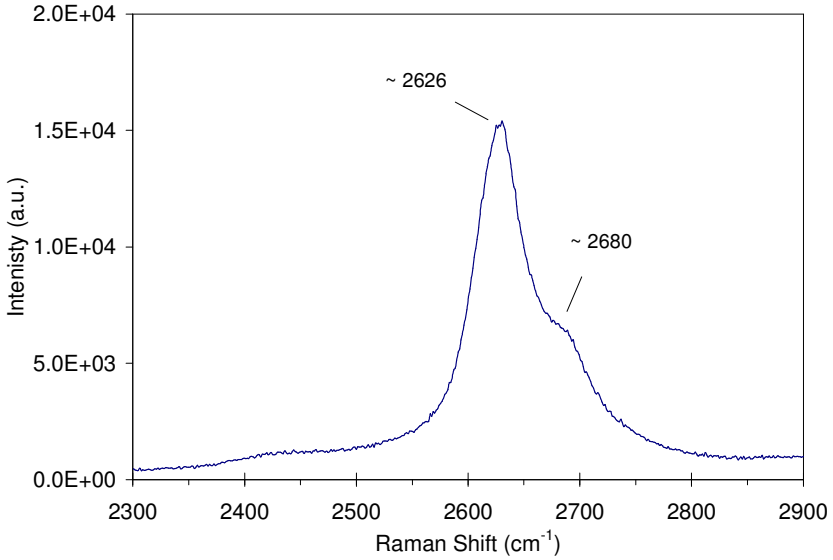

Figure 5.36: Raman G'-band of "non-SWNT" under 514 nm laser. The sample was held at 500°C for approximately 10 min in air.

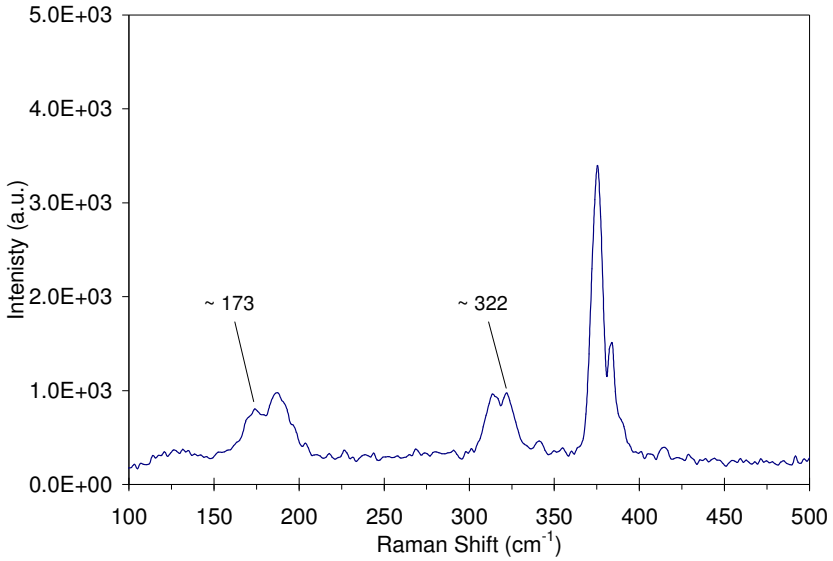

Figure 5.37: Raman RBM of "non-SWNT" under 514 nm laser. The sample was held at 500°C for approximately 10 min in air.

Mansfield et al. (2010), who studied the effectiveness of TGA analysis as a tool for nanotube quality control, observed some separation in the oxidation temperature between different species of carbon nanotubes (SWNT, DWNT, MWNT) from various mixed samples.[221] Taking advantage of the increased thermal stability for MWNT over SWNT and DWNT, a sample of thermally isolated "non-SWNT" carbon was generated by holding the TGA oven temperature at 500°C for approximately 40 min in air. It was hypothesized that this sample would have a relatively increased amount of MWNT, if present at all. Figure 5.38 displays the Raman spectrum for an area of this sample under 514 nm laser. The absence of RBM peaks, relatively low spectral intensity, and the large D-band vibration are characteristic of a MWNT or carbon nanofiber. Since no large diameter (10^2 nm) materials were observed by SEM or TEM (shown in later sections), the role of carbon nanofibers was ruled out. Thus, in addition to the high purity SWNT or DWNT, MWNT were also present in the CG200 sample. In order to confirm these observations, high resolution TEM was required.

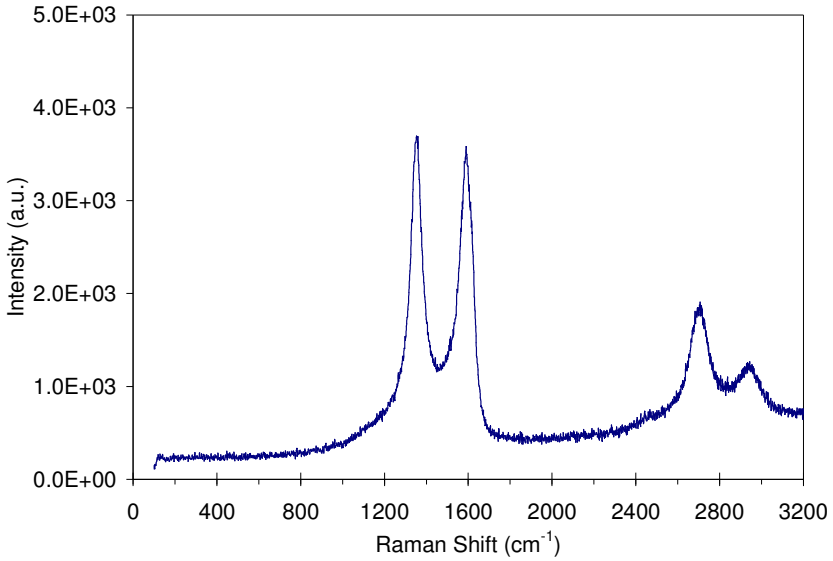

Figure 5.38: Raman spectrum of "non-SWNT" under 514 nm laser. The sample was held at 500°C for approximately 40 min in air.

The second batch of non-SWNT carbon sample, isolated by holding TGA oven temperature at 500°C for approximately 10 min, was swirled with a small amount of isopropyl alcohol and dropped onto a TEM grid. After solvent evaporation, the grid was analyzed using a JEOL ARM200F TEM and imaged with an 80 kV acceleration voltage. Figure 5.39 and Figure 5.40 display the sample under a magnification of 600,000 x and 2,000,000 x, respectively. In Figure 5.39, all three possible carbon nanotube species were observed: SWNT, DWNT, and MWNT. A horizontal bundle of SWNT was observed on the bottom of the image. In the center of the image, a horizontal and distended MWNT was observed. It appears that the thermal separation process had damaged the high strain innermost shell of the MWNT. The vertical or near vertical nanotubes appeared to be DWNT. In order to confirm this, a higher magnification image was shown by Figure 5.40. The narrow distance between the inner and outer shell of the DWNT was clearly observed, confirming conclusions from Raman analysis. In both samples the small dark spots represent CoMo catalyst and the large dark area appears to be a sintered CoMo catalyst particle. Note that the thermal isolation procedure also concentrates the catalyst.

By combining Raman, SEM, and TEM analysis, the "non-SWNT" carbon content of CG200 was found to contain SWNT, pristine DWNT, and MWNT. Based on the effect of sonication time and intensity, as observed using Raman and TGA, it appears the destruction of "non-SWNT" carbons into defective residues containing sp^3 hybridized structures skews the interpretation and analysis of Bingel functionalization data. Therefore, functionalization or processing methods requiring sonication are not appropriate for processing CG200 when certain metrics such as I_D/I_G are to be tracked. This finding has a broad impact on the field of carbon nanoscience as increasing numbers of researches utilize CoMoCAT SWNT.

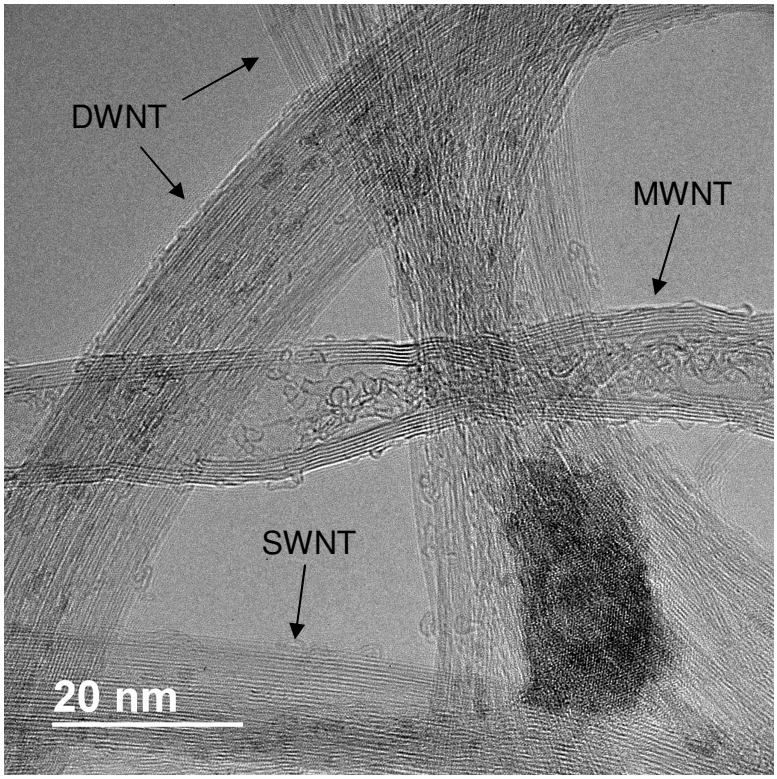

Figure 5.39: TEM image of isolated non-SWNT carbons by TGA oxidation at 500°C. Image magnification was 600,000 x showing SWNT, DWNT, and MWNT all present in the bulk CG200 sample. The dark spot was CoMo catalyst. The scale bar was 20 nm.

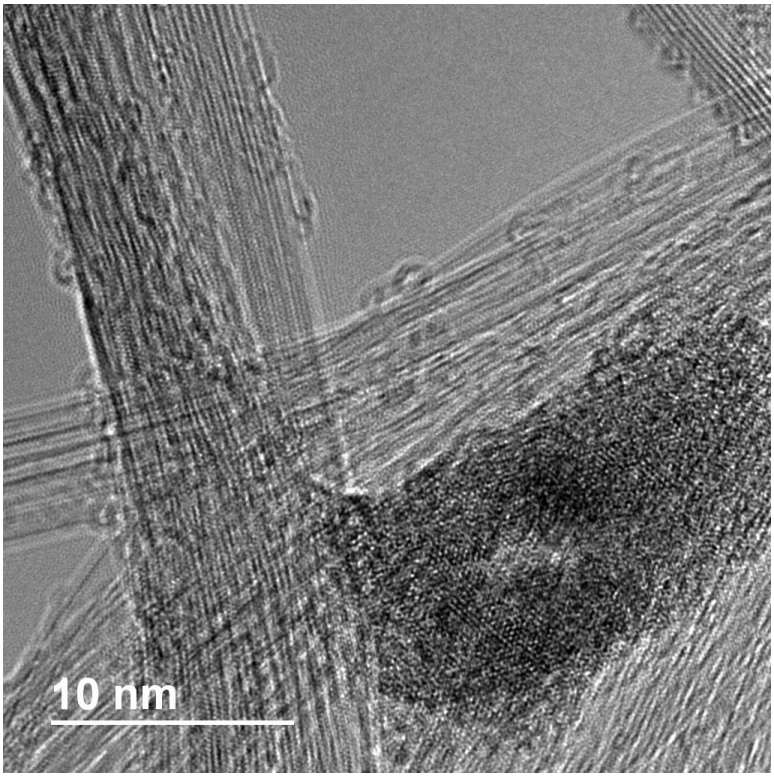

Figure 5.40: TEM image of isolated non-SWNT carbons by TGA oxidation at 500°C. The DWNT sidewalls are remarkable intact and pristine. Image magnification was 2,000,000 x showing inner and outer walls of DWNT. The scale bar was 10 nm.

5.1.11 Alternative Solvents for Bingel Reaction

Two main problems preventing accurate determination of the extent of functionalization were found to be a result of the inherent SWNT sample degradation and generation of substantial SP mass by sonication. Due to the difficulty in removing generated SP from the sample, an alternative solvent was desired. Note that there was no specific need to use oDCB for this reaction even though it was favored in past studies. For example, the seminal work of Bingel used toluene. The use of oDCB was likely favored due to its relatively high dispersion limit compared to other small molecule organic solvents and, more importantly, its efficiency in generating individual tubes.[166] Nevertheless, the only fundamental requirement for solvent selection would be a polar aprotic nature to avoid side reaction with DBU. To illustrate proof of

concept, the Bingel reaction was carried out for 12 h in anhydrous THF. This solvent is non-ideal, however, due to its low solvent properties compared to oDCB as well as having a relatively poor dispersion limit for SWNT. Table 5.8 displays preliminary analysis by Raman spectroscopy. Remarkably, even after 12 h of sonication the reacted SWNT show low I_D/I_G ratio which indicated functionalization or damage was minimal. Thorough analysis would be needed to determine the extent of damage. However, the preferred increase for metallic SWNT under 514 nm laser excitation was compelling evidence that damage was minimal, based off the reported nucleophilic mechanism of the reaction. Due to the existence of 1-D density of states in metallic SWNT at the Fermi level (Figure 5.41), metallic reactivity should be preferred.

	Raman I_D/I_G	
Type	514 nm	785 nm
CG200	0.09	0.07
Bingel THF	0.12	0.10

Table 5.8: Raman ratio for 12 h Bingel reaction in THF.

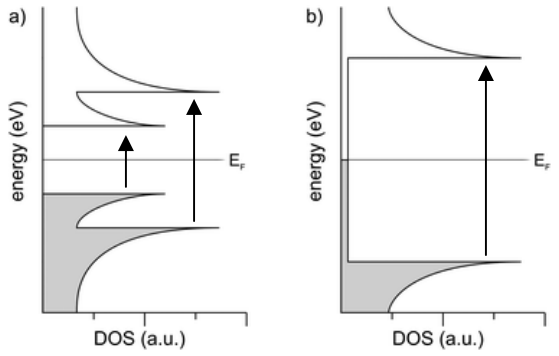

Figure 5.41: 1-D density of states for SWNT showing (left) S_{11} [short arrow], S_{22} [long arrow] and (right) M_{11} transitions.

5.2 Conclusions

A detailed investigation into the effect of Bingel reaction conditions on CoMoCAT SWNT was carried out for the sidewall esterification reaction. At 12 h of sonication time, the product was found to contain ~75 wt. % SP and functional groups. A mass balance in an oxidative

environment was required to determine the relative concentrations of material in the product since the SP persisted in argon, even at high temperatures. Unfortunately, this polyphenyl SP was found to be both thermally robust and relatively insoluble. The simultaneous thermal degradation of SP and functional group cleavage prevents accurate decoupling of the two species by TGA. But, the evolution of hydrogen chloride from pyrolyzed SP was readily observed as quantized HCl vibrations, providing a new metric for easily confirming SP presence. Raman analysis found uncharacteristically high extents of functionalization for a nucleophilic addition reaction on SWNT. Thus, further investigation was done on the influence of the sonication process on the SWNT using various non-polymerizing solvents. Detailed TGA analysis revealed degradation of the so-called "non-SWNT" carbon component in the mass loss spectra which was coupled with an up-shift in the SWNT oxidation temperature. This up-shift was also observed in Bingel functionalized SWNT samples. Unfortunately, the sonicated "non-SWNT" carbon degradation product skews TGA mass loss curves. In addition, the influence of the degradation material was observed in the Raman spectrum. As a result, the reported extent of functionalization was far too high for this chemistry. The supposed "non-SWNT" carbons were identified as high purity SWNT, high purity DWNT, and MWNT by Raman, SEM, and TEM analysis. Finally, the discovery and identification of the inherent processing instabilities of CoMoCAT SWNT has potential consequences for past, current and future nanotube researchers by generation of unintended experimental artifacts which skew data interpretation.

Due to the detrimental effect of SP on the dispersion if SWNT in UPR, a washing protocol in DMAc was investigated for functionalized and non-functionalized SWNT. Centrifugation was used in an attempt to fractionate samples. Based on TGA and Raman analysis, the non-functionalized sample containing only SP SWNT showed SP fractionation while maintaining

even SWNT defect distribution between supernatant and residue phases. Conversely, the increased affinity of the ester functionalized Bingel SWNT for the DMAc solvent failed to fractionate the SP but did fractionate the SWNT quality. Thus, the washing protocol was ineffective in separating functionalized samples.

Due to many coupled effects of processing on the analysis of Bingel SWNT, the bulk dispersion into UPR was used to determine the effects of SP and functional groups on dispersion. Interestingly, the non-functionalized SP SWNT show no dispersion into UPR without first treating with the washing protocol to induce desorption of SP material. By simply attaching the Bingel chemistry to the non-washed SP SWNT, bulk dispersion was restored. These experiments indicate that the adsorbed SP was detrimental to the dispersion of SWNT but this shortcoming was overcome by changing the surface chemistry, which dominated the dispersibility. Therefore, the best dispersion of Bingel SWNT would be anticipated for SP free material. To this end, exploration of alternate solvents than oDCB, such as THF, was pursued with preliminary success.

Finally, in contrast to HiPco SWNT, the sonication of CoMoCAT SWNT in oDCB did not show the effects of doping on electronic structure. This was investigated by Raman spectroscopy. The absence of Fe catalyst in the CoMoCAT sample was believed to be the reason for this observation.

Chapter 6

Non-covalent Functionalization by Polymer Wrapping

6.1 Stabilization and Interaction of SWNT with Polyvinylpyrrolidone and Unsaturated Polyester Resin

The non-covalent functionalization of SWNT by polymer adsorption has the benefit of not damaging the nanotube sidewall, as in covalent chemistries, but also has the disadvantage of introducing a third polymer component to the system. Therefore, the polymer must be carefully selected so as to not desorb or hinder dispersion in the intended solvent. This is challenging for application with many polymers, since the initial dispersion preparation often occurs in the aqueous phase. One relatively unique polymer is polyvinylpyrrolidone (PVP), which is soluble in water and in many organics due to its chemistry and interaction with its environment. The adsorption of PVP to SWNT in water is driven by the hydrophobic effect[183] and CH-π interactions. Recent success on the stabilization of graphene in PVP, and solvent switching from aqueous to organic by freeze drying, has motivated a thorough investigation on this method for SWNT.[222] The focus of the work herein, was on the specific interactions between each component to understand the intricacies of the system and characterize the applicability of PVP as a stabilizer for use in UPR.

6.1.1 Preparation of Polyvinylpyrrolidone Dispersions

The methodology for SWNT dispersion was based on the solvent switching experiments for graphene flakes in aqueous PVP by freeze-drying.[222] In the present study, a stock concentration of 10 mg PVP per mL of water (~1 wt. %) was used. This was stirred to dissolve the polymer. Previous studies have suggested a SWNT concentration of 0.36 mg/mL for various surfactants and polymers including PVP.[223] A concentration of 0.31 mg/mL (0.0172 vol. % after dilution) was chosen. Five mg of SWNT was added to a vial with 15 mL of PVP stock solution and this was bath sonicated for 20 min to start the dispersion and coating process. Bath sonicated was needed to prevent undesirable foaming during tip sonication. The sample was placed in an ice bath and allowed to cool for 20 min. Cooling was required to prevent selective PVP desorption.[186] The cold sample was tip sonicated at 60 % amplitude for 30 min with a 5 s on and 3 s off pulse within an ice bath. The sample was allowed to settle overnight to precipitate aggregated and high density material. The sample was then decanted and the residue discarded. Batch 1 was spun down at 5,000 RPM for 2.5 hr, based on results for graphene.[222] This condition was referred to as light centrifugation. Due to the higher density of graphene sheets, these experimental conditions were likely not ideal for SWNT. Batch 2 was spun down at 17,000 x g for 3 hours based on the isolation of SWNT in double-stranded DNA.[224] Samples were then decanted and diluted as necessary for qualitative UV-vis spectra. Note that optical properties are not affected by excess PVP.[200] Supernatant samples were placed in 50 mL polypropylene centrifuge tubes and frozen after the total volume was increased to ~19 mL with water. Finally, these were moved to a freeze dryer for 36 h. A second concentration of 0.13 mg/mL (0.00689 vol. % after dilution) with strong centrifugation conditions was also studied and used primarily for Raman studies.

6.1.2 Phase Behavior of SWNT Dispersions

CG200 SWNT have a manufacturer specified aspect ratio of 1000 and a mean diameter of 1.01 nm. Based on these dimensions, the relevant phase transitions for Brownian rigid rods in solutions can be compared.[78] Equation 24 displays the critical concentration for the dilute to semidilute transition ϕ_0. Equation 25 displays the upper semidilute limit $\phi_0^{'}$.

$$\phi_0 = 24\left(\frac{L}{d}\right)^{-2} \tag{24}$$

$$\phi_0^{'} = \frac{\pi}{4}\left(\frac{L}{d}\right)^{-1} \tag{25}$$

The dilute-semidilute critical concentration $\phi_0 \times 10^2$ was found to be 0.0024 vol. % and the upper limit of the semidilute regime $\phi_0^{'} \times 10^2$ was found to be 0.0785 vol. %. The initial dispersion concentrations were 0.31 mg/mL and 0.13 mg/mL SWNT. Those concentrations translate to 0.0229 vol. % and 0.0091 vol. %, respectively. Both of these concentrations are in the lower half of the semidilute regime where rods are free to translate. Increasing the total volume to ~19 mL prior to freezing further decreased the concentration to 0.0181 vol. % and 0.0073 vol. %, respectively. Thus, the initially 0.13 mg/mL sample approached the dilute transition after dilution. A more dilute SWNT concentration would decrease the probability of aggregation during lyophilization steps.

6.1.3 Physicochemical Effect of Solvent on Polyvinylpyrrolidone

A number of slightly different structural mesomers or tautomers of PVP exist depending on the nature of the solvent. This is a result of resonance in the conjugated structure between the unpaired electrons of N and C=O in the pyrrolidone group. When the resonance is stabilized,

however, the imidate like anion, C-O$^-$ is preferred.[177] The interconversion between these aforementioned structures is highlighted by Figure 6.1.

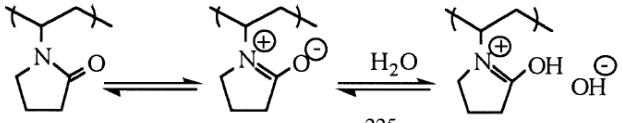

Figure 6.1: Induced mesomerism of hydrated PVP.[225] Shown are the (left) amidate-like and (center) imidate-like ion structures (with partial positive charge on tertiary N). Interaction with water (right) hydrates the anion and the charge is screened by hydroxide.

Although commonly referred to in the literature as tautomerism, PVP's interconversion has unique characteristics not typically found in classic tautomers. In organic chemistry, tautomerism can be thought of as a proton-transfer equilibrium resulting in the interconversion of a keto to enol structure (similarly, lactam to lactim and amide to amidic acid).[226] Typically, these transformations occur in acidic or basic media with equilibrium values favoring the ketone. PVP is inconsistent with a tautomer since the hydrogen atom typically transferred from the N-H in a lactam to a lactim structure does not exist due to bonding with the polymer backbone. Instead, the lone pair of electrons on N are conjugated with the double bond in the carbonyl. The interconversion is more of a resonance hybrid structure than a true tautomer. The unpaired electrons centered on PVP's N atom (not shown) are shared with the carbonyl carbon. This is further stabilized in hydrogen bond donating media. The interaction of water with PVP stabilizes the inter-conversion of the isomer by hydrating the imidate like anion.[225] This can be treated as a resonance hybrid structure and the ground state energy is lowered upon hydrogen bonding.[227] Due to steric constraints from the hydrocarbon backbone, the positive charge on the nitrogen was thought to be shielded from the environment. As a result, a partial charge on PVP was expected in solution; this attracts additional anions (see discussion on complexation with SDS). Interestingly, Rothschild (1972) also proposed sharing of a bond donor between O and N

in the pendant group of 1-ethyl-2-pyrrolidinone which decreased the conjugated C-N/C=N bond intensity.[177] Conversely, Türker et al. (1990) argued that simultaneous bond formation in PVP was unlikely due to partial positive charge on the N.[227] These arguments were tested by the proposed FTIR interpretation described in the next section. Note that the hydrated anion shown in Figure 6.1 is also susceptible to further tautomerization depending on the environment of solvated PVP such as shown by Figure 6.2.

Figure 6.2: Further tautomerization under certain solvent environments.[227]

As previously mentioned, various additional mesomer structures are shown in the literature. Figure 6.3 displays a tautomerization which suggests abstraction of an adjacent hydrogen from the -CH_2- group located next to the carbonyl. Finally, it was noteworthy that structures containing O-H bonds exist as shown by Figure 6.4. This was interesting due to the discussion on O-H bonds in anhydrous PVP in the following sections.

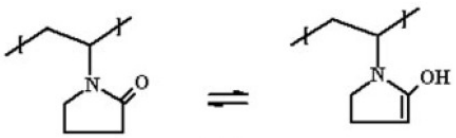

Figure 6.3: Tautomerization by hydrogen abstraction.[228]

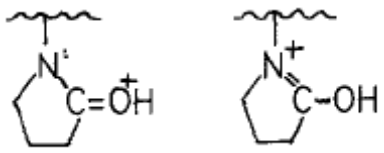

Figure 6.4: Protonated lactam and lactim.[227]

6.1.4 FTIR Study of Polyvinylpyrrolidone

The FTIR spectrum of as-received (wet) PVP is shown by Figure 6.5. Complete PVP spectral assignments were recently made by Bhajantri et al. (2009).[228] The most prominent feature was the carbonyl stretch at 1648 cm^{-1}. Interestingly, the broad characteristic band of an O-H stretch was also found at ~3400 cm^{-1}. This functional group was absent in the molecular structure of PVP, and therefore must the result of a contaminant. In order to test this hypothesis, PVP was oven dried under vacuum (~30 min) at 60°C and re-analyzed. As displayed by Figure 6.5, the spectrum of hot oven dried PVP showed no O-H stretching band. Thus, it can be concluded that PVP readily adsorbs atmospheric water that can easily be driven off by drying. As discussed in following sections, the interaction of PVP with water also results in the interconversion of PVP mesomers. In order to increase the handling time of dry PVP material was oven dried but cooled under vacuum. Figure 6.5 also shows the spectrum of oven dry and cooled PVP. The O-H stretching band was also absent in this sample which indicates that vacuum cooling does provide a sufficiently dry polymer. Furthermore, the hot and cold dried PVP sample spectra overlap well. Increased absorbance at low frequencies, however, was observed for the wet polymer sample. In addition, an apparent C=O shift to lower wavenumber was seen when moisture was present. This shift was displayed more readily by examining the carbonyl region highlighted in Figure 6.6 which is often referred to as the Amide I band. Comparison between the dried samples shows hardly any effect from temperature under experimental conditions. The cool, oven dried PVP shows a peak centered at 1667 cm^{-1}, whereas the hot sample shows only a slight up shift to 1668 cm^{-1}. Conversely, the wet PVP sample shows significant peak broadening and a shift to a lower energy wavenumber of 1648 cm^{-1}. For the scaled spectra, the full peak width at half max intensity (FWHM) were ~51 cm^{-1} for the wet sample and ~44 cm^{-1} for the cool and dry

PVP. Furthermore, this peak shift was closer to the peak position of O-H bending in water. Therefore, the interaction of PVP with water not only induces significant red shifting of ~21 cm^{-1} but the active oscillators contributing to the spectrum change in nature upon lactam-water interaction. This was in agreement with the measurements of Rothschild (1972).[177] Calculations have found that the peak broadening and red-shift results from zero, single, and double hydrogen bonding with the carbonyl in lactams.[229,230] A calculated red-shift of 27 cm^{-1} was found for a single H-bond interaction, consistent with observations in this work. Physically, the shift results from C=O bond weakening due to interaction with a proton.[231] This could be due to a number of effects regarding the hydrogen bonding interaction of water with PVP. For example, PVP contains two adjacent hydrogen bond acceptor sites; the carbonyl oxygen and the nitrogen atom. Water, on the other hand, acts as a donor molecule. One or more of these interactions appears to soften the carbonyl stretch vibration in combination with potential resonance/tautomerization of PVP. Saraydin and Karadağ (2000) found the interaction of water with PVP stabilizes the inter-conversion of the enolate like structure by hydrating the resonance anion.[225] This mesomer would bear a positive charge on the N and H-bonding would be focused on the O. This phenomenon was further investigated by FTIR studies.

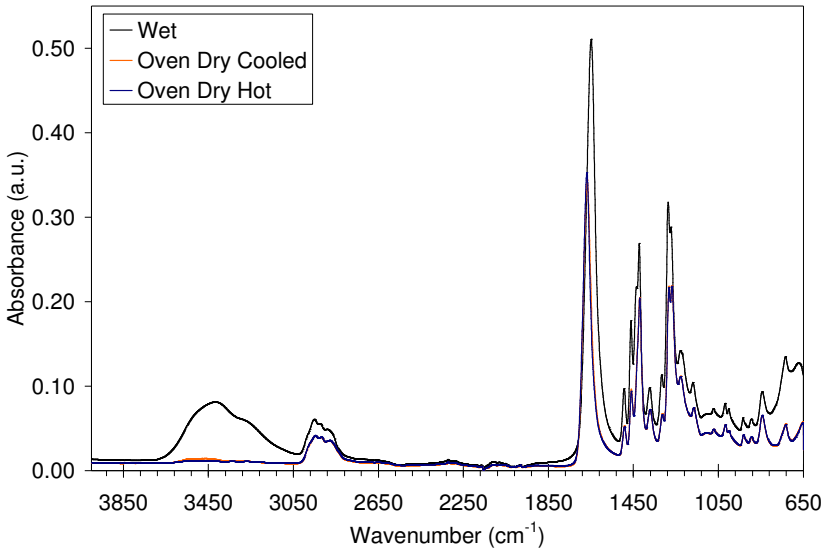

Figure 6.5: Comparison of pure PVP FTIR spectra with temperature and moisture content. The oven dried samples nearly overlap. Data not scaled.

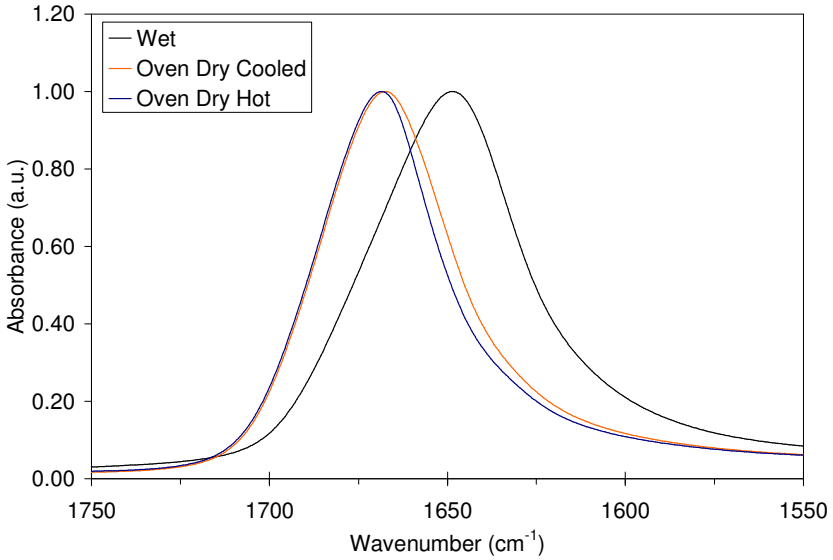

Figure 6.6: The effect of water on the PVP carbonyl vibration. Data scaled with max peak intensity. FWHM were ~51 cm^{-1} for the wet sample and ~44 cm^{-1} for the cool and dry PVP.

Figure 6.7 shows the C-N and C-H vibration region for PVP. Remarkably, in contrast to the C=O band, the peaks in this area exhibit slight blue-shifting towards higher wavenumber in the presence of moisture. For example, the peak found at 1419.8 cm^{-1} in the dry sample shifted up by 2.5 cm^{-1} to 1422.3 cm^{-1}. Table 6.1 summarizes the observed peak shifts. Furthermore, a

shoulder (location blue-shifted) appeared at 1435.3 cm^{-1} and the blue-shifted peak at 1272.8 cm^{-1} (1268.5 cm^{-1} dry) was depressed. Rothschild (1972) observed a decrease in peak intensity at 1425 cm^{-1} with increasing moisture content for 1-ethyl-2-pyrrolidone and assigned this peak as the conjugated C=N stretch.[177] Remarkably, they did not observe shifting for 1-ethyl-2-pyrrolidone, in contrast to the current PVP results. This may be due to the effect of shielding part of the molecule by the polymer backbone in PVP. For PVP, the shift in mesomer to form N^+, was not balanced by H-bonding access to the unpaired electrons of N in the native lactam. Thus, the observed blue-shift indicated a preference for the C=N over C-N^+ mesomer linkage. Based on the proposed mesomerism and interaction with water, the decrease in intensity of the wet peak at 1422.3 cm^{-1} and appearance of the shoulder at 1435.3 cm^{-1} were correlated with preferential resonance splitting of the C-N group to C=N. The effects of C=O redshifting and C-N/C-H blue-shifting were consistent with observations for PVP where the exact opposite trends in D_2O were observed from hydration in absence of H-bonding.[229] These effects are not observed in dilute PVP solutions in water.

The subtle loss in intensity of the blue-shifted peak doublet at 1272.8 cm^{-1} was believed to be related to the mesomer and interaction with water. The exact assignment of this peak was confusing. For example, the peak at 1285 cm^{-1} was assigned to a CH_2 deformation by some,[228] consistent with the CH_2 wagging at 1290 cm^{-1} observed elsewhere.[230] Ambiguously, however, peaks located from 1320 - 1210 cm^{-1} are common in carbonyl compounds. Specifically, from 1320 - 1280 cm^{-1}, carboxylic acid dimers can show a doublet for the C-O stretch. An interpretation of C-O band splitting upon resonance would make sense here, but upon H-bonding mesomerism, this band would be expected to red-shift from decreased double bond character, so this assignment was ruled out. Also misleading were assignments for peaks at 1496 cm^{-1} and

1372 cm^{-1} which were previously assigned to C-H deformations.[228] Conflictingly, the band at 1490 cm^{-1} by Liu[229] and 1481 - 1494 cm^{-1} by Madea[230] were also previously assigned to C-N in lactams. Behera and Ram (2012) assigned the peak at 1463 to C-N and 1381 to CH_2.[232] Peaks at 1497, 1466, 1447, 1321, and 1294 cm^{-1} have all been generally assigned to C-N.[233] The blue-shifting observed in the spectrum was not expected for these assignments, however, since these hydrogens do not participate in traditional H-bonding. An H-bonding blue-shift, however, has been observed elsewhere.[230] The phenomenon originates from an interaction between the C-H proton and water. Water has been shown to push electron density of H towards C-H bond via CH-O interactions. This effectively stiffens the C-H bond and results in a blue shift.[234] The observation of a blue-shifting hydrogen bond has been shown to be consistent in nature with red-shifting interactions.[235] Therefore the peak at ~1280 cm^{-1} was assigned to a C-H mode. In dilute solutions, the peak at ~1270 cm^{-1} was barely observed but not assigned.[230] Depending on the concentration it may have only a slight presence.[233] The peak was left unassigned for now, but its change in intensity indicates it was related to the H-bond induced mesomerism. Note that this peak lies in the so called Amide III band region.

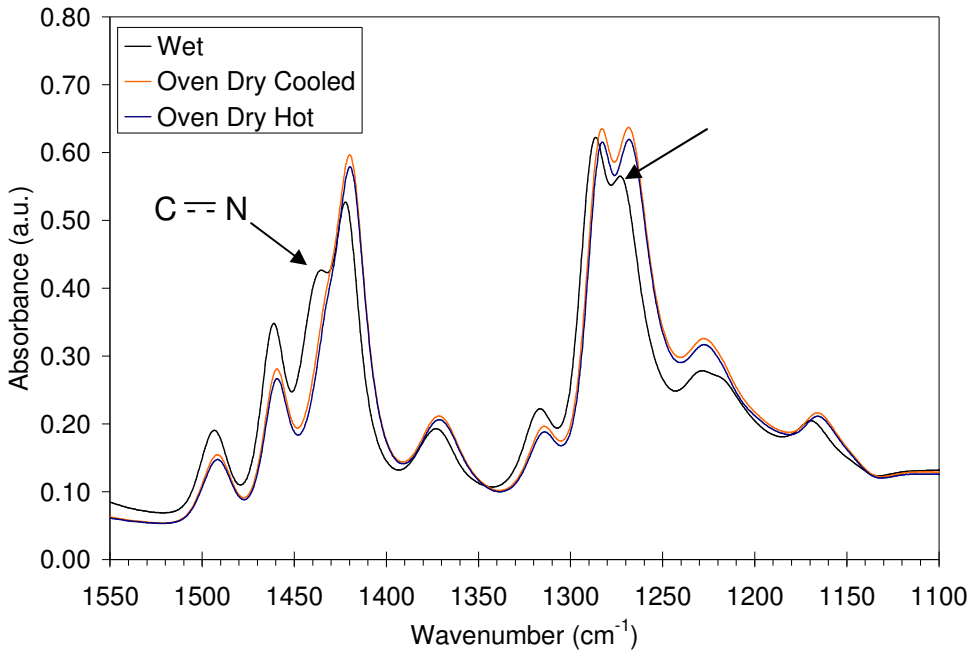

Figure 6.7: The effect of water on the C-N stretch of PVP.

Sample	ν_1 cm^{-1}	ν_2 cm^{-1}	ν_3 cm^{-1}
Dry	1419.8	1282.9	1268.5
Wet	1422.3	1286.3	1272.8

Table 6.1: Summary of peak shifts upon interaction with water.

Gaseous FTIR spectra were also obtained using coupled TGA-FTIR. Figure 6.8 displays the TGA mass loss and derivative curve for pure PVP. The degradation temperature of PVP in argon was measured to be ~433°C. Some residual mass remained at high temperatures and this was considered a contaminant included with the sample, as-received. Figure 6.9 shows the gas phase FTIR spectrum at peak TGA mass loss. Two prominent features were present and both assigned as carbonyl stretching vibrations. The first is located at 1631 cm^{-1} and the second is found at 1749 cm^{-1}. These were assigned to carbonyl vibrations in pyrrolidone rings tethered and cleaved free from the polymer backbone, respectively.

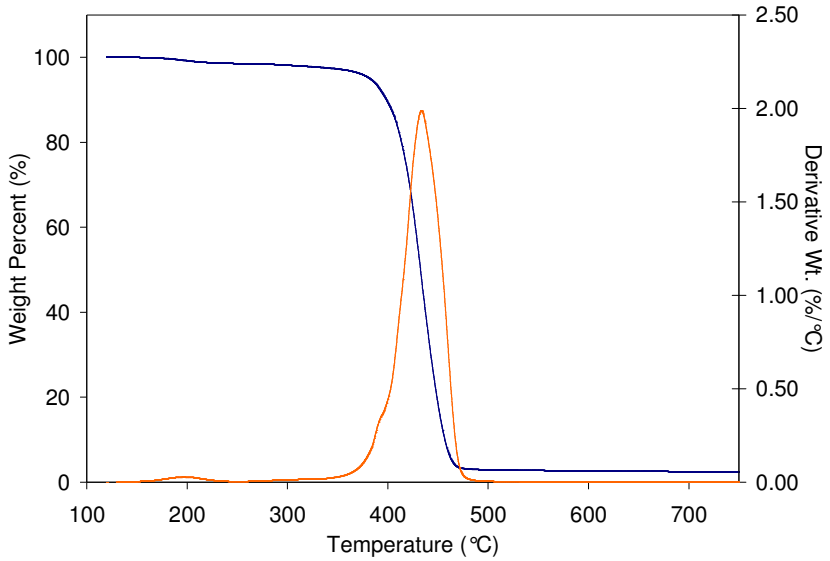

Figure 6.8: TGA mass loss curves for PVP in argon, 10°C/min ramp.

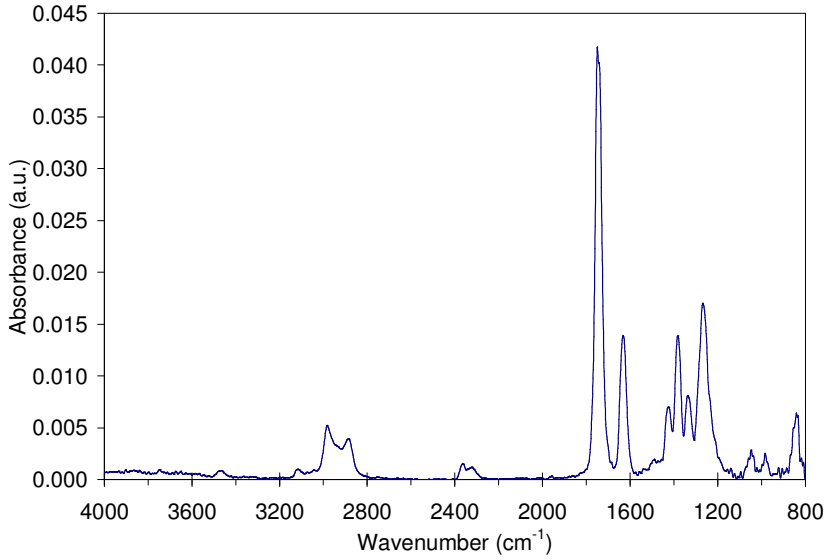

Figure 6.9: IR spectra of TGA oven gases during PVP peak mass loss.

6.1.5 The Effect of Sonication on Polyvinylpyrrolidone

The effect of sonication on PVP was investigated in order to determine if any experimental artifacts were introduced upon processing. In order to examine the effect of sonication on PVP, an aqueous PVP only dispersion was prepared with identical processing conditions used for the nanotube dispersions. To this end, PVP was dissolved in water at a concentration of 10 mg/mL

by magnetic stirring for 10 min. Subsequently, 15 mL of polymer solution was placed in a capped vial and submerged in an ice bath for 20 min. The tip of a probe sonicator was then immersed in the cold vial and vibrated at 60 % amplitude for 30 min treatment time with a 5 s on/off pulse. Additional ice was added after 20 min. Figure 6.10 displays the result.

Figure 6.10: PVP (10 mg/mL) in water, tip sonicated for 30 min.

The unexpected grey color is a result of tip erosion during the intense sonication process leading to dispersion of particles of a titanium alloy (confirmed by EDS), instead of the clear polymer solution. This sample was allowed to sit overnight. After centrifugation at 17,000 x g for 3 hours, the supernatant was collected as a clear liquid. Approximately 1 mL of this liquid was placed in a micro-centrifuge tube, frozen, and freeze-dried for 24 h. Figure 6.11 displays the IR spectrum for the polymer after oven drying (100°C) and cooling under vacuum. Noticeable O-H stretching bands were present even after freeze and oven drying, which indicated a structural change in the PVP itself or significant sample contamination. Detailed discussion is delayed until subsequent sections.

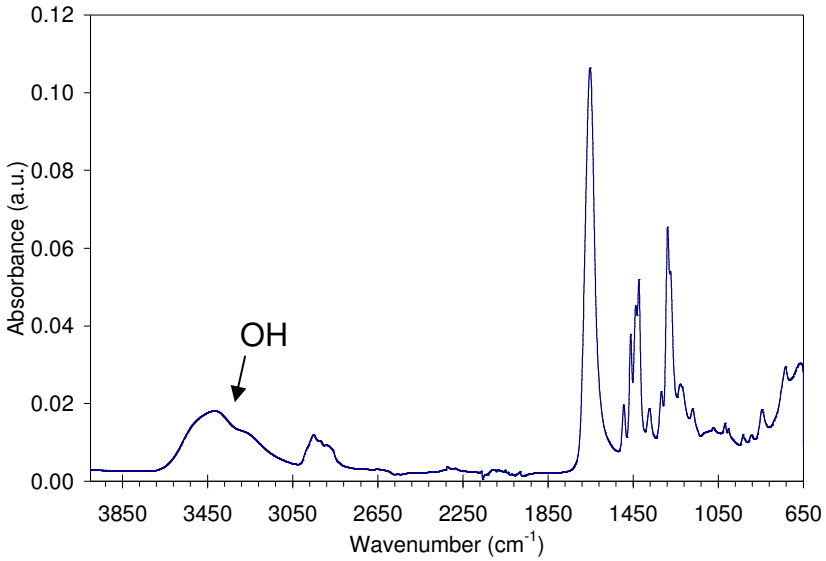

Figure 6.11: IR spectrum of dry tip sonicated PVP.

Due to potential for contamination from the sonicator tip from not only metal particles but also from residual compounds remaining from parallel experiments, long bath sonication of PVP was employed to simulate processing conditions and even exaggerate the sonication effect on PVP. In this experiment, the polymer solution was placed into a vial and capped before immersing into a bath sonicator for 8 h treatment time. After resting, the sample was centrifuged but no apparent residue was isolated. Interestingly though, a strong smell of charred polymer was apparent while working with this sample. Figure 6.12 displays the IR spectra of freeze dried and oven dried PVP after bath sonication compared to the dry and cool starting material. Similar to the tip sonicated spectra, the O-H stretch is readily apparent in the dry, bath sonicated sample. This region is magnified by Figure 6.13. The presence of the O-H vibrations in the bath sonicated sample confirms a structural change in the polymer itself and not the presence of sample contamination.

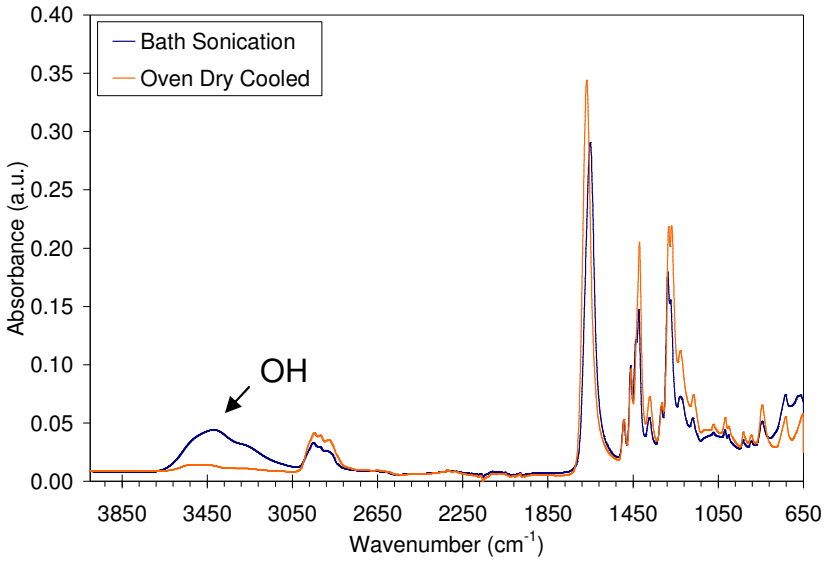

Figure 6.12: Effect of sonication on PVP spectra.

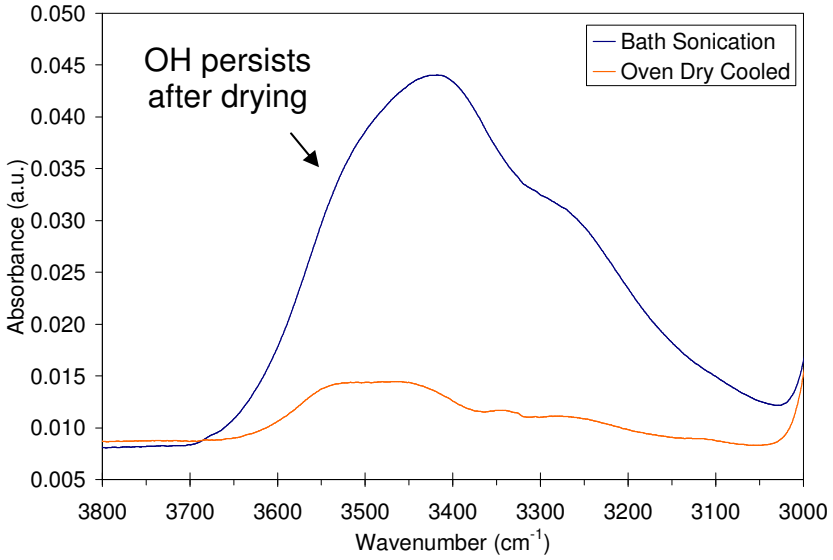

Figure 6.13: Effect of sonication on O-H stretching region.

Examining the carbonyl stretching vibration, shown by Figure 6.14, an apparent red shift was observed post-sonication. In this case, however, the spectra shifted 17 cm^{-1} from 1667 cm^{-1} to 1650 cm^{-1}, which was slightly less intense than the shift for the wet (~21 cm^{-1}) sample. Since no water was present, the apparent red shift was a result of PVP interacting with adjacent PVP molecules, proposed to be hydrated during sonication. Comparing the location of the O-H

vibrations, the peak position in the wet sample (3420 cm^{-1}) was similar to the sonicated sample (3424 cm^{-1}). The degree of redshifting was lessened with the sonicated PVP for both carbonyl and O-H vibrations. These results are summarized in Table 6.2. A closer examination of the C=O band was shown and compared to the wet sample in Figure 6.15. The bands were strikingly similar with a FWHM of ~46 cm^{-1} for the bath sonicated PVP and ~51 cm^{-1} for the wet sample. This seems to indicate the C=O hydrogen bonding structure was similar despite the differences in the reversibility of hydration between them. Remarkably, the C-H and C-N stretching vibrations also showed consistent features with the wet PVP sample as well. Notably a shoulder appeared at 1435.8 cm^{-1} and a depressed shoulder appears at 1273.8 cm^{-1}. Almost identical peak positions were obtained for the wet sample (Table 6.3). These results indicated that sonication of PVP in water had a similar physical interaction as PVP does with ambient water, even though sonication rendered the hydration irreversible. Furthermore, the consistency of the blue-shifted peak depression at ~1273 cm^{-1} between samples supports the assignment of this band to be related to the hydrated mesomer. While it was reasonable to assign this peak to out-of-plane CH_2 deformation, blue-shifted from H-O H-bond interaction, the decrease in intensity instead indicated this band was related to C-N and possibly coupling between C-N and neighboring C-H vibrations. Additional experiments to try and elucidate the nature of any structural change of PVP upon sonication were carried out using coupled TGA-FTIR.

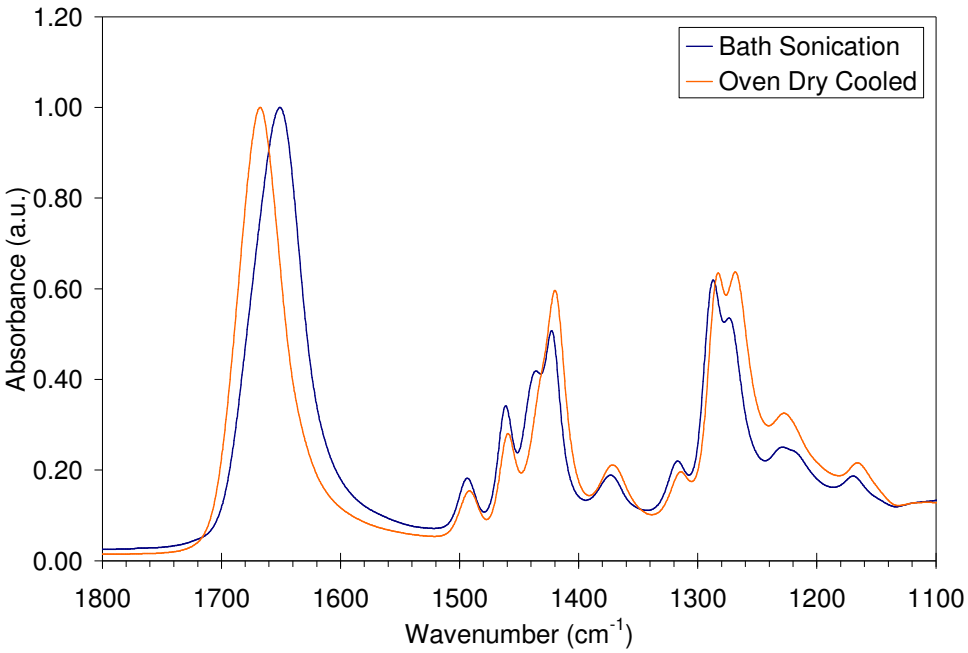

Figure 6.14: Effect of sonication on carbonyl stretching region. The C=O band FWHM were ~46 cm^{-1} for the sonicated sample and ~44 cm^{-1} for the cool and dry PVP.

Sample	$\nu_{C=O}$ cm^{-1}	ν_{O-H} cm^{-1}
Dry	1667	-
Wet	1648	3420
Bath	1651	3424

Table 6.2: Summary of FTIR peak positions in PVP samples.

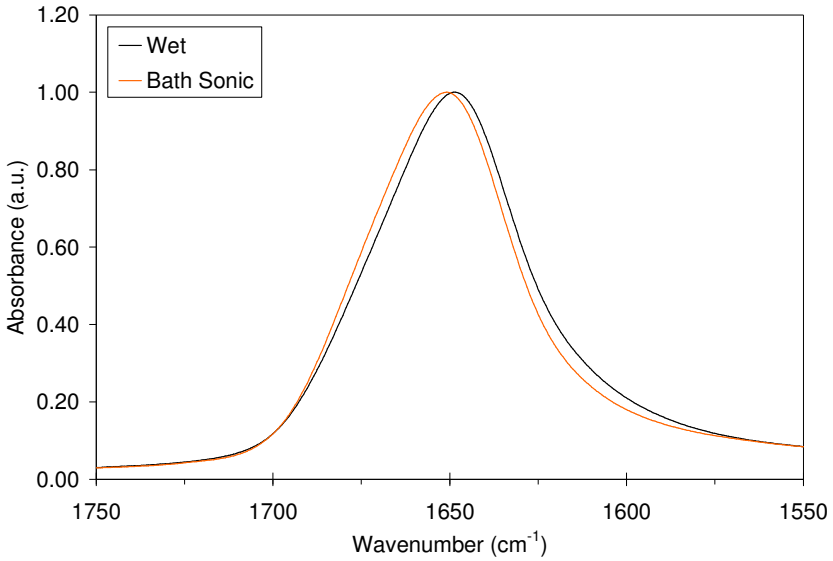

Figure 6.15: A comparison of the water - C=O interaction by reversible and irreversible hydration. Data scaled with max peak intensity. FWHM were ~51 cm^{-1} for the wet sample and ~46 cm^{-1} for the sonicated PVP.

Sample	$\nu_{shoulder}$ cm^{-1}	ν_1 cm^{-1}	ν_2 cm^{-1}	ν_3 cm^{-1}
Dry	-	1419.8	1282.9	1268.5
Wet	1435.3	1422.3	1286.3	1272.8
Bath	1435.8	1422.8	1286.8	1273.8

Table 6.3: Summary of peak shifts upon interaction with water and sonication.

In Figure 6.16, the thermal degradation of sonicated PVP samples were compared to the starting material. All samples were dried in the TGA oven at 120°C before ramping temperature to 800°C. Two trends with increased sonication energy input/time were observed: (1) mass loss prior to degradation increased (seen in Figure 6.17 derivative curve as well), indicating low molecular weight PVP created by chain scission was removed and (2) the presence of high temperature residues increased, indicating potential polymer crosslinking (recall noted smell). Measured degradation temperatures extracted from the derivative mass loss curves shown in Figure 6.17 showed similar values of 434.7°C for tip, 433.3°C for bath, and 433.4°C for the starting material.

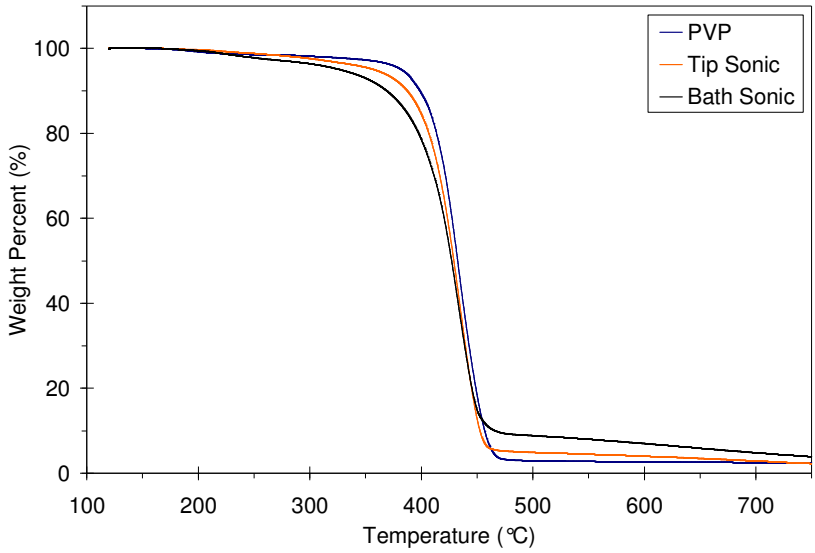

Figure 6.16: TGA mass loss curves of PVP with varied sonication treatment.

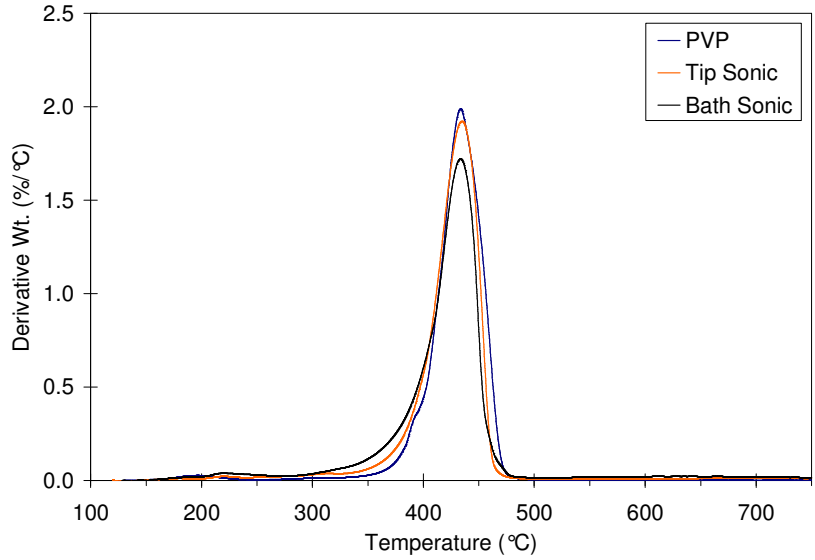

Figure 6.17: TGA derivative loss curves of PVP with varied sonication treatment.

FTIR analysis of the effluent gas during peak thermal loss showed no apparent difference from the starting material. Note that due to differences in initial mass loaded in the TGA pan, one must be careful not to over-generalize gas effluent analysis. Figure 6.18 shows the overlaid spectra. These results were inconclusive.

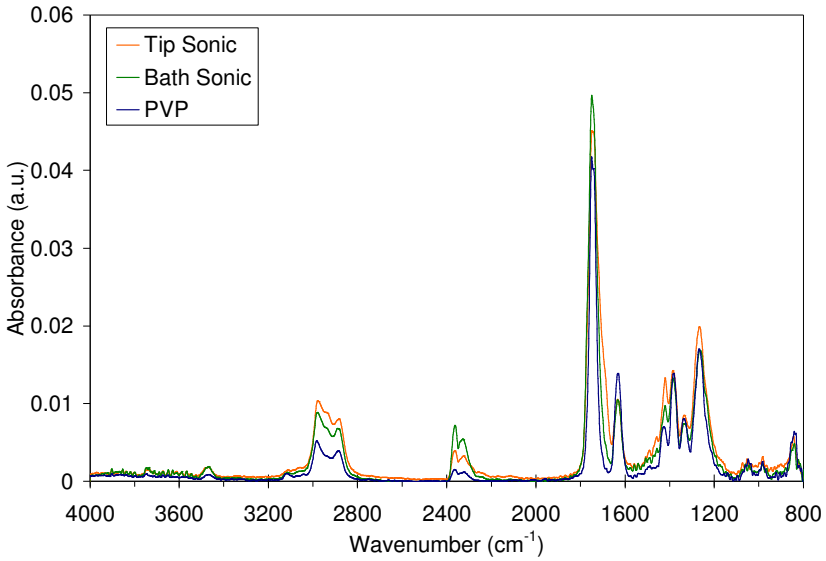

Figure 6.18: Peak loss IR spectra for sonication of PVP.

Even more evidence of a structural change in PVP with sonication was given by comparison of UV-vis absorbance spectra in Figure 6.19. With more extreme sonication treatment, there was a clear broadening of the spectra associated with the active chromophore, the lactam carbonyl.[227] Figure 6.20 displays the active chromophore's excitation from oxygen to carbon.

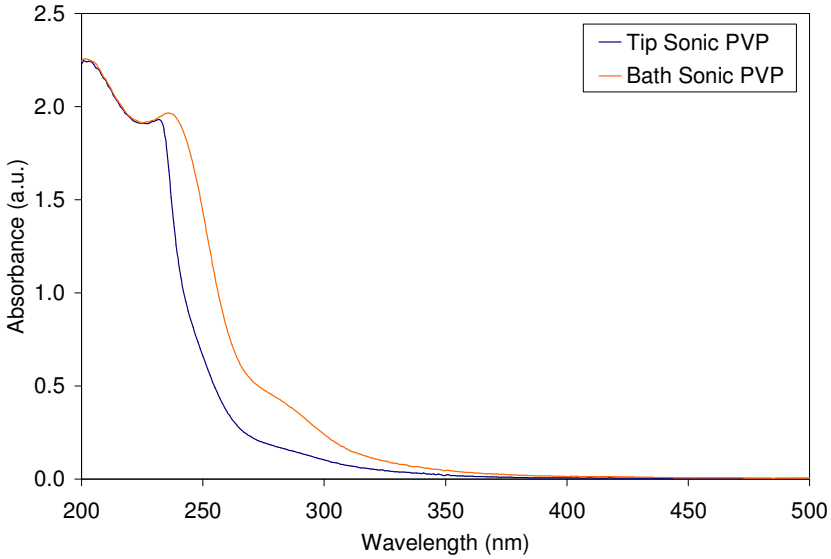

Figure 6.19: UV-vis spectra of PVP with varied sonication treatment.

$$C=O \xrightarrow{n\rightarrow\Pi^*} \dot{C}=\overline{O}_+$$

Figure 6.20: Transition from ground to excited state in the carbonyl.[227]

6.1.6 Interaction of Polyvinylpyrrolidone with UPR

In a quiescent state, PVP will dissolve in UPR to produce an optically clear resin with noticeably modified viscosity (see Figure 6.39). The dissolution process was slow, taking a day or so, likely due to the UPR viscosity inhibiting kinetics. After initially clouding the polymer, any apparent visible scattering from the PVP disappears with time. Both the isophthalic polyester and PVP are similar in that they lack any hydrogen bond donor sites but contain many acceptor sites in the carbonyl oxygen atoms located along the polymers. It would be reasonable to assume that the apparent solubility of PVP in UPR might be a result of so called general "like-like" interactions as a result of similar solubility parameters. In order to investigate this behavior, spectroscopic studies were carried out. Figure 6.21 displays the neat IR spectrum for UPR.

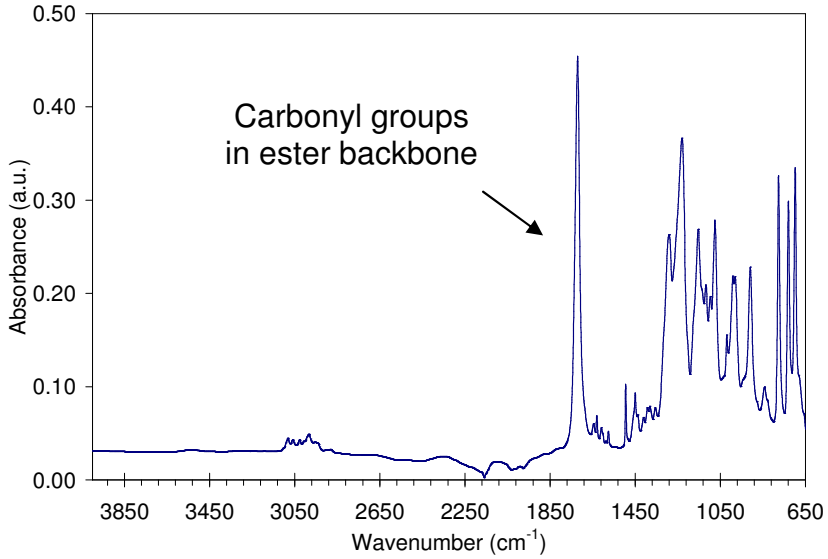

Figure 6.21: IR spectra of neat UPR.

The most prominent feature was the carbonyl stretch of the ester functional group in the UPR oligomer backbone located at 1720 cm^{-1}. The various aromatic C-H vibrations were also observed above 3000 cm^{-1}, originating from benzene rings in polyester and styrene. Next, cool and dry PVP was added to UPR at various concentrations and magnetically stirred to speed dissolution. The IR spectra of these liquids are shown by Figure 6.22. At a concentration of 10 mg/mL (0.9 wt. %), the PVP-UPR spectrum was indistinguishable from the neat UPR. Furthermore, there appeared to be no influence on the interaction between these two components as the C=O vibrations superimposed at 1720.3 cm^{-1}. This might simply be a consequence of the detection limit of the instrument, or more likely, the low intensity of these dilute contributions. Increasing the PVP concentration to 150 mg/mL (12 wt. %), a new peak in the PVP-UPR spectrum appeared at 1685 cm^{-1} (see arrow). Note that the carbonyl peak of sonicated PVP (150 mg/mL) in UPR was found at ~1680 cm^{-1}. The band at 1685 cm^{-1} was attributed to the carbonyl stretch in PVP. For point of reference, the dry PVP spectrum was overlaid. Recall, that in the dry and neat PVP sample, this peak was located at 1667 cm^{-1} and red-shifted substantially with moisture or sonication treatment. In the anhydrous environment of UPR, absent of H-bond donors, a substantial blue-shift of 18 cm^{-1} was observed. This shift to higher frequency was indicative of carbonyl bond stiffening. This result indicated that isolation and separation of adjacent PVP chains, by dissolution in UPR, does not show resonance stabilization and bond weakening from neighboring hydrated groups. Thus, at these concentrations, PVP was soluble in UPR at a molecular level. Remarkably, the C=O band in UPR did show a slight red-shift to 1719.3 cm^{-1} (Table 6.4) at this PVP concentration. Note that in blends of PVP and acid functional polyester resins (saturated), slight (5 cm^{-1}) UPR C=O blue-shifts were observed at concentrations from 10 - 90 wt. % PVP, indicating dipole-dipole interactions between UPR and

PVP carbonyls.[236] In addition, at 10 wt. % PVP, a new PVP C=O band shoulder emerged at ~1630 cm^{-1} which resulted from H-bond interaction of PVP carbonyls and carboxylic acid end groups on the polyester chains. No such behaviors were observed in the present work. This phenomenon might be observed at higher PVP concentrations, but with the intention herein for isolating SWNT, the current 150 mg/mL PVP concentration was already 1,400 % in excess of the desired concentration used to disperse SWNT. Thus, based on the observed PVP solubility at concentrations in excess of the required amount, the stabilization of SWNT with PVP is a feasible methodology for UPR compatibilization. Finally, as shown by Figure 6.23, interaction with C-H bonds was also ruled out. Nonetheless, since a specific interaction was not identified, the "like-like" solubility of PVP at even at a relatively high concentration was confirmed.

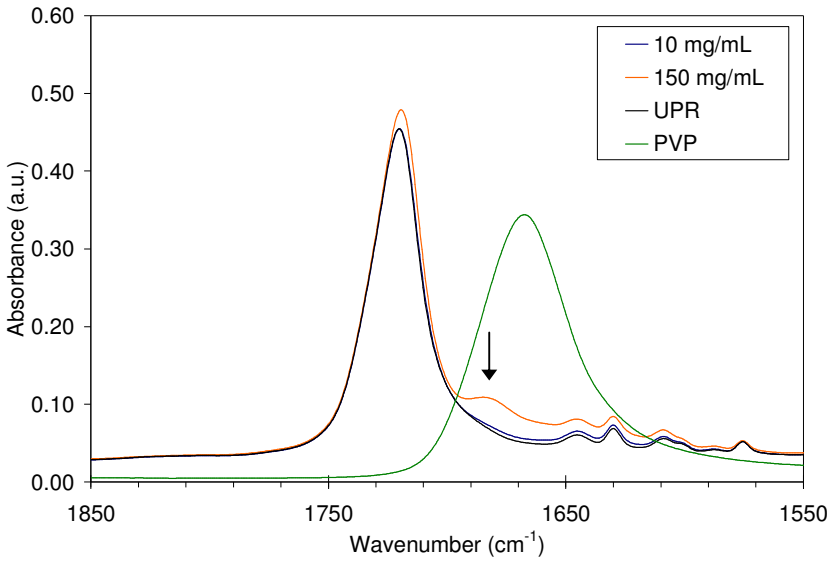

Figure 6.22: Carbonyl vibrations of PVP solutions in neat UPR.

Sample	$\nu_{shoulder}$ cm^{-1}
UPR	1720.3
10 mg/mL	1720.3
150 mg/mL	1719.3

Table 6.4: Carbonyl peak positions for UPR with PVP content.

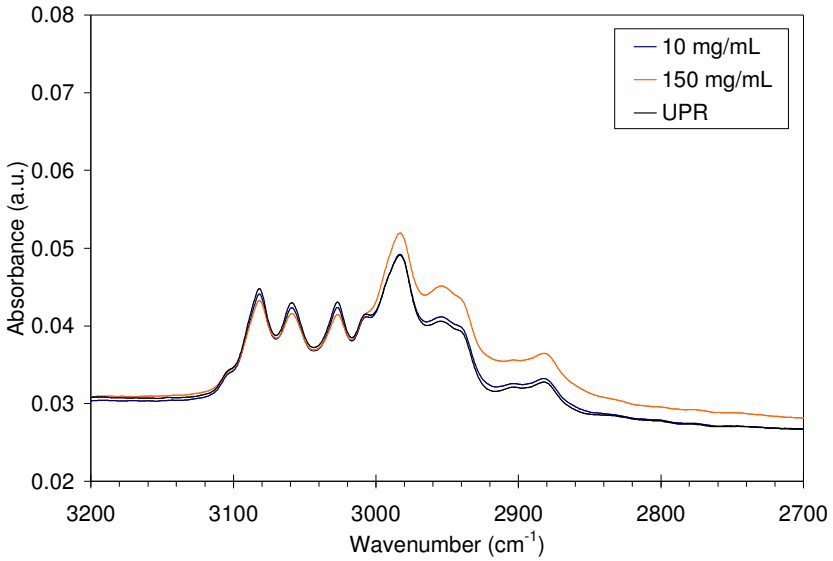

Figure 6.23: C-H vibrations of PVP solutions in neat UPR.

6.1.7 Polyvinylpyrrolidone SWNT Composites

PVP SWNT dispersions were created in identical fashion to the sonicated PVP solutions with the addition of SWNT to the initial PVP solution before sonication. After combination of SWNT with the aqueous PVP solution, a bath sonication step was carried out until the sample was free of large clusters (approximately 20 min). This step helped wet the SWNT and keep them in the dispersion during tip sonication, rather than floating out of the liquid. Initial SWNT dispersion concentrations of 0.33 mg/mL and 0.13 mg/mL were used. For 0.33 mg/mL samples, two different centrifugation speeds, as introduced previously, were used. Supernatant aliquots were collected and characterized by UV-vis spectra. The background absorption was zeroed and baseline corrected using 10 mg/mL aqueous PVP solution. Since a calibration curve was not known, the samples were simply diluted with the aqueous PVP solution until transmission was observed. This was required since initial dispersions allowed no transmission through the 10 mm path length cell. For point of reference, using an extinction coefficient for DNA stabilized SWNT of 25.7 mL/(mg-cm) at 745 nm absorbance, the initial concentration of the 5 mg SWNT

sample with light centrifugation (abs = 2.179 a.u., 10 mm path length) was found to be 0.085 mg/mL. This sample was diluted by approximately 50 vol. %, therefore the concentration after centrifugation was estimated to be in excess of 0.17 mg/mL, prior to dilution. For all samples, the presence of van Hove transitions confirmed the dispersibility of SWNT by PVP wrapping alone, and furthermore, were present over all concentrations measured. The efficiency of PVP as a dispersant was determined by comparison with DNA stabilized SWNT as displayed by Figure 6.24. Both samples shown were from the same nanotube batch. The PVP SWNT data shown was from the 0.13 mg/mL dispersion. The DNA sample was prepared in accordance with standard protocol for DNA developed by Ao et al. (2011).[224] Data shown was for a starting dispersion concentration of 0.1 wt. % SWNT and 0.75 wt. % DNA. Both samples were centrifuged for 3 h at 17,000 x g force. Data were scaled with the optical absorbance at 450 nm. The first van Hove transition of metallic nanotubes M_{11} can be found between 400 - 600 nm and the second van Hove transition S_{22} of semiconducting nanotubes is located between 550 - 800 nm.[66] Note that S_{11} is located in the nIR region. Figure 6.25 displays the UV-vis spectra over the range from 500 – 800 nm. The inset of Figure 6.25 was intended to show the highest concentration of PVP measured by UV-vis. This was not intended to be representative of the true dispersion limit, however. The presence of peaks in all samples confirms individualization. Remarkably, across the range of wavelengths studied, the dispersion of SWNT in PVP showed sharper peaks.

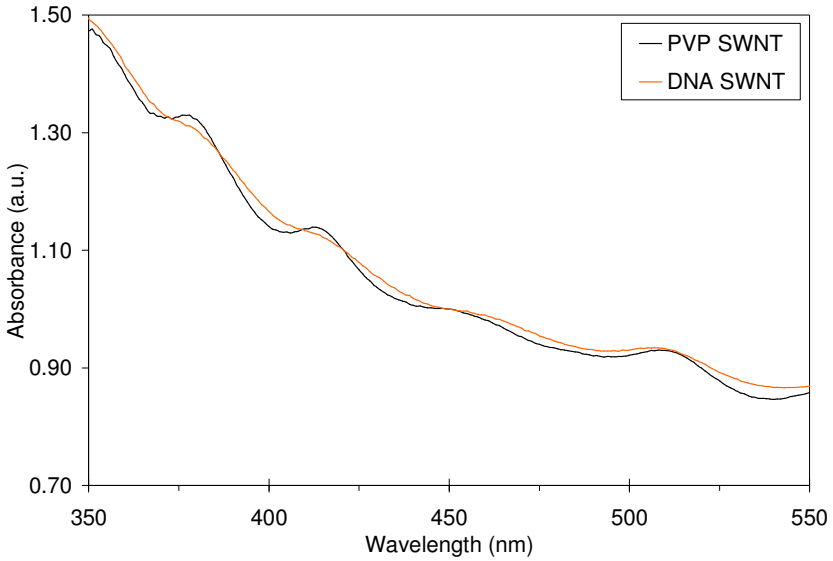

Figure 6.24: UV-vis spectra showing efficiency of nanotube dispersants. For reference, PVP SWNT (abs = 0.407 a.u. @ 745 nm) was estimated to be 0.016 mg/mL. DNA SWNT was dispersed at a concentration of 0.321 mg/mL. The different quartz cell pathlengths used for each sample explains the difference in concentration magnitudes.

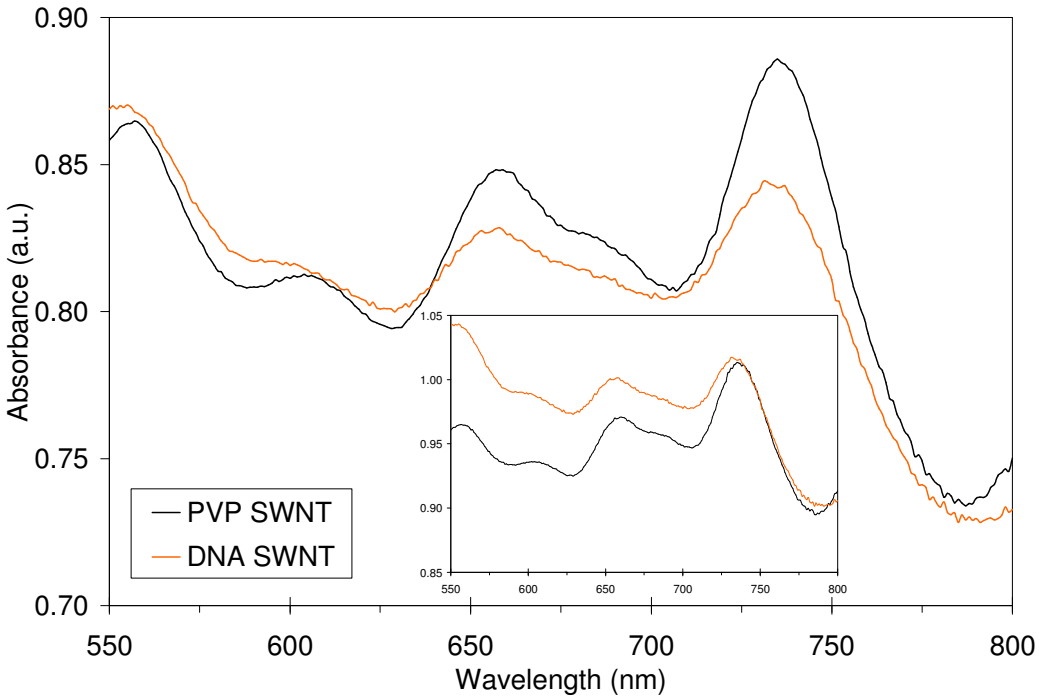

Figure 6.25: Visible absorbance spectra showing efficiency of nanotube dispersants. For a fairer comparison with DNA SWNT, the inset shows PVP SWNT absorbance at the highest concentration measured by UV-vis (not the highest concentration dispersed, however) of approximately 0.085 mg/mL. The y-axis of the DNA SWNT was up-shifted by 0.173 a.u. to overlay the spectra for comparison.

In order to remove the water while preserving the nanotube individualized structure, dispersions were frozen. Next, lyophilization was used to remove the frozen solvent without aggregating the SWNT by evaporative drying. After freeze drying, the samples held the shape of the frozen liquid and had a very low bulk density. The resulting PVP SWNT composite can be seen in Figure 6.26.

Figure 6.26: Freeze-dried PVP SWNT composite in 50 mL polypropylene centrifuge tube.

Surprisingly, this grey and dull lint-like material appeared colored under non-polarized reflected light, representing areas which showed wavelength specific reflections surrounded by dark nanotube-polymer film. Figure 6.27 displays these images. There was no evidence that this stained glass like phenomenon was related to nanotube alignment. Rather, this effect might be related to PVP morphology itself. These reflections were also unaffected by initial SWNT concentration in the dispersions studied. Figure 6.28 shows similar images from 0.13 mg/mL starting concentrations with the heavy centrifugation protocol used. Figure 6.29 also shows the texture of this film and provides comparison to a black and white image using a monochromatic filter.

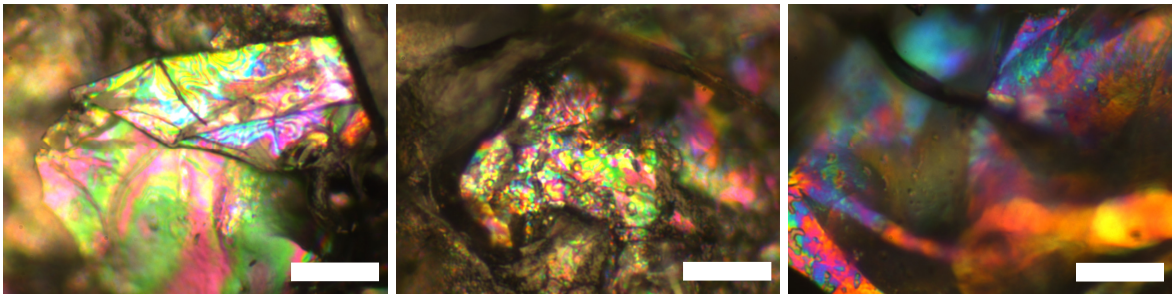

Figure 6.27: Reflected light microscopy of a PVP SWNT film having a starting SWNT concentration of 0.33 mg/mL with light centrifugation. A 50x SLWD objective with 2x magnification in front of CCD camera. Light was not polarized. Scale bar are 25 μm.

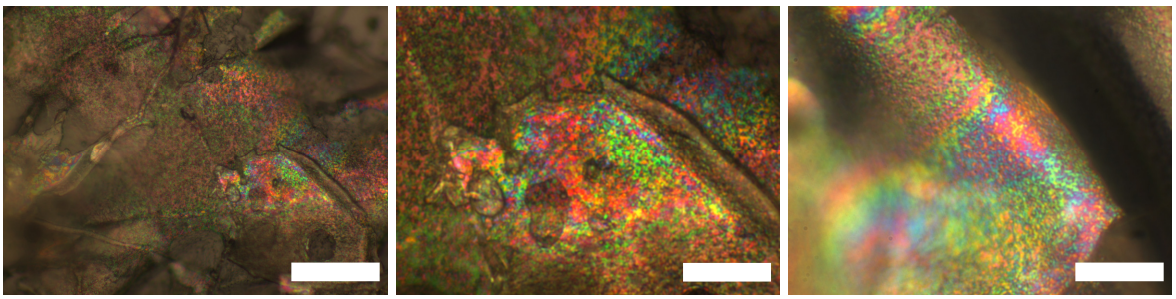

Figure 6.28: Reflected light microscopy of a PVP SWNT film having a starting SWNT concentration of 0.13 mg/mL with strong centrifugation. A 50x SLWD objective with 2x magnification in front of CCD camera. Light was not polarized. Scale bar are 25 μm.

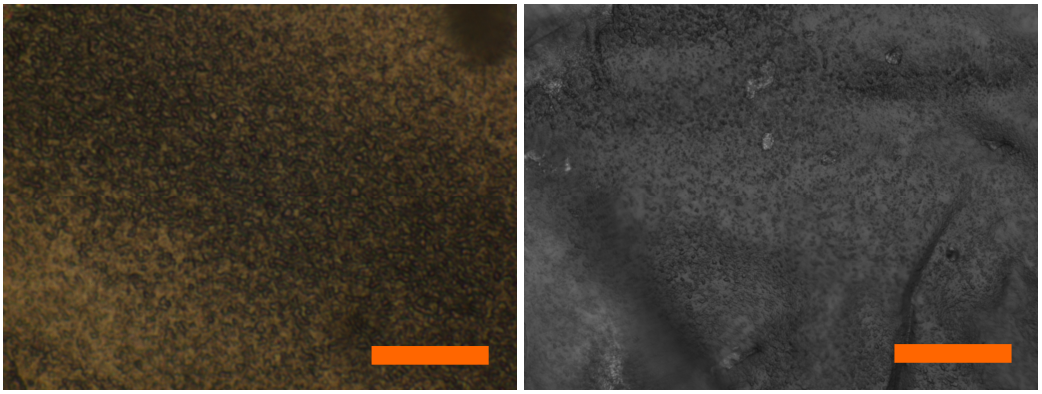

Figure 6.29: Reflected light microscopy of a PVP SWNT film having a starting SWNT concentration of 0.13 mg/mL with strong centrifugation. Left is a color image. Right is a monochromatic image. A 50x SLWD objective with 2x magnification in front of CCD camera. Light was not polarized. Scale bars are 25 μm.

Comparison between the FTIR spectra of PVP SWNT and bath sonicated PVP (Figure 6.30) revealed similar peaks. In fact, the two spectra are identical with the exception of lower overall

intensity from the nanotube containing sample. These results indicate that the SWNT surface was effectively "passivated" by the PVP. Due to the high optical absorbance of SWNT, the low wavenumber range of the PVP SWNT spectrum has substantial absorbance. Note that both samples, although dry, exhibit O-H vibrations.

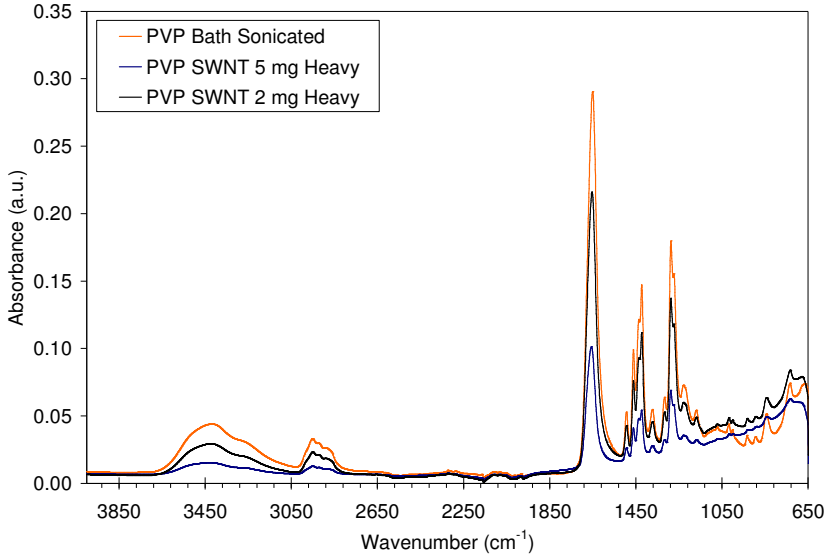

Figure 6.30: PVP SWNT comparison with sonicated PVP by FTIR.

Interestingly, the effect of moisture content on PVP SWNT samples showed different behavior than that observed for PVP alone. Figure 6.31 shows the IR spectra for samples with and without drying, and at varied temperature. Figure 6.32 shows the associated carbonyl region. Again, in all cases the O-H stretch remained, as expected post sonication treatment due to the structural change. The carbonyl, however, was located at 1656.6 cm^{-1} for both the hot and cool dry PVP SWNT samples. Thus, there was no temperature effect observed. Remarkably, the wet PVP SWNT sample showed a peak at 1655.6 cm^{-1} indicating the carbonyl peak position was nearly insensitive to moisture. This was in drastic contrast to the behavior of wet free (non-adsorbed) PVP where a 20 cm^{-1} red shift was measured. Recall that for free PVP the dry carbonyl vibration was at 1667 cm^{-1}. Therefore, with respect to the starting material, adsorption

of PVP to the SWNT surface resulted in a carbonyl red-shift of ~10 cm^{-1}. This observed shift does not include the effect of sonication, however. It was found that the carbonyl shifted to 1650 cm^{-1} in bath sonicated PVP (1652 cm^{-1} in tip sonicated sample). The smaller shift was interpreted to be a result of sonication energy absorption by the SWNT leading to less of a change to the polymer itself. This might also indicate some non-covalent charge transfer effects.

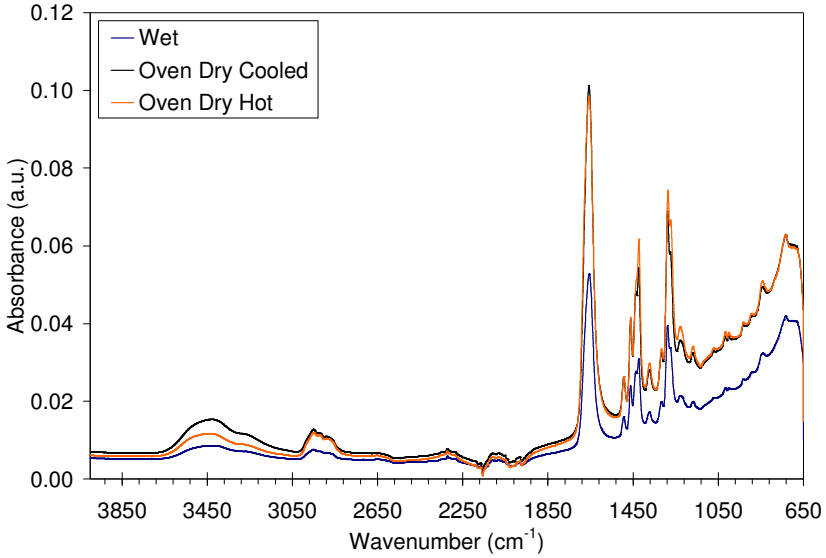

Figure 6.31: FTIR spectra showing effect of moisture on 5 mg SWNT starting concentration PVP SWNT composites.

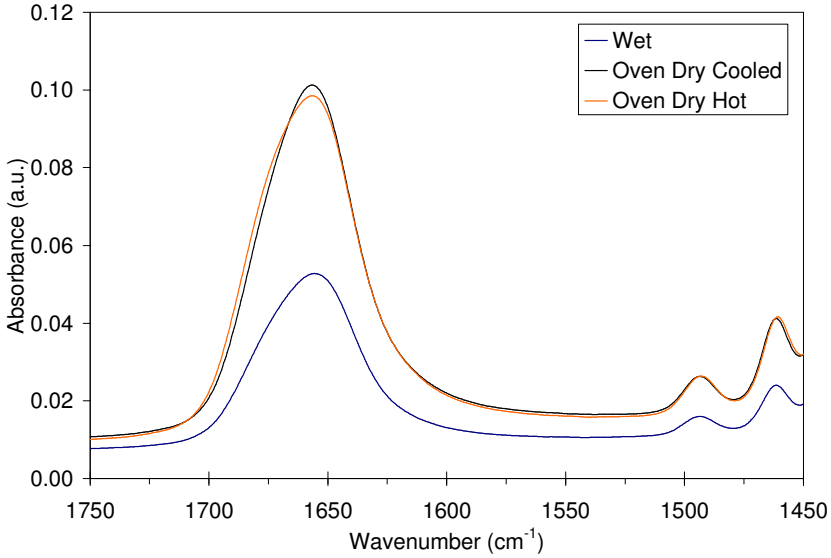

Figure 6.32: Effect of moisture on carbonyl stretch of 5 mg SWNT starting concentration PVP SWNT composites.

The PVP SWNT samples were also analyzed for relative polymer to SWNT content by TGA-FTIR analysis. Figure 6.33 shows the TGA mass loss curves in argon for the 5 mg SWNT starting materials with different centrifugation conditions. This was necessary to investigate the relative amount of SWNT and PVP remaining after various centrifugation conditions as well as the true starting SWNT content in the dispersions. With increased centrifugation time and intensity (heavy centrifugation), the amount of relative amount of polymer was decreased. The residual mass of SWNT for the samples shown in Figure 6.33 was found to be approximately 11.6 wt. % at 500°C for the heavy condition whereas the light centrifugation resulted in SWNT content of 7.8 wt. %. In comparison, the starting SWNT concentration was 3.23 wt. %, relative to PVP which indicates that some free PVP was removed by centrifugation. The peak degradation temperature was not significantly different between samples, although the onset of degradation appeared lower for the heavy condition. Although not shown here, the sample starting with 2 mg SWNT mass showed a residual SWNT content of 8.8 wt. %. The starting SWNT concentration was 1.32 wt. %, relative to PVP.

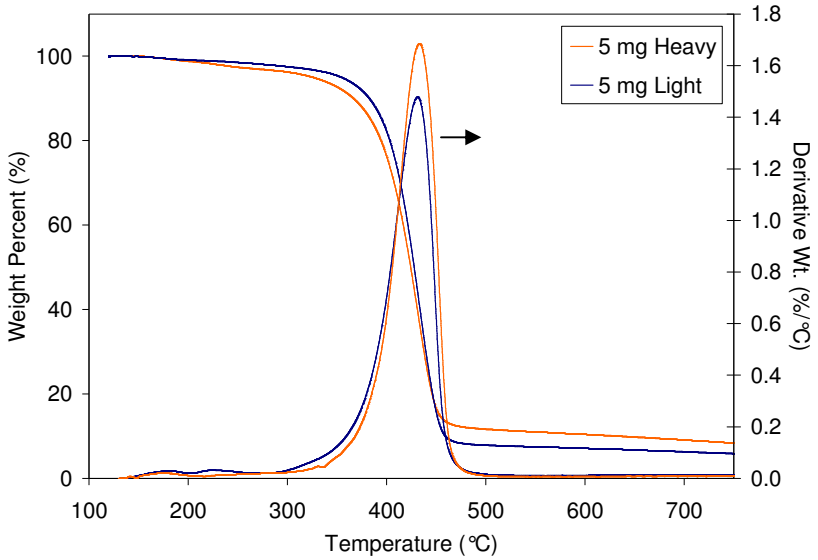

Figure 6.33: TGA curves of PVP SWNT composites.

6.1.8 Raman Spectroscopy of PVP SWNT Composites

To investigate the effect of processing on the SWNT structure and further explore PVP interaction with SWNT, resonant Raman scattering was measured under 514 nm and 785 nm excitation. These wavelengths primarily probe metallic and semiconducting species, respectively, based off of the Katura plot and the diameter range of CG200. Spectra are shown for the 0.13 mg/mL starting concentration (2 mg SWNT sample) processed with heavy centrifugation and plotted against pristine SWNT. All spectra were scaled with respect to the Raman G-band peak. Figure 6.34 shows the Raman spectra under 514 nm excitation. After processing, the PVP SWNT sample showed characteristics common to damaged or functionalized SWNT. Since PVP wrapping is a non-covalent process, these features were consistent with sidewall damage. For example, the I_D/I_G ratio increased from 0.08 to 0.20 after treatment. Loss of the metallic shoulder on the G-band was also indicative of covalent change. Peak position for the G'-band was monitored to look for the presence of doping. The average position of the G'-band in the starting material was 2668 cm^{-1} (σ = 1.35) and 2667 cm^{-1} (σ = 0.75) for the PVP wrapped sample. Based on these results, doping behavior cannot be confirmed. Note that at this wavelength, the polymer causes some background skewing. Also, a peak thought to arise from the PVP was seen at 2913 cm^{-1}.

Although it was remarkable that the sonication process appears to preferentially damage metallic SWNT, it was possible, however, that reactive species generated during sonication preferentially attach to the metallic sidewalls. In depth surface analysis, possibly by XPS, would be required to rule this out.

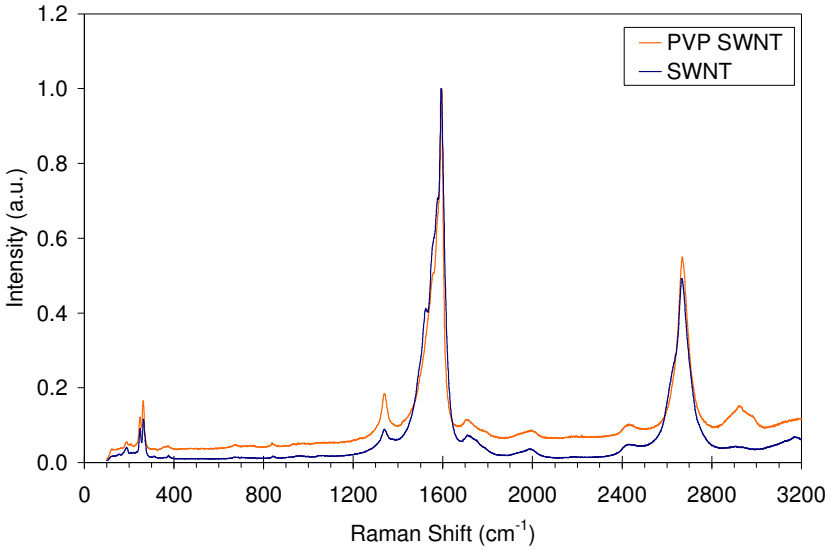

Figure 6.34: Raman spectra of PVP SWNT (0.13 mg/mL) under 514 nm laser.

Remarkably, PVP SWNT under 785 nm laser excitation displayed a different behavior from the 514 nm study, as displayed by Figure 6.35. The I_D/I_G increased from 0.07 to 0.12, a mild disturbance to the sp^2 sidewall from sonication. The shoulder found near the G^--band of semiconducting SWNT (~1563 cm^{-1}) in the starting material disappeared. This feature was more clearly seen in Figure 6.36. In addition, a slight G-band up-shift was observed. These characteristics are clear indications of non-covalent charge transfer.

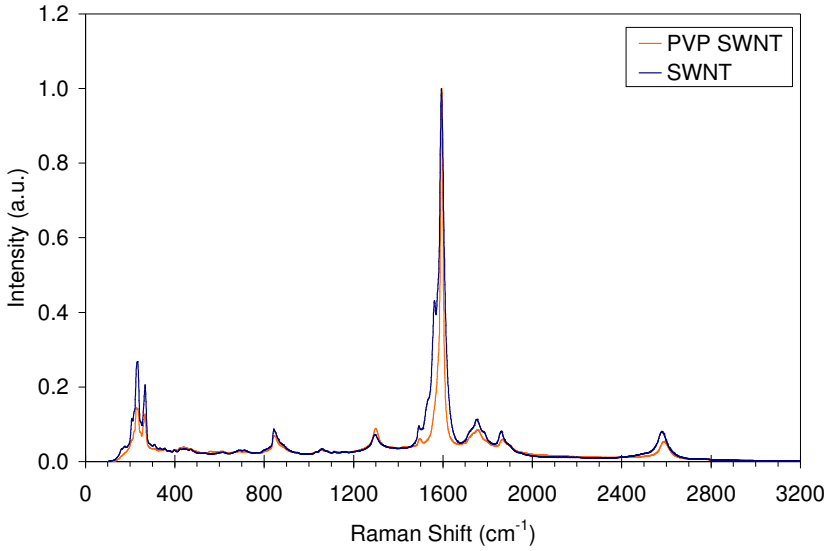

Figure 6.35: Raman spectra of PVP SWNT (0.13 mg/mL) under 785 nm laser.

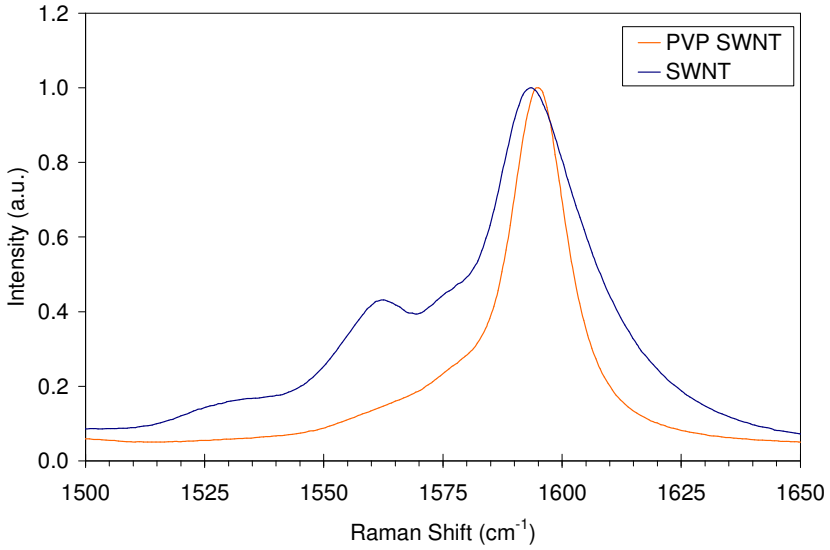

Figure 6.36: Raman G-band of PVP SWNT (0.13 mg/mL) under 514 nm laser.

The most convincing argument for PVP SWNT doping can be seen by examining the shift of the peak position for the G'-band shown in Figure 6.37. The average position of the G' - band in the starting material was 2580 cm^{-1} (σ = 1.05) and 2590 cm^{-1} (σ = 0.79) for the PVP wrapped sample. This blue-shift of 10 cm^{-1} was clear indication of p-type nanotube doping. Here, the origin of this shift was a decrease in the Fermi energy of SWNT by electron transfer from the

SWNT valence band to the adsorbed PVP. Furthermore, the G/G' ratio increased from 12 to 18 upon adsorption, another clear characteristic associated with doping.

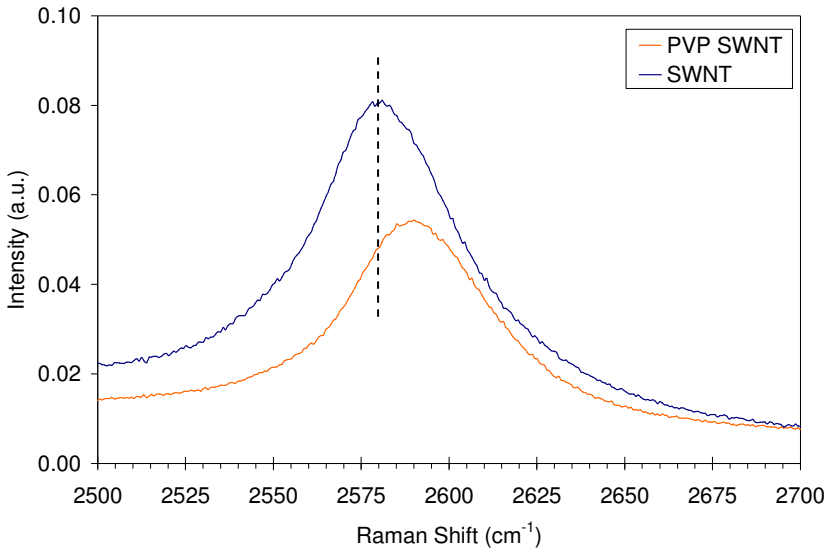

Figure 6.37: Raman G'-band of PVP SWNT (0.13 mg/mL) under 514 nm laser.

The selective doping of semiconducting SWNT by PVP further explains the chiral sorting of SWNT in PVP stabilized dispersions by Feng et al. (2011).[186] The authors reasoned this interaction was a result of the positive charge located on the carbonyl carbon (C5, Figure 6.38) in PVP interacting with the SWNT, as found by charge distribution calculations. Note that this is not an adjacent position to the SWNT and the unpaired electrons on position N1 would likely interfere with electron transfer. In addition, their Raman measurements were carried out in SDS/water. In this environment, the mesomerization of PVP would change the charge distribution from that modeled in their study. A more reasonable picture is the generation of a positive charge on position N1 by preferred mesomerism in hydrogen bonding media as found in this dissertation. This discussion was not meant to, nor does it, take away from the previously published results, it simply changes the interpretation of the data. Finally, it was noteworthy that

the up-shift measured by the authors was small at 3 cm^{-1}, compared to the anhydrous PVP SWNT films.

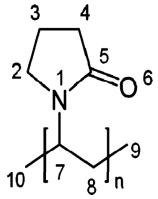

Figure 6.38: Reference PVP model with atomic assignments.

6.1.9 PVP SWNT Dispersion in Unsaturated Polyester Resin

The low-shear dispersion of PVP SWNT composite into UPR is shown by Figure 6.39. Figure 6.39 (a) and (b) show the PVP SWNT sample and dry PVP powder. Figure 6.39 (c) displays the samples just after initial UPR addition. Notice the clouding of the UPR by the white PVP. This clears up with time as shown by Figure 6.39 (d). Here, the PVP SWNT sample was agitated by a small magnetic stirrer rotating at approximately 450 rpm. Vial sizes were 3 drams.

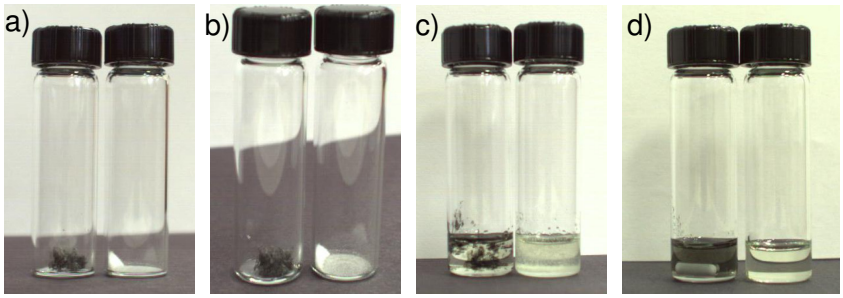

Figure 6.39: General demonstration of PVP SWNT and PVP dispersibility in UPR. Leftmost vial in each image contains PVP SWNT and right vial contains pure PVP. Displayed are (a, b) dry samples, (c) samples just after addition of UPR, and (d) samples after 3 days stirring/resting. The sample used was the 5 mg SWNT starting concentration with heavy centrifugation.

A more rigorous investigation into the dispersibility of PVP SWNT in UPR was carried out using high shear mixing. The PVP SWNT composite starting from 5 mg SWNT with heavy centrifugation was chosen in order to provide enough sample mass for reaching the necessary dispersion concentration. Both samples were shear mixed for 72 hr after 24 hr of high stress,

low shear rate mixing (see Appendix A1). Figure 6.40 displays the comparison between 100 ppm (by volume) dispersions of pristine CG200 starting material and the PVP SWNT using transmission optical microscopy. Samples were dispersed at 100 ppm by volume assuming an intrinsic SWNT specific gravity of 1.45. For the PVP SWNT, the residual mass at 500°C was obtained from TGA mass loss in argon (averaged between multiple runs to be 9.55 wt. % SWNT) and the appropriate mass of functionalized SWNT was calculated to be 30.3 mg, based on adjusting for PVP content (2.9 mg SWNT per 20 mL total dispersion volume). Remarkably, the dispersibility of the PVP SWNT was greatly improved over the starting material. The majority of small aggregates visible in the starting material were not present in the PVP SWNT sample, demonstrating the effectiveness of the polymer coating for UPR dispersion.

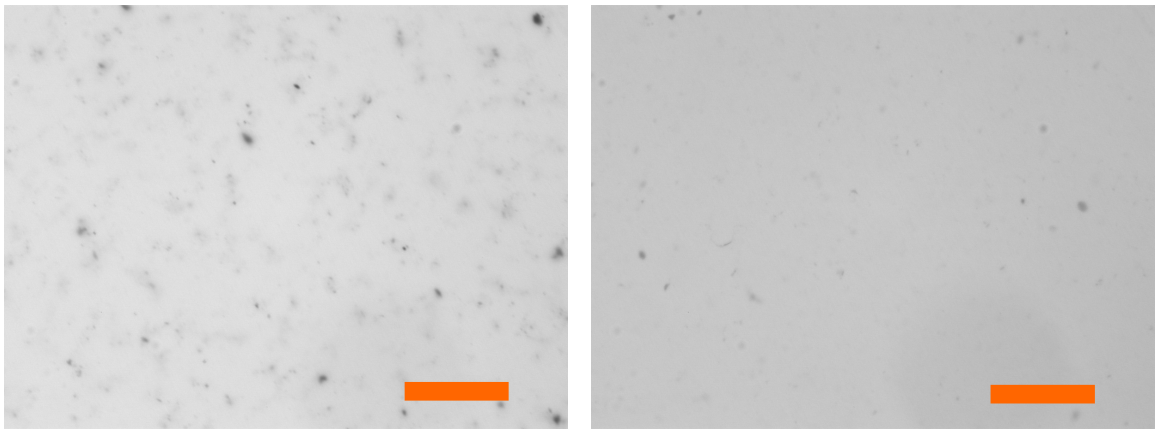

Figure 6.40: SWNT dispersion at 100 ppmv in UPR via high shear mixing protocol of (left) pristine CG200 SWNT and (right) PVP SWNT. PVP SWNT from 5 mg initial SWNT dispersion supernatant in 10 mg/mL PVP solution followed by centrifugation at 17,000 x g for 3 hr, decanting, freeze drying, and desiccation. Samples were imaged through a cover slip using a 20x objective with 2x magnification in from of digital camera (40x total magnification). Scale bars were 50 μm in length. Scale bars were 50 μm in length.

Dispersions were also characterized by small strain oscillatory shear measurements carried out in the linear viscoelastic regime. A 50 mm cone and plate rheometer operating in controlled strain mode was used to measure complex viscosity and modulus for each sample at 20°C.

Figure 6.41 displays the complex viscosity as a function of angular frequency for each sample. The inclusion of PVP SWNT increased the neat UPR viscosity from 1.7 to ~3.0 Pa-s and displayed Newtonian-like behavior over all shear rates. This observed viscosity increase resulted from the addition of well dispersed SWNT as well as the addition of excess non-adsorbed PVP. Interestingly, after the inclusion of pristine CG200 SWNT, the sample showed shear thinning behavior. This behavior, at this concentration, was previously seen for dispersions of pristine HiPco SWNT, existing as small bundles.[67,87] The disappearance of shear thinning behavior was attributed to the increased dispersion state of PVP SWNT observed in the optical micrographs. Figure 6.42 displays the corresponding storage modulus G' over the experimental range of shear rates. While both samples exhibit a measurable G', the magnitude of the modulus for the pristine CG200 sample was greater. The apparent and substantial break down of small aggregates and bundles in the CG200 sample by the non-covalent functionalization process with PVP appears to increase the complex viscosity but restore near-Newtonian behavior. The lack of shear thinning may be a result of decreased attractive interactions within the dispersed phase.

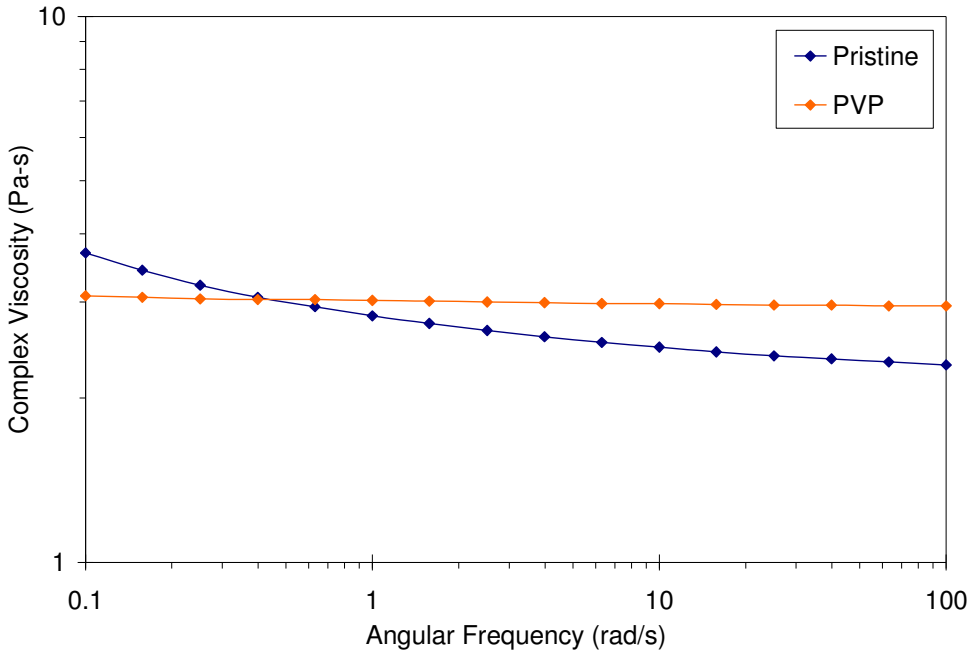

Figure 6.41: Complex viscosity of SWNT dispersions in UPR under small strain (5 %) oscillatory shear. All sample concentrations at 100 ppmv.

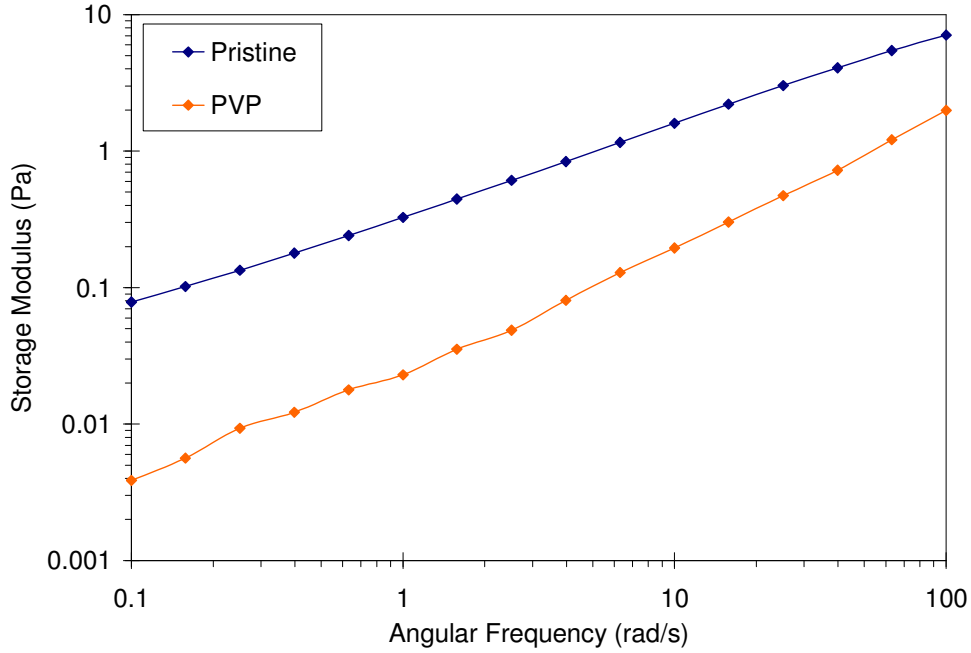

Figure 6.42: Linear viscoelastic response of SWNT dispersions in UPR under small strain (5 %) oscillatory shear. All sample concentrations at 100 ppmv.

6.1.10 Suggested Functionalization Schemes

The monomer of PVP, 1-vinyl-2-pyrrolidinone, is a potential candidate for in-situ polymerization under Billups conditions. Figure 6.43 displays the structure of this monomer.

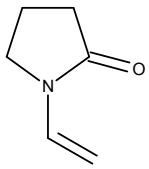

Figure 6.43: Molecular structure of 1-vinyl-2-pyrrolidinone

It is unknown if this chemistry will survive the environment of Billups reaction as the partial charge on the nitrogen would be a favorable site for Li association. Unpublished data from our lab, in collaboration with the Gorden research group, showed strong preference for vinyl bond activation in this environment, as displayed with multi-functional 4-bromostyrene. Furthermore, it has been shown in the literature that ketone containing compounds are attacked to form keto radicals, but not when directly attached to a ring structure.

A second, less challenging, strategy would be to employ a copolymer of 1-vinyl-2-pyrrolidinone and vinyl acetate in place of traditional PVP. Figure 6.44 displays the structure of poly(1-vinylpyrrolidone-co-vinyl acetate).

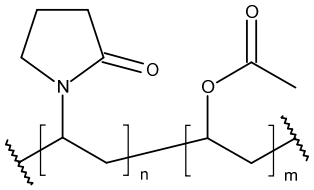

Figure 6.44: Molecular structure of 1-vinylpyrrolidone-co-vinyl acetate.

Since this polymer still contains the hydrophobic backbone and hydrophilic pendant groups it is a candidate molecule to replace of PVP. In this case, the potential benefit over PVP being due to the presence of ester functionalities which could interact favorably with UPR. Of course, if the

thermodynamic interaction is too far changed, desorption from the nanotube to surface to maximize mixing entropy may result. This could potentially happen if the UPR solvent and polymer are too closely matched. For example, the pluronic series of tribock copolymers [poly(ethylene oxide) and poly(propylene oxide]] stabilize nanotubes in water but not in solvents that are good solvents for both polymer blocks.[86]

6.2 Conclusions

PVP stabilized SWNT dispersions were prepared in the lower region of the rod semidilute regime, frozen to avoid re-aggregation, and freeze-dried to avoid capillary forces upon drying. In this manner, the anhydrous PVP stabilized SWNT were ready for dispersion into organic solvents or in this work, UPR. The processing of the PVP by sonication during dispersion results in structural changes to the polymer. These effects were investigated spectroscopically by studying the processing effects on PVP alone. PVP readily adsorbs atmospheric moisture and the interaction with water softens carbonyl vibrations, presumably by mesomerism inter-conversion of the pendant groups. This was observed by red shifting of the PVP carbonyl accompanied by additional subtle spectral changes. This effect was readily reversible upon gentle heating and vacuum drying. Upon sonication of PVP, identical effects observed for wet PVP persist even after extensive vacuum drying. This was attributed to a permanent structural change to the PVP pendant groups (carbonyl hydration) by the intense sonication environment, known to generate hot spots and radicals. UV-vis analysis of the processed PVP before freeze drying indicated structural changes to the active chromophore of PVP. This was remarkable since, in general, the observed structural changes in PVP have not been previously considered to influence the dispersion of PVP stabilized SWNT or graphene. A key finding of this work was

that the extent of these structural changes was substantial and could influence the specific interactions of PVP with solvents.

PVP was found to be readily soluble in UPR at concentrations at least as high as 150 mg/mL. FTIR analysis revealed bond stiffening of the PVP carbonyl vibration in UPR, seen by blue shifting of the spectrum which indicated molecular dissolution. This was the opposite behavior seen for aqueous solutions and was a consequence of the absence of the H-bond donors in UPR. The interaction was characterized as "like-like," meaning similar solubility parameters existed between components. This observation was promising for use of PVP adsorption to "re-shape" the potential energy of interaction between SWNT and concurrently compatibilize the nanotubes with UPR by PVP-UPR solubility. Adsorption and localization of the PVP to the SWNT surface appears to have some interaction as indicated by the red-shift of the PVP carbonyl in absence of solvents. This subtle effect was further investigated by Raman spectroscopy.

Interesting effects were observed from the PVP SWNT interaction and the structural change of SWNT from processing via Raman scattering. Under 514 nm laser excitation, the PVP SWNT composites showed evidence of structural damage, presumably from the tip sonication steps. Under 785 nm laser excitation, the characteristic features of non-covalent charge transfer from the SWNT to the polymer were observed. Specifically, characteristics of p-type doping were seen. The selective charge transfer between PVP and SWNT was previously observed and exploited for chiral sorting. With the observation of structural changes to PVP upon mesomerization and post-sonication, the interpretation of this effect was refined in this work. Finally, the dispersion of PVP stabilized SWNT into UPR with low shear stress was introduced. The dispersion process is very facile and therefore warrants further investigation, notably, on the influence of initial SWNT dispersion state and concentration regime prior to freeze drying. To

the author's knowledge, this was the first investigation into the effects of PVP SWNT dispersion into UPR, and these results provide a promising approach to stabilizing SWNT in this commercially relevant polymer resin.

Chapter 7

Conclusions

7.1 Summary of Results and Conclusions

Motivated by the dispersion of pristine SWNT into unsaturated polyester resin, the covalent and non-covalent functionalization of SWNT for compatibilization with unsaturated polyester resin was rationally investigated by considering potential specific and non-specific physicochemical interactions. To this end, the functionalization of reduced SWNT dispersions under Billups and organometallic reducing environments was explored. The discovery of the polymerization of 4-bromostyrene in Li/NH_3 led to the investigation of functionalization of SWNT with polystyrene. An alternate functionalization scheme avoiding strong reducing environments, the Bingel reaction, was used to functionalize SWNT with ester groups and study the influence of processing. Finally, the non-covalent adsorption of polyvinylpyrrolidone for dispersion of SWNT in UPR was investigated. It was found that the accessibility of final desired surface chemistries was dependant on the individualization method (reduction or sonication) used to expose surfaces for functionalization.

Stable dispersions of SWNT produced by the electrostatic repulsion between reduced nanotubes were used to functionalize SWNT on the individual level. The first attachment of phenanthrene groups to CoMoCAT SWNT was achieved by MeLi reduction in ether. Multifunctional alkyl and aryl halides were not compatible with any reducing environments studied but facile vinyl bond activation and polymerization in condensed NH_3/Li was observed.

This polymerization motivated the investigation of styrene functionalized SWNT for dispersion in unsaturated polyester resin. A single-pot method referred to as the "in-situ reaction cycling polymerization functionalization of SWNT" was developed. The effectiveness of this method to achieve high extents of functionalization was demonstrated for the reductive alkylation of SWNT with dodecyl chains and acrylic methyl methacrylate polymer. This reaction scheme opens the door for functionalization with many unsaturated monomers having exciting potential applications such as carbonized fibers.

The harsh reducing environment required to stabilize SWNT was bypassed by sidewall esterification using the Bingel reaction. The sonication required for functionalization introduced a number of complications for product characterization and processing, most notably formation of an undesirable sonopolymer. The relative concentration of sonopolymer prevents further utility of this reaction scheme for dispersion in unsaturated polyester resin. Thus, alternative solvents were investigated. In addition, unlike HiPco SWNT, sonication of CoMoCAT SWNT in 1,2-dichlorobenzene did not result in doping. Based on bulk dispersion, the effects of chemical functionalization dominate over the sonopolymer, controlling dispersibility.

A final approach utilizing non-covalent interactions between SWNT and polyvinylpyrrolidone to compatibilize nanotubes with unsaturated polyester resin was employed. Spectroscopically, the molecular solubility of PVP in UPR was discovered. By means of freeze drying the sonicated nanotube dispersions, effects from re-aggregation upon drying were avoided. The processing of polyvinylpyrrolidone by sonication induced structural changes to the polymer pendant groups, sprctroscopically in similar fashion to that in water. These changes were not reversible post-sonication, however. Evidence of non-covalent charge transfer between

semiconducting SWNT and polyvinylpyrrolidone were observed. Finally, the low shear dispersion of polyvinylpyrrolidone stabilized SWNT was displayed.

Some general observations were discovered across the functionalization studies carried out in this work. First, so-called "non-SWNT" carbons inherent to CG200 SWNT were identified to be high purity double-walled carbon nanotubes and multi-walled carbon nanotubes by resonant Raman spectroscopy and high-resolution transmission electron microscopy. The mechanical instability of "non-SWNT" carbons towards sonication was discovered using careful thermogravimetric measurements. The generated sonication degradation residues were found to skew the interpretation of functionalization effects. Next, the high temperature evolution from reaction based on formation of reduced SWNT (excluding polymerization reactions) was consistent between methods. Coupled TGA-FTIR analysis indicated introduction of a hydrogenation artifact.

In conclusion, based on the results of this study, further pursuit of the in-situ polymerization functionalization of SWNT and further investigation into the non-covalent stabilization with polyvinylpyrrolidone is recommended. These methodologies provide exciting and scalable routes towards future applications development of SWNT nanocomposites.

References

(1) Iijima, S. *Nature* **1991**, *354*, 56.
(2) Iijima, S.; Ichihashi, T. *Nature* **1993**, *363*, 603.
(3) Bethune, D. S.; Kiang, C. H.; Devries, M. S.; Gorman, G.; Savoy, R.; Vazquez, J.; Beyers, R. *Nature* **1993**, *363*, 605.
(4) Moniruzzaman, M.; Winey, K. I. *Macromolecules* **2006**, *39*, 5194.
(5) Baughman, R. H.; Zakhidov, A. A.; de Heer, W. A. *Science* **2002**, *297*, 787.
(6) Vaia, R. A.; Wagner, H. D. *Materials Today* **2004**, *7*, 32.
(7) Sandler, J. K. W.; Kirk, J. E.; Kinloch, I. A.; Shaffer, M. S. P.; Windle, A. H. *Polymer* **2003**, *44*, 5893.
(8) Rahatekar, S. S.; Koziol, K. K. K.; Butler, S. A.; Elliott, J. A.; Shaffer, M. S. P.; Mackley, M. R.; Windle, A. H. *Journal of Rheology* **2006**, *50*, 599.
(9) Gojny, F. H.; Wichmann, M. H. G.; Köpke, U.; Fiedler, B.; Schulte, K. *Composites Science and Technology* **2004**, *64*, 2363.
(10) Gojny, F. H.; Wichmann, M. H. G.; Fiedler, B.; Schulte, K. *Composites Science and Technology* **2005**, *65*, 2300.
(11) Wichmann, M.; Sumfleth, J.; Fiedler, B.; Gojny, F.; Schulte, K. *Mechanics of Composite Materials* **2006**, *42*, 395.
(12) Fan, Z. H.; Advani, S. G. *Journal of Rheology* **2007**, *51*, 585.
(13) Ma, W. K. A.; Chinesta, F.; Ammar, A.; Mackley, M. R. *Journal of Rheology* **2008**, *52*, 1311.
(14) Seyhan, A. T.; Gojny, F. H.; Tanoglu, M.; Schulte, K. *European Polymer Journal* **2007**, *43*, 374.
(15) Seyhan, A. T.; Gojny, F. H.; Tanoglu, M.; Schulte, K. *European Polymer Journal* **2007**, *43*, 2836.
(16) Battisti, A.; Skordos, A. A.; Partridge, I. K. *Composites Science and Technology* **2009**, *69*, 1516.
(17) Rodriguez, F.; Cohen, C.; Ober, C.; Atcher, L. A. *Principles of Polymer Systems*; 5 ed.; Taylor & Francis, 2003.
(18) Sandler, J.; Shaffer, M. S. P.; Prasse, T.; Bauhofer, W.; Schulte, K.; Windle, A. H. *Polymer* **1999**, *40*, 5967.
(19) Gong, X.; Liu, J.; Baskaran, S.; Voise, R. D.; Young, J. S. *Chemistry of Materials* **2000**, *12*, 1049.
(20) Lin-Gibson, S.; Pathak, J. A.; Grulke, E. A.; Wang, H.; Hobbie, E. K. *Physical Review Letters* **2004**, *92*, 048302.
(21) Thostenson, E. T.; Ziaee, S.; Chou, T.-W. *Composites Science and Technology* **2009**, *69*, 801.

(22) Malik, M.; Choudhary, V.; Varma, I. K. *Journal of Macromolecular Science* **2000**, *C40*, 139.
(23) Chanda, M.; Roy, S. K. *Plastics Technology Handbook*; Marcel Dekker, 1998.
(24) Mallick, P. K. *Composites Engineering Handbook*; CRC Press, 1997.
(25) Montarnal, D.; Capelot, M.; Tournilhac, F.; Leibler, L. *Science* **2011**, *334*, 965.
(26) Fried, J. R. *Polymer Science and Technology*; Prentice Hall PTR, 1995.
(27) Mallick, P. K. *Fiber-reinforced Composites: Materials, Manufacturing, and Design*; CRC Press, 1993.
(28) Leffingwell, R.; Newhardt, D. *Corvette: Fifty Years*; MotorBooks/MBI Publishing Company, 2002.
(29) Dyke, C. A.; Tour, J. M. *The Journal of Physical Chemistry A* **2004**, *108*, 11151.
(30) Yu, M.-F.; Lourie, O.; Dyer, M. J.; Moloni, K.; Kelly, T. F.; Ruoff, R. S. *Science* **2000**, *287*, 637.
(31) Gao, G. H.; Cagin, T.; Goddard, W. A. *Nanotechnology* **1998**, *9*, 184.
(32) Walters, D. A.; Ericson, L. M.; Casavant, M. J.; Liu, J.; Colbert, D. T.; Smith, K. A.; Smalley, R. E. *Applied Physics Letters* **1999**, *74*, 3803.
(33) Wong, E. W.; Sheehan, P. E.; Lieber, C. M. *Science* **1997**, *277*, 1971.
(34) Xinghui, L.; Changchun, Z.; Yukui, L. *Physica B: Condensed Matter* **2004**, *344*, 243.
(35) Frank, S.; Poncharal, P.; Wang, Z. L.; de Heer, W. A. *Science* **1998**, *280*, 1744.
(36) Kim, P.; Shi, L.; Majumdar, A.; McEuen, P. L. *Physical Review Letters* **2001**, *8721*.
(37) Wei, B. Q.; Vajtai, R.; Ajayan, P. M. *Applied Physics Letters* **2001**, *79*, 1172.
(38) Collins, P. G.; Avouris, P. *Scientific American* **2000**, *283*, 62.
(39) Dresselhaus, M. S.; Dresselhaus, G.; Eklund, P. C. *Science of Fullerenes and Carbon Nanotubes: Their Properties and Applications*; Academic Press, 1996.
(40) Durkop, T.; Kim, B. M.; Fuhrer, M. S. *Journal of Physics: Condensed Matter* **2004**, *16*, R553.
(41) Jorio, A.; Dresselhaus, M. S.; Saito, R.; Dresselhaus, G. *Raman Spectroscopy in Graphene Related Systems*; Wiley, 2011.
(42) Saito, R.; Hofmann, M.; Dresselhaus, G.; Jorio, A.; Dresselhaus, M. *Advances in Physics* **2011**, *60*, 413.
(43) Dresselhaus, M. S.; Dresselhaus, G.; Saito, R.; Jorio, A. *Physics Reports* **2005**, *409*, 47.
(44) Saito, R.; Dresselhaus, G.; Dresselhaus, M. S. *Physical Properties of Carbon Nanotubes*; Imperial College Press, 1998; Vol. 35.
(45) Minot, E. D. *Tuning the Band Structure of Carbon Nanotubes*; Cornell University, 2004.
(46) Jarillo-Herrero, P. D. *Quantum Transport in Carbon Nanotubes*; Delft University of Technology, 2005.
(47) Ouyang, M.; Huang, J. L.; Lieber, C. M. *Accounts of Chemical Research* **2002**, *35*, 1018.
(48) Dürkop, T.; Kim, B.; Fuhrer, M. *Journal of Physics: Condensed Matter* **2004**, *16*, R553.
(49) Biercuk, M.; Ilani, S.; Marcus, C.; McEuen, P. In *Carbon Nanotubes: Advanced Topics in the Synthesis, Structure, Properties and Applications*; Ado Jorio, G. D., M. S. Dresselhaus, Ed. 2008, p 455.
(50) Alfonsi, J. *Small Crystal Models for the Electronic Properties of Carbon Nanotubes*; University of Padova, 2008.
(51) Samsonidze, G. G.; Saito, A.; Jorio, D.; Pimenta, E.; Souza, F.; Gruneis, F.; Dresselhaus, D.; Dresselhausa, M. *Journal of Nanoscience and Nanotechnology* **2003**, *3*, 431.

(52) Thomsen, C.; Reich, S. In *Light Scattering in Solid IX*; Merlin, M. C. a. R., Ed. 2007, p 115.
(53) Kataura, H.; Kumazawa, Y.; Maniwa, Y.; Umezu, I.; Suzuki, S.; Ohtsuka, Y.; Achiba, Y. *Synthetic Metals* **1999**, *103*, 2555.
(54) Maruyama, S.; The University of Tokyo: 2002; Vol. 2011.
(55) Jorio, A.; Samsonidze, G. G.; Dresselhaus, G.; Saito, R.; Dresselhaus, M. *Nanotechnology* **2003**, *14*, 1130.
(56) Souza Filho, A.; Jorio, A.; Swan, A. K.; Ünlü, M.; Goldberg, B.; Saito, R.; Hafner, J.; Lieber, C.; Pimenta, M.; Dresselhaus, G. *Physical Review B* **2002**, *65*, 085417.
(57) Maciel, I. O.; Anderson, N.; Pimenta, M. A.; Hartschuh, A.; Qian, H.; Terrones, M.; Terrones, H.; Campos-Delgado, J.; Rao, A. M.; Novotny, L. *Nature materials* **2008**, *7*, 878.
(58) Samsonidze, G. G.; Saito, R.; Jorio, A.; Filho, A. G. S.; Grüneis, A.; Pimenta, M.; Dresselhaus, G.; Dresselhaus, M. *Physical Review Letters* **2003**, *90*, 27403.
(59) Kempa, K. *Physical Review B* **2002**, *66*, 195406.
(60) Dubay, O.; Kresse, G.; Kuzmany, H. *Physical Review Letters* **2002**, *88*, 235506.
(61) Reich, S.; Thomsen, C. *Philosophical Transactions of the Royal Society of London. Series A: Mathematical, Physical and Engineering Sciences* **2004**, *362*, 2271.
(62) Telg, H.; Maultzsch, J.; Reich, S.; Hennrich, F.; Thomsen, C. *Physical Review Letters* **2004**, *93*, 177401.
(63) Maultzsch, J.; Telg, H.; Reich, S.; Thomsen, C. *Physical Review B* **2005**, *72*, 205438.
(64) Rafailov, P. M.; Maultzsch, J.; Thomsen, C.; Kataura, H. *Physical Review B* **2005**, *72*, 045411.
(65) Thess, A.; Lee, R.; Nikolaev, P.; Dai, H. J.; Petit, P.; Robert, J.; Xu, C. H.; Lee, Y. H.; Kim, S. G.; Rinzler, A. G.; Colbert, D. T.; Scuseria, G. E.; Tomanek, D.; Fischer, J. E.; Smalley, R. E. *Science* **1996**, *273*, 483.
(66) O'Connell, M. J.; Bachilo, S. M.; Huffman, C. B.; Moore, V. C.; Strano, M. S.; Haroz, E. H.; Rialon, K. L.; Boul, P. J.; Noon, W. H.; Kittrell, C.; Ma, J.; Hauge, R. H.; Weisman, R. B.; Smalley, R. E. *Science* **2002**, *297*, 593.
(67) Kayatin, M. J. *Rheology, Structure, and Stability of Carbon Nanotube-Unstaturated Polyester Resin Dispersions*; Auburn University, 2008.
(68) Girifalco, L. A.; Hodak, M.; Lee, R. S. *Physical Review B* **2000**, *62*, 13104.
(69) Sun, C. H.; Yin, L. C.; Li, F.; Lu, G. Q.; Cheng, H. M. *Chemical Physics Letters* **2005**, *403*, 343.
(70) Davis, V. A.; Parra-Vasquez, A. N. G.; Green, M. J.; Rai, P. K.; Behabtu, N.; Prieto, V.; Booker, R. D.; Schmidt, J.; Kesselman, E.; Zhou, W. *Nature nanotechnology* **2009**, *4*, 830.
(71) Kumar, A.; Gupta, R. K. *Fundamentals of Polymer Engineering*; CRC Press, 2003.
(72) Duggal, R.; Pasquali, M. *Physical Review Letters* **2006**, *96*, 246104.
(73) Yakobson, B. I.; Couchman, L. S. In *Dekker Encyclopedia of Nanoscience and Nanotechnology*; James A. Schwarz, Christian I. Contescu, Putyera, K., Eds.; Marcel Dekker: 2004, p 587.
(74) Green, M. J.; Behabtu, N.; Pasquali, M.; Adams, W. W. *Polymer* **2009**, *50*, 4979.
(75) Fakhri, N.; Tsyboulski, D. A.; Cognet, L.; Weisman, R. B.; Pasquali, M. *Proceedings of the National Academy of Sciences* **2009**, *106*, 14219.
(76) Romanko, W. R.; Carr, S. H. *Macromolecules* **2002**, *21*, 2243.

(77) Flory, P. J. *Proceedings of the Royal Society of London. Series A. Mathematical and Physical Sciences* **1956**, *234*, 60.
(78) Larson, R. G. *The Structure and Rheology of Complex Fluids*; Oxford University Press, 1998.
(79) Jones, R. A. L. *Soft Condensed Matter*; Oxford University Press, 2002.
(80) Onsager, L. *Annals of the New York Academy of Sciences* **1949**, *51*, 627.
(81) Donald, A. M.; Windle, A. H.; Hanna, S. *Liquid Crystalline Polymers*; Cambridge University Press, 2006.
(82) Israelachvili, J. N. *Intermolecular and Surface Forces*; Academic Press, 1991.
(83) Anand, M.; You, S.-S.; Hurst, K. M.; Saunders, S. R.; Kitchens, C. L.; Ashurst, W. R.; Roberts, C. B. *Industrial & Engineering Chemistry Research* **2008**, *47*, 553.
(84) Dresselhaus, M. S.; Dresselhaus, G.; Saito, R. *Carbon* **1995**, *33*, 883.
(85) Shvartzman-Cohen, R.; Nativ-Roth, E.; Baskaran, E.; Levi-Kalisman, Y.; Szleifer, I.; Yerushalmi-Rozen, R. *Journal of the American Chemical Society* **2004**, *126*, 14850.
(86) Shvartzman-Cohen, R.; Levi-Kalisman, Y.; Nativ-Roth, E.; Yerushalmi-Rozen, R. *Langmuir* **2004**, *20*, 6085.
(87) Kayatin, M. J.; Davis, V. A. *Macromolecules* **2009**, *42*, 6624.
(88) Davis, V. A.; Ericson, L. M.; Parra-Vasquez, A. N. G.; Fan, H.; Wang, Y.; Prieto, V.; Longoria, J. A.; Ramesh, S.; Saini, R. K.; Kittrell, C. *Macromolecules* **2004**, *37*, 154.
(89) Tasis, D.; Tagmatarchis, N.; Bianco, A.; Prato, M. *Chemical Reviews* **2006**, *106*, 1105.
(90) Banerjee, S.; Hemraj‐Benny, T.; Wong, S. S. *Advanced Materials* **2005**, *17*, 17.
(91) Bergin, S. D.; Nicolosi, V.; Streich, P. V.; Giordani, S.; Sun, Z.; Windle, A. H.; Ryan, P.; Niraj, N. P. P.; Wang, Z. T. T.; Carpenter, L. *Advanced Materials* **2008**, *20*, 1876.
(92) Coleman, J. N. *Advanced Functional Materials* **2009**, *19*, 3680.
(93) Flory, P. J. *Principles of Polymer Chemistry*; Cornell University Press, 1953.
(94) Hansen, C. M. *Hansen Solubility Parameters: A User's Handbook*; CRC Press, 2007.
(95) Hildebrand, J. H.; Scott, R. L. *Regular Solutions*; Prentice-Hall, 1962.
(96) Bergin, S. D.; Sun, Z.; Rickard, D.; Streich, P. V.; Hamilton, J. P.; Coleman, J. N. *ACS Nano* **2009**, *3*, 2340.
(97) Patterson, D.; Delmas, G. *Off. Dig. Fed. Soc. Paint Technol* **1962**, *34*, 677.
(98) Delmas, G.; Patterson, D.; Somcynsky, T. *Journal of Polymer Science* **1962**, *57*, 79.
(99) Green, M. J.; Parra-Vasquez, A. N. G.; Behabtu, N.; Pasquali, M. *The Journal of Chemical Physics* **2009**, *131*, 084901.
(100) Liang, F.; Sadana, A. K.; Peera, A.; Chattopadhyay, J.; Gu, Z.; Hauge, R. H.; Billups, W. E. *Nano Letters* **2004**, *4*, 1257.
(101) Niyogi, S.; Hamon, M.; Hu, H.; Zhao, B.; Bhowmik, P.; Sen, R.; Itkis, M.; Haddon, R. *Accounts of Chemical Research* **2002**, *35*, 1105.
(102) Chen, Z.; Thiel, W.; Hirsch, A. *ChemPhysChem* **2003**, *4*, 93.
(103) Strano, M. S.; Dyke, C. A.; Usrey, M. L.; Barone, P. W.; Allen, M. J.; Shan, H.; Kittrell, C.; Hauge, R. H.; Tour, J. M.; Smalley, R. E. *Science* **2003**, *301*, 1519.
(104) Wunderlich, D.; Hauke, F.; Hirsch, A. *Journal of Materials Chemistry* **2008**, *18*, 1493.
(105) Joselevich, E. *ChemPhysChem* **2004**, *5*, 619.
(106) Aihara, J.; Yamabe, T.; Hosoya, H. *Synthetic Metals* **1994**, *64*, 309.
(107) Wiberg, E.; Wiberg, N.; Holleman, A. F. *Inorganic Chemistry*; Academic Press, 2001.
(108) Mazur, D. J.; Weinberg, N. L.; Abel, A. E.; U.S. Patent: 1989.
(109) Getman, G. D.; Rogers, J. E.; Hunter, W. E.; U.S. Patent: 2000.

(110) Abel, A. E.; Mouk, R. W.; Heyduk, A. F.; Blum, B. J.; Getman, G. D.; Steskal, M. D.; U.S. Patent: 1999.
(111) Wasse, J. C.; Hayama, S.; Skipper, N. T.; Benmore, C. J.; Soper, A. K. *The Journal of Chemical Physics* **2000**, *112*, 7147.
(112) Marzke, R. F.; Glaunsinger, W. S. *The Journal of Physical Chemistry* **1975**, *79*, 2976.
(113) Hall, S. S.; Lipsky, S. D.; McEnroe, F. J.; Bartels, A. P. *The Journal of Organic Chemistry* **1971**, *36*, 2588.
(114) Hall, S. S.; Bartels, A. P.; Engman, A. M. *The Journal of Organic Chemistry* **1972**, *37*, 760.
(115) Yamamura, S.; Nishiyama, S. In *Comprehensive Organic Synthesis - Selectivity, Strategy and Efficiency in Modern Organic Chemistry, Volumes 1 - 9*; Fleming, B. M. T. a. I., Ed. 1993; Vol. 8, p 307.
(116) Gu, Z.; Liang, F.; Chen, Z.; Sadana, A.; Kittrell, C.; Billups, W. E.; Hauge, R. H.; Smalley, R. E. *Chemical Physics Letters* **2005**, *410*, 467.
(117) Billups, W. E.; Liang, F.; Chattopadhyay, J.; Beach, J. In *209th ECS Meeting*; Electrochemical Society: 2007; Vol. 2.
(118) Borondics, F.; Bokor, M.; Matus, P.; Tompa, K.; Pekker, S.; Jakab, E. *Fullerenes, nanotubes, and carbon nanostructures* **2005**, *13*, 375.
(119) Borondics, F.; Jakab, E.; Pekker, S. *Journal of Nanoscience and Nanotechnology* **2007**, *4*, 1551.
(120) Peng, H.; Alemany, L. B.; Margrave, J. L.; Khabashesku, V. N. *Journal of the American Chemical Society* **2003**, *125*, 15174.
(121) Engel, P. S.; Billups, W. E.; Abmayr, D. W.; Tsvaygboym, K.; Wang, R. *The Journal of Physical Chemistry C* **2008**, *112*, 695.
(122) Liang, F.; Alemany, L. B.; Beach, J. M.; Billups, W. E. *Journal of the American Chemical Society* **2005**, *127*, 13941.
(123) Chattopadhyay, J.; Chakraborty, S.; Mukherjee, A.; Wang, R.; Engel, P. S.; Billups, W. E. *The Journal of Physical Chemistry C* **2007**, *111*, 17928.
(124) Chattopadhyay, J.; Sadana, A. K.; Liang, F.; Beach, J. M.; Xiao, Y.; Hauge, R. H.; Billups, W. E. *Organic Letters* **2005**, *7*, 4067.
(125) Mukherjee, A.; Combs, R.; Chattopadhyay, J.; Abmayr, D. W.; Engel, P. S.; Billups, W. E. *Chemistry of Materials* **2008**, *20*, 7339.
(126) Moniruzzaman, M.; Chattopadhyay, J.; Billups, W. E.; Winey, K. I. *Nano Letters* **2007**, *7*, 1178.
(127) Stephenson, J. J.; Sadana, A. K.; Higginbotham, A. L.; Tour, J. M. *Chemistry of Materials* **2006**, *18*, 4658.
(128) Clark, M. D.; Krishnamoorti, R. *The Journal of Physical Chemistry C* **2009**, *113*, 20861.
(129) Martínez-Rubí, Y.; Guan, J.; Lin, S.; Scriver, C.; Sturgeon, R. E.; Simard, B. *Chemical Communications* **2007**, 5146.
(130) Schmidt, G.; Gallon, S.; Esnouf, S.; Bourgoin, J. P.; Chenevier, P. *Chemistry - A European Journal* **2009**, *15*, 2101.
(131) Voiry, D.; Roubeau, O.; Pénicaud, A. *Journal of Materials Chemistry* **2010**, *20*, 4385.
(132) Guan, J.; Martinez-Rubi, Y.; Dénommée, S.; Ruth, D.; Kingston, C. T.; Daroszewska, M.; Barnes, M.; Simard, B. *Nanotechnology* **2009**, *20*, 245701.
(133) Deng, S.; Brozena, A. H.; Zhang, Y.; Piao, Y.; Wang, Y. H. *Chemical Communications* **2010**.

(134) Deng, S.; Zhang, Y.; Brozena, A. H.; Mayes, M. L.; Banerjee, P.; Chiou, W. A.; Rubloff, G. W.; Schatz, G. C.; Wang, Y. H. *Nature Communications* **2011**, *2*, 382.
(135) Gebhardt, B.; Syrgiannis, Z.; Backes, C.; Graupner, R.; Hauke, F.; Hirsch, A. *Journal of the American Chemical Society* **2011**.
(136) Wei, L.; Zhang, Y. *Chemical Physics Letters* **2007**, *446*, 142.
(137) Rowlands, G.; University of Sussex: 2006; Vol. 2011.
(138) Graupner, R.; Abraham, J.; Wunderlich, D.; Vencelová, A.; Lauffer, P.; Röhrl, J.; Hundhausen, M.; Ley, L.; Hirsch, A. *Journal of the American Chemical Society* **2006**, *128*, 6683.
(139) Maeda, Y.; Kato, T.; Hasegawa, T.; Kako, M.; Akasaka, T.; Lu, J.; Nagase, S. *Organic Letters* **2010**, *12*, 996.
(140) Fukuzumi, S.; Suenobu, T.; Hirasaka, T.; Arakawa, R.; Kadish, K. M. *Journal of the American Chemical Society* **1998**, *120*, 9220.
(141) Syrgiannis, Z.; Gebhardt, B.; Dotzer, C.; Hauke, F.; Graupner, R.; Hirsch, A. *Angewandte Chemie International Edition* **2010**, *49*, 3322.
(142) Bayazit, M. K.; Suri, A.; Coleman, K. S. *Carbon* **2010**, *48*, 3412.
(143) Chen, S.; Shen, W.; Wu, G.; Chen, D.; Jiang, M. *Chemical Physics Letters* **2005**, *402*, 312.
(144) Viswanathan, G.; Chakrapani, N.; Yang, H.; Wei, B.; Chung, H.; Cho, K.; Ryu, C. Y.; Ajayan, P. M. *Journal of the American Chemical Society* **2003**, *125*, 9258.
(145) Chen, S.; Chen, D.; Wu, G. *Macromolecular rapid communications* **2006**, *27*, 882.
(146) García-Gallastegui, A.; Obieta, I.; Bustero, I.; Imbuluzqueta, G.; Arbiol, J.; Miranda, J. I.; Aizpurua, J. M. *Chemistry of Materials* **2008**, *20*, 4433.
(147) Blake, R.; Coleman, J. N.; Byrne, M. T.; McCarthy, J. E.; Perova, T. S.; Blau, W. J.; Fonseca, A.; Nagy, J. B.; Gun'ko, Y. K. *Journal of Materials Chemistry* **2006**, *16*, 4206.
(148) Liang, F.; Beach, J. M.; Kobashi, K.; Sadana, A. K.; Vega-Cantu, Y. I.; James, M.; Billups, W. *Chemistry of Materials* **2006**, *18*, 4764.
(149) Billups, W. E.; Sadana, A. K.; Liang, F.; Hauge, R. H.; U.S. Patent: 2010.
(150) Bingel, C. *Chemische Berichte* **1993**, *126*, 1957.
(151) Camps, X.; Hirsch, A. *Journal of the Chemical Society, Perkin Transactions 1* **1997**, 1595.
(152) Nič, M. *IUPAC Compendium of Chemical Terminology Gold Book (1997)*; 2nd ed.; Oxford, 1997; Vol. 2.
(153) Coleman, K. S.; Bailey, S. R.; Fogden, S. n.; Green, M. L. H. *Journal of the American Chemical Society* **2003**, *125*, 8722.
(154) Worsley, K. A.; Moonoosawmy, K. R.; Kruse, P. *Nano Letters* **2004**, *4*, 1541.
(155) Niyogi, S.; Hamon, M. A.; Perea, D. E.; Kang, C. B.; Zhao, B.; Pal, S. K.; Wyant, A. E.; Itkis, M. E.; Haddon, R. C. *The Journal of Physical Chemistry B* **2003**, *107*, 8799.
(156) Moonoosawmy, K. R.; Kruse, P. *The Journal of Physical Chemistry C* **2009**, *113*, 5133.
(157) Dettlaff-Weglikowska, U.; Skákalová, V.; Graupner, R.; Jhang, S. H.; Kim, B. H.; Lee, H. J.; Ley, L.; Park, Y. W.; Berber, S.; Tománek, D.; Roth, S. *Journal of the American Chemical Society* **2005**, *127*, 5125.
(158) Umeyama, T.; Tezuka, N.; Fujita, M.; Matano, Y.; Takeda, N.; Murakoshi, K.; Yoshida, K.; Isoda, S.; Imahori, H. *The Journal of Physical Chemistry C* **2007**, *111*, 9734.
(159) Lee, R.; Kim, H.; Fischer, J.; Thess, A.; Smalley, R. E. *Nature* **1997**, *388*, 255.
(160) Rao, A. M.; Eklund, P. C.; Bandow, S.; Thess, A.; Smalley, R. E. *Nature* **1997**, *388*, 257.

(161) Kazaoui, S.; Guo, Y.; Zhu, W.; Kim, Y.; Minami, N. *Synthetic Metals* **2003**, *135-136*, 753.
(162) Kazaoui, S.; Minami, N.; Jacquemin, R.; Kataura, H.; Achiba, Y. *Physical Review B* **1999**, *60*, 13339.
(163) Takenobu, T.; Takano, T.; Shiraishi, M.; Murakami, Y.; Ata, M.; Kataura, H.; Achiba, Y.; Iwasa, Y. *Nature materials* **2003**, *2*, 683.
(164) Corio, P.; Santos, P. S.; Brar, V. W.; Samsonidze, G. G.; Chou, S. G.; Dresselhaus, M. S. *Chemical Physics Letters* **2003**, *370*, 675.
(165) Moonoosawmy, K. R.; Kruse, P. *Journal of the American Chemical Society* **2008**, *130*, 13417.
(166) Cheng, Q.; Debnath, S.; Gregan, E.; Byrne, H. J. *The Journal of Physical Chemistry C* **2010**, *114*, 8821.
(167) Baskaran, D.; Mays, J. W.; Bratcher, M. S. *Chemistry of Materials* **2005**, *17*, 3389.
(168) Chen, R. J.; Zhang, Y.; Wang, D.; Dai, H. *Journal of the American Chemical Society* **2001**, *123*, 3838.
(169) Zhang, J.; Lee, J. K.; Wu, Y.; Murray, R. W. *Nano Letters* **2003**, *3*, 403.
(170) Li, H.; Zhou, B.; Lin, Y.; Gu, L.; Wang, W.; Fernando, K. A. S.; Kumar, S.; Allard, L. F.; Sun, Y. P. *Journal of the American Chemical Society* **2004**, *126*, 1014.
(171) Zhao, J.; Lu, J. P.; Han, J.; Yang, C. K. *Applied Physics Letters* **2003**, *82*, 3746.
(172) Araki, S.; Seki, T.; Sakakibara, K.; Hirota, M.; Kodama, Y.; Nishio, M. *Tetrahedron: Asymmetry* **1993**, *4*, 555.
(173) Nishio, M.; Hirota, M.; Umezawa, Y. *The CH-[pi] interaction: Evidence, Nature, and Consequences*; Wiley-VCH, 1998; Vol. 21.
(174) Klopman, G. *Journal of the American Chemical Society* **1968**, *90*, 223.
(175) Wang, G.; Olofsson, G. *The Journal of Physical Chemistry B* **1998**, *102*, 9276.
(176) Yekeler, H. *Chemical Physics* **2001**, *270*, 391.
(177) Rothschild, W. G. *Journal of the American Chemical Society* **1972**, *94*, 8676.
(178) Roscigno, P.; Asaro, F.; Pellizer, G.; Ortona, O.; Paduano, L. *Langmuir* **2003**, *19*, 9638.
(179) Prasad, M.; Palepu, R.; Moulik, S. *Colloid & Polymer Science* **2006**, *284*, 871.
(180) Gurevitch, I.; Srebnik, S. *Chemical Physics Letters* **2007**, *444*, 96.
(181) Strano, M. S.; Huffman, C. B.; Moore, V. C.; Michael, J. O. C.; Haroz, E. H.; Hubbard, J.; Miller, M.; Rialon, K.; Kittrell, C.; Ramesh, S. *The Journal of Physical Chemistry B* **2003**, *107*, 6979.
(182) Zanette, D.; Froehner, S. J.; Minatti, E.; Ruzza, Â. A. *Langmuir* **1997**, *13*, 659.
(183) O'Connell, M. J.; Boul, P.; Ericson, L. M.; Huffman, C.; Wang, Y.; Haroz, E.; Kuper, C.; Tour, J.; Ausman, K. D.; Smalley, R. E. *Chemical Physics Letters* **2001**, *342*, 265.
(184) Boguslavsky, Y.; Fadida, T.; Talyosef, Y.; Lellouche, J. P. *Journal of Materials Chemistry* **2011**.
(185) Blanch, A. J.; Lenehan, C. E.; Quinton, J. S. *The Journal of Physical Chemistry B* **2010**.
(186) Feng, J.; Alam, S. M.; Yan, L. Y.; Li, C. M.; Judeh, Z.; Chen, Y.; Li, L. J.; Lim, K. H.; Chan-Park, M. B. *The Journal of Physical Chemistry C* **2011**.
(187) Doorn, S. K.; Strano, M. S.; Michael, J. O. C.; Haroz, E. H.; Rialon, K. L.; Hauge, R. H.; Smalley, R. E. *The Journal of Physical Chemistry B* **2003**, *107*, 6063.
(188) Lutz, T.; Donovan, K. J. *Carbon* **2005**, *43*, 2508.
(189) Zhang, X.; Liu, T.; Sreekumar, T. V.; Kumar, S.; Moore, V. C.; Hauge, R. H.; Smalley, R. E. *Nano Letters* **2003**, *3*, 1285.

(190) Li, L. J.; Nicholas, R.; Chen, C. Y.; Darton, R.; Baker, S. *Nanotechnology* **2005**, *16*, S202.
(191) Didenko, V. V.; Moore, V. C.; Baskin, D. S.; Smalley, R. E. *Nano Letters* **2005**, *5*, 1563.
(192) Shimamoto, D.; Muramatsu, H.; Hayashi, T.; Kim, Y. A.; Endo, M.; Park, J. S.; Saito, R.; Terrones, M.; Dresselhaus, M. S. *Applied Physics Letters* **2009**, *94*, 083106.
(193) Bravo-Sanchez, M.; Simmons, T. J.; Vidal, M. *Carbon* **2010**, *48*, 3531.
(194) Biswas, C.; Kim, K. K.; Geng, H. Z.; Park, H. K.; Lim, S. C.; Chae, S. J.; Kim, S. M.; Lee, Y. H.; Nayhouse, M.; Yun, M. *The Journal of Physical Chemistry C* **2009**, *113*, 10044.
(195) Hasan, T.; Scardaci, V.; Tan, P.; Rozhin, A.; Milne, W.; Ferrari, A. *Physica E: Low-dimensional Systems and Nanostructures* **2008**, *40*, 2414.
(196) Hasan, T.; Scardaci, V.; Tan, P. H.; Rozhin, A. G.; Milne, W. I.; Ferrari, A. C. *The Journal of Physical Chemistry C* **2007**, *111*, 12594.
(197) Manivannan, S.; Jeong, I. O.; Ryu, J. H.; Lee, C. S.; Kim, K. S.; Jang, J.; Park, K. C. *Journal of Materials Science: Materials in Electronics* **2009**, *20*, 223.
(198) Simmons, T. J.; Lee, S. H.; Park, T. J.; Hashim, D.; Ajayan, P.; Linhardt, R. *Carbon* **2009**, *47*, 1561.
(199) Hua, J.; Wang, Z.; Zhao, J.; Zhang, J.; Li, R.; Nie, H.; Sun, X. *Colloid & Polymer Science* **2011**, 1.
(200) Bonnet, P.; Buisson, J.; Martyr, N. N.; Bizot, H.; Buelon, A.; Chauvet, O. *Physical Chemistry Chemical Physics* **2009**, *11*, 8626.
(201) Chattopadhyay, J. *Chemistry of Carbon Nanomaterials: Uses of Lithium Nanotube Salts in Organic Syntheses and Functionalization of Graphite*; Rice University, 2008.
(202) Bodas, D.; Khan-Malek, C. *Microelectronic engineering* **2006**, *83*, 1277.
(203) Socrates, G. *Infrared and Raman Characteristic Group Frequencies: Tables and Charts*; Wiley, 2004.
(204) Roubeau, O.; Lucas, A.; Penicaud, A.; Derre, A. *Journal of Nanoscience and Nanotechnology* **2007**, *7*, 3509.
(205) Chen, R.; Kafafi, S.; Stein, S. *Journal of the American Chemical Society* **1989**, *111*, 1418.
(206) Pénicaud, A.; Poulin, P.; Derré, A.; Anglaret, E.; Petit, P. *Journal of the American Chemical Society* **2005**, *127*, 8.
(207) Birch, A. J.; Hinde, A. L.; Radom, L. *Journal of the American Chemical Society* **1980**, *102*, 3370.
(208) Buick, A.; Kemp, T. J.; Stone, T. J. *The Journal of Physical Chemistry* **1970**, *74*, 3439.
(209) Szwarc, M.; Levy, M.; Milkovich, R. *Journal of the American Chemical Society* **1956**, *78*, 2656.
(210) Ueno, K.; Williams, F.; Hayashi, K.; Okamura, S. *Transactions of the Faraday Society* **1967**, *63*, 1478.
(211) Szwarc, M.; Asami, R. *Journal of the American Chemical Society* **1962**, *84*, 2269.
(212) O'Driscoll, K.; Boudreau, R.; Tobolsky, A. *Journal of Polymer Science* **1958**, *31*, 115.
(213) O'Driscoll, K.; Tobolsky, A. *Journal of Polymer Science* **1958**, *31*, 123.
(214) O'Driscoll, K.; Tobolsky, A. *Journal of Polymer Science* **1959**, *37*, 363.
(215) Chakrabarti, N.; Jacobus, J. *Macromolecules* **1988**, *21*, 3011.
(216) Kato, Y.; Kanda, K.; Haruyama, Y.; Matsui, S. *Japanese Journal of Applied Physics* **2006**, *45*, 8839.

(217) Atkins, P. W.; Paula, J. D. *Physical Chemistry*; W.H. Freeman, 2006.
(218) Koshio, A.; Yudasaka, M.; Zhang, M.; Iijima, S. *Nano Letters* **2001**, *1*, 361.
(219) Pfeiffer, R.; Kuzmany, H.; Simon, F.; Bokova, S.; Obraztsova, E. *Physical Review B* **2005**, *71*, 155409.
(220) Dresselhaus, M. S.; Jorio, A.; Hofmann, M.; Dresselhaus, G.; Saito, R. *Nano Letters* **2010**, *10*, 751.
(221) Mansfield, E.; Kar, A.; Hooker, S. A. *Analytical and Bioanalytical Chemistry* **2010**, *396*, 1071.
(222) Wajid, A. S.; Das, S.; Irin, F.; Ahmed, H.; Shelburne, J. L.; Parviz, D.; Fullerton, R. J.; Jankowski, A. F.; Hedden, R. C.; Green, M. J. *Carbon* **2011**, *50*, 526.
(223) Wenseleers, W.; Vlasov, I. I.; Goovaerts, E.; Obraztsova, E. D.; Lobach, A. S.; Bouwen, A. *Advanced Functional Materials* **2004**, *14*, 1105.
(224) Ao, G.; Nepal, D.; Aono, M.; Davis, V. A. *ACS Nano* **2011**.
(225) Saraydin, D.; Karadağ, E. *Polymer Bulletin* **2000**, *44*, 501.
(226) Carey, F. A. *Organic Chemistry*; McGraw-Hill, 2003.
(227) Türker, L.; Güner, A.; Yigit, F.; Güven, O. *Colloid & Polymer Science* **1990**, *268*, 337.
(228) Bhajantri, R.; Ravindrachary, V.; Poojary, B.; Harisha, A.; Crasta, V. *Polymer Engineering & Science* **2009**, *49*, 903.
(229) Liu, T.; Chen, J.; Sugihara, S.; Maeda, Y. *Colloid & Polymer Science* **2012**, 1.
(230) Maeda, Y.; Nakamura, T.; Ikeda, I. *Macromolecules* **2002**, *35*, 217.
(231) Zhang, X. K.; Lewars, E. G.; March, R. E.; Parnis, J. M. *The Journal of Physical Chemistry* **1993**, *97*, 4320.
(232) Behera, M.; Ram, S. *Applied Nanoscience* **2012**, x.
(233) Behera, M.; Ram, S. *Journal of Inclusion Phenomena and Macrocyclic Chemistry* **2012**, *72*, 233.
(234) Gu, Y.; Kar, T.; Scheiner, S. *Journal of the American Chemical Society* **1999**, *121*, 9411.
(235) Scheiner, S.; Kar, T. *The Journal of Physical Chemistry A* **2002**, *106*, 1784.
(236) Senatore, D.; Berix, M. J. A.; Laven, J.; van Benthem, R. A. T. M.; de With, G.; Mezari, B.; Magusin, P. C. M. M. *Macromolecules* **2008**, *41*, 8020.

Appendix A

Experimental Methods

A.1 Experimental Methods, Materials, and Instrument Details

A1.1.1 Materials and Preparations

CoMoCAT SWNT (Grade CG200, Lot # 0004) were purchased direct from SouthWest NanoTechnologies. The SWNT had an average diameter of 1.01 +/- 0.3 nm and an average aspect ratio of 1000. The residual catalyst impurity was measured to be ~8 wt. % by TGA in air. Approximately 10 wt. % of the total carbon content was found to be DWNT and MWNT by TGA, Raman, and TEM. The relative metallic SWNT content was approximately 48 %, compared to 37 % in HiPco SWNT.[1]

Polylite 31003-00 unsaturated isophthalic polyester base resin having 40 wt. % styrene monomer was obtained from Reichhold (Lot # 632889). The resin was un-promoted and un-filled. The steady-shear viscosity was measured to be 1.73 Pa-s at 20°C using a 50 mm cone and plate rheometer.

Molecular sieves (0.3 nm, Grade 564, 8 - 12 mesh size) were purchased from Mallinckrodt and regenerated before use by heating in a furnace. An amount of molecular sieves were placed in a clean ceramic dish in a shallow layer and covered with aluminum foil. The dish was held at 250°C overnight to drive off water. After approximately 18 hr, the dish was moved to a vacuum oven and allowed to cool to room temp under vacuum (10^{-2} mbar). The cool and dry sieves were moved to clean vials, capped, and stored in a vacuum desiccators until use.

Ultra-high purity argon was purchased from Airgas. The gas was passed through a DRIERITE (# 26800) laboratory gas drying unit packed with 1.25 lb of 8 mesh color indicating calcium sulfate desiccant, rated to dry air to a dew point of -100°F. The dry argon was used to purge and blanket all reactions.

Anhydrous ammonia (15 lb, size 80 tank for safety considerations) was purchased from Airgas and metered with the properly rated corrosion-proof gas regulator. Dry ice was made as required by venting saturated liquid from a cylinder of carbon dioxide (Airgas) equipped with a siphon tube to atmospheric pressure in a denim bag. This was stored in an insulated bucket.

The monomers and reagents used for the in-situ polymerization study were stored in a cool dark cabinet in a vacuum desiccator. Styrene (99.5 % purity, stabilized with 4-tert-butylcatechol, 50 mL) was purchased from Alfa Aesar (# 16199) and stored over molecular sieves. The styrene used (Lot # 10158085) had 99.9 % purity and 10 - 15 ppm stabilizer. Methyl methacrylate (99 % purity, stabilized with 4-methoxyphenol, 10 g/100 mL) was purchased from Alfa Aesar (# A13030). 1-Iodododecane (98 % purity, stabilized with copper, 25 g) was purchased from Alfa Aesar (# A11909). Lithium granules (99 %) packed under argon were purchased from Alfa Aesar. Figure A.1 displays the general experimental setup. Dry argon entered from the right hand port on the reaction flask and exited out the left port to the bubbler. The condenser was fit into the center port of the reaction flask. Anhydrous ammonia was fed to the port on top of the dry ice condenser.

Figure A.1: General experimental setup for polymerization reaction studies.

For the Bingel reaction study, 1,2-dichlorobenzene (oDCB) was purchased from three different suppliers. Preliminary studies used certified grade oDCB (> 99 %, 1 L) purchased from Fisher Chemical (# 02231). The majority of experiments reported herein used anhydrous oDCB (99 %, 1 L) purchased from Sigma Aldrich (# 240664). Experiments were also carried out using oDCB (99 %, 500 g) purchased from Alfa Aesar (# A13881) and stored over molecular sieves. The solvent from Alfa Aesar was used to rule out experimental artifacts affecting the Bingel reaction and sonopolymerization. The reagent 1,8-diazabicyclo[5.4.0]-7-undecene (DBU, > 98 %, 25 g) was purchased from TCI America (# D1270) and stored over molecular sieves. The reagent diethyl bromomalonate (90+ %, 25 g) was purchased from Alfa Aesar (#A10965) and capped under argon to keep dry. Concerns over the acidity of molecular sieves towards the carbonyl in diethyl bromomalonate appeared to be unfounded based on ATR-FTIR analysis of the product after even months of storage with sieves. Nevertheless, fresh reagent was purchased halfway through all experiments. Figure A.2 displays the experimental setup. Dry argon entered

from the right port and exited out the left port to the oil bubbler pictured in the rear. The stir plate was replaced with a bath sonicator.

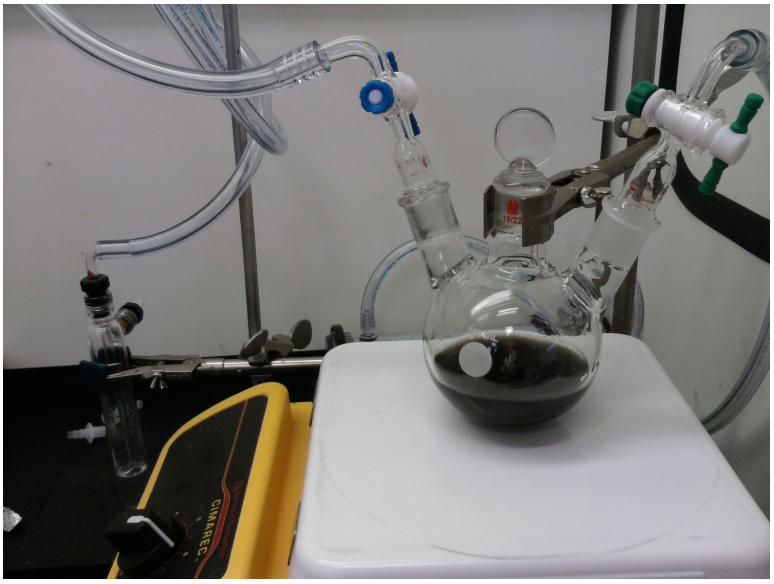

Figure A.2: General experimental setup for Bingel reaction studies.

Reagents used for the small molecule functionalization of nanotubes were as follows: Methyl 4-bromobenzoate (98+ %, 5 g) was purchased from Alfa Aesar (# A15517). 9-Bromophenanthrene (98 %, 25 g) was purchased from Alfa Aesar (# L09033). Ethyl alpha-bromophenylacetate (97 %, 10 g) was purchased from Alfa Aesar (# B21114). 4-Iodoaniline (98 %, 25 g) was purchased from Sigma Aldrich (# 129364). 3-Bromo-1-propanol (97 %, 5 g) was purchased from Sigma Aldrich (# 167169). 2-Dodecanone (> 97 %, 25 mL) was purchased from Sigma Aldrich (#30720). Acetone (HPLC, 99.8 %) was purchased from Acros Organics. Tetrahydrofuran (99.9 %, extra dry, anhydrous, 1 L, Acroseal) was purchased from Sigma Aldrich and was not stabilized. The isomer n-Hexane (anhydrous) was purchased from Alfa Aesar (# 43263).

Pellets for transmission FTIR were processed using potassium bromide (FT-IR grade, > 99 %) purchased from Sigma Aldrich (# 221864).

Polyvinylpyrrolidone (Ave. MW 58,000) was purchased from Acros Organics (K29-32) and desiccated.

Methyllithium (1.6 M in diethyl ether, 100 mL, Acroseal) was purchased from Acros Organics. To avoid syringe transfer, this reagent was handled in an argon purged bag by pipette and dripped into cold reaction flasks containing dry tetrahydrofuran. Tetrahydrofuran (99.9 %, extra dry, anhydrous, 1 L, Acroseal) was purchased from Sigma Aldrich and was not stabilized.

General use solvents were as follows: Acetone (ACS grade, 99.5 % min) was purchased from BDH. Reagent grade ethanol (ACS grade, 99.5 % alcohols) was purchased from BDH and was denatured with alcohols only. Isopropanol (BDH, 99 %) was purchased from BDH. Mixed isomer hexanes (ACS grade, > 60 % n-hexane) was purchased from BDH. Chloroform (HPLC, 99.5+ %) was purchased from Alfa Aesar. Dimethyl sulfoxide (ACS grade) was purchased from BDH. N,N-dimethylacetamide (HPLC, 99.5+ %) was purchased from Alfa Aesar (# 22916).

All reaction flasks were cleaned with dish soap and brush than kept overnight in ~1 M potassium hydroxide base bath. The base bath recipe used called for 2 L of general use ethanol, 0.5 L deionized water, and 150 g KOH. After rinsing with copious amounts of tap water, glassware was rinsed with deionized water, then finally acetone and checked for any visible residues.

A1.1.2 - Instrumentation Details and Experimental Techniques

ATR-FTIR experimental setup details were as follows: A Thermo Scientific Nicolet iS10 mid infrared spectrometer equipped with a Smart iTR ATR accessory was used for FT-IR measurements. The iS10 was equipped with a liquid nitrogen cooled mercury cadmium telluride (MCT-A) detector with a low wavenumber cutoff of 600 cm^{-1}. Experiments were carried out with 64 scans and resolution of 4, giving a data spacing of 0.482 cm^{-1}. The detector optical

velocity was set at 1.8988 cm/s. Both diamond and germanium single-bounce ATR crystals were used. Liquid samples were simply placed on a clean crystal. For solid samples such as powders and films, the high pressure clamp was used and was equipped with a 10,000 psi clutch. The diamond crystal had a depth of penetration of 2.03 μm at 1000 cm^{-1} and a refractive index of 2.4. The low wavenumber cutoff was 650 cm^{-1} in diamond and this crystal had an intrinsic absorption from 2300 to 1800 cm^{-1}. The germanium crystal had a high refractive index of 4.0 and a shallow depth of penetration of 0.67 μm at 1000 cm^{-1}, ideal for highly absorbing samples. The low wavenumber cutoff for Ge was 700 cm^{-1}. Crystals were cleaned using an appropriate solvent for the sample used and always wiped last with acetone before background spectrum collection. Liquid nitrogen was purchased from Airgas and dispensed into a Nalgene HDPE Dewar flask. The internal optics of the system was continuously purged with bone-dry instrument air.

Transmission FTIR spectra were collected using a Nicolet AVATAR 360 ESP spectrometer. KBr discs were fabricated by compressing 100 mg of KBr powder plus a tiny amount of sample in a twin polished screw pellitizer, held in a vise. Powders containing SWNT or sonopolymer were first ground in an agate mortar until uniformly grey.

FTIR spectra of TGA oven effluent gases was analyzed using a Thermo Scientific Nicolet iZ10 auxiliary module. The TGA-IR interface was used in conjunction with the iZ10 module. The iZ10 was connected as a sidecar to the iS10 unit. The iZ10 contained a deuterated L-alanine doped triglycine sulfate - cesium iodide (DTGS-CsI) detector with KBr optics, having a low wavenumber cutoff of 350 cm^{-1}. Experiments were carried out with 8 scans and resolution of 8, giving a data spacing of 0.964 cm^{-1}. This was found to be an acceptable balance between speed and resolution. The detector optical velocity was set at 0.4747 cm/s. The beam was passed

through a KBr window on a quartz glass gas cell regulated at 250°C. The effluent from the TGA oven was transferred through a heat traced stainless steel transfer line to the quartz gas cell and was regulated at 225°C. Gases exited the unit and were vented to the hood with no additional pumping required.

SEM samples were prepared by applying double sided carbon tape to a JEOL specimen mount stub and pressing powders to the surface using clean spatula or tweezers. Liquid samples were dropped directly onto the specimen mount stub. Materials of interest were examined using a JEOL 7000-F field emission-scanning electron microscope equipped with a Princeton Gamma-Tech energy-dispersive X-ray (EDS) detector. Samples were always imaged at a working distance of ~10 mm by adjusting the area of interest to the focal point/length of the beam. Typically, accelerating voltages of 15 or 20 kV were used, as indicated in each image.

TEM measurements were carried out at Florida State University using a JEOL ARM200F transmission electron microscope and imaged with an 80 kV acceleration voltage. SWNT residues were swirled with a small amount of isopropyl alcohol and dropped onto a TEM grid for analysis.

Optical micrographs were recorded using a Nikon Eclipse 80i optical microscope. Samples were illuminated by either transmission or reflected light and images were recorded digitally. Both 10x (0.3 NA) and 20x (0.45 NA) Nikon Luminous Universal plan fluor objectives were used without oil immersion. Either 1x or 2x magnification was also applied before the camera. Images were collected and processed ImagePro software by MediaCybernetics. Scale bars were calibrated and applied by means of a manufacturer supplied optical micrometer.

Raman spectra were obtained using a Renishaw inVia Raman microscope with a Leica optical microscope used to focus on the surface of interest. A Leica 50x (0.75 NA) N-plan objective

was always used for measurements. For 514 nm wavelength irradiation a Spectra-Physics 263C air-cooled ion laser was used. For 785 nm irradiation an Innovative Photonics Solutions, Inc. laser was used. All measurements were taken under ambient conditions. A total of 10 scans from a Raman shift of 3200 - 100 cm^{-1} were collected with a 10 s sample exposure time. The incident lasers were polarized by the microscope. Laser powers for SWNT analysis were set to 1 % for 785 nm and 5 % for 514 nm. These were the minimum power levels required for acceptable signal to background noise intensity in bulk SWNT samples. The instrument detector was calibrated by referencing the Raman shift to that of Si.

A Varian Cary 3E UV-Vis spectrophotometer was used for absorbance measurements. Samples were placed in a Starna semi-micro quartz cell with 10 mm path length and compared to a background of pure solvent. Typical scans were taken over a range on wavelengths from 800 - 200 nm.

The thermal stability of samples was characterized using a Q50 thermogravimetric analyzer (TGA) from TA Instruments, with integrated mass flow controllers. Gases were fed to the controllers at 15 psi. The microbalance was always purged with 10 mL/min ultra-high purity argon during use. Ultra-high purity argon or compressed air was used as sample purge gas with a flowrate of 90 mL/min. The standard furnace was exchanged for a quartz-lined evolved gas analysis furnace (~15 mL volume) and was connected to the heat-traced FTIR transfer line using an insulated Swagelock fitting. Only 100 μL platinum sample pans were used. For experiments in argon, typical measurements included a 20 min hold with 90 mL/min argon to both the balance and sample to purge any air. After this time, flowrates were decreased to 100 mL/min total and the test was started. A temperature ramp at 10°C/min to 120°C allowed time for the gases to stabilize. Samples were held at 120°C for a minimum of 30 min to drive off water

vapor. If coupled FTIR measurements were desired, background spectra were taken at this time. Finally, the temperature was ramped at 10°C/min to 800°C and held for 45 min. TGA pans were cleaned of catalyst residue by bath sonication in a 10 vol. % solution of nitric acid (70 %) in water. After rinsing the pan in clean organic solvent, the pan was flame cleaned using a butane torch before use.

Rheological experiments were performed using an Anton Paar Physica MCR 301 series rheometer. The torque limit for this instrument was 0.1 μNm with a torque resolution down to 0.001 μNm. The temperature of the lower plate was controlled using the P-PTD200 Peltier temperature control device located below the lower shear plate. Surrounding the upper plate was the H-PTD200 Peltier controlled hood. Both Peltier controlled devices were counter cooled with a Julabo F12 water recirculation bath maintained at 20°C. The Anton Paar CP50-2 cone and plate fixture was used for all measurements. The cone radius used in all experiments was 24.9985 mm with a cone angle α of 2.018°. The cone truncation and distance between the center of the upper and lower surfaces was constant at 52 μm for all measurements. At these distances the required sample volume was 1.14 mL and the gap distance at the edge was calculated to be 0.933 mm.

All rheology measurements were taken just below room temperature at 20°C in order to limit styrene evaporation. To load the instrument, an appropriate volume of sample was placed on the lower plate and the upper measuring surface was lowered to the proper gap. The gap-setting velocity of the upper plate was slowed upon close approach so as to not destroy the sample structure. The top plate was stopped at a gap of 65 μm so that excess sample could be removed. Excess sample was trimmed from the plate edge using a rubber policeman in order to eliminate

error from edge effects and the measuring position was set at 52 μm. The normal force was zeroed and the sample was given 10 min to achieve thermal equilibrium.

For oscillatory measurements, a sinusoidal varying strain wave $\gamma = \gamma_0 \sin(\omega t)$ of amplitude γ_0 was imposed on the sample, and the steady-state stress response was measured as a function of angular frequency, ω. The stress wave was of the form $\tau = \gamma_0[G' \sin(\omega t) + G'' \cos(\omega t)]$, where G' and G'' represent the storage and loss modulus, respectively. The magnitude of the complex modulus, G^*, was defined as $|G^*| = [(G')^2 + (G'')^2]^{1/2}$ and the complex viscosity, η^*, as $|\eta^*| = |G^*|\omega^{-1}$. All oscillatory measurements were performed within the linear viscoelastic regime of the fluid, which was experimentally determined using controlled frequency, variable strain measurements.

Controlled frequency, variable strain measurements were first performed to probe the structural stability of the sample and identify the range of linear viscoelastic strain. A controlled strain was imposed on the sample at a fixed frequency of 10 s^{-1} and the resulting storage and loss moduli were measured. When the storage modulus showed nonlinear behavior, the test was stopped and repeated to ensure the critical strain was correctly identified.

Controlled strain oscillatory measurements were carried out at variable angular frequency. The strain set point was chosen to be inside the linear viscoelastic regime. The typical measured frequency range was from 100 - 0.1 rad/s. For efficiency, all controlled strain oscillatory measurements were run from high to low frequency so that the long measuring times associated with the lowest frequencies could be terminated if the data was outside the measurable range of the torque transducer.

Shear mixer components were purchased primarily from Ace Glass. The flask head used in this work featured three top joints for access to the flask contents and a Teflon coated lower joint

(optional). The flask bottom was a round bottom type with a capacity of 50 mL. A 10 mm Trubore glass bearing and a 10 mm diameter Trubore Teflon coated, steel stirring shaft was used. A stock 48 mm wide Teflon stirring blade was purchased (Ace Glass) and hand cut to size. This was then affixed to the shaft using general use nylon hardware (screw, washers, two nuts) and offset with the center of the shaft. The offset geometry prevented settling on the bottom of the flask and provided sufficient "pumping" as required to apply shear to the entire sample over time. The stirring shaft was driven using a 1/4 hp solid state laboratory stirrer (Ace Glass) with a maximum output speed of 4,000 rpm. The motor was mounted upside down and connected to a 36" flexible stirring shaft linked via a nylon chuck. The mixer was then assembled and purged with ultra high purity argon (Airgas) before being sealed with oil to prevent humidity from interfering with the sample. Alignment between the bearing and shaft was ensured before sealing in order to prevent damaging the components and shredding the Teflon coating off the shaft and into the sample. A final adjustment was made to the mixing shaft after alignment where the chuck was loosened and a downward force was applied so that contact between the mixing blade and flask sidewall was maintained. The flask and contents were then submerged in a room temperature water bath with volume approximately 10 times the sample volume. This bath was simply used to absorb excess heat, although its effect was not studied. To facilitate initial dispersion, samples were mixed for 24 h under low shear rate, high shear stress conditions (lots of downforce and impeller/flask contact). Next, the impeller force was decreased and the mixer was run at approximately 500 - 1,000 RPM for 72 hours with intermittent stops (approximately 3) to allow the sample to settle off the flask wall.

The sample loading procedure was as follows: SWNT were weighed out on to the crease of a unfolded weighing paper. The weighing paper containing SWNT was closed and placed into the

mixer flask, which was held horizontally. The flask itself was also lined with two overlapping pieces of weigh paper. Once the sample was fully inserted, the flask was turned upright and gently tapped to empty the SWNT to the flask bottom. The SWNT weighing paper was removed when empty and the flask contents inspected to ensure the papers lining the flask were clean and could be removed as well. An appropriate mass of resin was poured directly into the tared flask wile monitoring the weight on a scale to ensure a proper volume was loaded.

Samples for freeze drying were transferred to a 50 mL disposable polypropylene centrifuge tube and placed in a standard freezer at -10°C for 2 hours. The centrifuge tube was angled during this step to increase the surface area exposed to vacuum. The frozen sample was then sealed with pierced laboratory film and placed inside a cold freeze-drying flask that was wrapped with insulation to prevent any sample melting. The flask was then connected to the manifold of a Labconco FreeZone 4.5 lyophilization chamber, and held for at least 36 h at -50°C and 0.0251 mbar.

Bath sonication was carried out using a One-Pint ultrasonic cleaner purchased from Cole Parmer and filled with tap water. The water volume (~450 mL) was adjusted until the surface of the water-filled sonicator was disturbed by a concentric ring pattern. The system had an effective operating frequency of 55 kHz. The output power was reported to be 20 W but the effective power is decreased depending on the nature of the container and solvent used.

A Vibra-Cell VC 750 from Sonics was used for tip sonication. A 1/2" probe with replaceable tip composed of Ti-6Al-4V alloy was used. The unit was rated at 750W with an operating frequency of 20 kHz.

Centrifugation was carried out using an accuSpin Micro 17 centrifuge purchased from Fisher Scientific. Polypropylene microcentrifuge tubes with 2 mL capacity were used.

References A1

(1) Naumov, A. V.; Kuznetsov, O. A.; Harutyunyan, A. R.; Green, A. A.; Hersam, M. C.; Resasco, D. E.; Nikolaev, P. N.; Weisman, R. B. *Nano Letters* **2009**, *9*, 3203.